

THE UNIVERSITY OF HULL

Laser-Generated Ultrasound with Applications  
to Non-destructive Evaluation

being a Thesis submitted for the Degree of

Doctor of Philosophy

in the University of Hull

by

Jeremy Adrian Cooper, B.Sc. (Hull)

May 1985



## IMAGING SERVICES NORTH

Boston Spa, Wetherby

West Yorkshire, LS23 7BQ

[www.bl.uk](http://www.bl.uk)

**BEST COPY AVAILABLE.**

**VARIABLE PRINT QUALITY**

Summary of Thesis submitted for Ph.D. degree

by J.A. Cooper

on

Laser-Generated Ultrasound with Applications

to Non-destructive Evaluation

The generation of ultrasound by laser interaction with materials was first studied by White in 1963. Since this time work has been published on both generation in liquids and solids using CW and pulsed lasers. It was first noted by Bondarenko in 1976, that laser generated ultrasound could be applied usefully to non-destructive evaluation (NDE). This method of generation has a major advantage over conventional methods of ultrasonic NDE, which involve the use of piezoelectric transducers acoustically bonded to material surfaces; the laser source is non-contacting giving it a wider range of applications. The present study was undertaken to fully characterise the acoustic source for its use as a new tool in NDE, and to explore some of the potential NDE techniques most suited to the laser-acoustic source.

A neodymium/YAG laser has been used to produce pulses of infra-red radiation which then interact with a metal surface to generate ultrasound. Such acoustic disturbances contain fast transients in contrast to conventional piezoelectric transducers. The transient nature of the source allowed a range of accurate "time-of-flight" and imaging techniques to be employed for NDE after first characterising the directional behaviour of the various acoustic modes.

In order to fully utilise the acoustic transients it was necessary to use wide bandwidth displacement transducers as acoustic detectors. Ideally these detectors should themselves be non-contacting so that both generation and detection can be carried out remotely. Results have been obtained using a laser interferometer developed by UKAEA, Harwell. However, other investigative work used a modified form of the capacitance type transducer. This capacitance transducer has been developed and characterised and has proved invaluable for the time-of-flight techniques.

Using displacement transducers it has been possible to compare acoustic disturbances from different generation mechanisms with displacements predicted by extended theoretical models originally used in seismology. It was found that the laser-acoustic source simulated natural impulsive acoustic emission events and could therefore be used as a diagnostic model in the development of acoustic emission applications.

A range of NDE techniques have been investigated: including visualisation of laminar defects with high spatial resolution, depth measurement of surface breaking cracks, thickness measurement of metal foils and plates, and imaging techniques to detect bulk flaws.

## ACKNOWLEDGEMENTS

There are many people who have contributed in one way or another throughout the course of this work and I would like to thank them all. In particular I would like to acknowledge the encouragement and assistance given by my supervisors, Dr. Stuart Palmer and Dr. Richard Dewhurst, and the help and enthusiasm provided by my friends and colleagues, Chris Edwards, Alan Aindow, Dave Hutchins and Steve Taylor. Thanks also go to Judy for typing the thesis and to the members of the technical staff for providing me with numerous, machined, pieces of metal and various mechanical devices. I would like to give a special thanks to Catherine for looking after me for the last few years and to my parents who have supported me in every way for more than the last few years.

# C O N T E N T S

## ACKNOWLEDGEMENTS

<u>Chapter</u>	<u>Title</u>	<u>Page</u>
1	INTRODUCTION	1
1.1	A Short Review of Laser Generated Acoustics	2
1.2	Work Covered by the Thesis	6
2	ACOUSTIC PROPAGATION IN SOLIDS	9
2.1	Stress-Strain Relationships	10
2.2	The Equation of Motion for an Isotropic Elastic Solid	14
2.3	Boundary Reflection	17
2.4	The Rayleigh Surface Wave	20
2.5	Propagation of Acoustic Transients	22
3	SURFACE FORCES GENERATED BY LASER-SURFACE INTERACTIONS	26
3.1	The Thermoelastic Source	27
3.2	The Plasma Source	34
3.3	The Oil-Layer Source	37

4	LASER GENERATED ACOUSTIC TRANSIENTS	40
4.1	The Thermoelastic Source	42
4.1.1	Surface Displacements from an Extended Source	42
4.1.2	Surface Displacements from a Point Source	49
4.1.3	Epicentre Displacements	63
4.2	The Plasma Source	68
4.2.1	Surface Displacements	68
4.2.2	Epicentre Displacements	70
4.3	Modified Surfaces	71
4.4	Multiple Arrivals	73
4.5	Absolute Displacements	75
4.6	The Plasma Driving Force	77
5	DIRECTIVITY OF THE LASER-ACOUSTIC SOURCE	82
5.1	Radial Displacements	83
5.2	Tangential Displacements	88
5.3	Experimental Directivity	90
5.4	Wavefront Energies	93
6	ACOUSTICS IN MATERIALS EVALUATION	98
6.1	Piezoelectric Transducers	99
6.2	The Shadow Technique	100
6.3	The Pulse-Echo Technique	101
6.4	Acoustic Emission	102
6.5	Application of the Laser-Acoustic Source to NDE	103

7	WIDEBAND ACOUSTIC TRANSDUCERS	106
7.1	Capacitance Transducers	106
7.1.1	The Spherical Capacitance Transducer	107
7.1.2	The Arc Capacitance Transducer	113
7.2	Electro-Magnetic Acoustic Transducers	115
7.3	Thick Piezoelectric Transducers	117
7.4	Laser Interferometer Detectors	119
8	LAMINAR DEFECT TESTING	121
8.1	The Testing of Plasma Sprayed Coatings	121
8.2	Amplitude Versus Time-of-Flight Measurements	123
8.3	Automated, Time-of-Flight, C-Scans	125
8.4	Laser Generation and Detection	129
8.5	Plate Thickness Measurement	130
9	SURFACE WAVE - DEFECT INTERACTIONS	132
9.1	Conventional Methods of Crack Depth Estimation	133
9.2	Pulse-Echo Surface Defect Location	134
9.3	Multiple Source-Detector Echo Enhancement	138
9.4	Acoustic Spectroscopy	140
9.5	Time Domain Analysis	144
9.6	Surface Pulse - Defect Interaction Process	147
9.6.1	Reflection from Narrow and Wide Slots	148
9.6.2	Interaction with a Down Step	149
9.6.3	Interaction with 90° and 270° Corners	149
9.7	Rayleigh-Shear-Rayleigh Interaction	150

10	SUMMARY AND CONCLUSIONS	153
APPENDIX 1	NUMERICAL AND COMPUTATION METHODS	
A.1	Chao's Solution for the Surface Displacement	159
A.2	The Elliptic Integrals	161
A.3	The Extended Thermoelastic Source	163
A.4	The Point Thermoelastic Source	164
A.5	Numerical Bandwidth Limitation	167
A.6	Wavefront Amplitude Directivity	168
A.7	Energy Partition for the Laser-Acoustic Source	170
A.8	The Spherical Capacitance Probe	171
REFERENCES		175

## CHAPTER 1

## INTRODUCTION

Generation of acoustic waves from the interaction of a laser beam with matter has been known since the early days of the development of the laser in 1960. For a solid, these acoustic waves propagate both into the bulk and along the surface of the material, and if the solid is within a gaseous environment, then acoustic waves also propagate into the gas. This latter phenomenon is known as the photo-acoustic effect and the acoustic waves - which depend upon the laser parameters and the physical properties of the surface material - have been investigated extensively. The acoustic waves that propagate in solids have been studied less thoroughly. From lasers producing short pulses these waves have a wide range of frequency components, extending well into the ultrasonic range, ( $> 30\text{KHz}$ ) and it is this phenomenon which is the subject of this thesis.

The acoustic energy generated by the interaction of a laser beam with solids has been suggested as an acoustic source for non-destructive evaluation (NDE). Conventional methods of acoustic generation in NDE are dominated by the use of piezoelectric transducers. These transducers require acoustic bonding to the sample over a relatively large area of contact and are restricted to certain operating environments. The non-contacting nature of laser-acoustic sources can circumvent these problems and these sources could prove to be a valuable tool for NDE.

The collimated optical beam from a laser provides a versatile method of transporting energy to a particular site where it can be

concentrated by optical means. The acoustic waves generated by this source of optical energy possess well defined and unique characteristics. It is these fundamental properties, as we shall see later, that provide a potentially useful acoustic source for the non-destructive evaluation of materials.

The first demonstration of the generation of acoustic waves by the interaction of a laser beam with an opaque solid material was by White (1962) following shortly after the invention of the laser itself in 1960. Many workers have subsequently investigated the phenomenon of laser generated acoustics. Calder and Wilcox (1973) and Giglio (1973) were the first to report the possibility of the use of laser generated acoustics for flaw detection.

#### 1.1 A SHORT REVIEW OF LASER GENERATED ACOUSTICS

White (1962) demonstrated the existence of high frequency elastic waves produced by the irradiation of a solid with a laser light pulse. This was followed by an analysis of the generation mechanism (White, 1963) which considered a one-dimensional model of thermal absorption, expansion and elastic wave propagation from the absorption of the laser light pulse. Ready (1965) carried out a similar one-dimensional study and predicted temperature changes and elastic wave generation at the surface of a metallic solid, and also included a calculation of material ablation at high laser power densities with the resulting elastic wave generation from the different mechanism of material recoil rather than thermally generated forces. Brienza (1967) demonstrated experimentally the existence of very high frequency elastic waves from the interaction of a picosecond pulse train from a mode-locked laser with a metallic

film. Brienza measured acoustic frequencies of 200MHz due to the repetition rate of the laser output and 2GHz generated by a single mode-locked laser pulse. Percival (1967) used the in-depth absorption of a laser beam in a glass rod to produce thermally generated elastic Love waves. The Love waves were then used in the first application of the laser-acoustic source, to predict the elastic constants of the glass material. Lee (1968) was the first to detect the existence of laser generated surface acoustic waves using an aluminium film as the absorption surface and a 5MHz interdigital transducer to detect the Rayleigh surface wave. These Rayleigh surface waves are an important product of the laser-acoustic source. Peercy (1970) also used a picosecond laser pulse from a mode-locked laser to produce acoustic transients by material ablation and noticed an increase in acoustic amplitude when the absorption surface was constrained by a transparent covering. O'Keefe (1972) noted similar enhancements with the irradiation of volatile coatings on metallic substrates.

Giglio (1973) and Calder (1973) were the first to report the possibility of using the laser acoustic source for flaw detection and their systems incorporated a laser interferometer for the detection of the surface displacements produced by the acoustic waves. Similarly Bondarenko in 1976, used 50MW laser pulses and a laser interferometer to detect the surface displacements of the order of a nanometre. Bondarenko used this remote generation and detection system for measuring the thickness of steel plate and to look at scattered signals generated by an artificial laminar bond between two steel plates, and he noted the possibility of using the wideband acoustic transients for flaw detection using spectroscopic

techniques. Von Gutfeld (1977) demonstrated the use of thermally generated acoustic waves for the evaluation of bonded materials and described an experiment using the laser source and a conventional piezoelectric transducer to detect the acoustic scatter from an artificial bulk defect. Von Gutfeld concluded the article by pointing out the important advantage of using an optically steerable acoustic source for NDE. Calder (1978) used a laser source and an interferometer to measure the velocity of sound in liquid lead at 320°C. This experiment would be difficult to perform using conventional methods incorporating piezoelectric transducers because these devices fail at these elevated temperatures. Calder also used the system to detect the acoustic scatter from a 1.75mm diameter hole in a block of metal. Bar-Cohen (1979) used a laser-acoustic source and a piezoelectric transducer to monitor the integrity of micro-welds, 0.5 - 1mm in diameter, between thin sheets of metal. Wellman (1980) used a laser source and interferometer to look at scatter signals from a sub-surface drill hole and acoustically detected the presence of a 2mm deep surface breaking crack in an artillery shell casing. All of these demonstrations of the use of the laser-acoustic source for the detection of defects were qualitative in nature; no attempt was made to relate the form of the acoustic scatter to the characteristics of the defect.

Work at the University of Hull has produced a more detailed study of the generation mechanisms and characteristics of laser-acoustics with the aim of developing a more quantitative approach to non-destructive evaluation. Scruby et al (1980) gave details of the epicentre acoustic displacements generated by the thermal expansion mechanism along with a theoretical description of the process.

Hutchins et al (1980) presented a technique for estimating the depth of liquids by laser-acoustic generation in a metallic membrane adjacent to a liquid and subsequent detection of the echoes within the liquid column by a piezoelectric transducer. Aindow et al (1981) showed the existence of longitudinal, shear and surface acoustic waves from the thermal expansion source (thermoelastic source) at low incident laser beam energies (3mJ) ranging through increasing energies and power densities to the ablation source (plasma source). The paper also described an experiment using the thermoelastic source to detect acoustic scatter from an artificial buried defect. The modifying effect of coating the surface of a sample with various materials has been investigated by Hutchins et al (1981a). An increase in acoustic amplitudes was found when the surface of the sample was coated with a transparent constraining layer, various volatile substances, and a layer of matt black absorbing paint. The far-field radial directivity of the various acoustic source mechanisms, measured by piezoelectric transducers have been compared with a theoretical description by Hutchins et al (1981b). The agreement between the epicentre displacements for different source mechanisms and the displacements predicted by elastic wave theory for simple surface force distributions is discussed by Scruby et al (1982a) and the laser source is suggested as an acoustic standard for modelling acoustic emission events (Hutchins 1981c). The generation of directional surface waves by focusing the laser into a line source has been demonstrated by Aindow et al (1982).

These lists of the published work on laser-acoustics are not exhaustive and many of the experimental results have been confirmed by other workers. The work cited here concentrates on the

generation of acoustic waves in metallic solids by laser beam irradiation and the applications of the phenomenon, but there has also been work on acoustic generation in glassy solids and liquids. A more detailed review of the relevant literature may be found in two articles by Scruby et al (1982b) and Birnbaum et al (1984).

## 1.2 WORK COVERED BY THE THESIS

The work presented in the first part of this thesis characterises the laser acoustic source with respect to its potential use for NDE. It develops an understanding of the physical processes underlying the different generation mechanisms, bringing together some of the previous work and including new representations of the acoustic source with resulting predictions of displacement fields. In the second part of the thesis those aspects of laser generated acoustics which may provide potential advantages over conventional methods of acoustic generation for NDE are identified and investigated. The experimental results substantiate some of these proposed advantages and demonstrate quantitative evaluation of artificial flaw characteristics both within and on the surface of materials.

Chapter 2 presents some of the basic properties of acoustic propagation in isotropic elastic solids and provides a foundation for later detailed discussions of laser-acoustics. Chapter 3 examines the interaction processes between an incident laser beam and the surface of a metallic solid, and a distinction is made between the different possible acoustic generation mechanisms. The thermal absorption and material expansion processes are investigated giving the resulting surface force distributions. In addition, a

qualitative description is presented of the ablative-recoil forces generated at higher incident laser intensities. The surface force distributions and their time histories are used in Chapter 4 to evaluate the expected far-field acoustic displacements. This chapter demonstrates the use of transient acoustic wave theory to predict the material displacements for both the epicentre and surface positions for the various acoustic source mechanisms, and these displacements are compared with those measured using wideband displacement transducers. Chapter 5 presents a comparison between the experimentally determined directivity of the acoustic wave arrival amplitudes for the various acoustic source regimes, with the corresponding expected directivity deduced using the force representations derived in Chapter 3. The partition of acoustic energy between the various modes is evaluated using the directivity information. Chapter 6 presents a brief introduction to the current methods used in the acoustic evaluation of material defects and discusses the application of the laser-acoustic source to this problem. Some consideration is given in Chapter 7 to the construction and performance of the wideband acoustic transducers used to measure the surface displacements. Capacitance, thick piezoelectric and EMAT devices are described which are not commercially available. A brief description is also given of a laser interferometer which was used for some of the experimental work in collaboration with the NDT Centre, AERE, Harwell. Chapter 8 presents experimental results on the application of the laser-acoustic source for the testing of laminar defects in thin plate materials and for measuring the thickness of thin plates. A comparison is made between experimental results and known defect

areas for artificial cavities in thin aluminium plates and induced de-bond areas in alumina coated steel substrates. Chapter 9 looks at more sophisticated experimental techniques for characterising surface defects using laser generated surface acoustic waves. The surface defects are visualised using a pulse-echo method employing some of the advantages of using an optical beam for acoustic generation. The interaction of a surface acoustic wave with a surface breaking slot is investigated experimentally using both spectroscopic and time-of-flight techniques. These techniques are only possible because of the brief time duration of laser generated acoustics. Information about the interaction process is used to estimate the depth of surface breaking slots. Finally, a summary of the work covered in this thesis is presented in Chapter 10.

## CHAPTER 2

## ACOUSTIC PROPAGATION IN SOLIDS

For the characterisation of the laser-acoustic source, and its possible applications to non-destructive evaluation, it is useful to first describe the nature of the acoustic transients generated from the laser-surface interactions. This section presents the basic theory of acoustic propagation in solids including the various types of bulk and boundary waves and concludes with a description of the more complex problems of transient acoustic propagation in various geometries of solids.

When a force does work against a body, energy is distributed such that the body reaches a state of equilibrium within itself and with its environment. Mechanics, specifically the dynamics of rigid bodies, deals with the macroscopic way in which the body as a whole reaches equilibrium with its environment and considers any applied forces to act instantaneously on every particle of a body. Acoustics, the dynamics of deformable bodies, deals with the way in which a body reaches equilibrium within itself due to an applied force. Information about the applied force is not transmitted instantaneously to every particle in the body, but is carried by acoustic waves. These acoustic waves are simply a progressive deformation of the atomic structure and are characterised by the physical properties of the material.

The following discussion considers acoustic propagation in a perfectly elastic, isotropic solid. These simplifications are valid

for our purpose of studying propagation within metals with a fine grain structure and for frequencies typically in the range 1-10 MHz.

## 2.1 STRESS-STRAIN RELATIONSHIPS

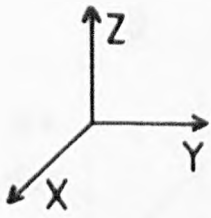
First consider the static relationship between the applied force per unit area, stress, acting on an element of a body and the resulting elastic deformation, strain (e.g. Timoshenko, 1970). Fig. 2.1.a shows components of stress acting on a unit cube of an isotropic solid.  $T_{xx}$ ,  $T_{yy}$ ,  $T_{zz}$  are the components of normal hydrostatic stress and  $T_{xy}$ ,  $T_{yx}$ ,  $T_{zx}$ ,  $T_{yz}$ ,  $T_{zy}$  are the six components of shear stress acting in the plane, where for  $T_{ij}$ ,  $i$  denotes the normal to the plane and  $j$  the direction of the applied force. The number of shear stress components reduces to three if we look at the force equilibrium of this static situation, fig. 2.1b. For no resultant rotation  $T_{zy} = T_{yz}$ , and similarly for the other terms.

Now consider the components of strain generated by this stress, fig. 2.2.a. If the body undergoes a deformation then the point  $P(x,y,z)$  will move to a point  $P'(x',y',z')$  given by

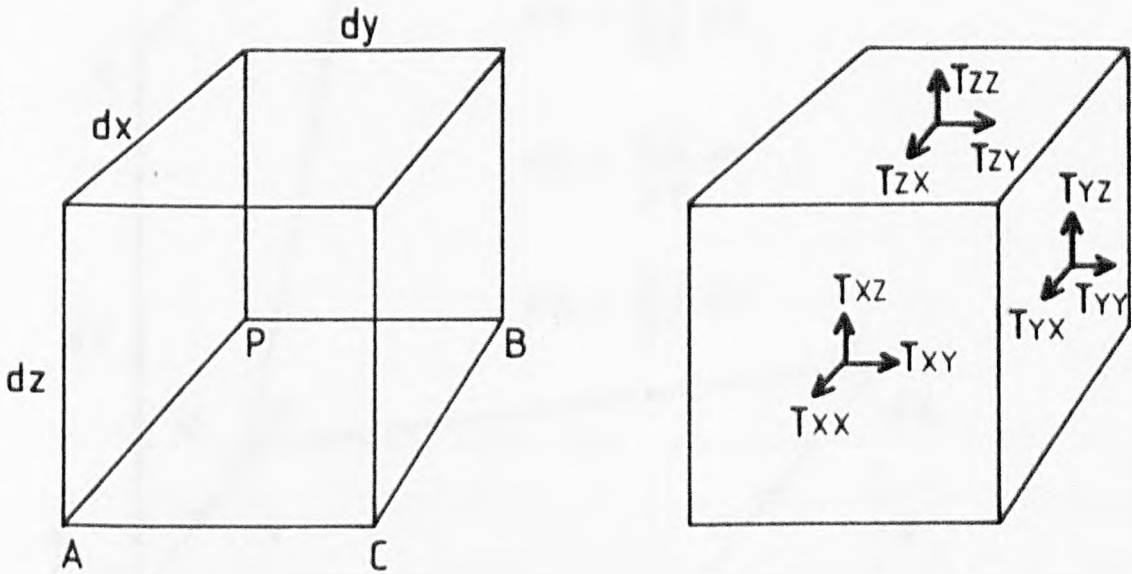
$$x' = x + u, \quad y' = y + v, \quad z' = z + w$$

where  $u$ ,  $v$ ,  $w$  are the components of displacement in the  $x,y,z$  directions respectively.  $u,v,w$  will each be functions of the position,  $(x,y,z)$ . Consequently, if  $P(x,y,z)$  moves a distance  $v$  in the  $y$  direction to the point  $P'$ , then an adjacent point  $A(x + dx, y, z)$ , will move a distance  $v + dv(a)$  in the  $y$  direction to the point  $A'$ , where  $dv(a)$  is the distortion due to the relative positions of the points  $P$  and  $A$ . Similarly the point  $P$  will move a

Fig. 2-1

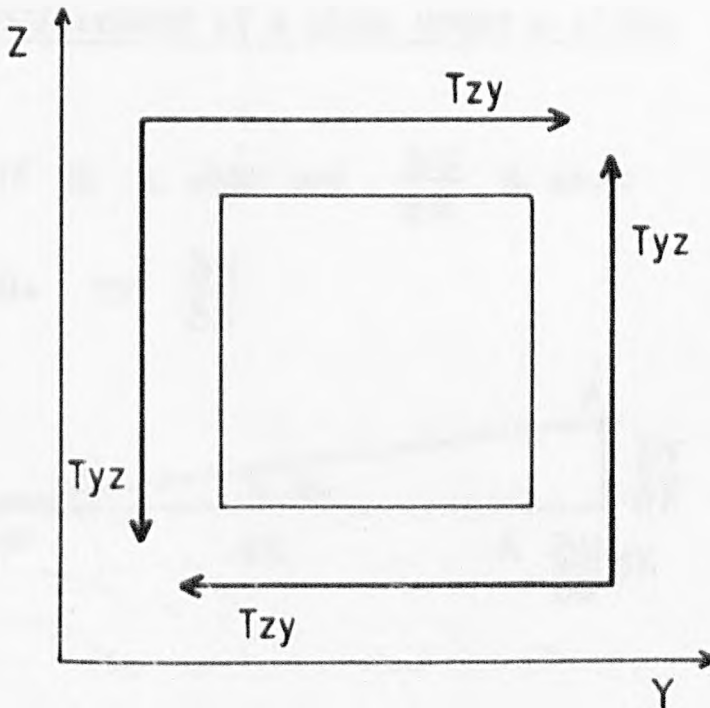


(a)



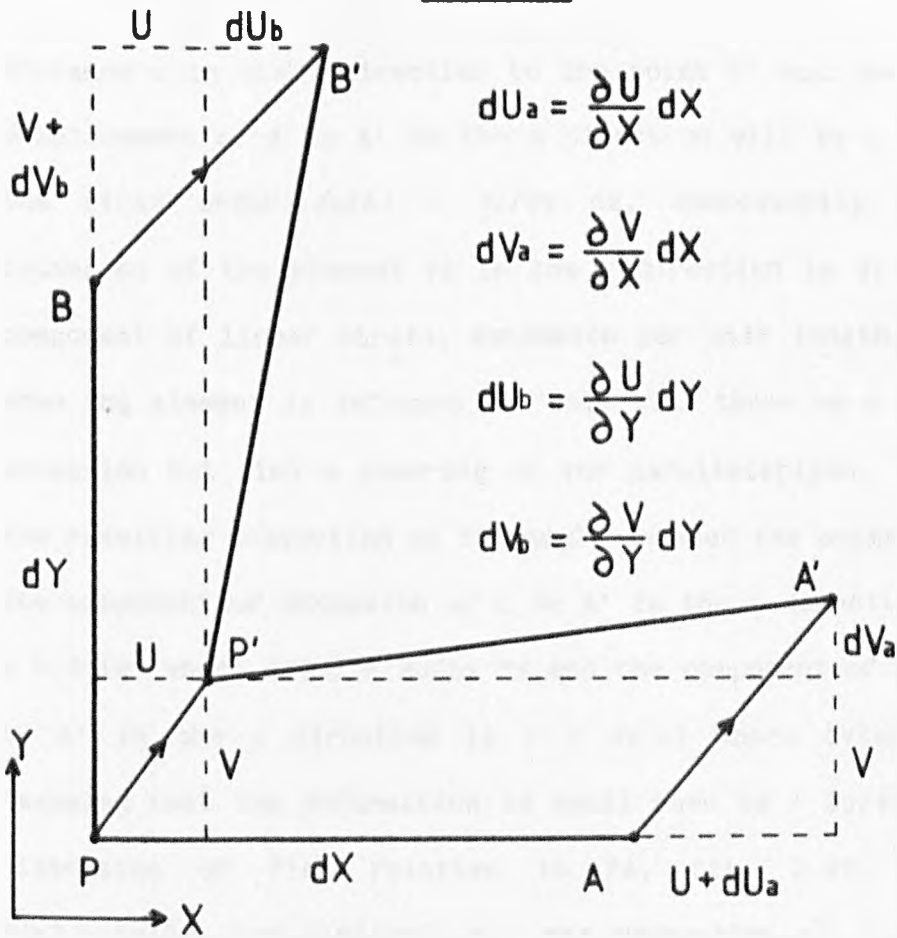
The components of stress acting on a unit cube.

(b)



The components of stress acting on a plane.

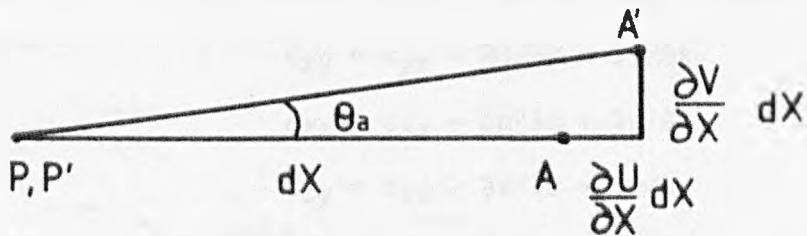
Fig. 2-2



(a) The displacement of a plane under a strain.

if  $\theta_a$  is small and  $\frac{\partial U}{\partial X}$  is small

$$\theta_a \approx \frac{\partial V}{\partial X}$$



(b) One of the components of shearing deformation.

distance  $u$  in the  $x$  direction to the point  $P'$  and the corresponding displacement of  $A$  to  $A'$  in the  $x$  direction will be  $u + du(a)$ . To the first order  $du(a) = \partial u / \partial x dx$ , consequently the resultant extension of the element  $PA$  in the  $x$  direction is  $\partial u / \partial x dx$  and the component of linear strain, extension per unit length,  $\epsilon_{xx} = \partial u / \partial x$ . When the element is deformed not only will there be a compression or extension but also a shearing of the parallelepiped. Now, consider the resulting distortion of the angle between the segments  $PA$  and  $PB$ . The component of extension of  $A$  to  $A'$  in the  $x$  direction is given by  $u + du(a)$  where  $du(a) = \partial u / \partial x dx$  and the component of extension of  $A$  to  $A'$  in the  $y$  direction is  $v + dv(a)$  where  $dv(a) = \partial v / \partial x dx$ . Assuming that the deformation is small then  $dx + \partial u / \partial x = dx$  and the distortion of  $P'A'$  relative to  $PA$ , fig. 2.2b, is given by  $\theta(a) = \partial v / \partial x$ , and similarly for the distortion of  $P'B'$  relative to  $PB$ , giving  $\theta(b) = \partial u / \partial y$ . The overall angular distortion between  $PAB$  and  $P'A'B'$  =  $\theta(a) + \theta(b) = \partial v / \partial x + \partial u / \partial y$ . For small strains this angular distortion is defined as the shear strain,  $\epsilon_{xy}$ , between the  $x$  and  $y$  segments. In conclusion the components of linear shear strain are

$$\epsilon_{xx} = \partial u / \partial x, \quad \epsilon_{yy} = \partial v / \partial y, \quad \epsilon_{zz} = \partial w / \partial z$$

$$\epsilon_{xy} = \epsilon_{yx} = \partial u / \partial y + \partial v / \partial x$$

$$\epsilon_{xz} = \epsilon_{zx} = \partial u / \partial z + \partial w / \partial x$$

$$\epsilon_{zy} = \epsilon_{yz} = \partial v / \partial z + \partial w / \partial y$$

(Timoshenko, 1970, P7)

## 2.1

The relationship between applied stress and resulting strain can now be derived in the case of a perfectly elastic medium. In the

simple case of the extension of a wire due to an applied force,  $\epsilon_{xx} = T_{xx}/E$ , where  $E$  is defined as Young's modulus. The extension will be accompanied by a thinning of the wire given by

$$\epsilon_{yy} = -\sigma T_{xx}/E$$

$$\epsilon_{zz} = -\sigma T_{xx}/E$$

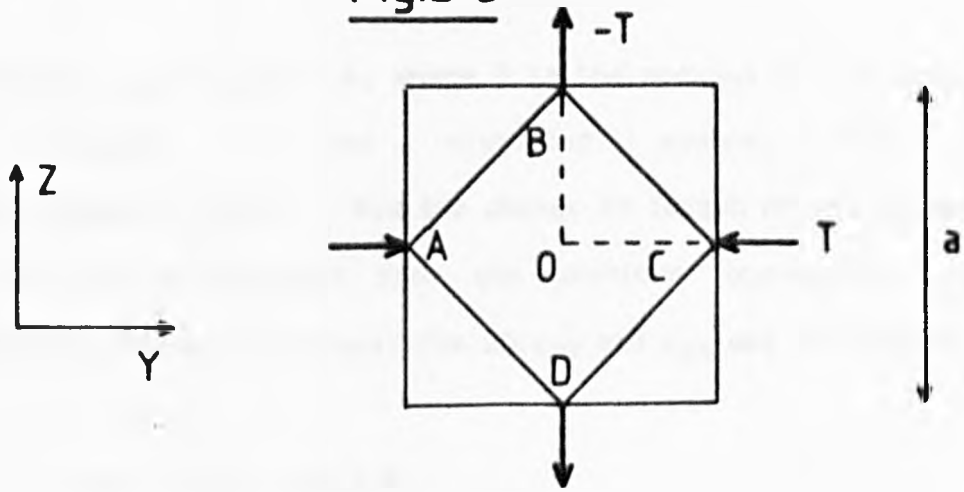
where  $\sigma$  is defined as the Poisson's ratio of the material. If a cubic element of material is subjected to hydrostatic stress from all sides then the component of strain in the  $x$  direction will have a contribution from the stress in that direction, producing a strain  $T_{xx}/E$  and contributions from the two components from stress in the  $y$  and  $z$  directions causing strain extensions in the  $x$  direction through the Poisson's ratio relationship,  $-\sigma T_{yy}/E$ ,  $-\sigma T_{zz}/E$ . The combined strain in the  $x$  direction will be given by

$$\epsilon_{xx} = (T_{xx} - \sigma(T_{yy} + T_{zz}))/E$$

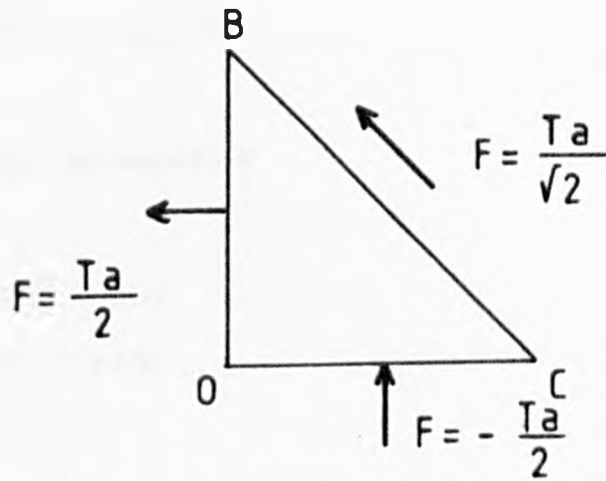
similarly for the other components. This has given a relationship between linear strain and hydrostatic stress. Now consider the relationship between shearing strain and shearing stress. The stresses in 2D acting on a square, fig. 2.3(a) will produce a pure shear deformation on the square sub-element ABCD. Calculating the components of force acting on one side of this element of length  $a$ , fig. 2.3b, there is no normal component of force along BC and the tangential component of force is given by  $F = T_a/\sqrt{2}$ , thus the stress in this direction,  $T(BC) = (T_a/\sqrt{2})/(a/\sqrt{2}) = T$ . The distortion of the square element, fig. 2.3c, is given by the shearing angle and by

Fig.2.3

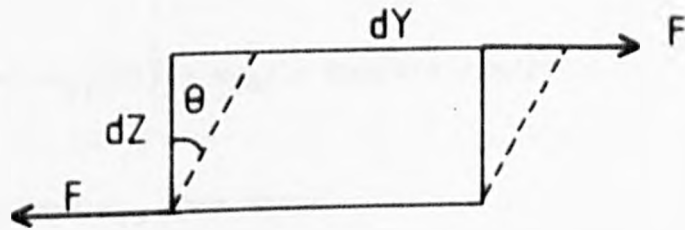
(a)



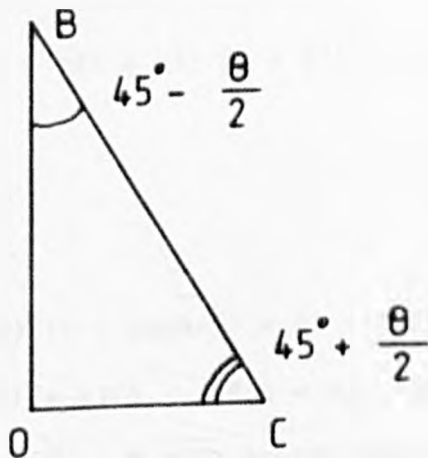
(b)



(c)



(d)



The shearing deformation of a square element.

definition  $\epsilon_{yz} = T_{yz}/G = \theta$ , where  $G$  is the modulus of rigidity. For the element of the distorted square, fig. 2.3d,  $OC/OB = \tan(\pi/4 - \theta/2)$ . Now the change in length of the elements  $OC$  and  $OB$  can be obtained from the previous expressions relating hydrostatic stress to strain, for 2D  $\epsilon_{yy}$  and  $\epsilon_{zz}$  may be written

$$\epsilon_{yy} = (T_{yy} - \sigma T_{zz})/E$$

$$\epsilon_{zz} = (T_{zz} - \sigma T_{yy})/E$$

now  $T = -T_{yy} = T_{zz}$  consequently

$$\epsilon_{yy} = -T(1 + \sigma)/E$$

$$\epsilon_{zz} = T(1 + \sigma)/E$$

The ratio of the deformed sides of the elements may be written

$$OC/OB = (1 + \epsilon_{yy})/(1 + \epsilon_{zz}) = \tan(\pi/4 - \theta/2)$$

Substituting for  $\epsilon_{yy}$  and  $\epsilon_{zz}$  from above

$$\tan(\pi/4 - \theta/2) = (1 - T(1 + \sigma))/(1 + T(1 + \sigma))$$

expanding the multiple angle

$\tan(\pi/4 - \theta/2) = (1 - \tan\theta/2)/(1 + \tan\theta/2) = (1 - \theta/2)/(1 + \theta/2)$  for small  $\theta$ . From this,  $\theta = 2T(1 + \sigma)/E$ . If  $\theta = \epsilon_{yz}$ , the shear strain between the  $y$  and  $z$  segments, then  $T$  will be the applied stress  $T_{yz}$ . Thus the relationship between shear stress and shear strain may be

written

$$\epsilon_{yz} = 2T_{yz}(1 + \sigma)/E$$

In summary, the relationship between stress and strain for the deformed unit cube

$$\epsilon_{xx} = (T_{xx} - \sigma(T_{yy} + T_{zz}))/E$$

$$\epsilon_{yz} = 2T_{yz}(1 + \sigma)/E$$

(Timoshenko, 1970, P10)

2.2

and similarly for the other components.

## 2.2 THE EQUATION OF MOTION FOR AN ISOTROPIC ELASTIC SOLID

The equation of motion for a solid can now be obtained from Newton's second law and the derived expressions relating applied forces and the resulting material deformation. Consider the following situation of the forces acting in the x direction on a stationary cube. The applied stresses being  $T_{xx}$ ,  $T_{xy}$ ,  $T_{xz}$  and the resulting opposing stresses on the opposite faces adjusted by an appropriate amount to take into account the finite separation of the stresses, fig. 2.4.

$$T'_{xx} = T_{xx} + \partial T_{xx}/\partial x dx$$

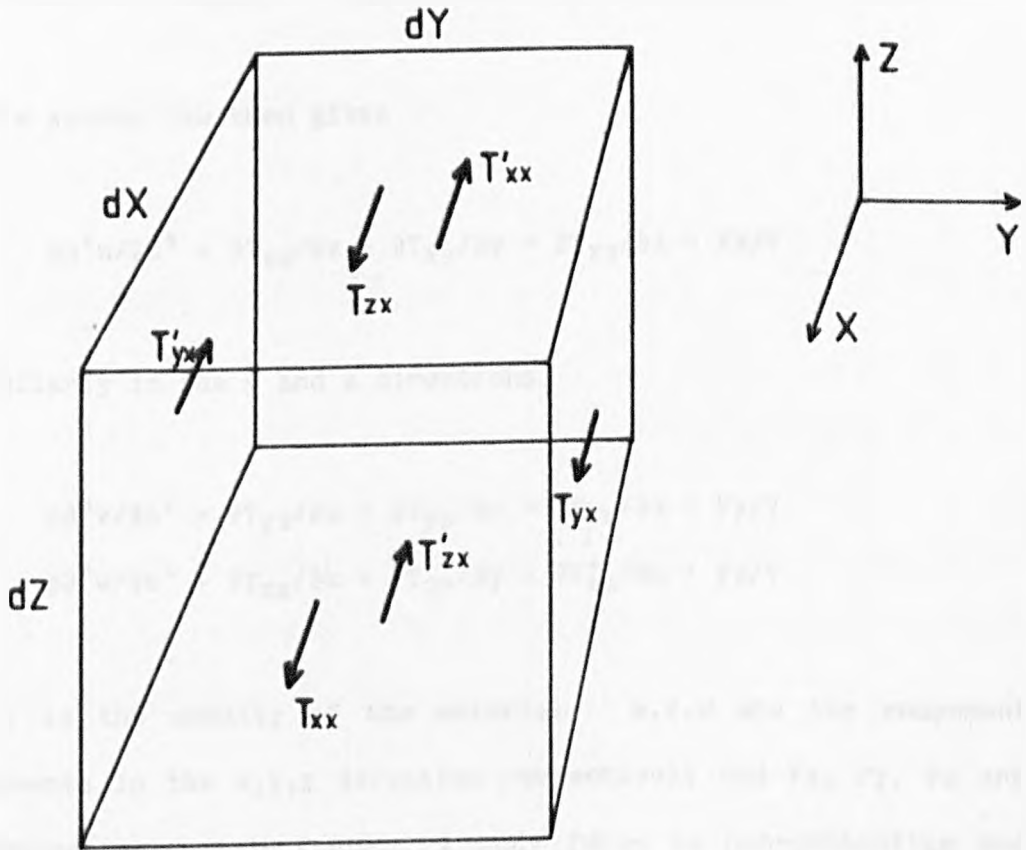
$$T'_{xy} = T_{xy} + \partial T_{xy}/\partial y dy$$

$$T'_{xz} = T_{xz} + \partial T_{xz}/\partial z dz$$

The sum of forces acting in the x direction then becomes

$$\Sigma F = T'_{xx} dydz - T_{xx} dydz + T'_{xy} dx dz - T_{xy} dx dz + T'_{xz} dy dx - T_{xz} dy dx$$

Fig.2-4



$$T'_{xx} = T_{xx} + \frac{\partial T_{xx}}{\partial X} dX$$

$$T'_{yx} = T_{yx} + \frac{\partial T_{yx}}{\partial Y} dY$$

$$T'_{zx} = T_{zx} + \frac{\partial T_{zx}}{\partial Z} dZ$$

The X-direction components of stress acting on a unit cube.

$$\Sigma F = (\partial T_{xx}/\partial x + \partial T_{xy}/\partial y + \partial T_{xz}/\partial z) dx dy dz, \quad (dx dy dz = V = \text{volume})$$

Newton's second law then gives

$$\rho \partial^2 u / \partial t^2 = \partial T_{xx} / \partial x + \partial T_{xy} / \partial y + \partial T_{xz} / \partial z + F_x / V$$

and similarly in the y and z directions.

$$\rho \partial^2 v / \partial t^2 = \partial T_{yx} / \partial x + \partial T_{yy} / \partial y + \partial T_{yz} / \partial z + F_y / V$$

$$\rho \partial^2 w / \partial t^2 = \partial T_{zx} / \partial x + \partial T_{zy} / \partial y + \partial T_{zz} / \partial z + F_z / V$$

Where  $\rho$  is the density of the material;  $u, v, w$  are the component displacements in the  $x, y, z$  direction respectively and  $F_x, F_y, F_z$  are the components of body force. A body force is non-contacting and acts on an interior volume of the bulk of the body, e.g. gravity. We can usually ignore the effect of uniform body forces; and so for small displacements we have, in the  $x$  direction

$$\rho \partial^2 u / \partial t^2 = \partial T_{xx} / \partial x + \partial T_{xy} / \partial y + \partial T_{xz} / \partial z$$

Returning to the relationship between stresses and strains for small deformations

$$\epsilon_{xx} = \partial u / \partial x, \quad \epsilon_{xz} = \partial u / \partial z + \partial w / \partial x, \quad \epsilon_{xy} = \partial v / \partial x + \partial u / \partial y$$

and also that

$$T_{xy} = E \epsilon_{xy} / (2 * (1 + \sigma))$$

and

$$\epsilon_{xx} = (T_{xx} - \sigma(T_{yy} + T_{zz}))/E$$

$$\epsilon_{yy} = (T_{yy} - \sigma(T_{xx} + T_{zz}))/E$$

$$\epsilon_{zz} = (T_{zz} - \sigma(T_{xx} + T_{yy}))/E$$

re-arranging these three equations gives

$$T_{xx} = E(1-\sigma) \epsilon_{xx}/((1+\sigma)(1-2\sigma)) + E\sigma(\epsilon_{yy} + \epsilon_{zz})/((1+\sigma)(1-2\sigma))$$

At this point it is useful to introduce two constants to reduce the complexity of the algebra. These constants are known as the Lamè constants and may be defined as

$$\lambda = E\sigma/((1+\sigma)(1-2\sigma)), \quad \mu = E/(2*(1+\sigma)) \quad (\text{e.g. Achenbach, 1980})$$

In terms of these constants the relationships between stress and strain may therefore be written

$$T_{xx} = 2\mu\epsilon_{xx} + \lambda(\epsilon_{xx} + \epsilon_{yy} + \epsilon_{zz})$$

$$T_{xy} = \mu\epsilon_{xy} \quad 2.3$$

and similarly for the other terms. The equation of motion in the x direction can now be written out in full

$$\rho \partial^2 u / \partial t^2 = \mu \partial^2 u / \partial x^2 + \partial^2 u / \partial y^2 + \partial^2 u / \partial z^2 +$$

$$(\lambda + \mu) \partial / \partial x (\partial u / \partial x + \partial v / \partial y + \partial w / \partial z)$$

$$\rho \partial^2 u / \partial t^2 = \mu \nabla^2 u + (\lambda + \mu) \partial D / \partial x$$

Where  $D$ , in the limit, is the increase in volume per unit volume, and similarly for the other components

$$\begin{aligned}\rho \partial^2 v / \partial t^2 &= \mu \nabla^2 v + (\lambda + \mu) \partial D / \partial y \\ \rho \partial^2 w / \partial t^2 &= \mu \nabla^2 w + (\lambda + \mu) \partial D / \partial z\end{aligned}\quad 2.4$$

Now considering a harmonic solution to these equations consisting of a plane wave travelling in the  $x$  direction, these equations reduce to

$$\begin{aligned}\rho \partial^2 u / \partial t^2 &= (\lambda + 2\mu) \partial^2 u / \partial x^2 \\ \rho \partial^2 v / \partial t^2 &= \mu \partial^2 v / \partial x^2, \quad \rho \partial^2 w / \partial t^2 = \mu \partial^2 w / \partial x^2\end{aligned}\quad 2.5$$

The solution to the first equation is a wave of dilatation travelling with velocity,  $V_p = ((\lambda + 2\mu)/\rho)^{1/2}$ , in the  $x$  direction termed the compressional wave. The second wave corresponds to a wave of shear strain travelling in the  $x$  direction with a velocity,  $V_s = (\mu/\rho)^{1/2}$ , termed the shear wave.

These two types of wave motion characterise acoustic propagation in solids, with further wave motion arising purely from boundary restraints on the solid.

### 2.3 BOUNDARY REFLECTIONS

The effect of a free boundary on these two types of wave motion will now be considered, and from this the types of wave motion that arise from the existence of one or more boundaries can be demonstrated.

The fundamental requirement for the reflection of a wave at a boundary is that the displacements in the wave should remain continuous from the incident to the reflected waves. At a free surface it is also required that no normal component of stress may be supported, i.e. the final layer of the material is not restrained by an adjacent layer. With the introduction of a boundary it is necessary to distinguish between two possible types of shear wave motion relative to that boundary; shear waves with a component of particle motion perpendicular to the plane of the boundary, termed SV waves, and shear waves with a particle motion parallel to the boundary, termed SH waves.

The acoustic equivalent of what is known in optics as Snell's law becomes more complicated due to the existence of two wave types. In the first interaction, fig. 2.5a, consider the reflection of a compressional P wave and the possibility of a new "mode converted" SV wave as a result of the interaction at the surface. For the boundary conditions of a continuous displacement and disappearing normal stress it is possible to determine that, (Achenbach, 1980, P175)

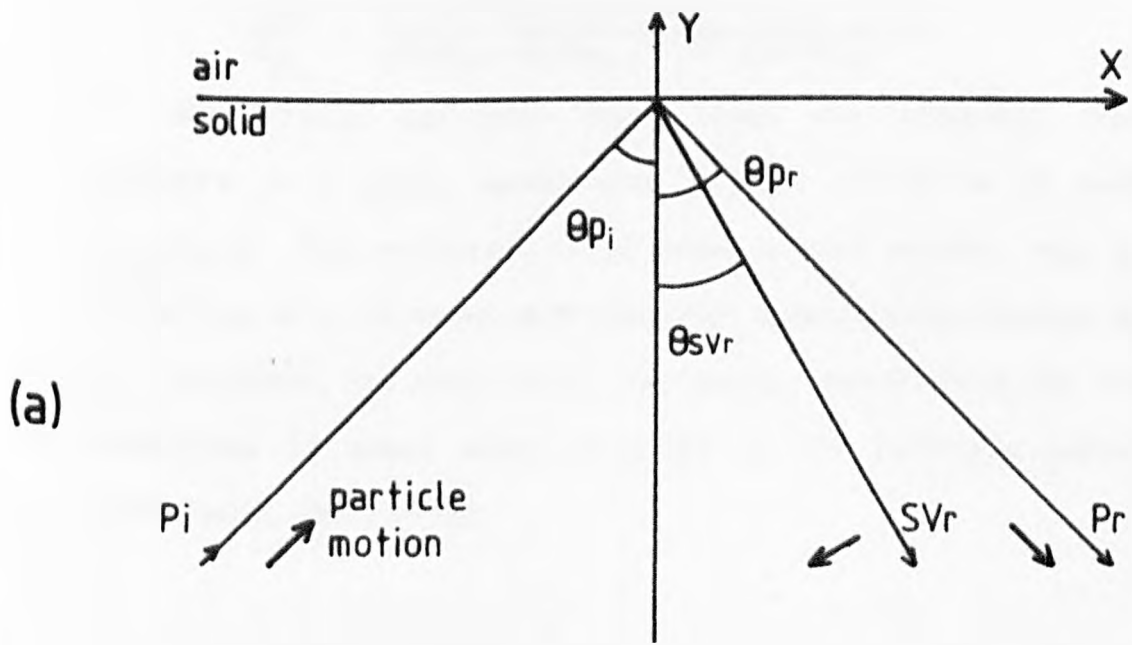
$$\theta_{pi} = \theta_{pr}$$

$$\sin\theta_{svr} = (\sin\theta_{pi})/k$$

where  $k$  is the apparent wavenumber given by  $k = V_p/V_s$ . The angular variation of the relative amplitudes of the various waves can be found from, (Achenbach, 1980)

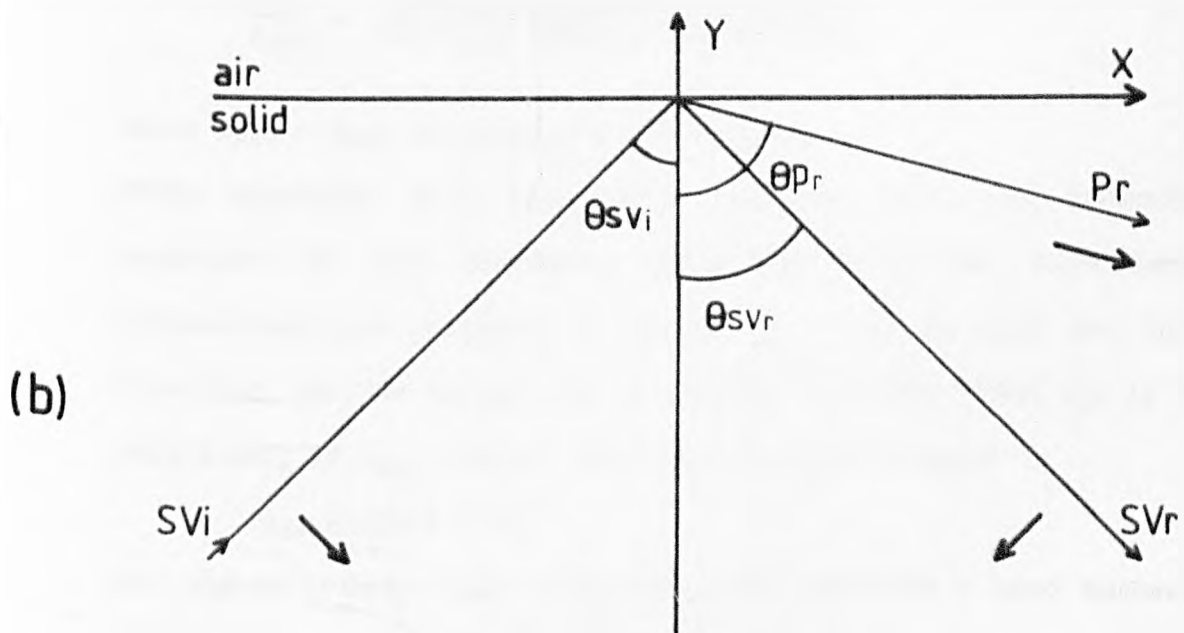
$$\frac{A_{pr}}{A_{pi}} = \frac{\sin 2\theta_{pi} \sin 2\theta_{svr} - k^2 \cos^2 2\theta_{svr}}{\sin 2\theta_{pi} \sin 2\theta_{svr} + k^2 \cos^2 2\theta_{svr}} \quad 2.6$$

Fig. 2.5



i - incident wave  
r - reflected wave

P - longitudinal wave  
SV - shear wave



The reflection of plane waves from a boundary.

$$\frac{A_{svr}}{A_{pi}} = \frac{2k \sin 2\theta_{pi} \cos 2\theta_{svr}}{\sin 2\theta_{pi} \sin 2\theta_{svr} + k^2 \cos^2 2\theta_{svr}}$$

Horizontally polarised shear waves are reflected from the boundary in a simple manner with no mode conversion or change of amplitude. The reflection of SV waves is more complex, fig. 2.5(b), resulting in a reflected mode converted compressional wave as well as the reflected, SV, shear wave. The angular variation of the relative amplitudes of these waves is given by the following expressions (Achenbach, 1980, P179)

$$\frac{A_{pr}}{A_{svi}} = \frac{-k \sin^4 \theta_{svi}}{\sin 2\theta_{svi} \sin 2\theta_{pr} + k^2 \cos^2 2\theta_{svi}}$$

$$\frac{A_{svr}}{A_{svi}} = \frac{\sin 2\theta_{svi} \sin 2\theta_{pr} + k^2 \cos^2 2\theta_{svi}}{\sin 2\theta_{svi} \sin 2\theta_{pr} + k^2 \cos^2 2\theta_{svi}}$$

2.7

where  $\theta_{svi} = \theta_{svr}$  and  $\sin \theta_{pr} = k \sin \theta_{svi}$ .

These equations will have some relevance when the directional behaviour of the acoustics generated from the laser-surface interactions are analysed in Chapter 5. Notice from the latter equations, for the reflection of incident SV waves, that  $\theta_{pr}$  is real valued only if  $\theta_{svi}$  remains less than a critical angle

$$\theta_{cr} = \sin^{-1} (1/k)$$

For angles greater than this, the mode converted P wave becomes a wave that is confined to the surface region of the material, its amplitude decreasing exponentially with depth. This surface wave has arisen purely from the boundary conditions.

#### 2.4 THE RAYLEIGH SURFACE WAVE

Rayleigh (1887) was the first to consider the possibility of a unique wave confined to the surface of an elastic half-space. The form of this wave can be found by considering it to be a linear combination of compressional and shear components satisfying the boundary conditions at the surface (Timoshenko, 1970, P505). In the following discussion consider a wave confined to the surface  $y = 0$  and travelling in the  $x$  direction, there are assumed to be no particle motion components in the  $z$  direction. The directional components of the longitudinal part of the solution may be written

$$u_1 = s e^{-ry} \sin(pt-sx), \quad v_1 = -r e^{-ry} \cos(pt-sx)$$

This is the usual form of a wave solution propagating in the  $x$  direction.  $p$ ,  $r$  and  $s$  are constants and the exponential term restricts displacements to the surface. The wave is travelling with a velocity  $V_r = p/s$ , and is known as the Rayleigh surface wave. These components will be a solution to the expression for compressional wave motion, eq. 2.5. Similarly a solution to the shear wave motion can be given by

$$u_2 = A b e^{-by} \sin(pt-sx), \quad v_2 = -A s e^{-by} \cos(pt-sx)$$

where  $A$  and  $b$  are constants.

By superposition, the combined displacements in the surface are then given by

$$u = u_1 + u_2, \quad v = v_1 + v_2$$

These expressions will satisfy eq. 2.5 if, for the compressional component,

$$r^2 = s^2 = (\rho p^2)/(\lambda + 2\mu)$$

using the notation  $h^2 = (\rho p^2)/(\lambda + 2\mu) = p^2/V_p^2$

$$r^2 = s^2 - h^2$$

and for the shear component

$$b^2 = s^2 - k^2$$

where  $k^2 = (\rho p^2)/\mu = p^2/Vs^2$ . The values of the constants A, b, s, p, r can be found such that they satisfy the boundary conditions. The boundary, being free, cannot support any normal component of stress.

$$T_{xy} = \mu \epsilon_{xy} = \mu(\partial v/\partial x + \partial u/\partial y) = 0$$

and

$$T_{yy} = 2\mu \epsilon_{yy} + \lambda(\epsilon_{xx} + \epsilon_{yy}) = 0$$

Using the expressions for h and k the following relationship can be derived

$$\mu = \lambda/(k^2/h^2 - 2)$$

the boundary condition then becomes

$$2\partial v/\partial y + (k^2/h^2 - 2)(\partial u/\partial x + \partial v/\partial y) = 0$$

substituting the differential expressions for u and v evaluated at  $y = 0$ , we find

$$(2s^2 - k^2)^2 - 4(s^2 - h^2)^{1/2}(s^2 - k^2)^{1/2} s^2 = 0$$

$$\text{or } (2 - k^2/s^2)^4 - 16(1 - h^2/s^2)(1 - k^2/s^2) = 0$$

now  $k^2/s^2 = Vr^2/Vs^2$  and  $h^2/s^2 = Vr^2/Vp^2$ , thus

$$(2 - Vr^2/Vs^2)^4 - 16(1 - Vr^2/Vp^2)(1 - Vr^2/Vs^2) = 0 \quad 2.8$$

This is known as the Rayleigh equation, (Achenbach, 1980, P189) and will be encountered in the discussion on transient acoustic propagation in Chapter 4.

Now, assuming that  $\lambda = \mu$ , corresponding the  $\sigma = 0.25$ , then the resulting simplification reduces the algebraic manipulation required to solve the Rayleigh equation. The Rayleigh equation reduces to a

simple quartic with three roots, only one of which satisfies the condition that the wave displacement should decrease exponentially with depth. The velocity of the Rayleigh surfacewave is given for  $\lambda = \mu$  by

$$V_r^2/V_s^2 = 2 - 2/\sqrt{3}$$

Characteristic wave velocities can be obtained in a similar, if more involved manner, for acoustic propagation in plates, rods and other simple geometries. In general the velocity of propagation of these waves will decrease with an increase in the number of boundaries.

## 2.5 PROPAGATION OF ACOUSTIC TRANSIENTS

So far the characteristic or "normal mode vibrations" of an elastic solid in the absence of any external forces has been investigated. In considering the acoustic disturbance generated by the laser interaction with the material surface, it is the displacement of the solid under the influences of the external driving force of this interaction that is of interest. In general this driving force will be transient in nature; by transient the arbitrary definition is taken that the duration of the applied force will be of the order of the time taken for a compressional wave to travel from the acoustic source to the detector. An acoustic system stimulated by a transient force will eventually "ring" at its normal modes of vibration, analogous to the tone of a bell when it is struck by a hammer. If we wish to characterise the acoustic source, and utilise its transient nature, for example, to examine defects localised within a material, then it is necessary to determine the "first motions" of the material before it settles down into

resonance. The problem may be formally stated as: the transient response of an elastic solid under the influence of a transient driving force and subject to the boundary conditions of one or more free surfaces.

Historically this type of problem was first investigated in the field of seismology to determine the motion of the Earth's surface in the vicinity of an earthquake. The initiative was taken by Lamb (1904), who calculated the displacement of the surface of an elastic half-space due to an impulsive normal load. The calculated displacements showed distinct features at times corresponding to the characteristic velocities of the compressional, shear and Rayleigh waves with continuous displacements for all other times. Lamb's approach to solving the problem involved synthesising the effect of an impulse using a Fourier summation of the harmonic response. The solution was lengthy and approximate and it was not until 1939 that Cagniard developed an exact and general method for solving this type of problem. Dix (1954) applied the method of Cagniard to solve the seismic pulse problem. Referring to Cagniard's work he states "The mathematics involved in this book is, in many instances, so difficult and complicated as to render the book inaccessible to a great many readers who really need to understand the material in it." Numerical calculation of the final results has become easier but the method is still lengthy and will be considered in more detail in Chapter 4. The general approach to the problem is to use Laplace and other integral transforms to get the appropriate equation of motion into a form where the variables may be separated. The transformed equations are then solved subject to the transformed boundary conditions and the inverse integral transforms are applied to obtain a real

solution. The main difficulty in the process is usually that of finding the inverse Laplace transform, and numerous exact and approximate methods are used to obtain a solution, generally in integral form, which may be evaluated numerically.

Using Cagniard's method as a basis many authors have evaluated solutions to Lamb's problem. Pekeris (1955) generates an exact solution for the horizontal and vertical displacements of an elastic half-space due to normal force with step-function time dependence. Knopoff (1958) gives an exact solution for the similar problem of the displacement of a plate at an epicentral point due to step-function source. Chao (1960) solves the more difficult non-axisymmetric problem of the surface displacement due to tangential loading. Afandi and Scott (1972) calculate surface displacements due to dipolar surface forces and Johnson (1974) gives a general expression for the displacements due to a variety of sources and their spatial derivatives.

Breckenridge et al (1975) applied these solutions, developed for seismology, to the problem of acoustic emission. The characterisation of acoustic emission events has become an important area of research; the phenomenon and the relevance of the laser-acoustic source to this topic will be described in Chapter 6.

The latest development in the solution to these types of problems has been by Pao et al (1979) who have applied the "generalised ray theory" to solve the displacement of a plate due to various sources. They approach this complex problem by separating the acoustic disturbance at some point on the plate into groups of ray paths consisting of longitudinal and shear segments arriving from the source. The displacements are then evaluated in terms of integrals

for each ray group. A comparison of theoretically predicted displacements with those using the laser source will be made in Chapter 4.

With the development of increasingly larger, faster, and more accurate computers it has become possible to apply numerical techniques to directly solve the partial differential equations describing the problem. Most successful amongst these techniques has been that of finite-difference methods in which the partial differential equation is replaced by its approximate finite-difference form. These equations are then used in conjunction with a numerical grid to represent points in space, and deformations of this grid are then calculated as the disturbance propagates from some initial condition. The accuracy of the technique is affected by several factors: the model adopted to describe the boundary conditions, where various methods have been used with differing success (Ilan, 1975); the ability of the technique to handle sharp discontinuities in the material boundary; and the accuracy of the approximations at the high frequencies corresponding to the first motions of the material.

The method has been applied to the otherwise intractable problem of the interaction of a surface pulse with a surface crack (Bond, 1979) and a comparison of this work with experimental results using the laser-acoustic source will be made in Chapter 9 .



## CHAPTER 3

## SURFACE FORCES GENERATED BY LASER-SURFACE INTERACTIONS

This chapter presents an investigation of the processes by which incident laser energy is converted into surface forces on the metallic solid. It is these transient surface forces which are then responsible for the generation of acoustic displacements.

It has been pointed out in many publications (review by Scruby et al, 1982) that the generation of acoustics by laser irradiation falls into two distinct regimes. At relatively low incident power densities, say  $< 10^7 \text{ W cm}^{-2}$ , the laser energy is partially absorbed at the metallic surface, resulting in surface heating with no change in phase of the material. The energy is absorbed in a thin layer at the surface and the accompanying thermal expansion of the thin disc of material gives rise to a stress distribution generating acoustic transients. This type of acoustic source will be referred to as the thermoelastic source.

At higher incident power densities, say  $> 10^8 \text{ Wcm}^{-2}$ , the absorbed energy rapidly creates an expanding ionised vapour above the surface of the material and the development of acoustic transients in this case is dominated by stresses generated from surface recoil as material is evaporated to form the plasma. This type of source will be referred to as the plasma source.

It is also possible to modify the acoustic source using various thin layers on the metallic surface (Hutchins et al, 1981). The modified interaction tends to increase the amplitude and transient

nature of the acoustic disturbance. An acoustic source of this type using a thin layer of grease or oil on the surface is used extensively in some of the experiments described in later chapters. This type of acoustic source will be referred to as the oil layer source.

For the purpose of this thesis it is necessary to derive the force distributions resulting from the various interactions, which will then be used in conjunction with transient acoustic theory to predict the resulting acoustic displacements (Chapter 4). The derivations of force distributions presented in this chapter are approximations which give reasonable agreement between theory and experiment. They are not intended to be a rigorous analysis of the complex interaction processes.

In the following discussion the laser pulse is taken to be that from a Q-switched Nd/YAG laser, generating at  $1.06\mu\text{m}$ . The pulse has an energy of about 30mJ and a time duration of about 30ns with an approximately Gaussian temporal and spatial distribution.

### 3.1 THE THERMOELASTIC SOURCE

The incident electro-magnetic energy is absorbed by conduction electrons in the metallic surface, penetrating to the electro-magnetic skin depth. The absorbed energy is then re-radiated minus the losses due to the electron-phonon collisions within the lattice. The absorbed laser energy (7% of the incident energy for  $1.06\mu\text{m}$  on aluminium) thus appears as heat within a very short time,  $\sim 10^{-13}\text{s}$ , (Ready 1971) confined to the volume defined by the beam radius and electro-magnetic skin depth of 2-5nm. This heat is rapidly distributed throughout the material by thermal conduction. Over the

timescale of the incident laser pulse, 30ns, the heat penetrates to the thermal skin depth,  $\sqrt{4kT}$ , typically in the range 0.5 - 10 $\mu$ m, three orders of magnitude greater than the depth over which it is absorbed. The diameter of the beam is still many orders of magnitude greater than this penetration depth and the heat flow problem can be considered to be one dimensional on the timescale of interest.

The one dimensional heat flow distribution due to a laser pulse of arbitrary time duration and spatial distribution at the surface of an infinite block may be written as (Ready 1971),

$$T(x,y,z,t) = \frac{I_0 S(x,y)}{C \rho \sqrt{k\pi}} \int_0^t \frac{e^{-z^2/4kt'}}{\sqrt{t'}} p(t-t') dt' \quad 3.1$$

where  $T(x,y,z,t)$  is the temperature at a point  $x,y,z$  and time  $t$ ,

$z = 0$  defines the surface given by the plane  $xy$  at  $z = 0$ ,

$I_0$  is the peak absorbed laser intensity,

$C$  is the specific heat,

$\rho$  is the density,

$k$  is the thermal diffusivity,

$p(t)$  is the normalised laser temporal profile,

$s(x,y)$  is the normalised laser spatial profile.

Assuming a Gaussian spatial distribution this may be re-written in cylindrical co-ordinates as

$$T(r,z,t) = \frac{I_0 e^{-r^2/a^2}}{C \rho \sqrt{k\pi}} \int_0^t \frac{e^{-z^2/4kt'}}{\sqrt{t'}} p(t-t') dt' \quad 3.2$$

where  $a$  is the Gaussian radius of the beam and  $r$  is the radial position. Evaluation of this expression for various materials, laser energies and beam radii used in later experiments are such that the maximum surface temperature rarely rises above a hundred degrees centigrade so that there is usually no permanent damage to the material surface.

One method of calculating the acoustic displacements due to the thermal expansion of this heated surface material would require solving the thermoelastic form of the wave equation subject to the boundary conditions which include extended source distributions. Some work has been published on the transient motions of an elastic solid from extended source distributions in relation to displacements expected from seismological disturbances (e.g. Maiti, 1978, 1979; Mitra, 1964) but none have considered a thermoelastic stress distribution as the acoustic source. The thermoelastic source has been previously modelled as the sum of three co-incident edge dislocation loops (Scruby et al, 1980) and more recently as a surface, point volume expansion (Rose, 1984). Rose has calculated displacements due to a "surface centre of expansion" without giving the full explicit solution for the surface displacements. The surface displacements are characterised by the finite area of the source and in order to make reasonable comparison with observation it is necessary to account for this distribution. The extended force distribution is derived in the next section and a representation of this will be used in Chapter 4 to synthesise the expected surface displacements.

The incident laser energy is assumed to instantaneously heat a thin surface layer of material with uniform thickness corresponding

to the thermal skin depth. The incident energy and resulting temperature distribution is axially symmetric. The absorbed laser energy density is given by

$$E_d = \frac{E_T}{\pi a^2} e^{-r^2/a^2} \quad 3.3$$

where,  $E_T$  is the total absorbed energy and  $a$  is the Gaussian radius of the beam. Consider an annulus of material  $\Delta r$  wide such that there is uniform irradiation across its surface, fig. 3.1. The energy absorbed at the surface of this annulus will be given by

$$E = E_d * \pi((r + \Delta r)^2 - r^2) \approx 2\pi r \Delta r E_d$$

$$E = \frac{2r \Delta r E_T}{a^2} e^{-r^2/a^2} \quad 3.4$$

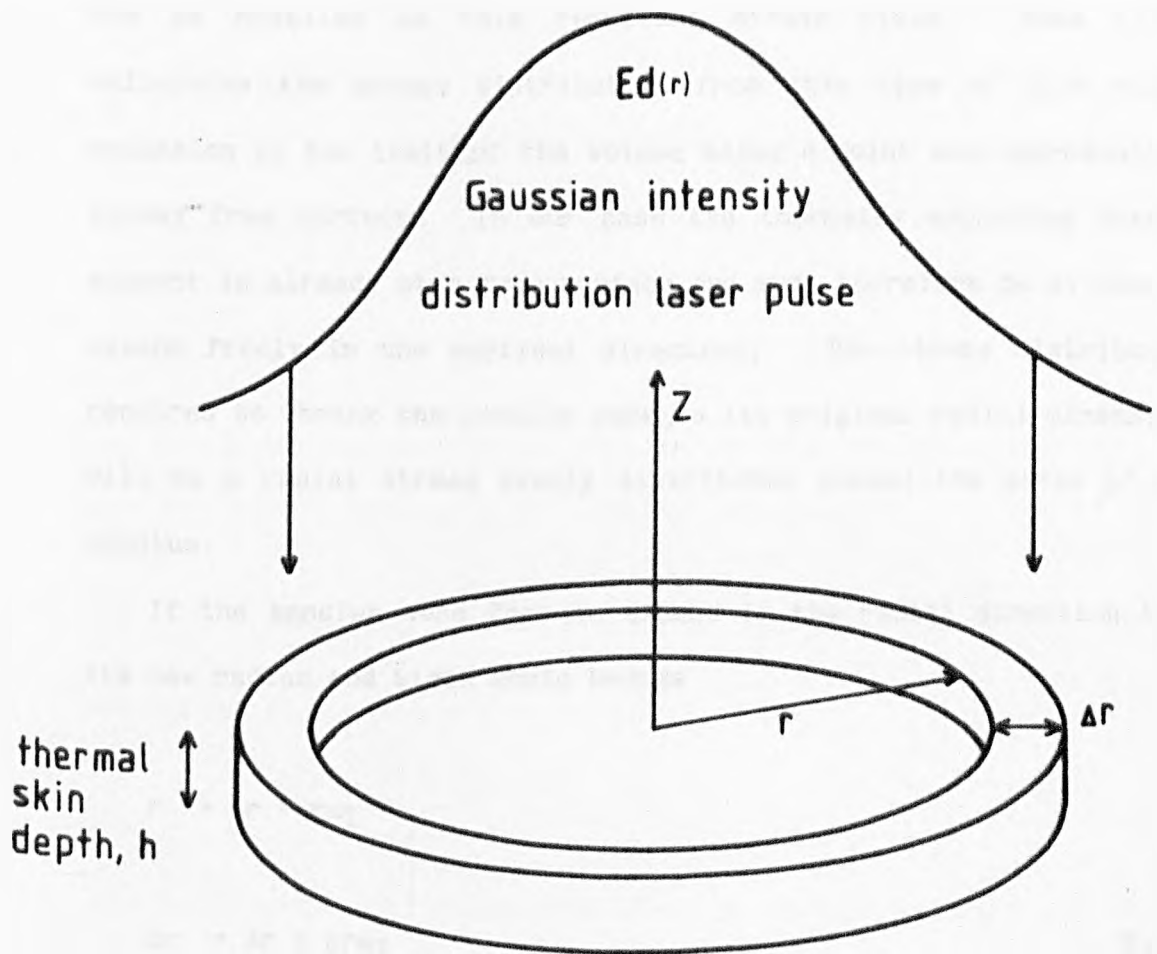
This energy is assumed to be uniformly distributed throughout the volume of the annulus, resulting in a uniform temperature rise

$$T = \frac{E}{C\rho V} = \frac{E_T}{a^2 C\rho\pi h} e^{-r^2/a^2} \quad 3.5$$

Each annular element in the surface will thermally expand against the surrounding material giving an overall force distribution.

The force representation for volume expansion sources is discussed by Aki and Richards, 1980. The representation relies on the following concepts. First the source volume is imagined to have been cut free from the surrounding material, the source material then undergoes a transformational stress free strain, in our case this is a thermal expansion of the annular element, finally a stress distribution is applied to the surface of the source volume such that

Fig. 3-1



A thin annular element of the surface material is  
uniformly heated by the laser pulse.

the resulting strain deformation allows the volume to be replaced exactly in the cavity from which it was cut. The seismic source can now be modelled as this resultant stress field. Rose (1984) calculates the stress distribution from this type of bulk volume expansion in the limit of the volume being a point and approaching a stress free surface. In our case the thermally expanding annular element is already at a free surface and must therefore be allowed to expand freely in the vertical direction. The stress distribution required to shrink the annulus back to its original radial dimensions will be a radial stress evenly distributed around the sides of the annulus.

If the annulus were free to expand in the radial direction then its new radius and width would become

$$r \rightarrow r + r\alpha_T$$

$$\Delta r \rightarrow \Delta r + \Delta r\alpha_T \tag{3.6}$$

where  $\alpha$  is the coefficient of linear expansion. The radial and tangential elastic contraction (strain), required to counteract this expansion becomes

$$\epsilon_r = \epsilon_\theta = \frac{-\alpha_T}{1 + \alpha_T} \approx -\alpha_T \tag{3.7}$$

The only remaining components of stress for this axially symmetric problem are  $T_{rr}$ ,  $T_{\theta\theta}$ ,  $T_{zz}$ . All three shear strains and stresses being zero because of the symmetry about the axis and in the z-direction. The stress-strain equations related to those derived in

Chapter 2, eq. 2.3, in cylindrical coordinates may be written (Achenbach, 1980, eqs. 2.144-2.146, 2.140)

$$\begin{aligned} T_{rr} &= \frac{E}{(1+\sigma)(1-2\sigma)} \left[ (1-\sigma) \epsilon_{rr} + \sigma(\epsilon_{\theta\theta} + \epsilon_{zz}) \right] \\ T_{\theta\theta} &= \frac{E}{(1+\sigma)(1-2\sigma)} \left[ (1-\sigma) \epsilon_{\theta\theta} + \sigma(\epsilon_{rr} + \epsilon_{zz}) \right] \\ T_{zz} &= \frac{E}{(1-\sigma)(1-2\sigma)} \left[ (1-\sigma) \epsilon_{zz} + \sigma(\epsilon_{rr} + \epsilon_{\theta\theta}) \right] \end{aligned} \quad 3.8$$

For a thin disc at a free surface the vertical stresses are relieved, eq. 3.7 and 3.5 then give the vertical strain as

$$\epsilon_{zz} = \frac{2\sigma}{(1-\sigma)} \alpha T \quad 3.9$$

The radial stress may now be derived

$$T_{rr} = \frac{-E\alpha T}{(1-\sigma)} \quad 3.10$$

Substituting for the temperature from eq. 3.5, the radial stress for the annular element is given by

$$T_{rr} = \frac{E \alpha E_T}{(1-\sigma)a^2 C \rho h \pi} e^{-r^2/a^2} \quad 3.11$$

The total radial force acting on the sides of the resultant ring is given by

$$F(r) = 2\pi r h T_{rr} = \frac{2r E \alpha E_T}{(1-\sigma)C \rho a^2} e^{-r^2/a^2} \quad 3.12$$

This is the radial force distribution required to model the thermoelastic source at a free surface and the stress follows the form of the Gaussian irradiation with the forces acting symmetrically out from the maximum stress at the centre. The total radial force

produced by the thermal expansion may be estimated from eq. 3.12. Integrating the expression over the surface, using the values of 30mJ for the incident laser pulse and 7% absorption at the surface, gives a total dipole moment of  $3 \times 10\text{Nm}^{-4}$ . This moment, if it were concentrated at a Gaussian radius of 1mm, would produce a radial force of 0.3N.

The time dependence of this resultant force distribution will depend on the rate of thermal diffusion into the material. When all the material has reached a uniform temperature then there will be no resultant stress. Taking the thermal skin depth as a measure of the heat penetration with time then it can be shown that the thermal velocity will decrease with distance from the source. The assumption that there is a predominantly radial stress distribution at the surface relies upon the fact that within the time duration of the laser pulse, the heated region consists of a thin disc, with a diameter that of the incident beam and a depth corresponding to the relevant thermal penetration depth. This assumption will no longer hold when the penetration depth is of the same order as the diameter of the beam, (neglecting lateral heat flow). This condition corresponds to a time duration of 50ms for a 4mm Gaussian diameter beam incident on aluminium. The acoustic events which are the concern of work presented in this thesis will rarely exceed 30 $\mu$ s from the onset of laser irradiation. This is the time taken for the slowest bulk wave to travel through 9cm of aluminium, approximately the maximum size of a sample under test. On these timescales the stress distribution is changing only very slowly and for the purposes of evaluation of the displacements due to this source, the stress distribution can be considered to have a Heaviside, step function

time dependence.

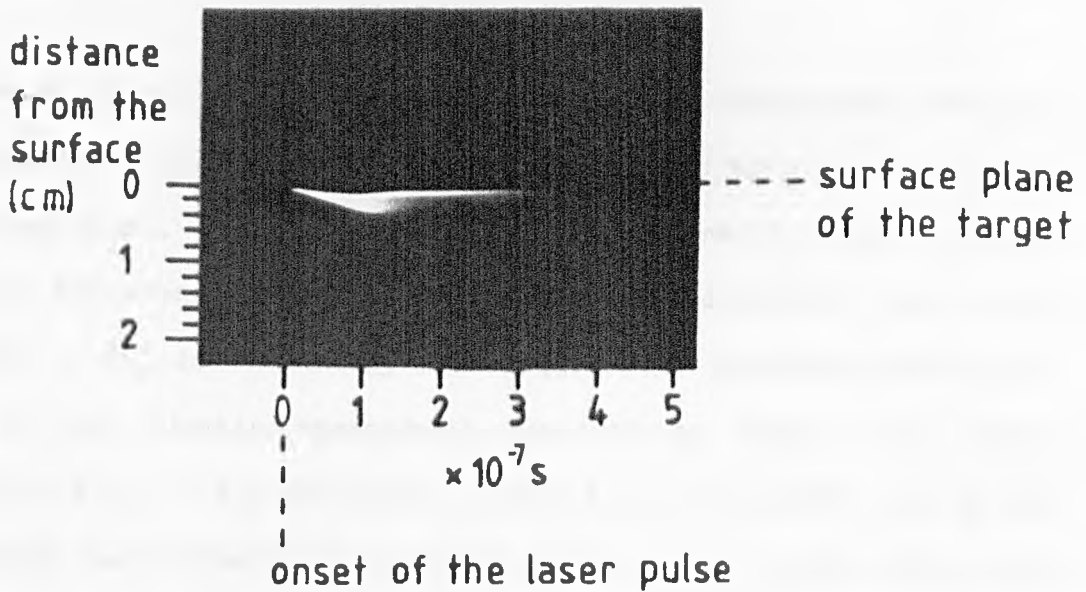
### 3.2 THE PLASMA SOURCE

At high incident power densities the optical radiation is sufficiently intense to directly ionise the surface of the solid. The exact nature of the interaction involves many processes and depends on the duration, wavelength and energy of the laser pulse, as well as the nature of the target material. Ready (1971) has reviewed this area of work.

High speed streak photographs for the particular case of a 30mJ, 30ns pulse on an aluminium surface have indicated that the luminous front on the plasma expands with a supersonic velocity of  $1.6 \times 10^4 \text{ms}^{-1}$  throughout the duration of the laser pulse, fig. 3.2. The direction of the plasma expansion is anisotropic, tending to follow the direction of the incoming laser pulse. High speed framing photographs show a luminous ball of material forming at the surface during the first few nanoseconds which then migrates in the direction of the incident beam (Ready, 1971). The expanding material remains luminous for about  $1\mu\text{s}$ , well after the termination of the incident laser pulse at 100ns. When the laser pulse has terminated the expansion velocity decreases rapidly to the sound speed of about  $3 \times 10^2 \text{ms}^{-1}$  and the vapour expansion now becomes isotropic.

An "order of magnitude" calculation can be carried out using simplifications in order to determine the expected magnitude and time history of the driving force at the surface. If we calculate the laser energy required to heat a small volume of material through its various phases and into a plasma which is singly ionised, then the

Fig. 3·2



1.06  $\mu\text{m}$  laser pulse: energy = 32 mJ

multimode

FWHM duration = 36 ns

2cm focal length lens

A streak photograph of the luminous emission  
from a Nd/YAG laser pulse focussed onto a  
polished aluminium surface in air.

amount of material ablated from the surface can be approximated in the following way.

$$E_t = E_s + E_{s1} + E_l + E_{lv} + E_i \quad 3.13$$

Where  $E_t$  is the energy/mole required to ionise the material from room temperature.  $E_s$  is the energy/mole required to heat the solid to its melting point.  $E_{s1}$  is the energy/mole required to melt the solid.  $E_l$  is the energy/mole required to heat the liquid to its boiling point.  $E_{lv}$  is the energy/mole required to vapourise the liquid.  $E_i$  is the kinetic energy/mole required to ionise the vapour.  $E_s = T_1 \times C_s = 1.6 \times 10^4$  J/mole, where  $C_s = 25$  J/mole/K, and is the specific heat capacity of solid aluminium.  $T_1 = 642$ K, and is the difference between room temperature at 290K and the melting point of aluminium at 932K.  $E_{s1} = 10^4$  J/mole, and is the latent heat of fusion of aluminium.  $E_l = T_2 \times C_l = 5 \times 10^4$  J/mole, where  $C_l = 29$  J/mole/K, and is the specific heat capacity of liquid aluminium.  $T_2$  is the temperature difference between the melting point and boiling point of aluminium at 2673K.  $E_{lv} = 3 \times 10^5$  J/mole, and is the latent heat of vapourisation of liquid aluminium.  $E_i = 5.8 \times 10^5$  J/mole, and is the energy required for the single ionisation of the aluminium atoms. Physical data was taken from **Stull** "The Thermodynamic Properties of the Elements" (1956). Assuming that all the laser energy goes into producing the plasma then  $E_t$  can be calculated from these values as,  $E_t = 9.6 \times 10^5$  J/mole.

The derivation does not take into account some processes which are known to occur. For example, no allowance has been made for heat loss due to thermal conduction. Also, the build up of a

pressurised vapour above the surface of the material can substantially increase the boiling point. The creation of a plasma proceeds by an inverse Bremsstrahlung interaction with the incident light field to give multiply ionised species (T.P. Hughes, 1975). Within the plasma a boundary can be created acting as perfect reflector for the laser wavelength, thus shielding the surface and the bulk of the plasma from further heating by the laser pulse.

Neglecting these effects, the mass of material ejected by a 30mJ laser pulse can be calculated to be  $8.4 \times 10^{-7} \text{g}$  with a corresponding volume of  $3 \times 10^{-13} \text{m}^3$ . Electron micrographs of surface damage due to the focussed laser pulse show that a pit is formed with a radius of approximately  $25 \mu\text{m}$  and a depth of about  $5 \mu\text{m}$ , corresponding to a volume of  $1 \times 10^{-14} \text{m}^3$ , or equivalent to  $2.7 \times 10^{-8} \text{g}$  of removed material. This value indicates that the interaction is not as efficient as has been presented.

The initial reaction at the surface will be the recoil force as this volume of material is evaporated. Assuming that the evaporation process is fast compared to the laser pulse, then the rate of evaporation and hence the recoil force will follow the form of the laser pulse, ie. the force on the surface will be of the form  $F(t) = F_0 e^{-t^2/a^2}$ , where  $F_0$  is the peak force and  $a$  is the rise time of the laser pulse. The corresponding impulse,  $\int F(t) dt = F_0 \sqrt{\pi} a / 2$  equivalent to the momentum acquired by the evaporated material. Taking the experimentally calculated mass of material and the average velocity of the expanding vapour plume as  $1.6 \times 10^4 \text{ms}^{-1}$  then the peak force delivered by a 30mJ laser pulse can be estimated to be about 20N. We shall see in Chapter 4 that forces of the same magnitude can be calculated from the acoustic displacement

measurements by a deconvolution process.

On timescales longer than the incident laser pulse the plasma is continuing to expand and will be exerting a pressure on the surface. The corresponding force will follow the ratio of the pressure within the gas to the circular area over which it is acting. The pressures within the cooling volume of gas will be approximated by its ideal gas law value of  $P = nRT/V$ , with  $V = \frac{2}{3}\pi r^3$  for a hemisphere. The value of the force acting on the surface will then be approximated by

$$F = \frac{3nR\pi Tr^2}{2\pi r^3} \propto \frac{1}{r} \quad 3.14$$

The velocity of the expanding vapour will eventually be decreasing from  $10^4 \text{ms}^{-1}$  to the sound speed at  $3 \times 10^2 \text{ms}^{-1}$  and below, but assuming that it is constant on the timescale of interest, then the force on the surface will fall as the inverse of the time,  $F \propto 1/t$ .

To summarise, the normal force developed by the plasma interaction should be an order of magnitude greater than that developed by the thermoelastic interaction and will therefore dominate the latter, and its time dependence will consist of two basic components. First the recoil force of evaporating surface material which will follow the laser temporal profile, and secondly a longer timescale decreasing force due to the pressure exerted over an increasing circular area by the expanding gas.

### 3.3 THE OIL LAYER SOURCE

The application of a thin layer of oils or grease to the surface will affect the interaction process in several ways. At high incident flux densities the oil vapour will form a plasma and the resulting acoustic displacements are similar to those obtained in the

case of a metal vapour-plasma. At lower incident power densities the interaction will be similar to that of the thermoelastic source. The oil layer will be substantially transparent to the incoming radiation and the absorbed energy at the metal-oil interface will induce a rapid thermal expansion of the metal surface. However, this thermal expansion is now constrained in the vertical direction due to the presence of the oil layer above and this will result in normal forces. In this latter case of oil ablation there is no visual emission that usually accompanies the formation of a plasma, and there is no visible damage to the metal surface, but oil droplets are ejected from the surface probably by the rapid acceleration of the expanding metal.

A value for this acceleration may be evaluated in the following way. The vertical thermoelastic strain of the thin heated disc of metal in the central region of incidence is given by eq. 3.9 as  $\epsilon_{zz} = 2\alpha T / (1 - \sigma)$ . Which for  $\sigma = 1/3$  and  $T_0$  at the centre from eq. 3.5 then the vertical extension of the central element is given by  $\Delta Z = \alpha E_T / a^2 c \rho \pi$ . Evaluation of this expression for a 30mJ laser pulse, 7% absorption and a 2mm radius beam give a vertical thermoelastic displacement of 1.6nm. This value is in good agreement with the experimental value of  $1.75\text{nm} \pm 20\%$ , obtained by interferometric measurements (Aindow, 1984). If this expansion takes place in the rise time of the laser pulse, 30ns, then resulting average acceleration is given by  $a = 2 \times \Delta Z / t^2 = 3.5 \times 10^6 \text{ms}^{-2}$ . In view of this fast surface acceleration it is not unreasonable to assume that the layer of oil will be ejected from the surface.

There will be a normal impulsive force due to the projection of this material, but unlike the plasma source, with its expanding

vapour cloud, there will be no continuing force. Experimentally the amplitude of acoustic signals generated by this type of source are larger than the plasma source, indicating that the normal driving force is also larger than that of the plasma force. This is because most of the absorbed incident energy is now simply converted into the kinetic energy of the ejected oil particles without the intervening process of ionisation.

The impulsive driving force generates sharp acoustic transients with a wide frequency bandwidth. As such these acoustic transients are an ideal tool for investigating the interaction processes with material boundaries, eg. the reflection and transmission of longitudinal and shear pulses at corners, steps and cracks described in Chapter 9.

## CHAPTER 4

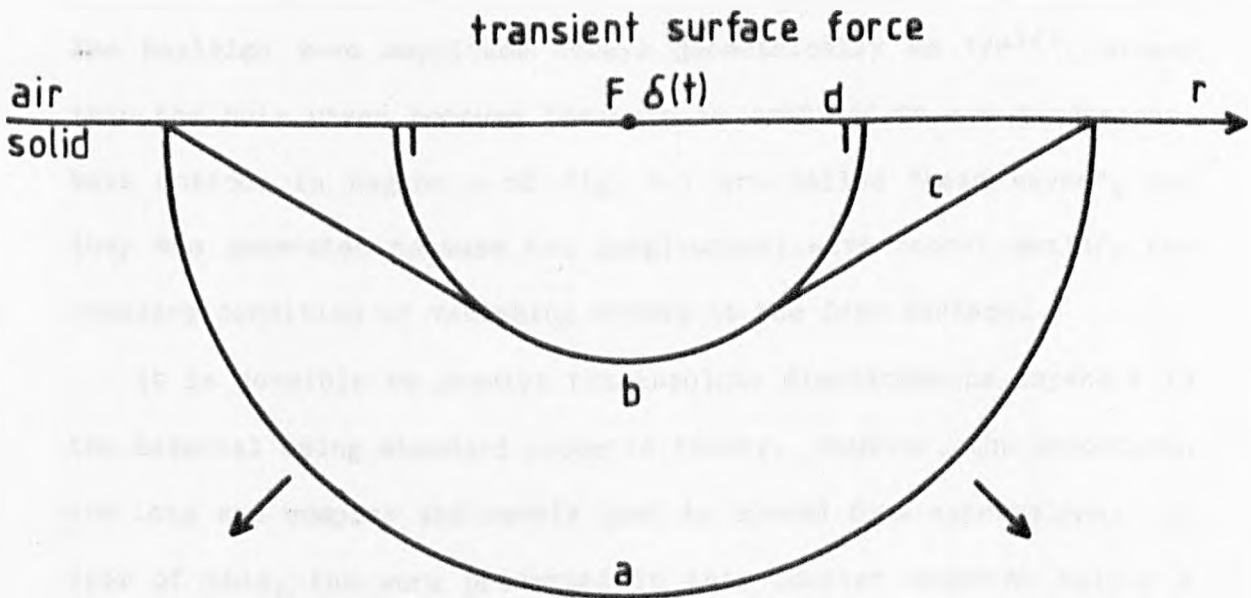
## LASER GENERATED ACOUSTIC TRANSIENTS

In this chapter a comparison is made between experimentally measured laser generated acoustic transients and displacements predicted by acoustic theory for the force distributions derived in Chapter 3.

Epicentre (on-axis) displacements produced by the laser acoustic plasma and thermoelastic sources have been previously compared with unpublished, expected displacements predicted using acoustic theory (Scruby et al, 1980) and a preliminary analysis has been given for the surface waves generated by the laser-source (Aindow et al, 1983). In this chapter the description of surface waves has been extended to model the effects of a distributed force for the thermoelastic source. A new model for the point thermoelastic source is also proposed and the displacements predicted by this model are derived using acoustic theory. This theoretical description predicts both surface and epicentre displacements and these are compared with experimental results. Experimental displacements from the plasma and oil-layer acoustic sources are compared with predicted displacements derived from published results of the theoretically predicted displacements produced by a normal surface force.

The transient surface forces generate acoustic displacements propagating both into the bulk and along the surface of the material. The form of the resulting displacement is characterised by arrivals at the wave velocities corresponding to the longitudinal, shear, Rayleigh modes etc. Fig. 4.1 shows the pattern of these wavefronts

Fig. 4.1



- a - longitudinal wavefront
- b - shear            "
- c - head waves
- d - Rayleigh surface wave

Acoustic wavefront distribution generated in a solid by

a transient point source.

at some point in time from a point source. The longitudinal and shear waves form spherically expanding wavefronts geometrically decaying in amplitude as  $1/r$ . The Rayleigh surface wave, travelling just slower than the shear wave, is confined to a shallow region on the surface, the displacements penetrating to about one wavelength. The Rayleigh wave amplitude decays geometrically as  $1/r^{1/2}$ , slower than the bulk waves because the wave is confined to two dimensions. Wave motions in region c of fig. 4.1 are called "head waves", and they are generated because the longitudinal wave cannot satisfy the boundary condition of vanishing stress at the free surface.

It is possible to predict the absolute displacements anywhere in the material using standard acoustic theory. However, the procedures are long and complex and rarely lead to closed form expressions. In view of this, the work presented in this chapter concerns mainly a comparison of experimental and theoretically predicted displacements on the surface of the material and on epicentre. For these two cases the theoretical treatment is reduced in complexity. Chapter 5 presents a comparison of experimental and theoretically predicted bulk radiation patterns of the wavefront amplitudes for the various modes.

Both surface and epicentre displacements are investigated experimentally using broadband capacitance transducers developed for the purpose of measuring typical nanometre displacements. The nature of operation and characteristics of these and other broadband transducers used in the experiments is given in Chapter 7.

Some of the computer programs designed to generate displacement waveforms from the expressions used in this chapter are described in Appendix 1.

## 4.1 THE THERMOELASTIC SOURCE

### 4.1.1 SURFACE DISPLACEMENTS FROM AN EXTENDED SOURCE

The surface displacements are characterised by the spatial extent of the source, typically 4mm in diameter for the incident unconstrained laser spot of the same diameter. The source is treated as a collection of independent forces with the form of the radial force distribution derived in Chapter 3, eq. 3.12, and is taken to act with Heaviside time dependence on the timescales of interest. The displacements at some point on the surface can be synthesised by adding together the individual displacements due to each force. The force at any point in the source is considered to be a single force acting radially from the source centre on the surface. The force is assumed to appear instantaneously and maintain a constant value over the period of interest, i.e. the form of the Heaviside function for the force amplitude given by eq. 3.12. The vertical displacement,  $U_z$ , due to a tangential surface force has been calculated by Chao (1960, eq. 67). For a force lying parallel to the observer-source direction he gives

$$\begin{aligned}
 U_{z,T,r} &= \frac{\sqrt{6} F_T}{32\pi^2\mu r} \left\{ 6K(m) - 18\Pi(8 m^2, m) \right. \\
 &\quad - (4\sqrt{3}-6) \Pi(-(12\sqrt{3}+20)m^2, m) \quad \left. \frac{1}{\sqrt{3}} < T < 1 \right. \\
 &\quad \left. + (4\sqrt{3}+6) \Pi((12\sqrt{3}+20)m^2, m) \right\} \\
 U_{z,T,r} &= \frac{\sqrt{6n} F_T}{32\pi^2\mu r} \left\{ 6K(n) - 18\Pi(8, n) \right. \\
 &\quad - (4\sqrt{3}-6) \Pi(-(12\sqrt{3}-20), n) \\
 &\quad \left. + (4\sqrt{3}+6) \Pi((12\sqrt{3}+20), n) \right\} \quad 1 < T < \gamma
 \end{aligned}
 \tag{4.1}$$

$$\begin{aligned}
 U_{z,T,r} = & \frac{\sqrt{6n} F_T}{32\pi^2\mu r} \left\{ 6K(n) - 18\Pi(8,n) \right. \\
 & - (4\sqrt{3}-6) \Pi(-(12\sqrt{3}-20),n) \\
 & \left. + (4\sqrt{3}+6) \Pi((12\sqrt{3}+20),n) \right\} \\
 & + \frac{F_T}{8\pi\mu r(T^2-\gamma^2)^{1/2}} \quad \gamma < T
 \end{aligned}$$

where  $U_{z,T,r}$  is the vertical displacement at some time,  $T$ , and at some point  $r$ , from the source of magnitude  $F$ .

$T = \frac{V_S t}{r}$  is the time normalised to shear arrival.

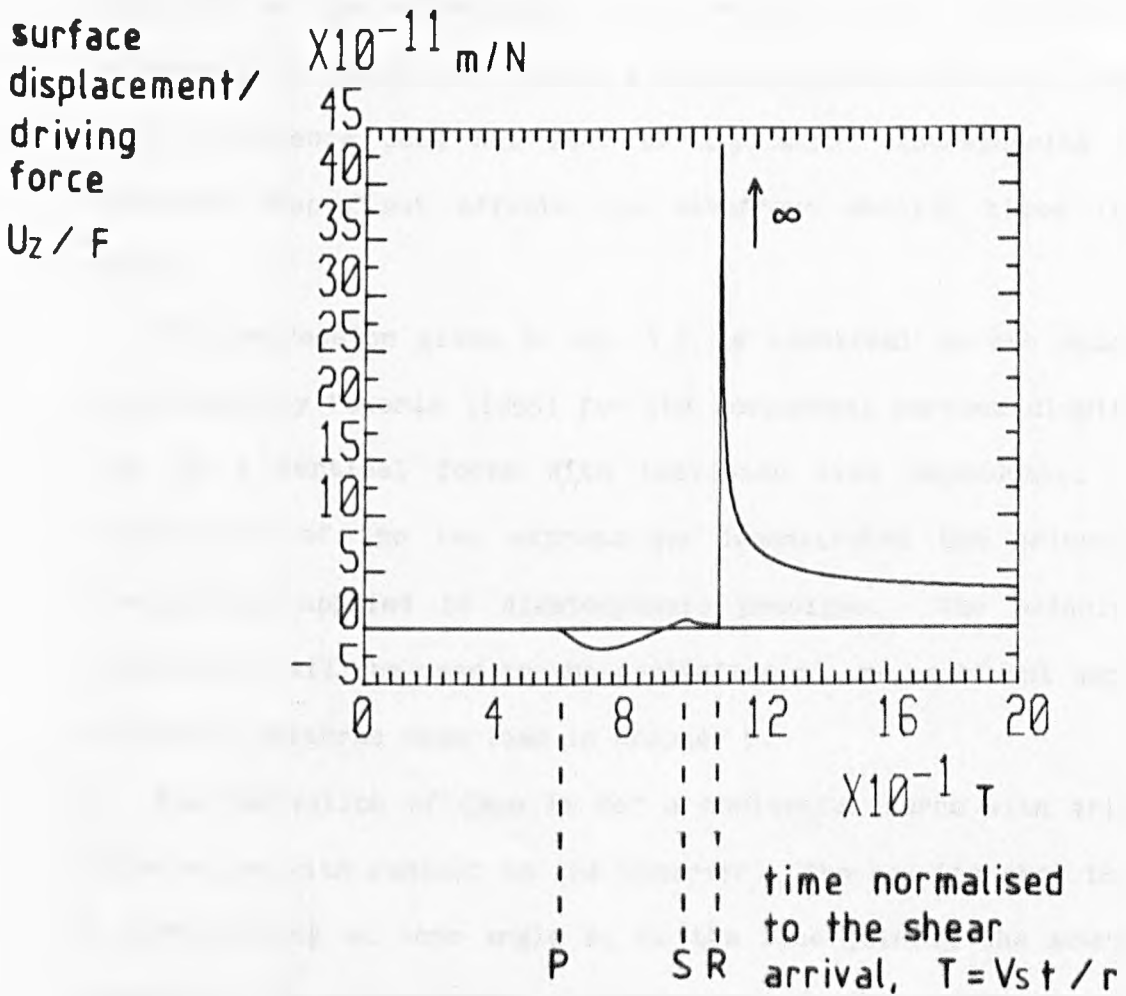
$$m = \frac{3T^2-1}{2}, \quad n = \frac{1}{m}, \quad \gamma = \frac{1}{2} (3+\sqrt{3})^{1/2}$$

$$K(x) = \int_0^{\pi/2} \frac{d\theta}{(1-x^2\sin^2\theta)^{1/2}}, \quad \Pi(y,x) = \int_0^{\pi/2} \frac{d\theta}{(1-y\sin^2\theta)(1-x^2\sin^2\theta)^{1/2}}$$

$K(x)$  and  $\Pi(y,x)$  are standard elliptic integrals.

The form of this displacement is shown in fig. 4.2. The time is normalised to the shear arrival and shows a distinct arrival at a time corresponding to the longitudinal velocity, the shear arrival corresponds to a change in gradient close to the major feature at the arrival time of the Rayleigh surface wave. The Rayleigh arrival includes a singularity which does not exist physically and is a consequence of using a Heaviside source function with an infinitely fast rise time. The calculation is made for a Poisson's ratio of 0.25 for which the algebraic manipulation required to solve the preceding integral form of the displacement is simplified. Mooney (1974) includes an appendix describing how the formulation for this type of

Fig. 4.2



Poisson's ratio = 0.25

$r$  = source-detector distance = 5cm

P = longitudinal arrival

S = shear                    "

R = Rayleigh                "

Chao's solution for the vertical displacement of a half-space subject to a tangential, Heaviside driving force.

problem may be adapted for an arbitrary Poisson's ratio. The majority of the experimental work presented here is performed on aluminium for which the Poisson's ratio is greater than 0.3, however, this difference does not lead to any major discrepancies in the waveform shapes but affects the wavefront arrival times (Mooney, 1974).

The expression given in eq. 4.1 is identical to one calculated previously by Pekeris (1955) for the horizontal surface displacement due to a vertical force with Heaviside time dependence. The equivalence of the two expressions demonstrates the principle of reciprocity applied to elastodynamic problems. The principle of reciprocity will be used in the derivation of the wavefront amplitude radiation patterns described in Chapter 5.

The derivation of Chao is for a horizontal force with arbitrary orientation with respect to the observer. The results show that for a force acting at some angle  $\theta$ , to the line joining the source and observer, the displacement is equivalent to that given by eq. 4.1 with a cosine weighting term, i.e. a force acting perpendicular to the direction of the observer gives rise to no vertical displacement at the observation point. Using this fact, the surface displacement may be synthesised by adding the displacement components due to point elements of the source. An observer at some position,  $O$ , fig. 4.3, will receive displacement information from each set of equidistant points lying on arcs across the source distribution. The radial force acting out from the centre of the source,  $S$ , is given by eq. 3.12 but only the component of this force lying in the direction of the observer gives rise to any displacement at  $O$ . The total displacement at  $O$  is numerically calculated for the component force

distribution across the arc and a set of arcs are scanned to include the area covered by six Gaussian beam radii from the source centre.

From fig. 4.3 the components of the force  $F$ , acting in the direction of the observer is given by  $F\cos\theta$ . The force components are integrated across the major arc defined by constant  $R$  out to the limits of the source at  $r(\max) = a$ . From the cosine law,  $r^2 = R^2 + D^2 - 2RD\cos\phi$ , or  $\cos\phi = (R^2 + D^2 - r^2)/2RD$ , and  $\phi_{\max}$  for  $r = 6a$  is given by

$$\phi_{\max} = \cos^{-1} \left( \frac{R^2 + D^2 - (6a)^2}{2RD} \right) \quad 4.2$$

Again from the cosine law,  $D^2 = r^2 + R^2 - 2rR\cos\phi$ , or

$$\cos\phi = \frac{r^2 + R^2 - D^2}{2rR} = \frac{R - D \cos\phi}{(R^2 + D^2 - 2RD\cos\phi)^{1/2}} \quad 4.3$$

Now  $\cos\theta = -\cos\phi$ , and for the force distribution of eq. 3.12 of the form  $F(r) = F_0 e^{-r^2/a^2}$ , the total force contribution from any arc of constant  $R$  is given by

$$F(R) = 2F_0 R \int_0^{\phi_{\max}} e^{-(R^2 + D^2 - 2RD\cos\phi)/a^2} \times \frac{D \cos\phi - R}{(R^2 + D^2 - 2RD\cos\phi)^{1/2}} d\phi \quad 4.4$$

where  $F_0$  is the local radial force line density, calculated from eq. 3.12 as

$$F_0 = \frac{E \alpha E_T}{\pi(1-\sigma) cpa^2} \quad 4.5$$

The total force for each arc element across the source is evaluated numerically. This force is then used to generate the expected displacements at the observer position and these displacements are

overlaid for each arc as  $R$  extends from one side of the source to the other, from  $R = D - 6a$  to  $R = D + 6a$ . The displacement for a particular force is calculated from eq. 4.1.

Numerically it is unnecessary to re-evaluate eq. 4.1 for each new position of  $R$  because the form of the displacement is fixed, requiring only a simple adjustment to take into account different source-observer separations. The following method helps to minimise computational time. For variations in source-observer distance the displacement will be temporally distorted, fig. 4.4. If the source force moves a distance  $r$  closer to the observer then displacement events will arrive at earlier times. For example, if the source-observer distance is  $R$  the arrival time of the longitudinal disturbance will be given by  $t_p = R/V_p$ , where  $V_p$  is the velocity of the longitudinal wave. If the source now moves a distance  $r$ , closer to the observer then the arrival time of the longitudinal disturbance will be given by

$$t'_p = \frac{R-r}{V_p} = t_p - \frac{r}{V_p} = t_p \left(1 - \frac{r}{R}\right)$$

or for any general time

$$t' = t \left(1 - \frac{r}{R}\right) \quad 4.6$$

The variation in amplitude of the surface displacement with source position may be neglected if it is assumed that the movement of the source,  $r$ , is a lot smaller than the source-observer separation. This is not the situation shown in fig. 4.4, the large value of  $r$  is used simply to illustrate the temporal distortion.

The simplification allows the displacement to be calculated for any position on the force distribution without the need to

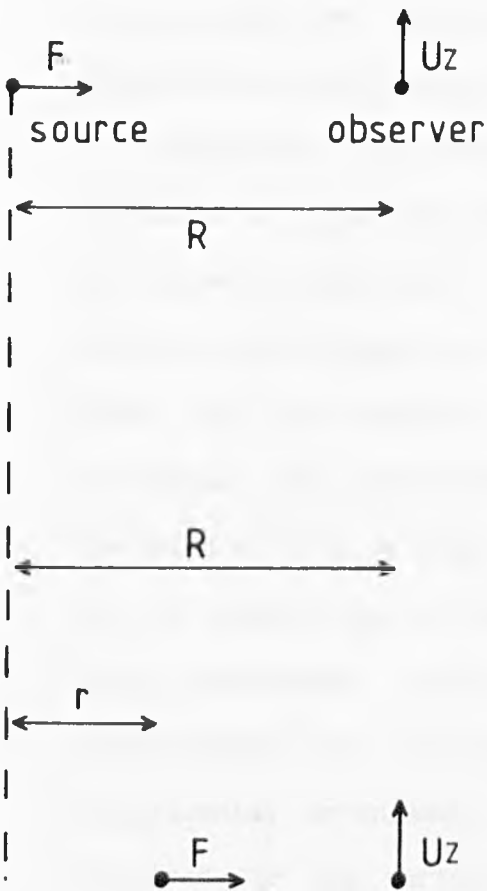
Fig. 4.4

$t_R$  = Rayleigh arrival time

$t_P$  = longitudinal " "

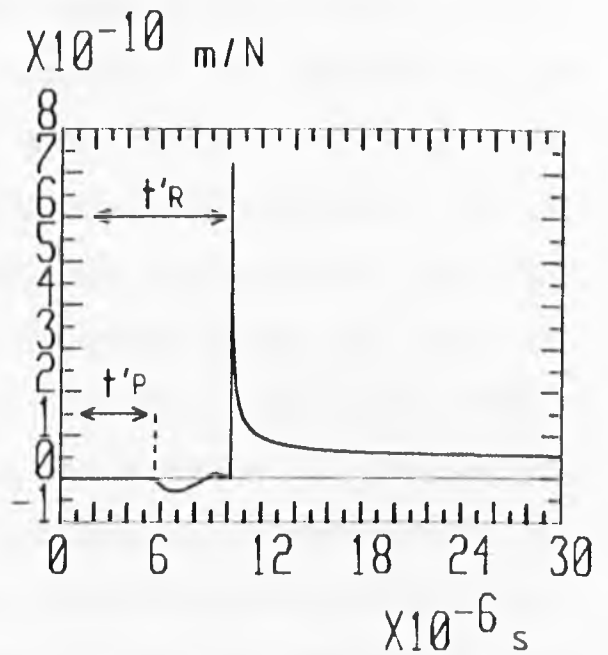
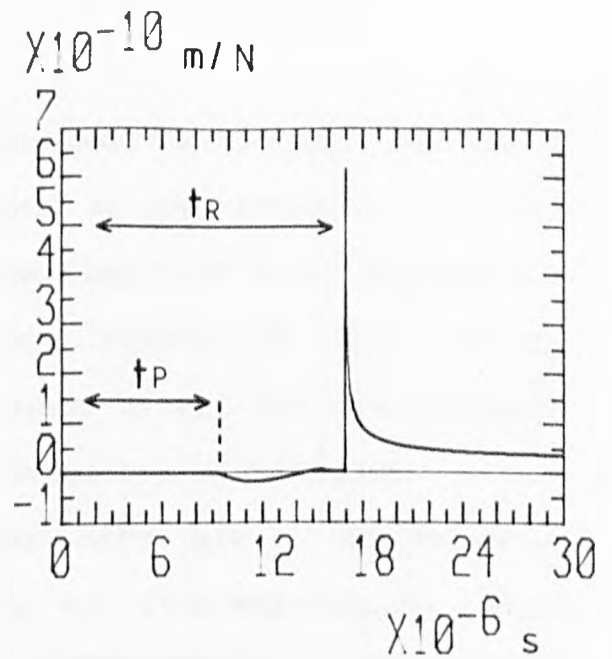
$R = 5\text{cm}$

$r = 2\text{cm}$



arrival retardation

$$t' = t(1+r/R)$$



The temporal distortion of the surface displacement due to a variation in the source-observer separation.

re-calculate the complicated displacement function corresponding to the new positions. The displacement at some position,  $0$ , is thus produced by summation of displacements generated by the expression in eq. 4.1, incorporating the force contribution from the arc corresponding to this position given by eq. 4.4 and temporally adjusted according to eq.4.6 for the position on the source.

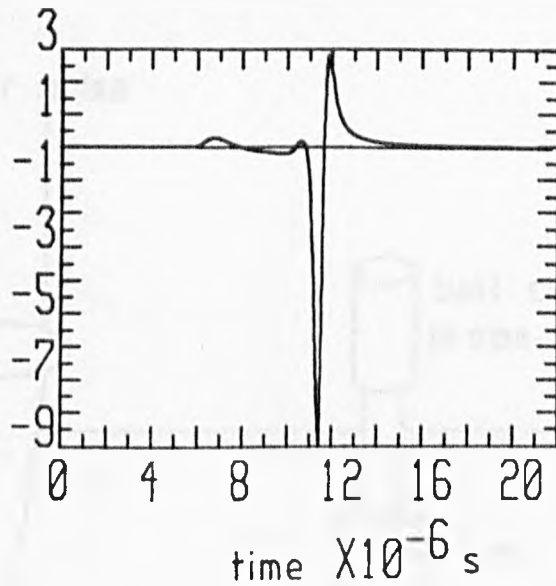
Evaluation for various source radii and a source-observer distance of 3.3cm are shown in fig. 4.5, (the computational details are given in Appendix 1 ). The Rayleigh arrival, which has been inverted with respect to fig. 4.2, is now bipolar and it can be seen from the two waveforms that the width of the Rayleigh arrival increases with increasing beam diameter. The amplitude of the Rayleigh arrival in these figures is not absolute in that the effect of the singularity in the displacement function expression has not been considered. For comparison, the experimentally determined displacements for two beam radii are shown in fig. 4.7, using the experimental arrangement shown in fig. 4.6. The laser energies required for the various acoustic source regimes and the absolute displacements that they produce, are discussed in section 4.5. The experiment was carried out on an aluminium surface using a ball capacitance detector (see Chapter 7 for the details of this detector). There is broad agreement between the figs. 4.5 and 4.7, the theoretical waveforms predicting the form of the wave arrivals and in particular the broadening of the Rayleigh bipolar pulse due to the increase in diameter of the source. Differences in relative arrival times between the theoretical and experimental waveforms is a consequence of the value of Poisson's ratio chosen to model the problem.

Fig. 4.5

(a)

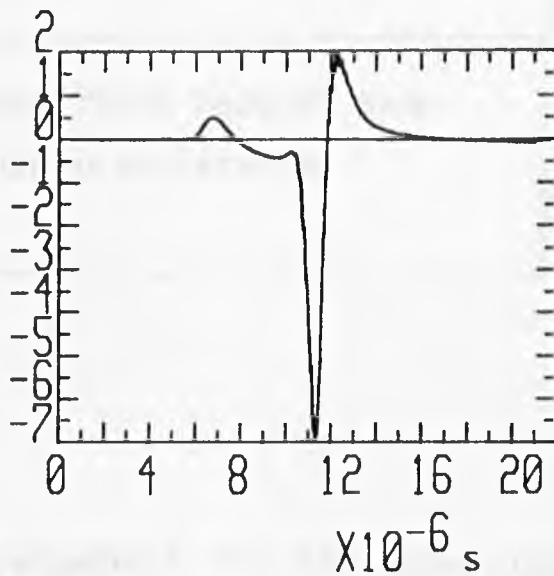
surface  
displacement,  
arbitrary  
units

source  
diameter  
= 2 mm



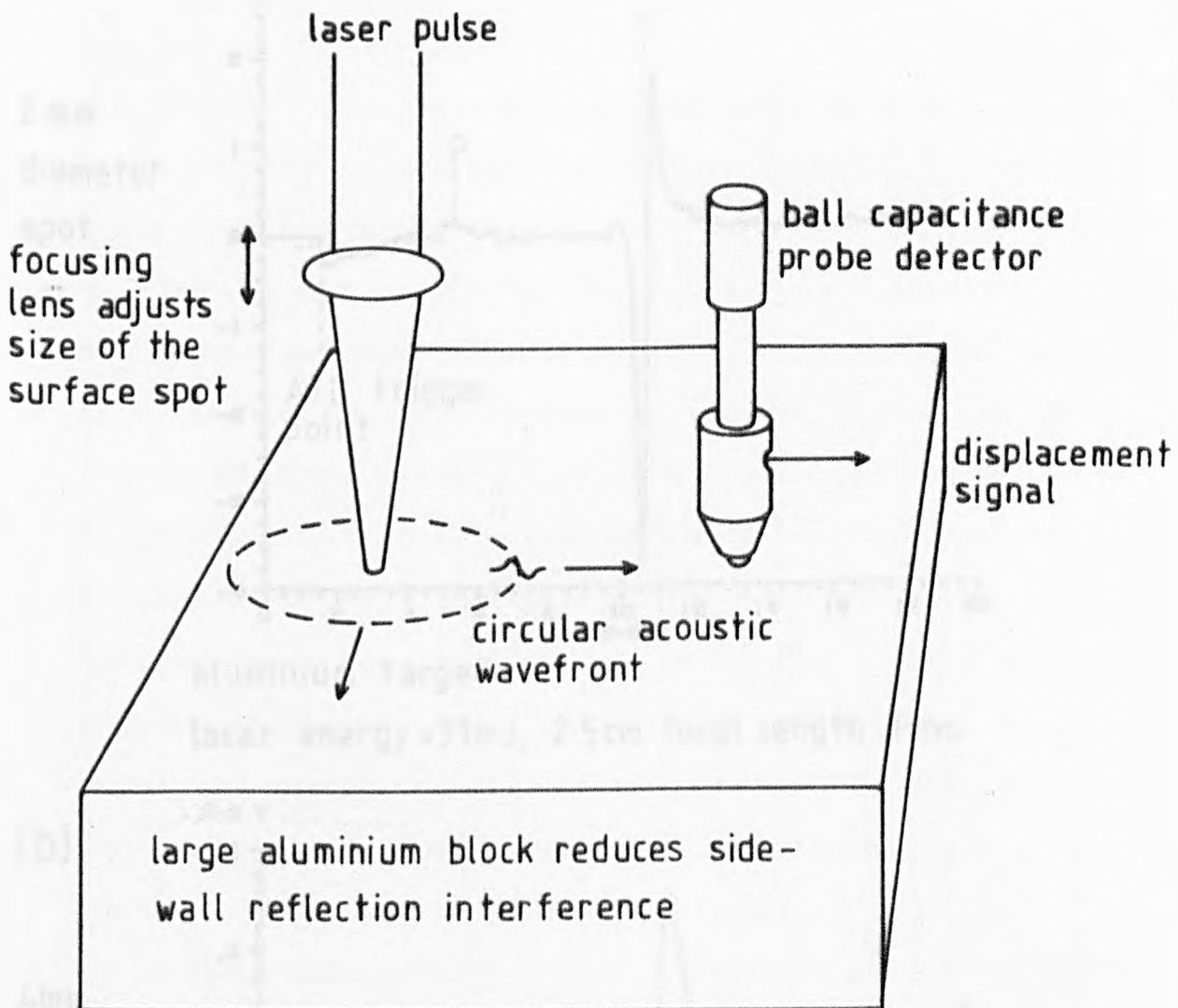
(b)

source  
diameter  
= 4 mm



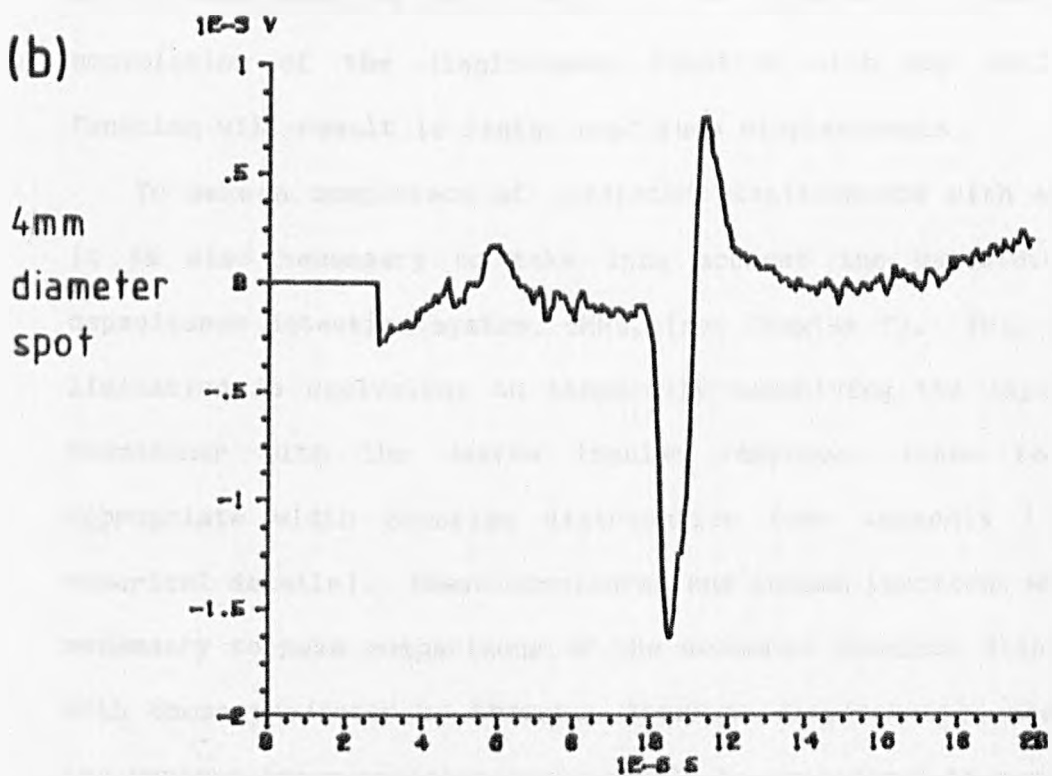
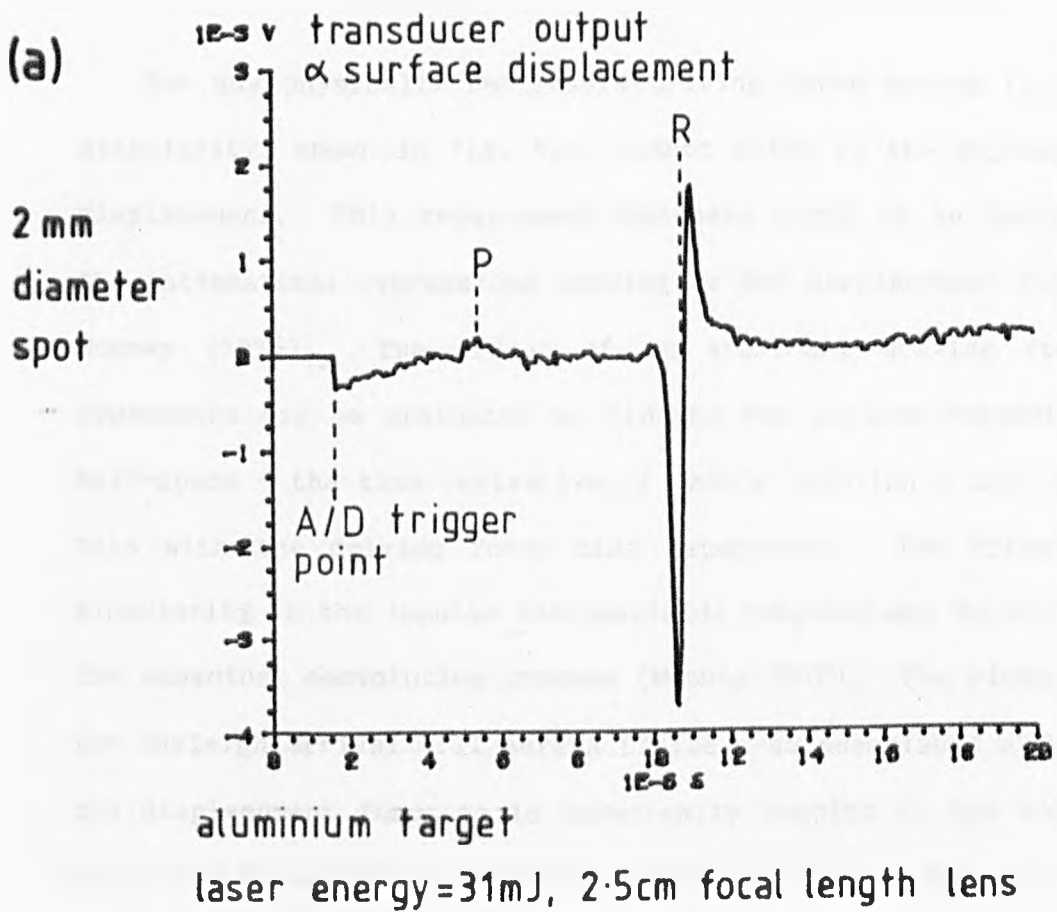
The theoretically simulated surface displacements from extended thermoelastic sources 3.3 cm from the source position. Poisson's ratio = 0.33.

Fig. 4.6



Experimental arrangement for the generation and detection of laser produced surface acoustic transients.

Fig. 4.7



The variation of the surface wave arrivals with thermoelastic source diameter for a source-observer separation of 3.3 cm on aluminium surface using a ball capacitance detector.

For any physically realisable driving force source function the singularity, shown in fig. 4.2, cannot exist in the expressions for displacement. This requirement has been shown to be satisfied for the mathematical expressions leading to the displacement function by Mooney (1976). The effect of an arbitrary driving force time dependence may be evaluated by finding the impulse response of the half-space - the time derivative of Chao's solution - and convolving this with the driving force time dependence. The effect of the singularity in the impulse and Heaviside response may be minimised by the numerical convolution process (Mooney 1976). The singularity at the Rayleigh arrival will have a finite area associated with it. If the displacement function is numerically sampled in the convolution sufficiently accurately that the summation covers most of its area without any sampling point being at the singularity, then numerical convolution of the displacement function with any well defined function will result in finite amplitude displacements.

To make a comparison of predicted displacements with experiment it is also necessary to take into account the bandwidth of the capacitance detection system, 6MHz, (see Chapter 7). This bandwidth limitation is equivalent to temporally convolving the input to the transducer with the device impulse response, taken to be the appropriate width Gaussian distribution (see Appendix 1 for the numerical details). These considerations become important when it is necessary to make comparisons of the measured absolute displacements with those predicted by theory. Absolute displacements produced by the various laser-acoustic sources will be considered in section 4.5.

#### 4.1.2 SURFACE DISPLACEMENTS FROM A POINT SOURCE

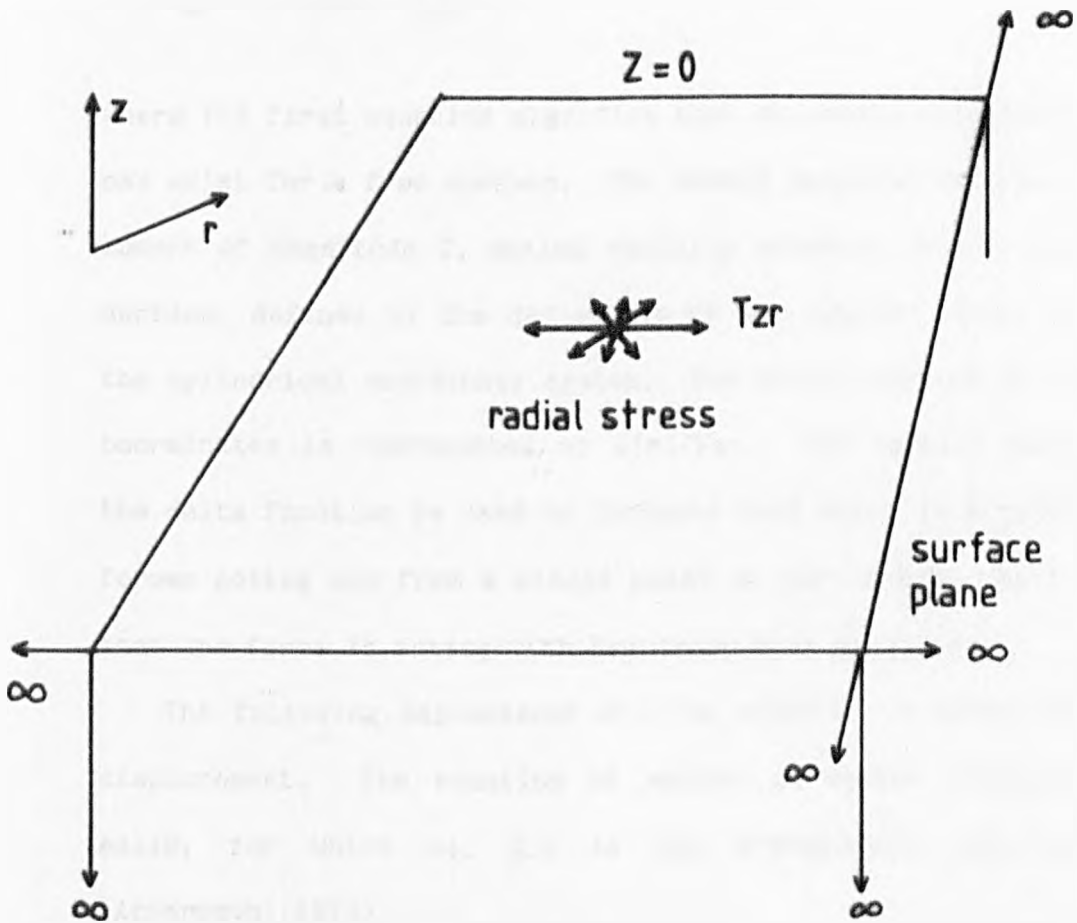
It was shown in the previous section that the extended thermoelastic source can be modelled by numerical summation using Chao's solution for the displacement due to an unbalanced tangential surface force. A more practical and elegant comparison can be made between the experimental thermoelastic displacements and a point thermoelastic source model.

A point thermoelastic source is experimentally difficult to realise. Reducing the surface area of the source and maintaining a thermoelastic rather than plasma interaction process decreases the absorbed energy. Less absorbed energy leads to smaller acoustic displacements which fall below the limit which can be measured experimentally. Theoretically the acoustic displacements due to a point thermoelastic source can be predicted from first principles using some of the general methods that are applied to transient elastic displacement problems.

The proceeding derivation follows the outline of a method used by Achenbach (1973) in which he derives the surface displacement of a half-space due to a normal point load. Here the method is expanded considerably and applied to a point, radial, tangential loading of arbitrary magnitude, corresponding to a point representation of the thermoelastic source.

An isotropic half-space,  $Z < 0$ , fig. 4.8, has a free surface which is subjected to a concentrated tangential, radial loading of magnitude  $Q$  and Heaviside time dependence. The boundary conditions at  $Z = 0$  may be expressed as

Fig. 4.8



A model for the thermoelastic source - the surface,  
point, radial loading of an elastic half-space.

$$T_{zz} = 0$$

$$T_{zr} = QH(t) \frac{\delta'(r)}{2\pi r} \quad 4.7$$

where the first equation signifies that no normal component of stress can exist for a free surface. The second equation denotes the source moment of magnitude  $Q$ , acting radially outwards from a point on the surface, defined by the derivative of the spatial delta function in the cylindrical coordinate system. The delta function in cylindrical coordinates is represented by  $\delta(r)/2\pi r$ . The spatial derivative of the delta function is used to indicate that there is a radial ring of forces acting out from a single point at the centre.  $H(t)$  indicates that the force is acting with Heaviside time dependence.

The following expressions will be required in order to find the displacement. The equation of motion in vector notation for the solid, for which eq. 2.4 is the x-component, may be written (Achenbach, 1973)

$$\mu \nabla^2 \underline{u} + (\lambda + \mu) \nabla \nabla \cdot \underline{u} = \rho \ddot{\underline{u}} \quad 4.8$$

where  $\underline{u}$  is the displacement vector. For ease of manipulation it is convenient to express this displacement vector in terms of a vector and scalar potential.

$$\underline{u} = \nabla \phi + \nabla \times \underline{\psi} \quad 4.9$$

This decomposition of the displacement vector satisfies the equation of motion.  $\phi$  is the scalar potential and is associated with the longitudinal motion.  $\underline{\psi}$  is the vector potential and is associated

with the shear motion. The component displacements of the general displacement vector,  $\underline{u}$ , can be written in terms of these potentials in cylindrical co-ordinates as (Achenbach, 1973)

$$u = \frac{\partial \phi}{\partial r} + \frac{1}{r} \frac{\partial \psi_z}{\partial \theta} - \frac{\partial \psi_\theta}{\partial z}$$

$$v = \frac{1}{r} \frac{\partial \phi}{\partial \theta} + \frac{\partial \psi_r}{\partial z} - \frac{\partial \psi_z}{\partial r}$$

4.10

$$w = \frac{\partial \phi}{\partial z} + \frac{1}{r} \frac{\partial(\psi_\theta r)}{\partial r} - \frac{1}{r} \frac{\partial \psi_r}{\partial \theta}$$

and the wave equation in terms of these potentials becomes

$$\nabla^2 \phi = \frac{1}{v_p^2} \ddot{\phi}$$

$$\nabla^2 \psi_r - \frac{\psi_r}{r^2} - \frac{2}{r^2} \frac{\partial \psi_\theta}{\partial \theta} = \frac{1}{v_p^2} \ddot{\psi}_r$$

$$\nabla^2 \psi_\theta - \frac{\psi_\theta}{r^2} + \frac{2}{r^2} \frac{\partial \psi_r}{\partial \theta} = \frac{1}{v_s^2} \ddot{\psi}_\theta$$

4.11

$$\nabla^2 \psi_z = \frac{1}{v_s^2} \ddot{\psi}_z$$

where, in cylindrical coordinates the Laplacian is given by

$$\nabla^2 = \frac{\partial^2}{\partial r^2} + \frac{1}{r} \frac{\partial}{\partial r} + \frac{1}{r^2} \frac{\partial^2}{\partial \theta^2} + \frac{\partial^2}{\partial z^2}$$

The stress-displacement relations were given in Chapter 2, eq. 2.3

and their equivalent in cylindrical coordinates are

$$T_{zz} = \lambda \left( \frac{\partial u}{\partial r} + \frac{u}{r} + \frac{1}{r} \frac{\partial v}{\partial \theta} + \frac{\partial w}{\partial z} \right) + 2\mu \frac{\partial w}{\partial z}$$

$$T_{rr} = \lambda \left( \frac{\partial u}{\partial r} + \frac{u}{r} + \frac{1}{r} \frac{\partial v}{\partial \theta} + \frac{\partial w}{\partial z} \right) + 2\mu \frac{\partial u}{\partial r}$$

$$T_{\theta\theta} = \lambda \left( \frac{\partial u}{\partial r} + \frac{u}{r} + \frac{1}{r} \frac{\partial v}{\partial \theta} + \frac{\partial w}{\partial z} \right) + 2\mu \left( \frac{u}{r} + \frac{1}{r} \frac{\partial v}{\partial \theta} \right)$$

$$T_{r\theta} = \mu \left( \frac{\partial u}{\partial r} - \frac{v}{r} + \frac{1}{r} \frac{\partial u}{\partial \theta} \right)$$

$$T_{\theta z} = \mu \left( \frac{1}{r} \frac{\partial w}{\partial z} + \frac{\partial v}{\partial z} \right)$$

4.12

$$T_{zr} = \mu \left( \frac{\partial u}{\partial z} + \frac{\partial w}{\partial r} \right)$$

For the axi-symmetric problem being considered, terms in  $\theta$  will be zero and only the vector component  $\psi_\theta$  exists. Finally, if the half-space is at rest before  $t = 0$  then, everywhere except the source, the potentials and their derivatives will be zero.

$$\phi(r, z, 0) = \dot{\phi}(r, z, 0) = \psi_\theta(r, z, 0) = \dot{\psi}_\theta(r, z, 0) = 0 \quad 4.13$$

These basic equations, 4.7 to 4.13 inclusive, provide all the information that is required to solve the problem. The method of solution requires using Laplace and Hankel integral transforms to reduce the appropriate equations to a form where they may be solved, and then applying the inverse transforms to obtain the real solution. The Hankel transform, based on the Bessel functions, is chosen because of the cylindrical symmetry of the problem. The wave

equations for the axi-symmetric case are

$$\frac{\partial^2 \phi}{\partial r^2} + \frac{1}{r} \frac{\partial \phi}{\partial r} + \frac{\partial^2 \phi}{\partial z^2} = \frac{1}{v_p^2} \ddot{\phi} \quad 4.14$$

$$\frac{\partial^2 \psi_\theta}{\partial r^2} + \frac{1}{r} \frac{\partial \psi_\theta}{\partial r} + \frac{\partial^2 \psi_\theta}{\partial z^2} - \frac{\psi_\theta}{r^2} = \frac{1}{v_s^2} \ddot{\psi}_\theta$$

The one-sided Laplace transform is defined as

$$\bar{f}(p) = \mathcal{L}[f(t)] = \int_0^{\infty} f(t) e^{-pt} dt \quad 4.15$$

where the bar denotes the transform variable, and  $p$  is the transform parameter. Applying this transform to equations 4.14, the wave equations become

$$\frac{\partial^2 \bar{\phi}}{\partial r^2} + \frac{1}{r} \frac{\partial \bar{\phi}}{\partial r} + \frac{\partial^2 \bar{\phi}}{\partial z^2} = \frac{p^2}{v_p^2} \bar{\phi} \quad (a)$$

$$\frac{\partial^2 \bar{\psi}_\theta}{\partial r^2} + \frac{1}{r} \frac{\partial \bar{\psi}_\theta}{\partial r} + \frac{\partial^2 \bar{\psi}_\theta}{\partial z^2} - \frac{\bar{\psi}_\theta}{r^2} = \frac{p^2}{v_s^2} \bar{\psi}_\theta \quad (b) \quad 4.16$$

These equations are further reduced by applying the Hankel transform with respect to the variable,  $r$ . The Hankel transform of order  $n$  of a function  $f(r)$  is defined as

$$f^{Hn}(\xi) = \int_0^{\infty} f(r) J_n(\xi r) r dr = H_n [f(r)] \quad 4.17$$

Sneddon (1972) proves the following useful relationships between Hankel transforms of derivatives of functions.

$$H_1 \left[ \frac{\partial}{\partial r} g(r) \right] = -\xi H_0 [g(r)]$$

$$H_1 \left[ \frac{\partial^2}{\partial r^2} g(r) + \frac{1}{r} \frac{\partial}{\partial r} g(r) - \frac{g(r)}{r^2} \right] = -\xi^2 H_1 [g(r)]$$

$$H_0\left[\frac{1}{r} \frac{\partial}{\partial r} (rg(r))\right] = \xi H_1[g(r)] \quad 4.18$$

$$H_0\left[\frac{\partial^2}{\partial r^2} g(r) + \frac{1}{r} \frac{\partial}{\partial r} g(r)\right] = -\xi^2 H_0[g(r)]$$

Applying the zero order transform to equation 4.16(a) and the first order transform to equation 4.16(b), the wave equations simplify to

$$\frac{d^2 \bar{\phi}^{H0}}{dz^2} - \alpha^2 \bar{\phi}^{H0} = 0$$

$$\frac{d^2 \bar{\psi}_\theta^{H1}}{dz^2} - \beta^2 \bar{\psi}_\theta^{H1} = 0 \quad 4.19$$

$$\text{where } \alpha^2 = \left(\xi^2 + \frac{p^2}{v_p^2}\right) \text{ and } \beta^2 = \left(\xi^2 + \frac{p^2}{v_s^2}\right)$$

These equations may be seen to be satisfied by solutions of the form

$$\bar{\phi}^{H0} = \phi(\xi, r) e^{-\alpha z}, \quad \bar{\psi}_\theta^{H1} = \psi(\xi, r) e^{-\beta z} \quad 4.20$$

where  $\phi$  and  $\psi$  are the modified transform scalar and vector potentials. These solutions show appropriate behaviour for large values of  $z$ . Application of the Laplace and appropriate Hankel transforms to the displacement components, equation 4.10, for the axi-symmetric case, gives the transformed vertical and horizontal displacements as

$$\bar{w}^{H0} = \frac{d\bar{\phi}^{H0}}{dz} + \xi \bar{\psi}_\theta^{H1}$$

$$\bar{u}^{H1} = -\xi \bar{\phi}^{H0} - \frac{d\bar{\psi}_\theta^{H1}}{dz} \quad 4.21$$

The required stress equations from equation 4.12 are

$$\begin{aligned} T_{zz} &= (\lambda + 2\mu) \frac{\partial w}{\partial z} + \lambda/r \frac{\partial(ru)}{\partial r} \\ T_{zr} &= \mu \left( \frac{\partial u}{\partial z} + \frac{\partial w}{\partial r} \right) \end{aligned} \quad 4.22$$

Taking Laplace and appropriate Hankel transforms, substituting from eq. 4.21 and remembering that

$$\begin{aligned} \frac{\lambda+2\mu}{\mu} &= \frac{V_p^2}{V_s^2}, \text{ gives} \\ \bar{T}_{zz}^{H0} &= \mu \left( (S_s^2 p^2 + 2\xi^2) \bar{\phi}^{H0} + 2\xi \frac{d\bar{\psi}_\theta^{H1}}{dz} \right) \\ \bar{T}_{zr}^{H1} &= -\mu \left( 2\xi \frac{d\bar{\phi}^{H0}}{dz} + (S_s^2 p^2 + 2\xi^2) \bar{\psi}_\theta^{H1} \right) \end{aligned} \quad 4.23$$

where  $S_s$  is the inverse shear wave speed. The boundary conditions, eq. 4.7, are transformed in the following way

$$\begin{aligned} \bar{T}_{zz}^{H0} &= 0 \\ \bar{T}_{zr} &= \int_0^\infty [Q H(t) \frac{\delta'(r)}{2\pi r}] = \frac{Q}{p} \frac{\delta'(r)}{2\pi r} \\ \bar{T}_{zr}^{H1} &= \frac{Q}{2\pi p} \int_0^\infty \delta'(r) J_1(\xi r) dr \\ &= -\left( \frac{Q}{2\pi p} J_1'(\xi r) \right) \Big|_{r=0}^\infty = \frac{-Q\xi}{2\pi p} \left( J_0(\xi r) - \frac{1}{\xi r} J_1(\xi r) \right) \\ \lim_{r \rightarrow 0} & \quad \lim_{r \rightarrow 0} \\ &= \frac{-Q\xi}{4\pi p} \end{aligned} \quad 4.24$$

Applying these boundary conditions to eq. 4.22 gives

$$(S_S^2 p^2 + 2\xi^2)\bar{\phi}^{HO} = -2\xi \frac{d\bar{\psi}_0^{H1}}{dz}$$

$$\frac{Q\xi}{4\pi\mu p} = 2\xi \frac{d\bar{\phi}^{HO}}{dz} + (S_S^2 p^2 + 2\xi^2)\bar{\psi}_0^{H1} \quad 4.25$$

At  $z = 0$  and introducing eq. 4.20 these equations become

$$(S_S^2 p^2 + 2\xi^2)\phi = 2\xi \beta \psi$$

$$\frac{Q\xi}{4\pi\rho\mu} = -2\xi\alpha\phi + (S_S^2 p^2 + 2\xi^2)\psi \quad 4.26$$

on re-arranging, these give the modified transform vector and scalar potentials

$$\psi = \frac{Q\xi(2\xi^2 + S_S^2 p^2)}{4\pi\rho\mu((2\xi^2 + S_S^2 p^2)^2 - 4\xi^2\alpha\beta)}$$

$$\phi = \frac{2 Q\xi^2\beta}{4\pi\rho\mu((2\xi^2 + S_S^2 p^2)^2 - 4\xi^2\alpha\beta)} \quad 4.27$$

Substitution of these into eq. 4.21 gives the vertical displacement as

$$\bar{w}^{HO} = \frac{Q}{4\pi\rho\mu} \frac{\xi^2((2\xi^2 + S_S^2 p^2) - 2\alpha\beta)}{((2\xi^2 + S_S^2 p^2)^2 - 4\xi^2\alpha\beta)} \quad 4.28$$

This is the Laplace-Hankel transform of the vertical displacement of the half-space. To obtain a real solution it is now necessary to apply the inverse Hankel and Laplace transforms. The inverse zero order Hankel transform is straightforward and gives

$$\bar{w} = \frac{Q}{4\pi\rho\mu} \int_0^\infty \frac{\xi^3((2\xi^2 + S_S^2 p^2) - 2\alpha\beta)}{(2\xi^2 + S_S^2 p^2)^2 - 4\xi^2\alpha\beta} J_0(\xi r) d\xi \quad 4.29$$

A change of variable is now made to extract the Laplace transform parameter  $\xi = p_n$ .

$$\bar{W} = \frac{Qp}{4\pi\mu} \int_0^{\infty} \frac{n^3((2n^2+S_S^2) - 2(S_S^2+n^2)^{1/2}(S_P^2+n^2)^{1/2})}{((2n^2+S_S^2)^2 - 4n^2(S_S^2+n^2)^{1/2}(S_P^2+n^2)^{1/2})} J_0(pnr) dn \quad 4.30$$

In general the Laplace transform is now found by coercing the expression, eq. 4.30, into the form of the Laplace transform equation 4.15, from which the inverse transform may be seen by inspection. This inversion procedure is known as the Cagniard-de Hoop method (Achenbach, 1973). First the integral is simplified by making the change of variable  $n = m S_S$ . The integral, eq. 4.30, then becomes

$$\bar{W} = \frac{QpS_S^2}{4\pi\mu} \int_0^{\infty} \frac{m^3((2m^2+1) - 2(m^2+1)^{1/2} (m^2+(\frac{S_P}{S_S})^2)^{1/2})}{((2m^2+1)^2 - 4m^2(m^2+1)^{1/2}(m^2+(\frac{S_P}{S_S})^2)^{1/2})} J_0(pm S_S r) dm \quad 4.31$$

The algebra in the following procedures is greatly simplified if it is assumed that  $\lambda = \mu$ , corresponding to a Poisson's ratio of 0.25, and for which the inverse wave speeds are related by  $(S_P/S_S)^2 = 1/3$ . Multiplying the top and bottom of the integrand expression in eq. 4.31 by

$$(2m^2+1)^2 + 4m^2(m^2+1)^{1/2} (m^2+1/3)^{1/2}$$

for  $\lambda = \mu$  gives

$$\bar{W} = \frac{QpS_s^2}{4\pi\mu} \int_0^{\infty} \frac{m^3((2m^2+1)-2(m^2+1)^{\frac{1}{2}}(m^2+1/3)^{\frac{1}{2}})((2m^2+1)^2+4m^2(m^2+1)^{\frac{1}{2}}(m^2+1/3)^{\frac{1}{2}})}{((2m^2+1)^4 - 16m^4(m^2+1)(m^2+1/3))} dm$$

4.32

The denominator of the integrand in equation 4.32 is the Rayleigh equation, eq. 2.8, and can be factorised in a simple fashion for the case of  $\lambda = \mu$ . Eq. 4.32 may thus be re-written

$$\bar{W} = \frac{3QpS_s^2}{4*32\pi\mu} \int_0^{\infty} \frac{m^3(\frac{4}{3}(m^2+A^2)(m^2+B^2)-2(2m^2+1)(m^2+1)^{\frac{1}{2}}(m^2+1/3)^{\frac{1}{2}})}{(1/4+m^2)(m^2+C^2)(m^2+D^2)} dm$$

$$= \frac{3QpS_s^2}{4*32\pi\mu} \int_0^{\infty} F(m) J_0(pm S_s r) dm$$

4.33

where

$$A^2 = \frac{5+\sqrt{13}}{4}, \quad B^2 = \frac{5-\sqrt{13}}{4}$$

$$C^2 = \frac{3-\sqrt{3}}{4}, \quad D^2 = \frac{3+\sqrt{3}}{4}$$

In order to find the inverse Laplace transform, the Bessel function is re-written in one of its integral expansion forms, (McClachlan, 1955)

$$J_0(x) = \frac{2}{\pi} \text{II} \int_1^{\infty} \frac{e^{-xs}}{(s^2-1)^{1/2}} ds$$

4.34

Where  $\text{II}$  denotes the imaginary part of the result of the integral.

Eq. 4.33 can then be written

$$\bar{W} = \frac{3QpS_s^2}{64\pi\mu} \prod \int_0^{\infty} F(m) \int_1^{\infty} \frac{e^{ipm S_s r_s}}{(s^2-1)^{1/2}} ds dm \quad 4.35$$

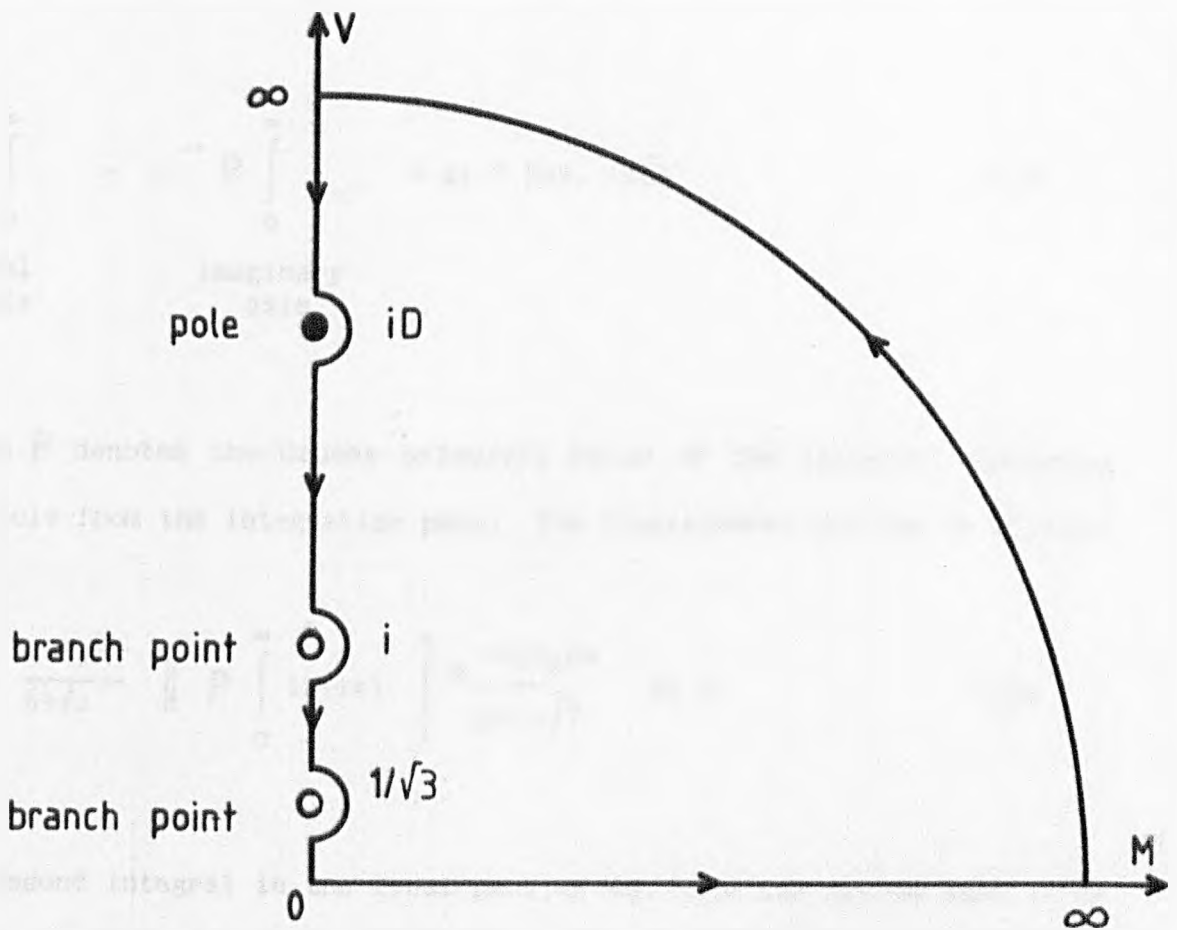
In order to coerce this integral into the form of the Laplace transform equation it is necessary to expand the integral into the complex plane,  $z = m+iv$ , for which eq. 4.35 corresponds to the integral along the real axis of the complex function

$$\frac{3QpS_s^2}{64\pi\mu} \prod \int_0^{\infty} F(z) \int_1^{\infty} \frac{e^{izpS_s r_s}}{(s^2-1)^{1/2}} ds dz \quad 4.36$$

In general the Cagniard-de Hoop inversion method will lead to a particular integration path in the complex plane, not necessarily along the axes. In the case of the surface and epicentre displacements this integration path simplifies. Consider the integration contour path shown in fig. 4.9. The path of integration along the imaginary axis encounters a pole at  $iD$  and two branch points at  $i$  and  $1/\sqrt{3}i$  of the function  $F(z)$ . The additional poles of  $F(z)$  at  $1/2i$  and  $iC$  do not affect the integral since the numerator of  $F(z)$  can be shown to also be zero at these points. The path of integration excludes the poles and branch points, so by the residue theorem the contour integral is zero. The branch points give no contribution to the integral along the imaginary axis, and the pole gives a contribution of  $i\pi$  times the residue at the pole.

$$\oint = C = \int_0^{\infty} \text{real axis} + \int_{\infty}^{\text{arc at } \infty} + P \int_0^{\infty} \text{imaginary axis} - \pi i * \text{Res. } (iD)$$

Fig. 4.9



Integration path in the complex plane for evaluating

the surface displacement from the point thermoelastic source.

The integral along the arc of infinite radius can be shown to be zero, and so the integral along the real axis may be replaced by one along the imaginary axis plus the contribution at the pole.

$$\int_0^{\infty} = \text{P} \int_0^{\infty} + \pi i * \text{Res. (iD)} \quad 4.37$$

real axis
imaginary axis

where  $\text{P}$  denotes the Cauchy principle value of the integral, excluding the pole from the integration path. The displacement may now be written

$$\bar{W} = \frac{3QS_s^2}{64\pi^2\mu} \text{P} \int_0^{\infty} iF(iv) \int_1^{\infty} \frac{e^{-vpS_s r s}}{(s^2-1)^{1/2}} ds dv \quad 4.38$$

The second integral in the first part of eq. 4.38 can now be seen to be approaching the form of the Laplace transform equation. The change of variable  $y = VS_s r s$  is now made in this integral.

$$\bar{W} = \frac{3QS_s^2 p}{64\pi^2\mu} \text{P} \int_0^{\infty} iF(iv) \int_{vrS_s}^{\infty} \frac{e^{-py}}{(y^2 - v^2 r^2 S_s^2)^{1/2}} dy dv$$

+  $\pi i * \text{Res. (iD)}$ 
4.39

Looking at those parts of eq. 4.39 which involve the Laplace transform parameter, the inverse transform may be seen by inspection from the following relationship

$$\begin{aligned}
 & \mathcal{L}^{-1} \left[ p \int_{VrS_S}^{\infty} \frac{e^{-py}}{(y^2 - v^2 S_S^2 r^2)^{1/2}} dy \right] \\
 &= \mathcal{L}^{-1} \left[ p \int_0^{\infty} \frac{e^{-py}}{(y^2 - v^2 r^2 S_S^2)^{1/2}} H(y - VrS_S) dy \right] \quad 4.40 \\
 &= \frac{\partial}{\partial t} \left[ \frac{H(t - VrS_S)}{(t^2 - v^2 r^2 S_S^2)^{1/2}} \right]
 \end{aligned}$$

The displacement is then given by

$$\begin{aligned}
 W &= \frac{3Q S_S^2}{64\pi\mu} \left\| \left\| p \frac{\partial}{\partial t} \int_0^{\infty} \frac{iF(iv) H(t - VrS_S)}{(t^2 - v^2 r^2 S_S^2)^{1/2}} dv \right. \right. \\
 &\quad \left. \left. + \mathcal{L}^{-1} [\pi i * \text{Res. (iD)}] \right\| \right. \quad 4.41
 \end{aligned}$$

The time may be normalised to the shear arrival by making the substitution  $t = TrS_S$ .

$$\begin{aligned}
 W &= \frac{3Q}{64\pi\mu r^2} \left\| \left\| p \frac{\partial}{\partial T} \int_0^{\infty} \frac{iF(iv) H(T - V)}{(T^2 - v^2)^{1/2}} dv \right. \right. \\
 &\quad \left. \left. + \mathcal{L}^{-1} [\pi i * \text{Res. (iD)}] \right\| \right. \quad 4.42
 \end{aligned}$$

The term still containing the inverse Laplace transform may be expanded as

$$\begin{aligned}
 \pi i * \text{Res. (iD)} &= \frac{3QpS_S^2}{4*32\mu} * \\
 &= \frac{-iD^3(A^2 - D^2)(B^2 - D^2) + 2(1 - 2D^2)(D^2 - 1)^{1/2}(D^2 - 1/3)^{1/2}}{(1/4 - D^2)(C^2 - D^2)} J_0(iDS_S r p)
 \end{aligned}$$

4.43

Using the previous method to find the inverse Laplace transform of the residue expression leads to the total expression for the displacement as

$$W = \frac{3Q}{64\pi\mu r^2} \left\| \left[ P \frac{\partial}{\partial T} \int_0^T \frac{v^3 \left( \frac{4}{3}(A^2 - v^2)(B^2 - v^2) - 2(1 - 2v^2)(1 - v^2)^{1/2}(1/3 - v^2)^{1/2} \right)}{(1/4 - v^2)(C^2 - v^2)(D^2 - v^2)(T^2 - v^2)^{1/2}} dv \right. \right. \\ \left. \left. + \frac{3Q}{64\pi\mu r^2} \frac{\partial}{\partial T} \left[ \frac{D^3 \left( \frac{4}{3}(A^2 - D^2)(B^2 - D^2) + 2(1 - 2D^2)(D^2 - 1)^{1/2}(D^2 - 1/3)^{1/2} \right)}{(1/4 - D^2)(C^2 - D^2)(T^2 - D^2)^{1/2}} \right] * H(T - D) \right] \right.$$

4.44

This expression for the displacement may be separated into various time intervals giving

$$W = 0 \quad T < 1/\sqrt{3}$$

$$W = \frac{-3Q}{32\pi\mu r^2} \frac{\partial}{\partial T} P \int_{1/\sqrt{3}}^T \frac{v^3 \left( (1 - 2v^2)(1 - v^2)^{1/2}(v^2 - 1/3)^{1/2} \right)}{(1/4 - v^2)(C^2 - v^2)(D^2 - v^2)(T^2 - v^2)^{1/2}} dv \quad 1/\sqrt{3} < T < 1$$

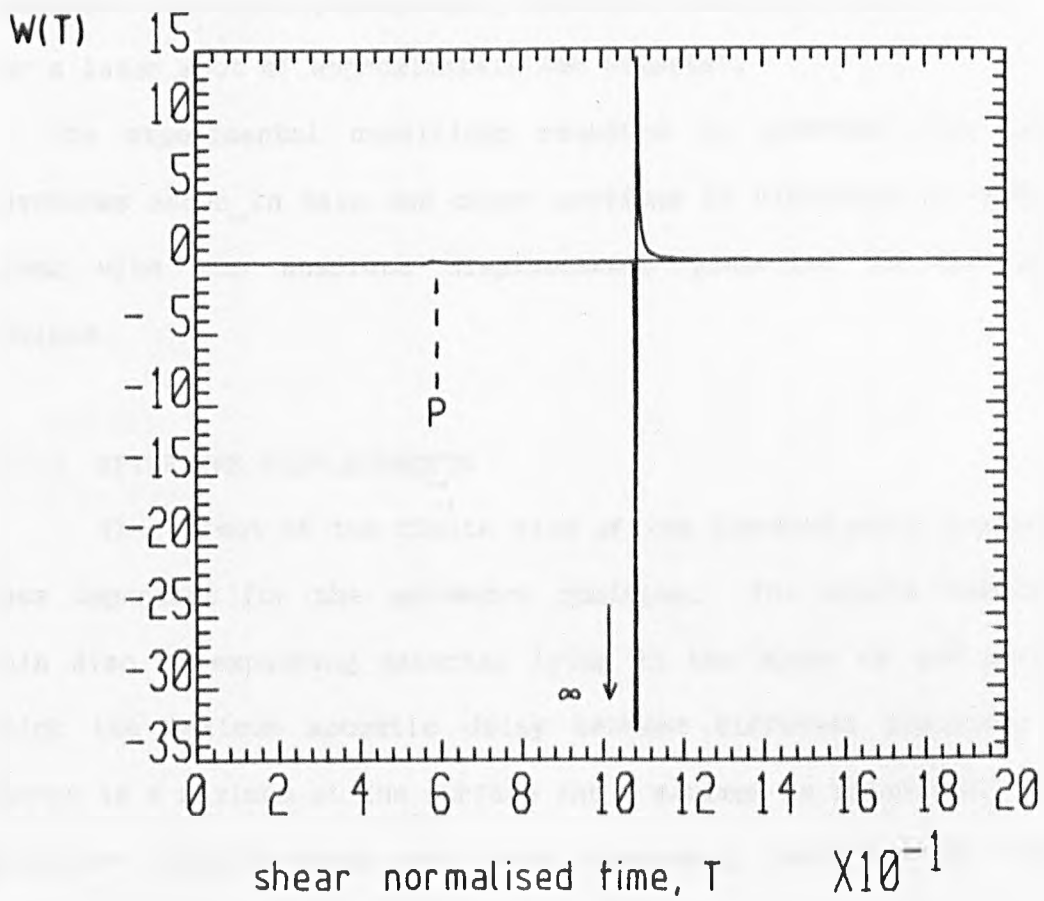
$$W = \frac{-3Q}{32\pi\mu r^2} \frac{\partial}{\partial T} P \int_{1/\sqrt{3}}^1 \frac{v^3 \left( (1 - 2v^2)(1 - v^2)^{1/2}(v^2 - 1/3)^{1/2} \right)}{(1/4 - v^2)(C^2 - v^2)(D^2 - v^2)(T^2 - v^2)^{1/2}} dv = I_1(T) \quad 1 < T < D$$

4.45

$$W = I_1(T) + \frac{3Q}{64\pi\mu r^2} \frac{\partial}{\partial T} \left[ \frac{D^3 \left( \frac{4}{3}(A^2 - D^2)(B^2 - D^2) + 2(1 - 2D^2)(D^2 - 1)^{1/2}(D^2 - 1/3)^{1/2} \right)}{(1/4 - D^2)(C^2 - D^2)(T^2 - D^2)^{1/2}} \right] \quad T > D$$

Eq. 4.45 gives the first description of the surface displacement due to a thermoelastic point source, modelled as a point radial expansion at the surface of an elastic half-space. The waveform corresponding to eq. 4.45 is shown in fig. 4.10. The expression contains a discontinuity at the Rayleigh arrival which may be accounted for in the way described in section 4.1 by a convolution with the measuring system impulse

Fig. 4.10



$T = V_s t / r$ ,  $Q =$  source radial moment

surface displacement =  $W(T) / 32 \pi \mu r^2 \times 3Q \times 200$

The theoretically predicted surface displacement of a half-space from a point radial loading with Heaviside time dependence.

response. This leads to the waveform shown in fig. 4.11(a) which may be compared with the experimentally observed waveform shown in fig. 4.11(b) for a laser spot of approximately 1mm diameter.

The experimental conditions required to generate this and other waveforms shown in this and other sections is discussed in section 4.5, along with the absolute displacements generated in the different regimes.

#### 4.1.3 EPICENTRE DISPLACEMENTS

The effect of the finite size of the thermoelastic source becomes less important for the epicentre position. The source consists of a thin disc of expanding material lying in the plane of the surface for which the maximum acoustic delay between different positions on the source is a maximum at the surface and a minimum on epicentre. The epicentre displacements are thus adequately modelled by the point representation of thermoelastic source discussed in section 4.1.2.

Eq. 4.21 gives the Laplace-Hankel transform of the vertical displacement anywhere in the half-space as

$$\bar{W}^{HO} = \xi \psi e^{-\beta z} - \alpha \phi e^{-\alpha z} \quad 4.46$$

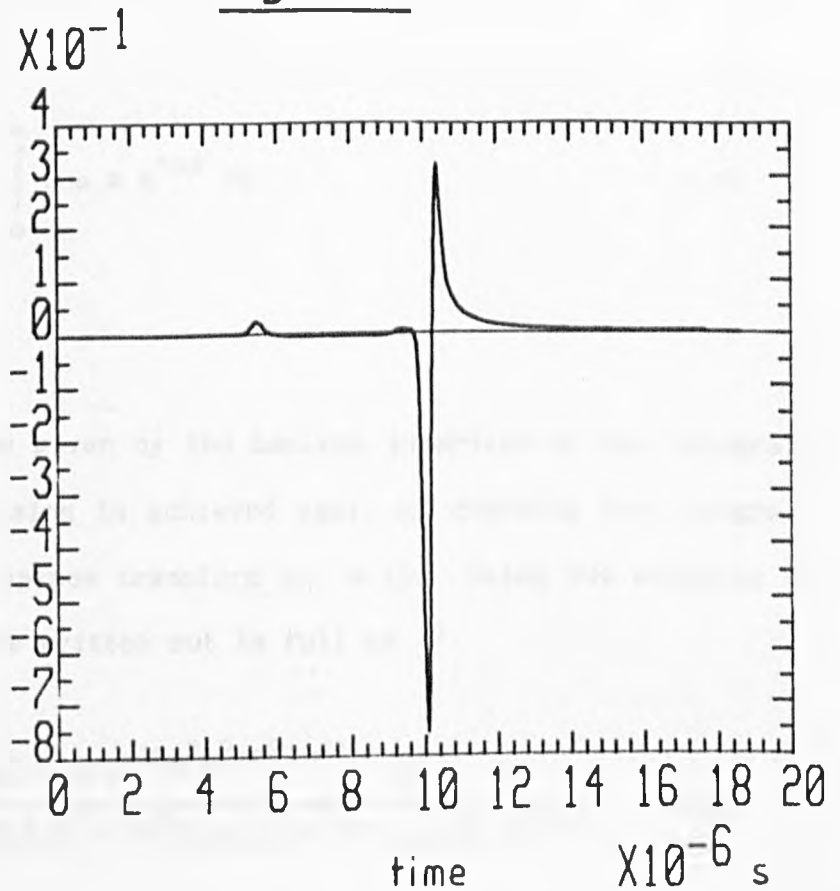
In order to find the epicentre displacement the zero order Hankel inversion is first performed

$$\bar{W} = \int_0^{\infty} \xi^2 \psi e^{-\beta z} J_0(\xi r) d\xi - \int_0^{\infty} \xi \alpha \phi e^{-\alpha z} J_0(\xi r) d\xi \quad 4.47$$

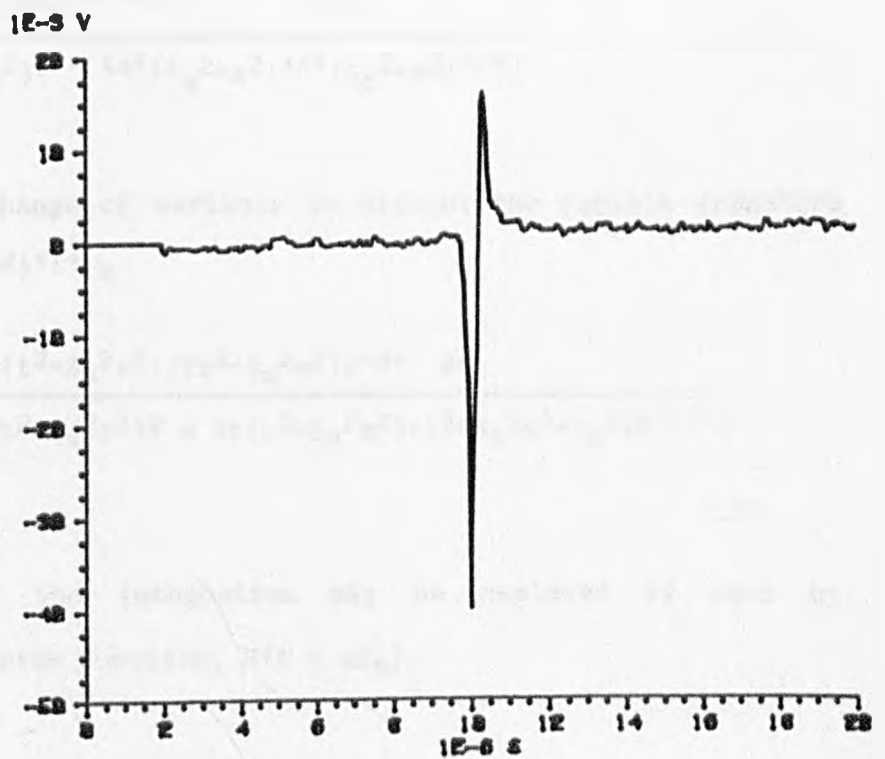
On epicentre,  $r = 0$  and  $J_0(0) = 1$ , giving

Fig. 4-11

(a) predicted displacement using a 6MHz Gaussian bandwidth detection system. arb. units



(b) ball capacitance detector output source diameter = 1mm source - detector separation = 2.9cm, aluminium



A comparison of predicted and experimental point thermoelastic displacements.

$$\begin{aligned}\bar{W} &= \int_0^{\infty} \xi^2 \psi e^{-\beta z} d\xi - \int_0^{\infty} \xi \alpha \phi e^{-\alpha z} d\xi \\ &= \bar{W}_1 - \bar{W}_2\end{aligned}\quad 4.48$$

The displacement is now given by the Laplace inversion of the integrals  $W_1$  and  $W_2$ . The inversion is achieved again by coercing the integrals into the form of the Laplace transform eq. 4.15. Using the notation of section 4.1.2,  $W_1$  may be written out in full as

$$\bar{W}_1 = \frac{Q}{4\pi p \mu} \int_0^{\infty} \frac{(2\xi^2 + S_s^2 p^2) \xi^3 e^{-(S_s^2 p^2 + \xi^2)^{1/2} z} d\xi}{((2\xi^2 + S_s^2 p^2)^2 - 4\xi^2 (S_s^2 p^2 + \xi^2)^{1/2} (S_p^2 p^2 + \xi^2)^{1/2})} \quad 4.49$$

changing the variable,  $\xi = px$  gives

$$\bar{W}_1 = \frac{Qp}{4\pi \mu} \int_0^{\infty} \frac{x^3 (2x^2 + S_s^2) e^{-p(S_s^2 + x^2)^{1/2} z} dx}{((2x^2 + S_s^2)^2 - 4x^2 (S_s^2 + x^2)^{1/2} (S_p^2 + x^2)^{1/2})} \quad 4.50$$

now making a final change of variable to extract the Laplace transform parameter,  $t = (S_s^2 + x^2)^{1/2} z$

$$\bar{W}_1 = \frac{Qp}{4\pi \mu z^2} \int_{S_s z}^{\infty} \frac{t(t^2 - S_s^2 z^2)(2t^2 - S_s^2 z^2) e^{-pt} dt}{((2t^2 - S_s^2 z^2)^2 - 4t(t^2 - S_s^2 z^2)(t^2 - S_s^2 z^2 + S_p^2 z^2)^{1/2})} \quad 4.51$$

The lower limit of the integration may be replaced by zero by introducing the Heaviside function,  $H(t - zS_s)$

$$\bar{W}_1 = \frac{Qp}{4\pi \mu z^2} \int_0^{\infty} f(t) H(t - zS_s) e^{-pt} dt \quad 4.52$$

Eq. 4.52 is now in the form of the Laplace transform and the inversion may now be seen by inspection as

$$\begin{aligned}
 W_1(t) &= \frac{Q}{4\pi\mu z^2} \frac{\partial}{\partial t} \left( f(t) H\left(t - \frac{z}{V_S}\right) \right) \\
 &= \frac{Q}{4\pi\mu z^2} \left( \dot{f}(t) H\left(t - \frac{z}{V_S}\right) + \delta\left(t - \frac{z}{V_S}\right) f(t) \right)
 \end{aligned}$$

4.53

where  $f(t)$  is given by

$$f(t) = \frac{t(t^2 - S_S^2 z^2)(2t^2 - S_S^2 z^2)}{((2t^2 - S_S^2 z^2)^2 - 4t(t^2 - S_S^2 z^2)(t^2 + S_P^2 z^2 - S_S^2 z^2))}$$

The delta function term in eq. 4.53 reduces to zero because  $f(t = z/V_S) = 0$ . The component of displacement from the first expression in eq. 4.48 can now be written

$$W_1(t) = \frac{Q}{4\pi\mu z^2} \dot{f}(t) H\left(t - \frac{z}{V_S}\right) \quad 4.54$$

This can be seen to be the component of displacement associated with the shear motion. A similar analysis of the second part of eq. 4.48 leads to an expression associated with the longitudinal component of displacement

$$W_2(t) = \frac{Q}{2\pi\mu z^2} \dot{g}(t) H\left(t - \frac{z}{V_P}\right) \quad 4.55$$

where

$$g(t) = \frac{t^2(t^2 - z^2 S_P^2)(t^2 + S_S^2 z^2 - S_P^2 z^2)^{1/2}}{(2t^2 + S_S^2 z^2 - 2S_P^2 z^2)^2 - 4t(t^2 - S_P^2 z^2)(t^2 + S_S^2 z^2 - S_P^2 z^2)^{1/2}}$$

In terms of the notation used in section 4.1.2 for dimensionless time, the displacement may be normalised to the shear arrival in the same manner by making the substitution  $t = S_s z T$ .

$$W(T) = \frac{Q}{2\pi\mu z^2} \frac{\partial}{\partial T} \left[ \frac{T^2(T^2-R^2)(T^2+1-R^2)^{1/2} H(T-R)}{((2T^2+1-2R^2)^2 - 4T(T^2-R^2)(T^2+1-R^2)^{1/2})} \right. \\ \left. - \frac{T(T^2-1)(2T^2-1) H(T-1)}{2((2T^2-1)^2 - 4T(T^2-1)(T^2+R^2-1)^{1/2})} \right]$$

4.56

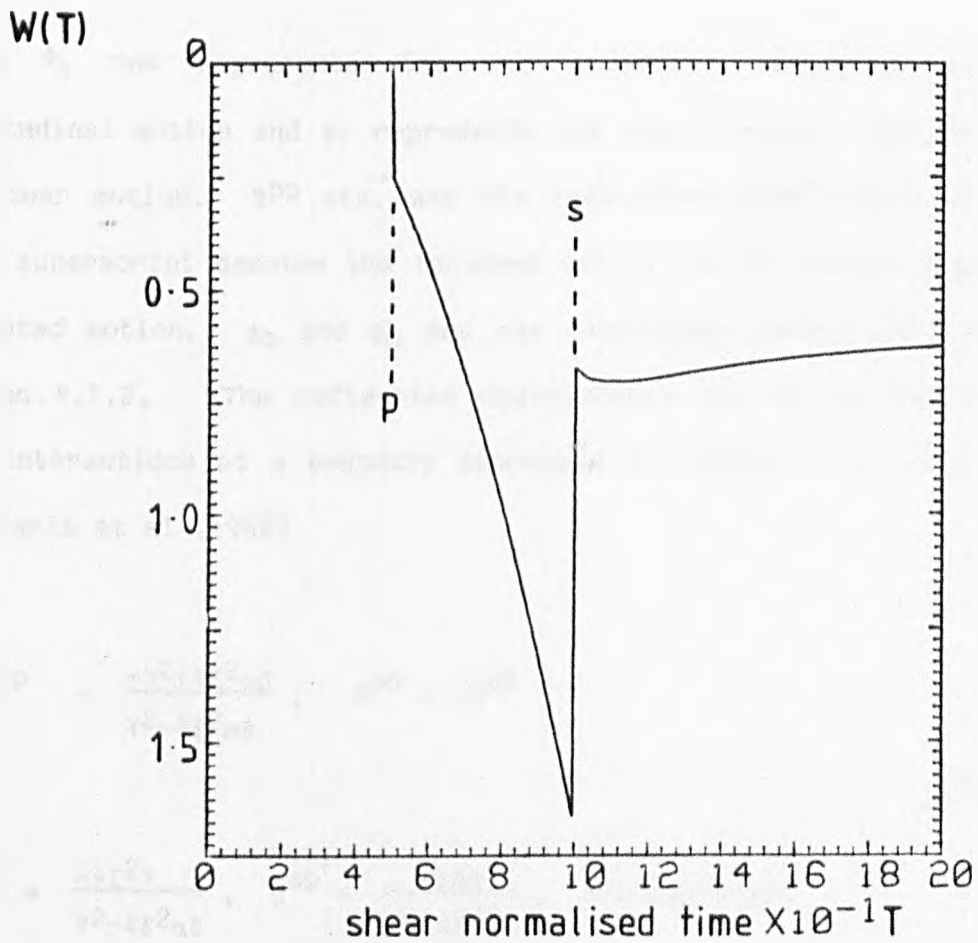
Where  $R$  is the ratio of shear to longitudinal velocities. The waveform given by eq. 4.56 is shown in fig. 4.12.

It should be noted that this expression for the displacement is for points internal to the bulk of the half-space. Experimental measurements are carried out on a plate and the effect of this extra free surface at  $z = h$ , the plate thickness, should be recognised. Formally this would be accounted for by solving the equation of motion subject to the two sets of boundary conditions at  $z = 0$  and  $z = h$ . An alternative and convenient way of approaching this problem is to take the extra free surface into account by means of the reflection coefficients for a free surface for the various modes.

In general, a longitudinal disturbance incident on the boundary will give rise to reflected longitudinal and mode converted shear motion. Likewise, incident shear motion will give rise to reflected shear and mode converted longitudinal motion. After reflection from a boundary, the wave potential for the half-space, eq. 4.27 will be modified by the interaction in the following way

$$\phi_1 = (1 + R^{pp} + R^{ps}) \phi_0 e^{-\alpha z}$$

Fig. 4.12



$$\text{epicentre displacement} = W(T) / 2\pi\mu z^2 \times Q$$

$$T = \sqrt{s} t/z, \quad Q = \text{source radial moment}$$

The theoretically predicted epicentre displacement of a half-space from a point radial loading with Heaviside time dependence.

4.57

$$\psi_1 = (1 + R^{ss} + R^{sp}) \psi_0 e^{-\beta z}$$

Where  $\phi_1$  now represents the new potential associated with the longitudinal motion and  $\psi_1$  represents the new potential associated with the shear motion.  $R^{pp}$  etc. are the reflection coefficients where the first superscript denotes the incident motion and the second denotes the reflected motion.  $\phi_0$  and  $\psi_0$  are the half-space potentials derived in section 4.1.2. The reflection coefficients can be derived from the wave interactions at a boundary discussed in Chapter 2.3 and are given by Pekeris et al (1965)

$$R^{pp} = \frac{-\gamma^2 + 4\xi^2\alpha\beta}{\gamma^2 - 4\xi^2\alpha\beta}, \quad R^{ss} = -R^{pp}$$

4.58

$$R^{ps} = \frac{-4\xi^2\gamma}{\gamma^2 - 4\xi^2\alpha\beta}, \quad R^{sp} = \frac{4\gamma\alpha\beta}{\gamma^2 - 4\xi^2\alpha\beta}, \quad \gamma = (2\xi^2 + S_s^2)$$

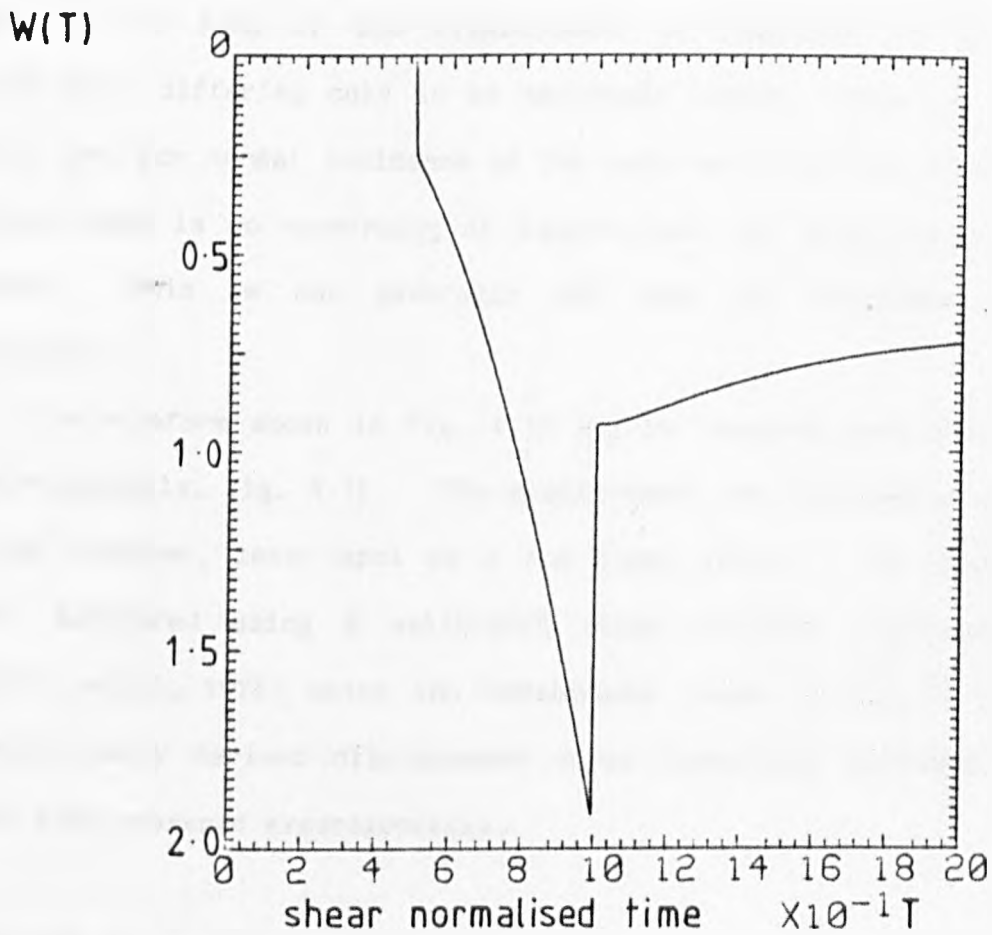
It is now possible to derive the vertical displacement on a plate by substitution of the potentials into eq. 4.21. The inverse Laplace-Hankel transform is performed in the same way as for the half-space leading to an epicentre plate response in dimensionless time of

$$W(T) = \frac{4Q}{\pi\mu z^2} \frac{\partial}{\partial T} \left[ \frac{T^2(T^2 - R^2)(1 - R^2 + T^2)^{1/2} (1 - 2R^2 + 2T^2) H(T - R)}{((1 - 2R^2 + 1 + 2T^2)^2 - 4T(T^2 - R^2)(1 - R^2 + T^2)^{1/2})^2} \right. \\ \left. - \frac{T^2(T^2 - 1)(T^2 - 1 + R^2)^{1/2} (2T^2 - 1) H(T - 1)}{((2T^2 - 1)^2 - 4T(T^2 - 1)(T^2 - 1 + R^2)^{1/2})^2} \right]$$

4.59

The waveform from this expression is shown in fig. 4.13 and is consistent with that derived recently by Rose (1984).

Fig. 4.13



$$\text{epicentre displacement} = W(T) / \pi \mu h^2 \times 4Q$$

The theoretically predicted epicentre displacement of the surface of a plate from a point radial loading with Heaviside time dependence.

For times up to and including the first longitudinal and shear arrival the form of the displacement is identical to that of the half-space differing only in an amplitude factor. This is due to the fact that for normal incidence of the wave motion on the epicentre of a plate there is no conversion of longitudinal and shear motion to other modes. This is not generally the case for positions away from epicentre.

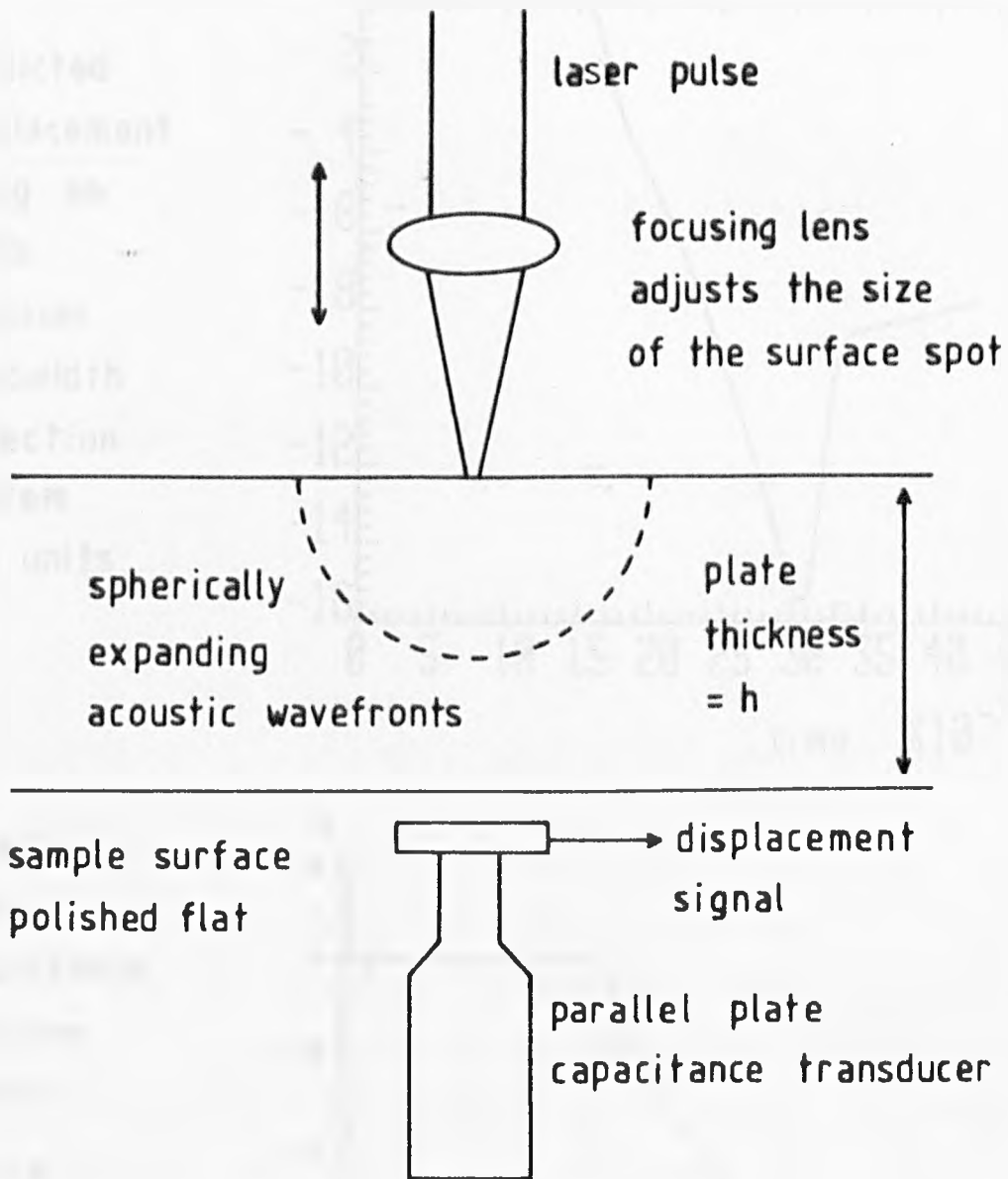
The waveform shown in fig. 4.13 may be compared with that measured experimentally, fig. 4.15. The displacement was obtained using a 32mJ, 2.5mm diameter, laser spot on a 1cm steel plate. The displacements were monitored using a calibrated plane parallel capacitance probe (Scruby et al, 1978) using the arrangement shown in fig. 4.14. The theoretically derived displacement shows reasonable agreement in form with that measured experimentally.

## 4.2 THE PLASMA SOURCE

### 4.2.1 SURFACE DISPLACEMENTS

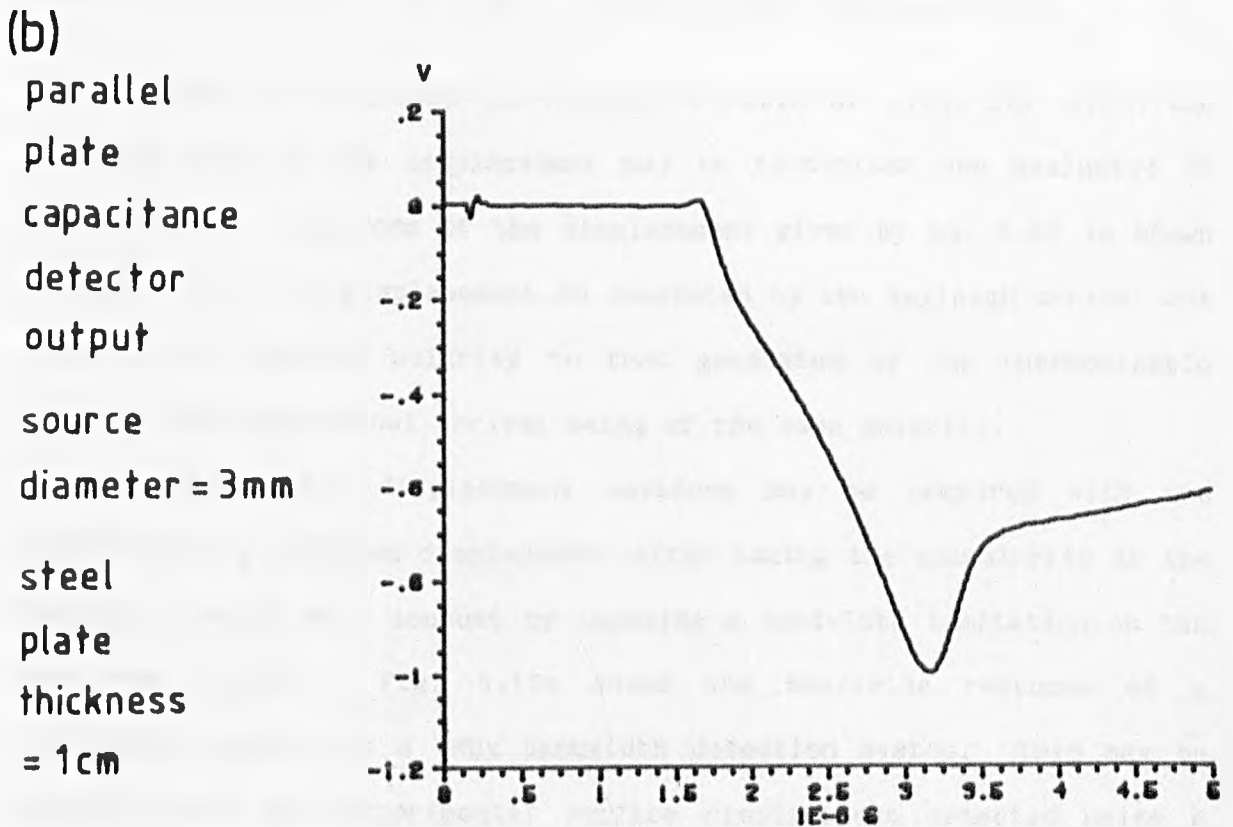
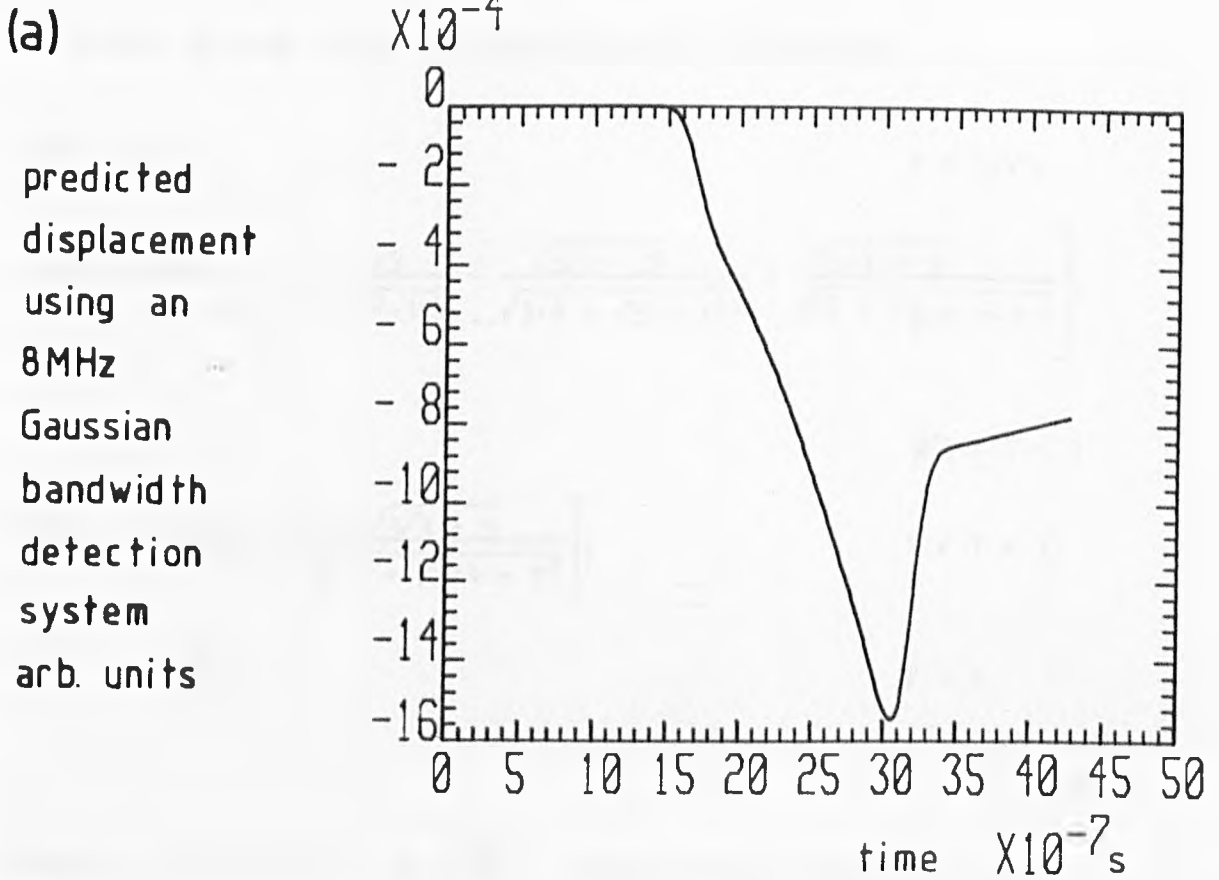
From the discussion of the force distribution produced by the plasma interaction, Chapter 3, it may be seen that this source may be modelled as the transient response of an elastic half-space due to the application of a normal, point force at the surface, with arbitrary time dependence. This problem was first tackled by Lamb (1904) in order to explain some of the effects of seismic events. "Lamb's problem" for the surface displacement, as it has become known, has been covered by many authors since the introduction of modern integral transform techniques: eg. Pekeris (1955); Mooney (1974). The results of Pekeris are quoted here for the normal displacement of a surface due to the application of

Fig. 4.14



Experimental arrangement for measuring the epicentral response of a plate to the laser-acoustic source.

Fig. 4-15



A comparison of predicted and experimental epicentre displacements of a plate from the thermoelastic source.

a normal driving force with Heaviside time dependence.

$$W(T) = 0$$

$$T < 1/\sqrt{3}$$

$$W(T) = \frac{-F}{32\pi\mu r} \left[ 6 - \frac{\sqrt{3}}{\sqrt{T^2 - 1/4}} - \frac{\sqrt{3\sqrt{3} + 5}}{\sqrt{3/4 + \sqrt{3/4} - T^2}} + \frac{\sqrt{3\sqrt{3} - 5}}{\sqrt{T^2 + \sqrt{3/4} - \sqrt{3/4}}} \right],$$

$$1/\sqrt{3} < T < 1$$

$$W(T) = \frac{-F}{16\pi\mu r} \left[ \frac{6 - \sqrt{3\sqrt{3} + 5}}{\sqrt{3/4 + \sqrt{3/4} - T^2}} \right],$$

$$1 < T < \gamma$$

$$W(T) = \frac{-3F}{8\pi\mu r},$$

$$T > \gamma$$

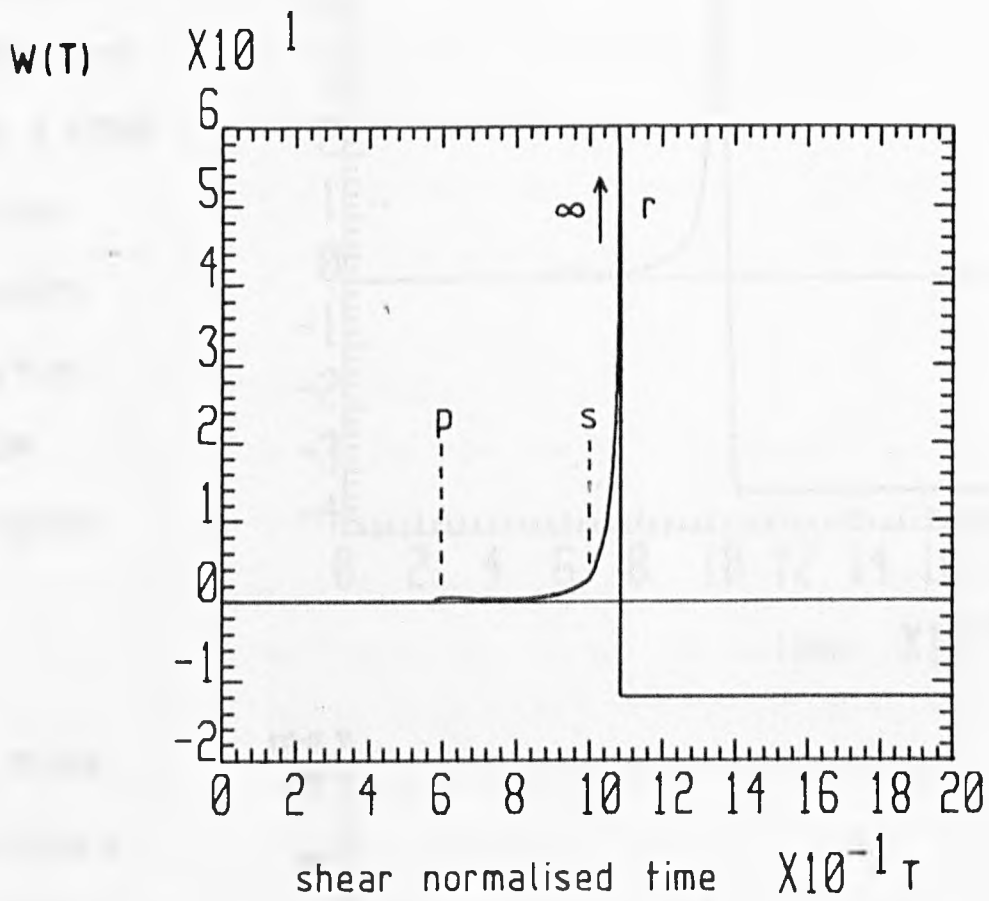
4.60

where  $\gamma = \frac{1}{2}(3 + \sqrt{3})^{1/2}$ ,  $T = \frac{V_{st}}{r}$ , shear arrival normalised time.

These results are derived for Poisson's ratio of 0.25, for which the integral form of the displacement may be factorised and evaluated in closed form. The form of the displacement given by eq. 4.60 is shown in fig. 4.16. The displacement is dominated by the Rayleigh arrival but this is of opposite polarity to that generated by the thermoelastic source, the longitudinal arrival being of the same polarity.

The theoretical displacement waveform may be compared with the experimentally obtained displacement after taking the singularity at the Rayleigh arrival into account by imposing a bandwidth limitation on the predicted signal. Fig. 4.17a shows the Heaviside response of a half-space subject to a 6MHz bandwidth detection system. This may be compared with the experimental surface displacement detected using a ball capacitance probe and a 30mJ, fully focused ( $f = 5\text{cm}$ ) laser pulse in the arrangement shown in fig. 4.6. The two waveforms share the same

Fig. 4.16

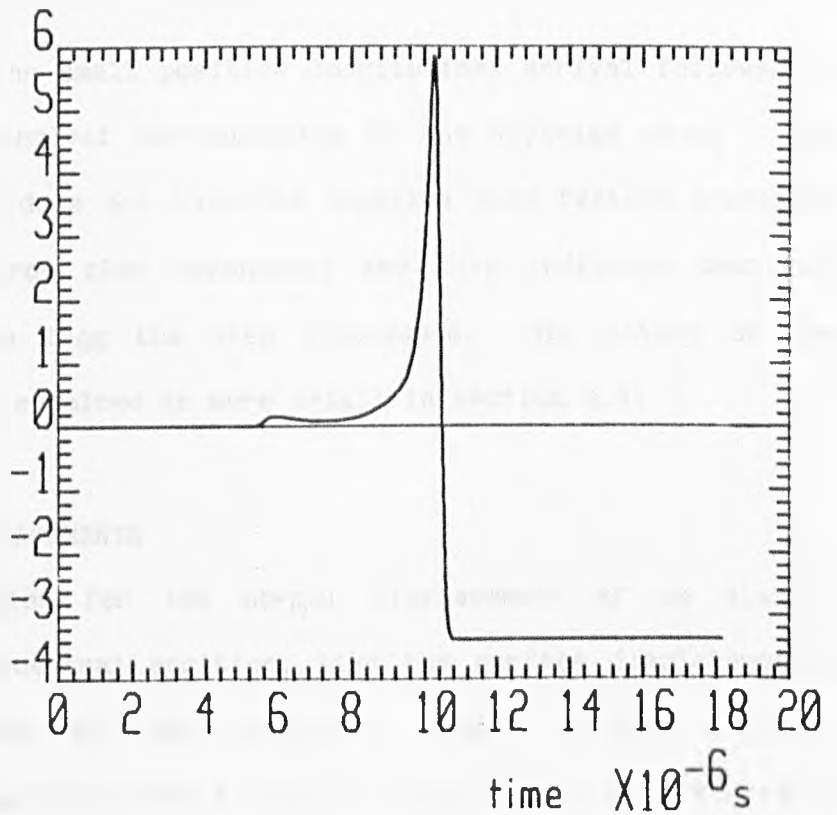


$$\text{surface displacement} = W(T) / 32\pi r \times F$$

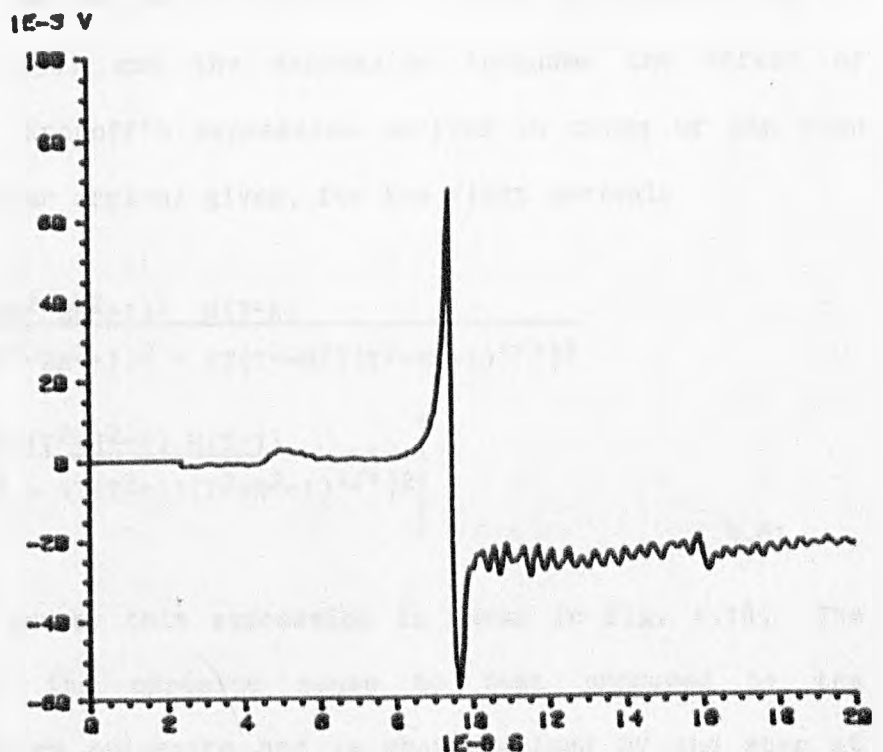
Pekeris' solution for the surface displacement of a half-space from a point normal load with Heaviside time dependence.

Fig. 4.17

(a)  
predicted  
displacement  
using a 6MHz  
Gaussian  
bandwidth  
detection  
system.  
arb units



(b)  
ball probe  
capacitance  
transducer  
output  
source-detector  
separation  
= 2.9 cm  
aluminium



A comparison of the surface displacement produced by the plasma source and the predicted surface displacement for a source force with Heaviside time dependence.

overall features of the small positive longitudinal arrival followed by the bigger positive arrival corresponding to the Rayleigh wave. The experimental waveform does not have the negative step feature predicted using a Heaviside force time dependence and this indicates that the driving force differs from the step dependence. The nature of the driving force will be examined in more detail in section 4.6.

#### 4.2.2 EPICENTRE DISPLACEMENTS

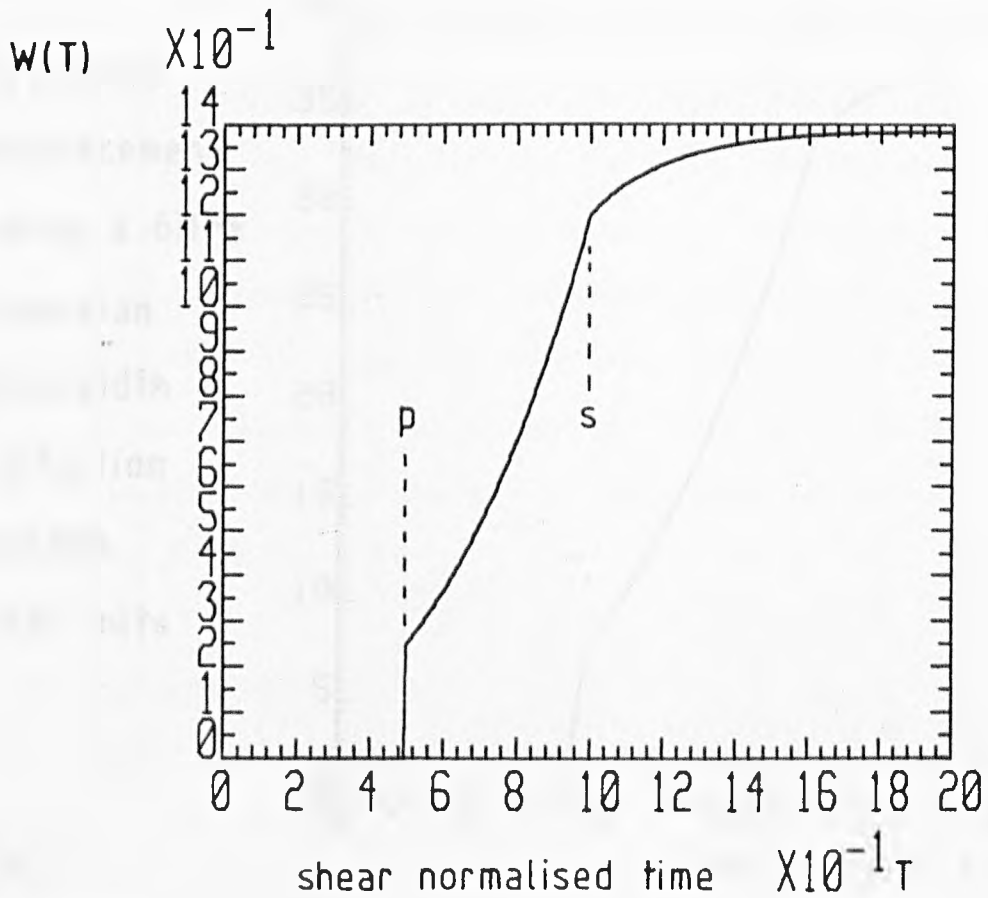
Lamb's problem for the normal displacement of an elastic half-space for an epicentral position, like the surface displacements, has been investigated by many authors: eg. Knopoff (1958), Sinclair (1979). The displacement from a normal force with Heaviside time dependence on the epicentral point of a plate was written down in full by Knopoff (1958) and the expression includes the effect of multiple arrivals. Knopoff's expression derived in terms of the time normalised to the shear arrival gives, for the first arrivals

$$W(T) = \frac{F}{\pi\mu h} \left[ \frac{T^2(2T^2-2R^2+1)^2 H(T-R)}{((2T^2-2R^2+1)^2 - 4T(T^2-R^2)(T^2-R^2+1)^{1/2})^2} - \frac{4T^2(T^2-1)(T^2+R^2-1) H(T-1)}{((2T^2-1)^2 - 4T(T^2-1)(T^2+R^2-1)^{1/2})^2} \right]$$

4.61

The displacement given by this expression is shown in fig. 4.18. The displacement is in the opposite sense to that produced by the thermoelastic source on epicentre and is characterised by the step at the longitudinal arrival followed by a change in gradient at the shear arrival. The predicted displacement may be compared with the experimentally determined displacement using the arrangement shown in fig. 4.14. Fig. 4.19a shows the predicted displacement after imposing a

Fig. 4.18



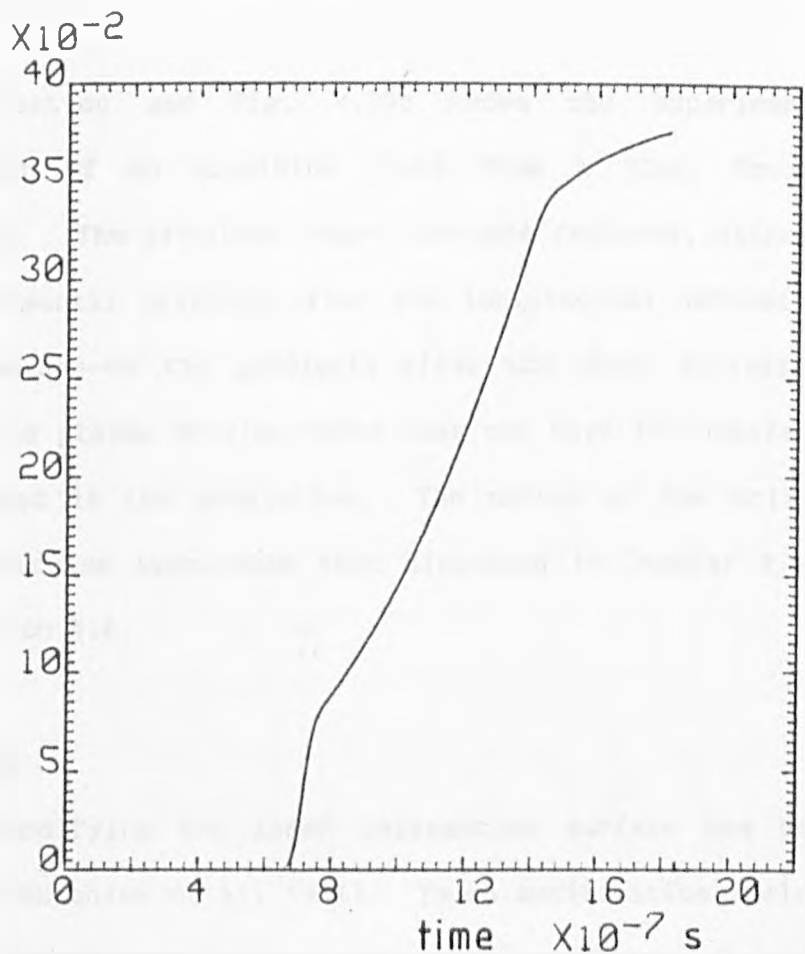
surface displacement =  $W(T) / \pi \mu h \times F$

Knopoff's solution for the epicentral displacement  
of a plate from a point normal load with  
Heaviside time dependence.

Fig. 4-19

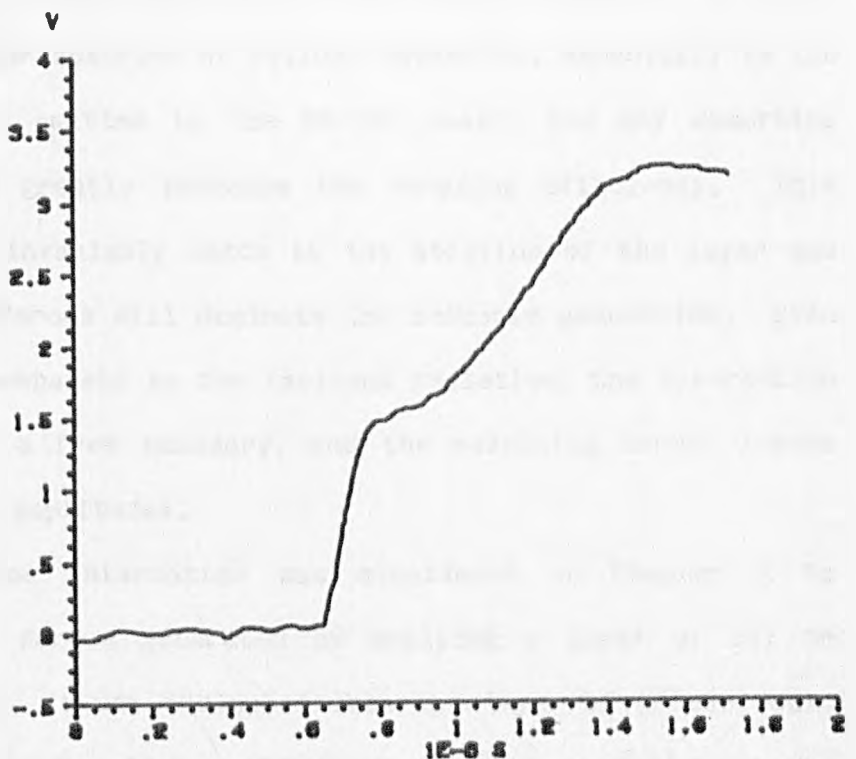
(a)

predicted  
displacement  
using a 6MHz  
Gaussian  
bandwidth  
detection  
system.  
arb. units



(b)

parallel  
plate  
capacitance  
detector  
output  
aluminium  
plate  
thickness  
= 5mm



A comparison of predicted and experimental epicentre  
displacements of a plate from the plasma source.

6MHz bandwidth limitation and fig. 4.19b shows the experimental epicentre displacement of an aluminium plate from a 32mJ, focused ( $f = 5\text{cm}$ ) laser pulse. The waveforms share the same features, although the dip in the experimental waveform after the longitudinal arrival at  $0.7\mu\text{s}$ , and the difference in the gradients after the shear arrival at  $1.4\mu\text{s}$  indicate that the plasma driving force does not have the Heaviside time dependence assumed in the prediction. The nature of the driving force for longer timescales approaches that discussed in Chapter 3 and is considered in section 4.6.

#### 4.3 MODIFIED SURFACES

The effect of modifying the laser interaction surface has been considered in detail (Hutchins et al, 1981). These modifications include applying layers of various materials to the metal surface. A clean metal surface is a poor absorber of optical radiation, especially in the near infra-red region emitted by the Nd/YAG laser, and any absorbing layer will therefore greatly increase the coupling efficiency. This increased absorption invariably leads to the ablation of the layer and the resulting normal forces will dominate the acoustic generation. Even when the layer is transparent to the incident radiation, the interaction surface is no longer a free boundary, and the resulting normal forces may increase acoustic amplitudes.

A modified surface interaction was considered in Chapter 3 to describe the surface forces generated by applying a layer of oil or grease to the sample. It was indicated that the layer of grease would produce a normal, impulsive force and may therefore be modelled as the transient response of the half-space to a driving force with delta function time dependence, modified by the time dependence of the

impulsive force and, in the limit, by the bandwidth of the detection system. The response of a half-space to a delta function, normal driving force may be obtained from the Heaviside response, eq. 4.61, by differentiation with respect to time.

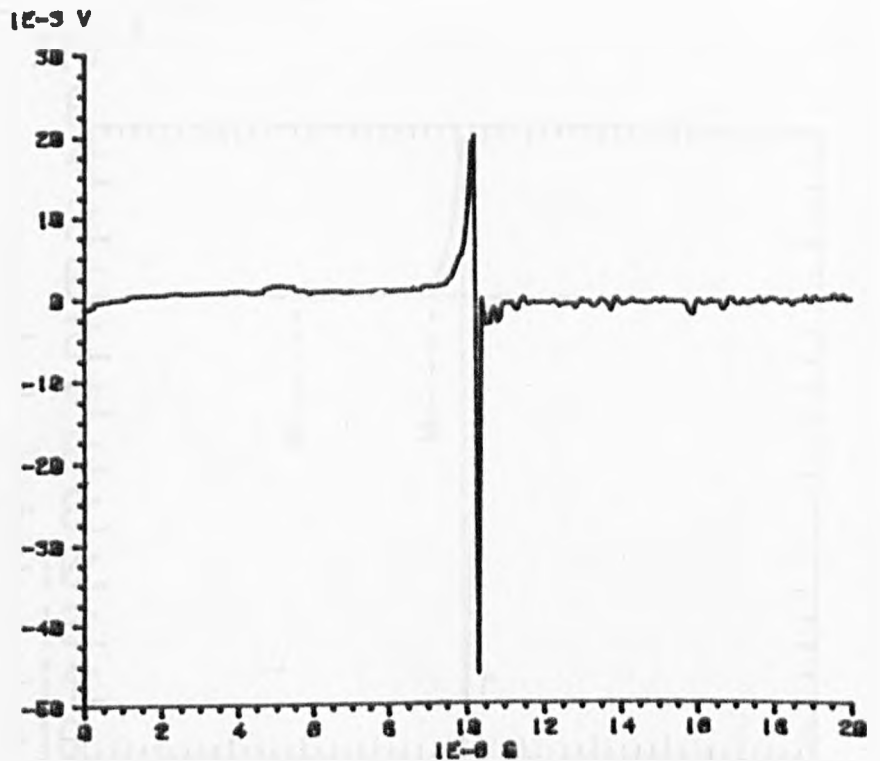
Fig. 4.20 shows the experimentally measured surface and epicentre responses of a plate using a 3mJ laser pulse focused onto a thin layer of grease. The laser energy density was sufficient to cause ablation of the grease but there was no visible emission which usually accompanies the production of a plasma. A comparison of these waveforms with those generated by the plasma and thermoelastic sources show that this type of source is dominated by the longitudinal arrival in the bulk and by the Rayleigh arrival on the surface, both of which exhibit a sharp pulse-like nature. A comparison of absolute displacements, section 4.5, with those produced by the other sources, show that this source also generates the largest amplitude acoustic displacements. Because of these useful properties this type of source is used extensively in the experimental investigations, presented in Chapter 9, on the interaction of acoustic pulses with material boundaries and simulated cracks.

Theoretically this type of source is described, as mentioned above, by a pulse-like driving force. Fig. 4.21 shows the predicted surface and epicentre impulse responses of a plate with a 6MHz detection system.

Fig. 4.22 shows the frequency components of the experimental surface wave pulse, obtained by the "Fast Fourier Transform" (FFT). The pulse contains a broad band of frequency components extending more uniformly over a greater range than is easily obtainable by conventional, broad-band, damped piezoelectric transducers, (Silk, 1984). The broad-band frequency range allows the investigation of acoustic spectroscopy techniques, one of which will be discussed in Chapter 9.

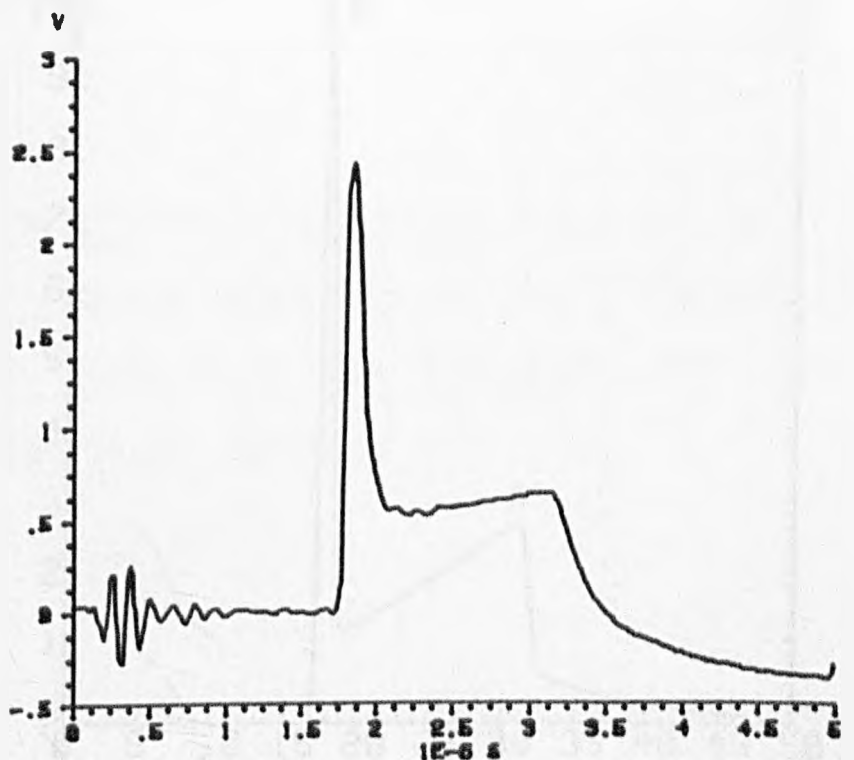
Fig. 4.20

ball capacitance  
detector output  
source-detector  
separation = 2.9 cm



(a) Surface displacement of an aluminum block from a focused laser spot on an oil layer.

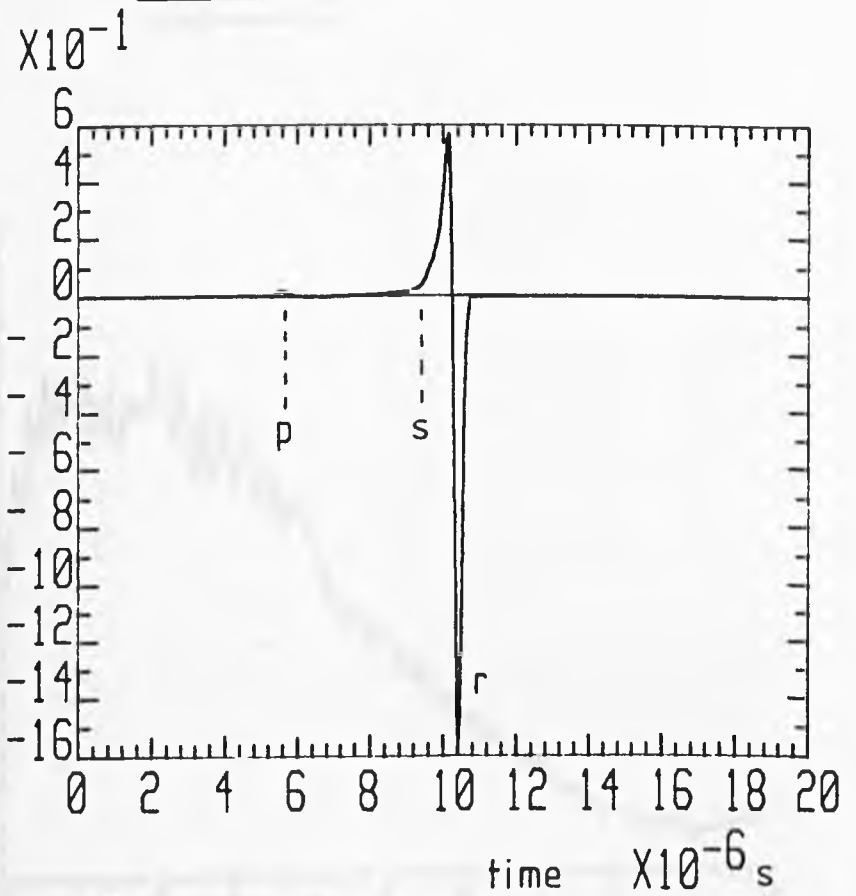
parallel plate  
capacitance  
detector  
plate thickness  
= 1 cm



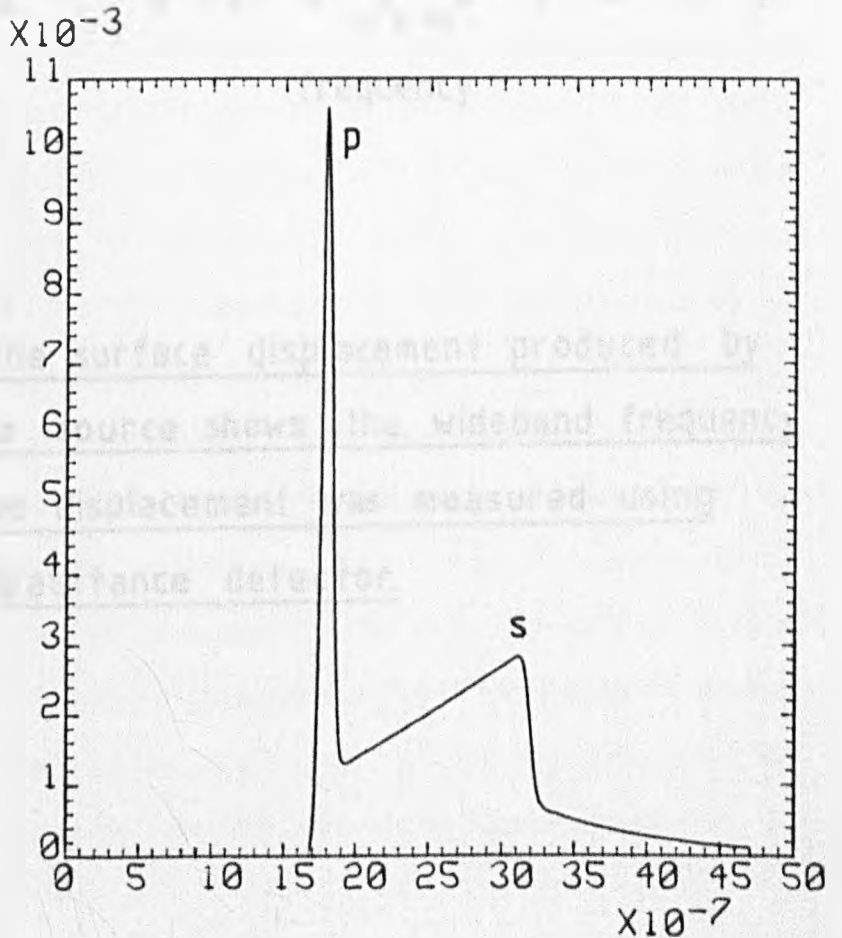
(b) Epicentral displacement of a steel plate from a focused laser spot on an oil layer.

Fig. 4.21

(a)  
predicted  
surface  
displacement  
arb. units  
6 MHz system  
bandwidth

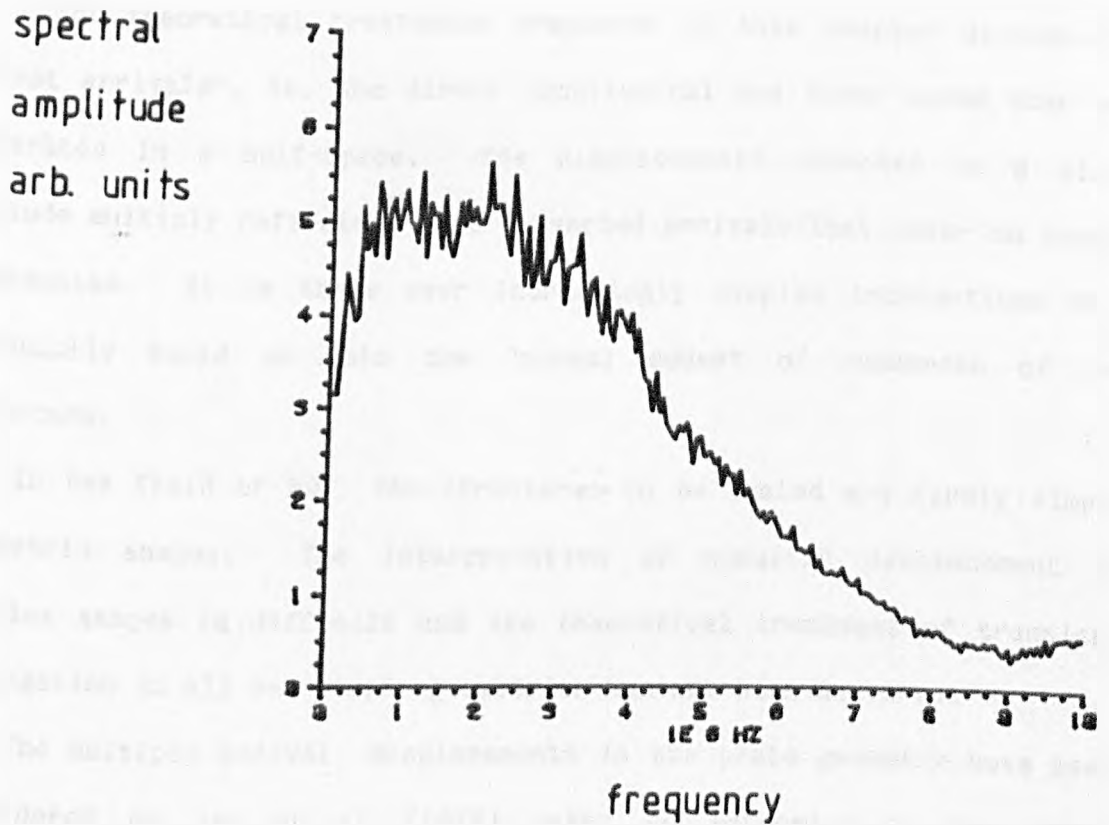


(b)  
predicted  
epicentre  
displacement  
arb. units  
6 MHz system  
bandwidth



Predicted displacements from an impulsive normal force.

Fig. 4-22



An F.F.T. of the surface displacement produced by the oil-layer source shows the wideband frequency content. The displacement was measured using the ball capacitance detector.

#### 4.4 MULTIPLE ARRIVALS

The theoretical treatments presented in this chapter discuss the "first arrivals", ie. the direct longitudinal and shear waves that are generated in a half-space. The displacements detected on a plate include multiply reflected, mode converted arrivals that occur on longer timescales. It is these ever increasingly complex interactions that eventually build up into the "normal modes" of resonance of the structure.

In the field of NDE the structures to be tested are rarely simple geometric shapes. The interpretation of acoustic displacement in complex shapes is difficult and the theoretical treatment of transient propagation in all but simple geometries has not been achieved.

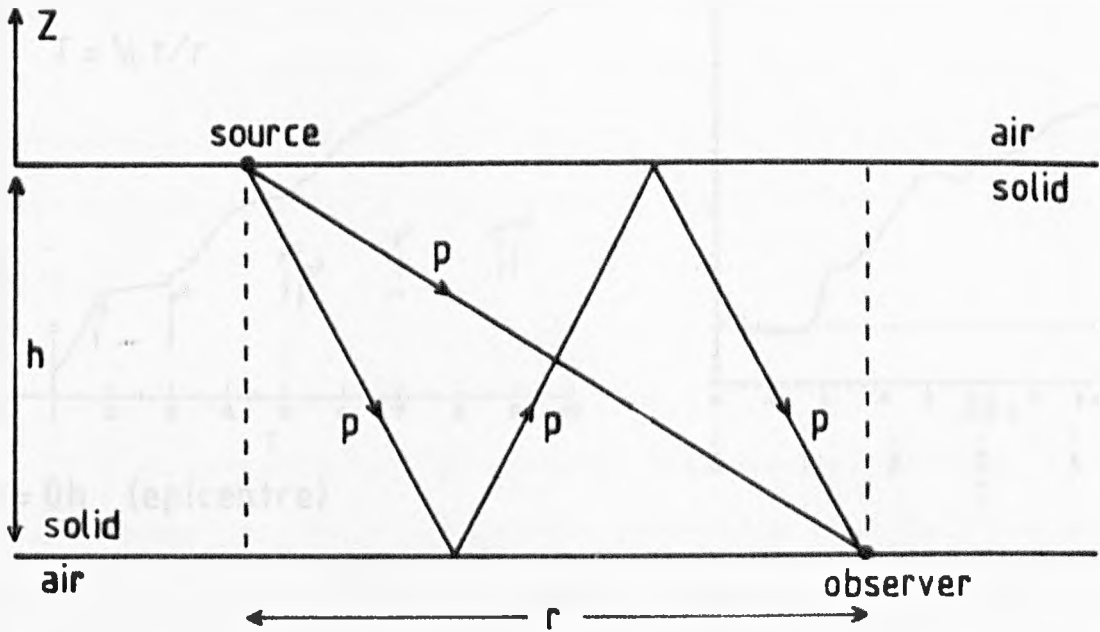
The multiple arrival displacements in the plate geometry have been considered by Pao et al (1977) using an extension to the basic analytical methods presented in section 4.1.2 and 4.1.3. The "Generalised Ray Theory" presented in Pao's paper allows the displacements of a plate to be evaluated for any position on either surface and for a variety of force distributions. All derivations of acoustic displacements in this chapter are for observer positions on either the surface or on the epicentre positions. For these two positions the displacement, given by the inverse Laplace-Hankel transform of some function, is obtained by the Cagniard-de Hoop method. For positions away from epicentre this method leads to a general contour integration in the complex plane which can be lengthy and involved. Pao et al (1977) used this method in their description of the generalised ray theory.

The arrivals at some point on a plate are separated into "ray

groups" for different ray paths, fig. 4.23. The problem is then split into various components. A source function is derived for the longitudinal and shear motion within the solid due to the type of source force. This source function is combined with the appropriate reflection coefficients, mentioned in section 4.1.3, for each segment of the ray path within the group, depending on whether a longitudinal or shear component is reflected from the top or lower surface. Finally, this expression is then combined with a receiver function depending on which component of motion is being monitored at the surface. The expression for the entire ray group is then doubly inverted to give the displacement expression. This process is continued for all ray groups arriving at the observer position in the time of interest.

The results of this process for various observer positions, for a normal force with Heaviside time dependence, are shown in fig. 4.24a. The results are taken from Pao et al (1979) and may be compared with the displacement measured experimentally, for the same positions, generated by the laser plasma source (32mJ, focused) on a 5mm thick aluminium plate, fig. 4.24b. The displacements were measured using a parallel plate capacitance probe which imposes a geometrical bandwidth limitation on the signal, increasing with distance away from epicentre. Discrepancies arise from the difference in Poisson's ratio between the experiment for aluminium,  $\sigma = 0.34$ , and the theoretical waveform,  $\sigma = 0.29$ . This difference will alter the arrival time of the numerous ray groups - eg. 31 arrivals within  $T = 7$  for  $r = 5h$  (Pao et al, 1977) - leading to a change in the waveform profile. There is also a discrepancy because the laser force is not Heaviside in nature on the longer timescales in fig. 4.24b. However, there are similarities and the experiment demonstrates a use of the laser source in physically

Fig. 4.23



possible ray groups

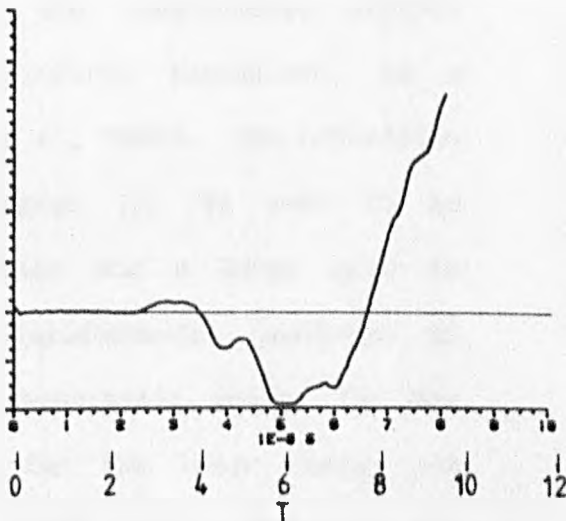
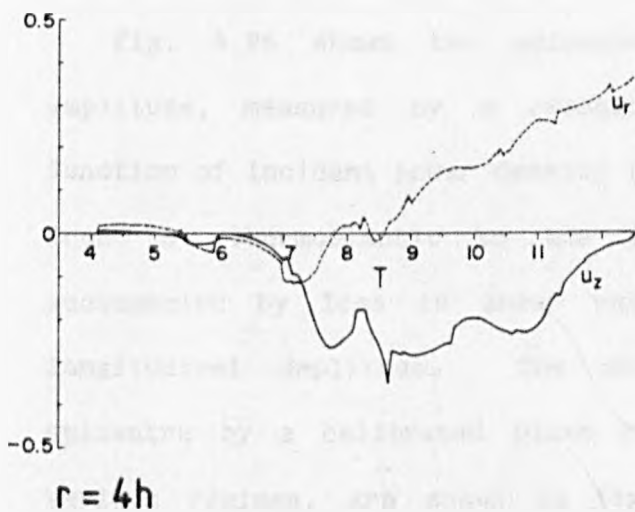
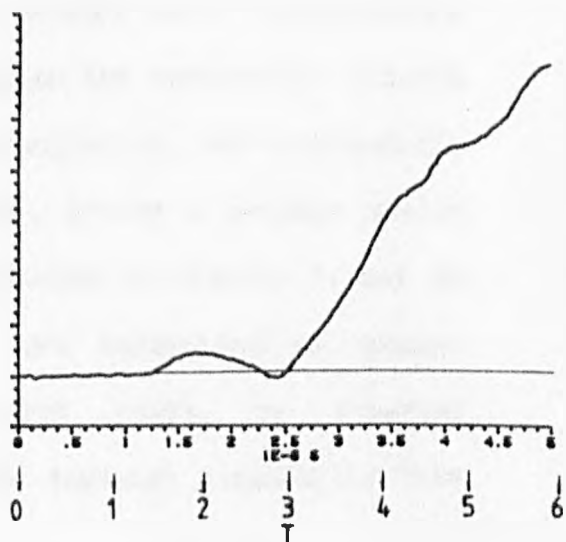
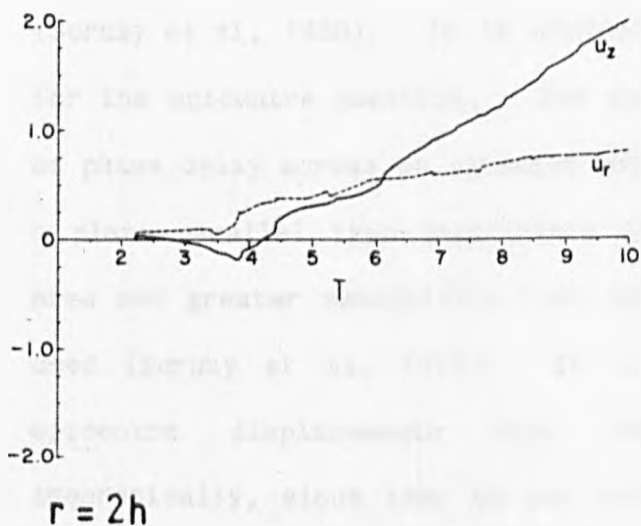
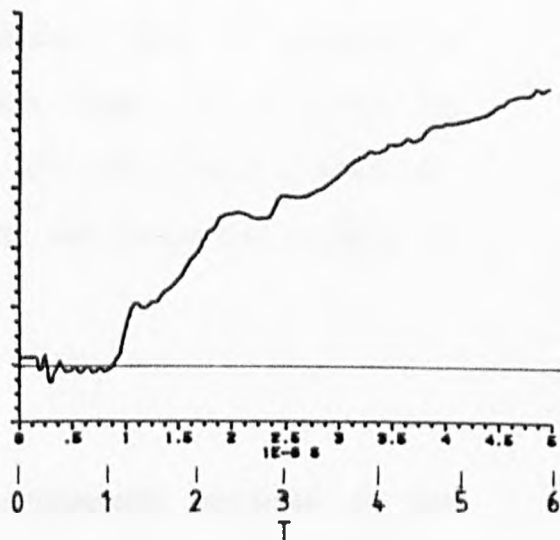
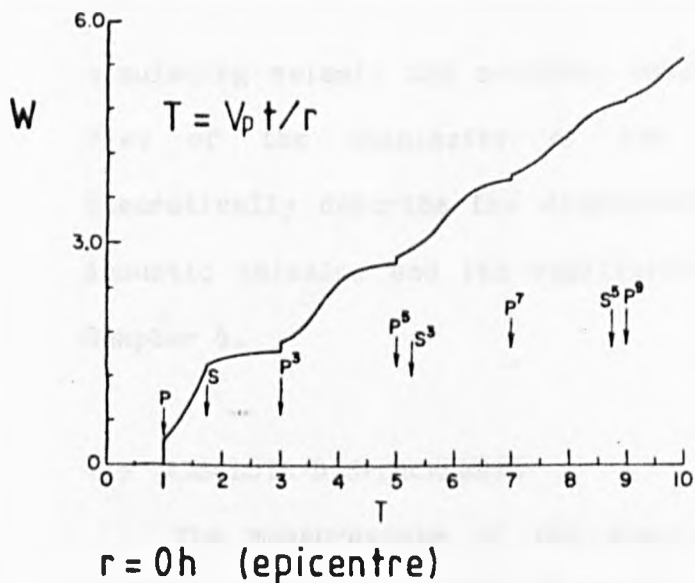
p	s	
ppp	sss	p - longitudinal ray segment
psp	sps	s - shear ray segment
spp	pss	
pps	ssp	
etc.		

Some ray paths for the acoustic arrivals at an observer position on the surface of a plate due to a transient surface force. Mode conversions can occur at either surface.

Fig. 4.24

(a) predicted displacement

(b) experimental displacement



A comparison of predicted plate displacements with the experimental displacements of a 5mm thick Al. plate.

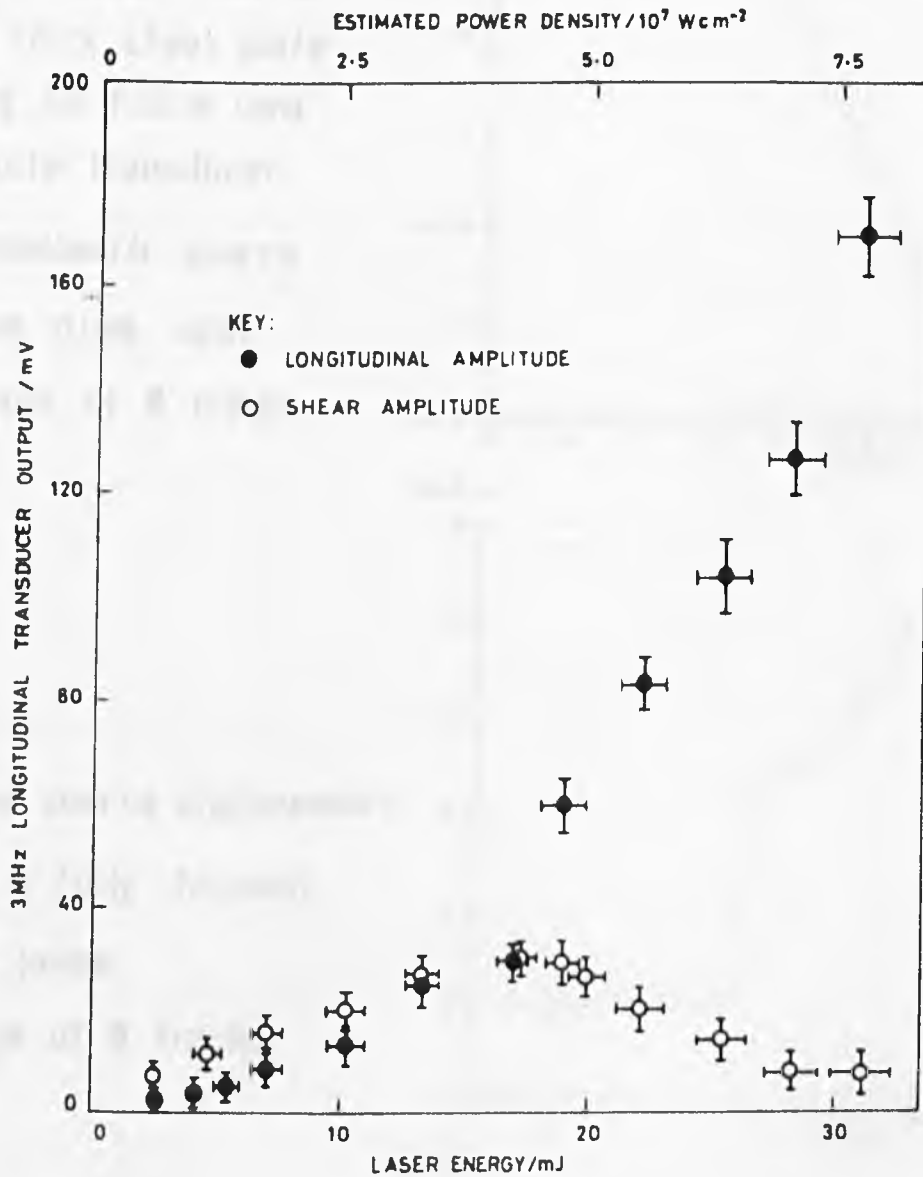
simulating seismic and acoustic emission events. This is valuable in view of the complexity of the treatment that is required to theoretically describe the displacements in all but simple geometries. Acoustic emission and its application to NDE are described briefly in Chapter 6.

#### 4.5 ABSOLUTE DISPLACEMENTS

The measurements of the absolute displacements produced by the various modes of laser generation have been reported previously (Scruby et al, 1980). It is convenient to measure these displacements for the epicentre position. For this position the geometrical effects of phase delay across an extended source are minimised, and consequently a plane parallel type capacitance transducer, having a greater active area and greater sensitivity than those discussed in Chapter 7, may be used (Scruby et al, 1978). It is also more convenient to compare epicentre displacements with those which might be expected theoretically, since they do not contain the Rayleigh singularity that dominates the surface displacements.

Fig. 4.25 shows the epicentre shear and longitudinal arrival amplitude, measured by a resonant piezoelectric transducer, as a function of incident power density (Scruby et al, 1980). The transition from the thermoelastic to the plasma regime can be seen to be accompanied by loss in shear wave amplitude and a large gain in longitudinal amplitude. The absolute displacements, measured on epicentre by a calibrated plane parallel capacitance probe, for the various regimes, are shown in fig. 4.26, for the laser energy and geometries shown in the figure. The oil layer source dominates the displacement magnitudes producing approximately 0.6nm/mJ of incident

Fig. 4-25

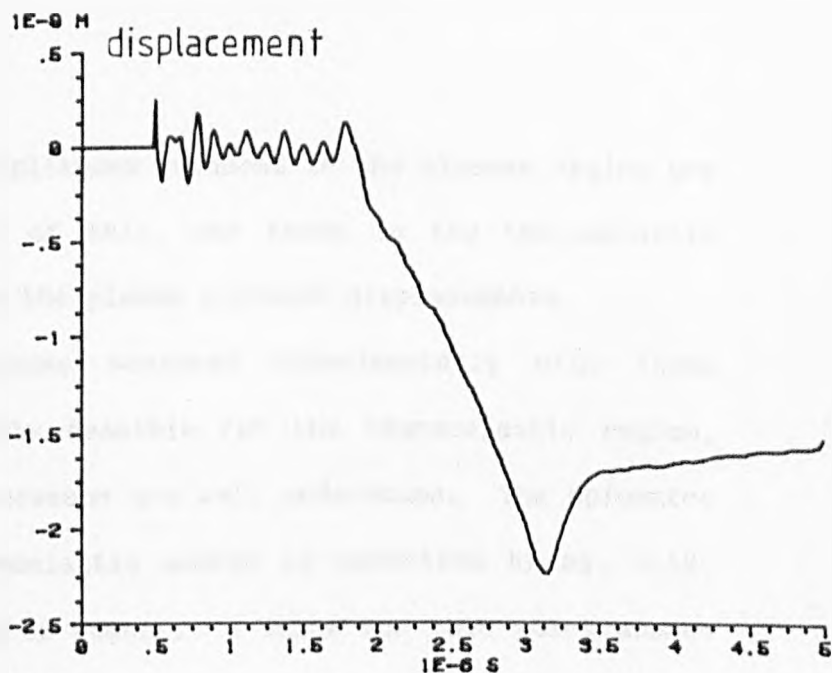


Wavefront amplitudes measured by a 3MHz, resonant longitudinal, PZT transducer as a function of laser energy.

**Fig. 4:26**

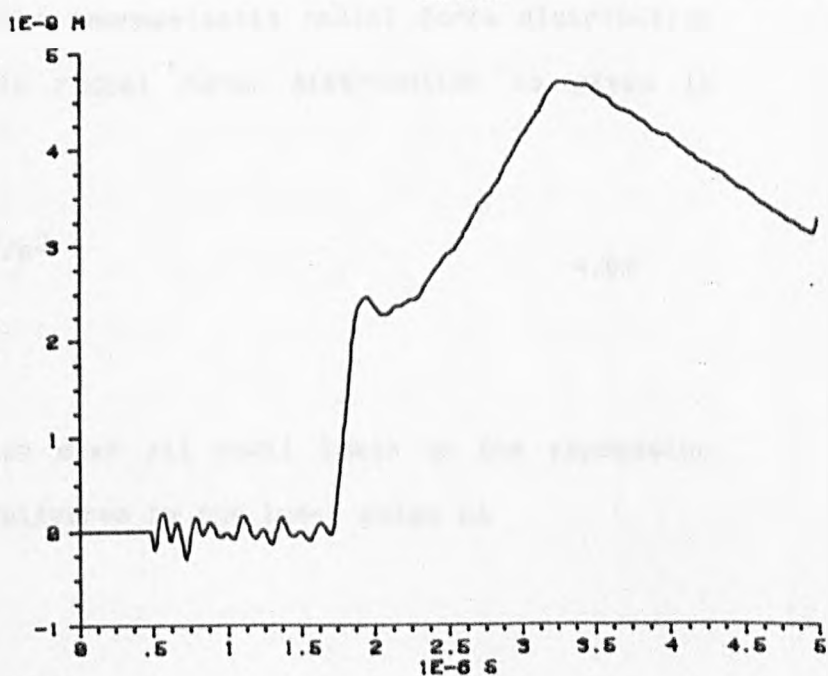
(a)

laser energy = 32 mJ  
FWHM = 35ns  
pulse incident on a  
1cm thick steel plate  
using an f=5cm lens  
& plate transducer  
thermoelastic source  
2.5mm diam. spot  
average of 8 traces



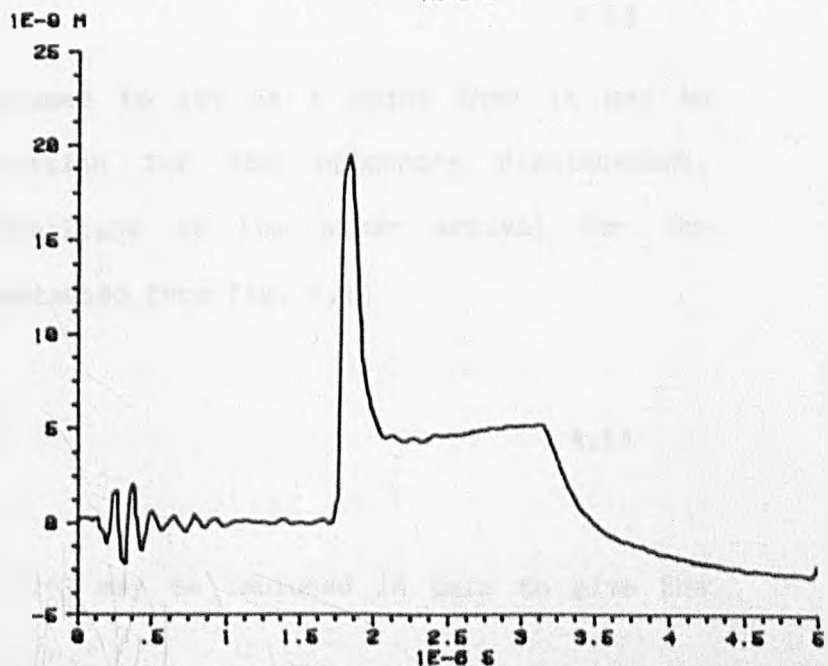
(b)

plasma source displacement  
using a fully focused  
laser pulse  
average of 8 traces



(c)

oil-layer source  
displacement using a  
focused spot - no visible  
emission



Calibrated epicentre displacements from the laser-acoustic source.

laser energy. The maximum amplitudes produced in the plasmas regime are typically about 1/4 to 1/10 of this, and those in the thermoelastic regime are again smaller than the plasma produced displacements.

A comparison of amplitudes measured experimentally with those expected theoretically is only feasible for the thermoelastic regime, for which the interaction processes are well understood. The epicentre plate response for the thermoelastic source is described by eq. 4.59, for which  $Q$  is the point source moment. A value for this point source moment can be obtained from the thermoelastic radial force distribution derived in Chapter 3. This radial force distribution is given in eq. 3.12 as

$$F(r) = \frac{2r E \alpha E_T}{(1-\sigma)c_p a^2} e^{-r^2/a^2} \quad 4.62$$

Integration of this expression over all radii leads to the expression for the total radial moment delivered by the laser pulse as

$$Q = \frac{E \alpha E_T}{(1-\sigma) c_p} \quad 4.63$$

If this radial moment is assumed to act at a point then it may be incorporated into the expression for the epicentre displacement, eq. 4.59. The predicted amplitude at the shear arrival for the thermoelastic source may be estimated from fig. 4.13

$$W_s \approx \frac{2 * 4 * Q}{\pi \mu h^2} \quad 4.64$$

The expression for  $Q$  in eq. 4.63 may be included in this to give the

epicentre displacement as

$$W_S = \frac{2 * 4 * E \alpha E_T}{(1-\sigma) c \rho \pi \mu h^2} \quad 4.65$$

The displacement may be calculated from the various thermal and elastic constants for a steel plate (Kaye & Laby, 1973)

$$W_S = 2.75 \times 10^{-11} * E_T/h^2 \quad 4.66$$

Using the conditions shown in fig. 4.26a; a 32mJ laser pulse incident on 1cm thick steel plate, and assuming an optical absorption coefficient of 36% for the infra-red pulse (Aindow et al 1984) gives the displacement at the shear arrival as 3.2nm which is in reasonable agreement with the experimentally determined displacement of approximately 2.5nm, fig. 4.26a. The lower experimental displacement may be accounted for by the variability of optical absorption at the steel surface and the acoustic attenuation in steel which is not considered in the model.

#### 4.6 PLASMA REGIME DRIVING FORCE

Calculation of the absolute epicentre displacements generated in the plasma regime is not possible because of the complex nature of the laser plasma-surface interaction (Chapter 3). However, it is possible to deduce the magnitude and time history of the driving force at the surface from a knowledge of the experimental displacements that this force produces. The driving force is obtained by deconvolution of the experimental displacement with the theoretical impulse response at the same position. There are numerous numerical methods for deconvolution

of data with a known system response (e.g Eisenstein et al, 1976; Rhoads et al, 1968; Hunt, 1972).

Perhaps the simplest numerical deconvolution technique is performed by convolution of the experimental data with the inverse system impulse response. The impulse response, in our case, is the displacement waveform generated at some point when an impulsive driving force is applied to the surface of the plate; the inverse impulse response is the time dependent driving force that must be applied to the surface in order to obtain an impulsive displacement at some point. The process may be written as

$$F(t) * I(t) = W(t)$$

4.67

$$W(t) * I^{-1}(t) = F(t)$$

Where  $F(t)$  is the driving force,  $I(t)$  is the impulse response,  $W(t)$  is the displacement,  $I^{-1}(t)$  is the inverse impulse response and  $*$  denotes the convolution operator. Using acoustic theory it is not usually possible to derive explicitly the inverse impulse response, but it may be obtained numerically from the impulse response itself. The process of convolution may be carried out numerically using the method of serial products (Bracewell, 1965).

$$W(t) = W_{i+1} = \sum_{j=0}^i F_j I_{(i-j)} = \int_{-\infty}^{\infty} f(t') g(t-t') dt' \quad 4.68$$

$$i = 0, 1, 2 \dots$$

Using this notation, there exists an identity relationship between the impulse response and its inverse

$$\sum_{j=0}^i I_j I^{-1}(i-j) = \{ 1, 0, 0, 0, 0 \dots \dots \} \quad 4.69$$

$$i = 0, 1, 2, 3 \dots \dots$$

The inverse impulse response may thus be determined from the following serial product

$$I^{-1}_{i+1} = \sum_{j=0}^i \frac{-(I_{j+1}) I^{-1}(i-j)}{I_0} \quad 4.70$$

where  $I_0^{-1} = 1/I_0$ .

This method of calculating the inverse response has the disadvantage that successive division quickly leads to large numerical errors appearing as oscillations in the result. However, for an impulse response for which most of the large displacements are concentrated at the beginning of the pulse, then the errors are kept to a minimum and a satisfactory inverse is obtained.

In general this is not the case and an alternative approach must be adopted. It is a well known property of the convolution theorem that a convolution in the time domain may be replaced by a multiplication in the frequency domain. Deconvolution of two time signals therefore reduces to a division in the frequency domain

$$F(t) * I(t) = W(t)$$

4.71

$$\bar{F}(f) \times \bar{I}(f) = \bar{W}(f)$$

Where  $f$  denotes the frequency domain and the bar denotes the Fourier transform. The driving force may now be written as the inverse

transform of the following frequency division

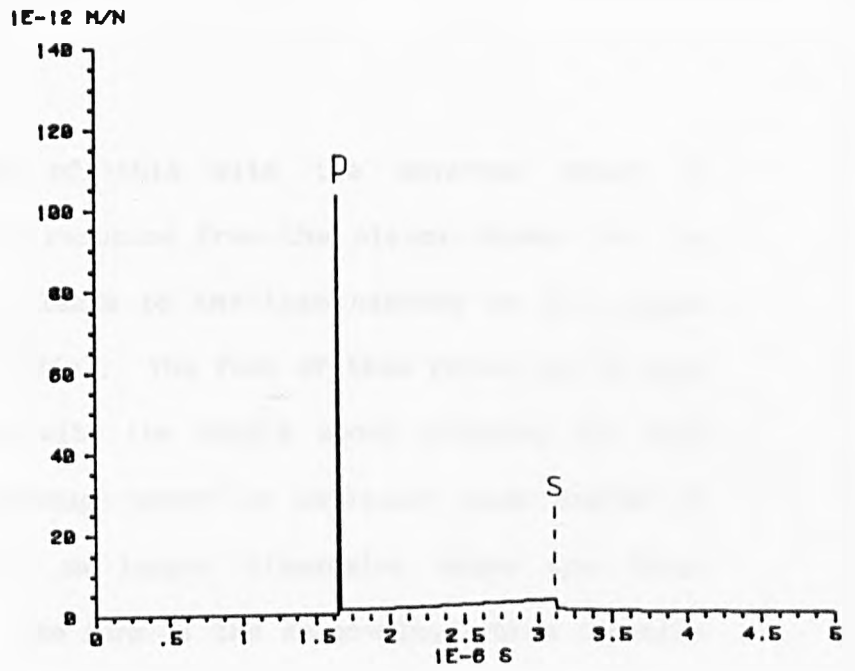
$$\bar{F}(f) = \frac{\bar{W}(f)}{\bar{I}(f)} \quad 4.72$$

However, care must be taken in evaluating this division numerically. Hunt's method (1972) uses this process and gives adequate results. The time dependent data is usually transformed to the frequency domain using the Cooley-Tukey, FFT algorithm (1965). This algorithm assumes that the data is periodic in nature by wrapping around the beginning and end of the time window. If the data is aperiodic or shows a discontinuity in amplitude levels between the first and last data points, then it must be gradually matched in order to avoid the generation of spurious frequency components. This is usually achieved by applying a numerical taper to the beginning and end points of the time domain data. Points at which frequency components of the impulse response are zero must also be neglected since the displacement frequency should also be zero in amplitude at these points, although in practice experimental noise will give rise to finite values. Included in this latter effect is the fact that, theoretically, the higher frequency components in the displacement will decay in amplitude at the same rate or faster than those in the impulse response. In practice it will not, again because of experimental noise on the data. This noise is therefore removed from the displacement data by digital filtering.

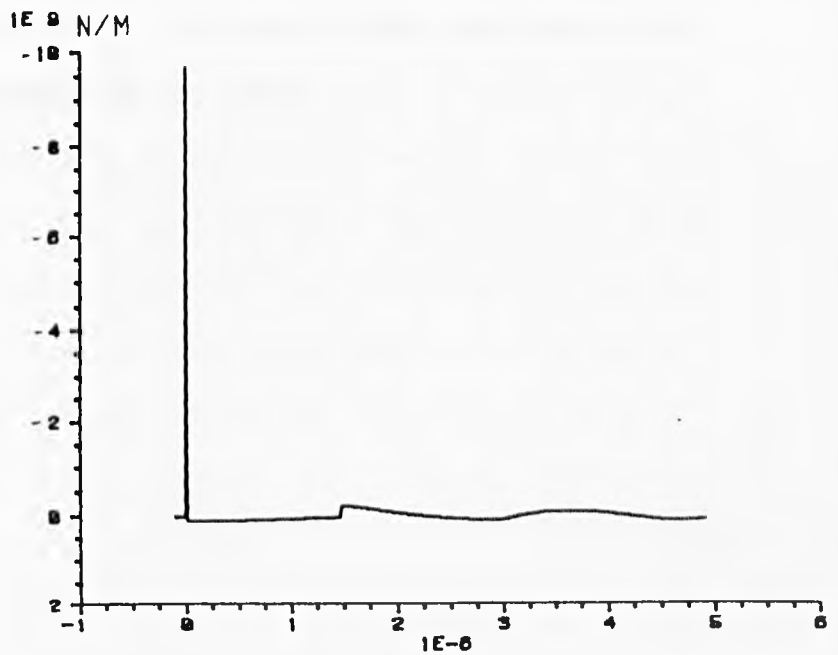
Fig. 4.27(a) shows the predicted epicentre impulse response for a normal driving force on a 1cm thick steel plate. The waveform has most of its amplitude concentrated at the initial longitudinal arrival and deconvolution may be carried out using the serial product method. The inverse impulse response obtained using this method is shown in

Fig. 4.27

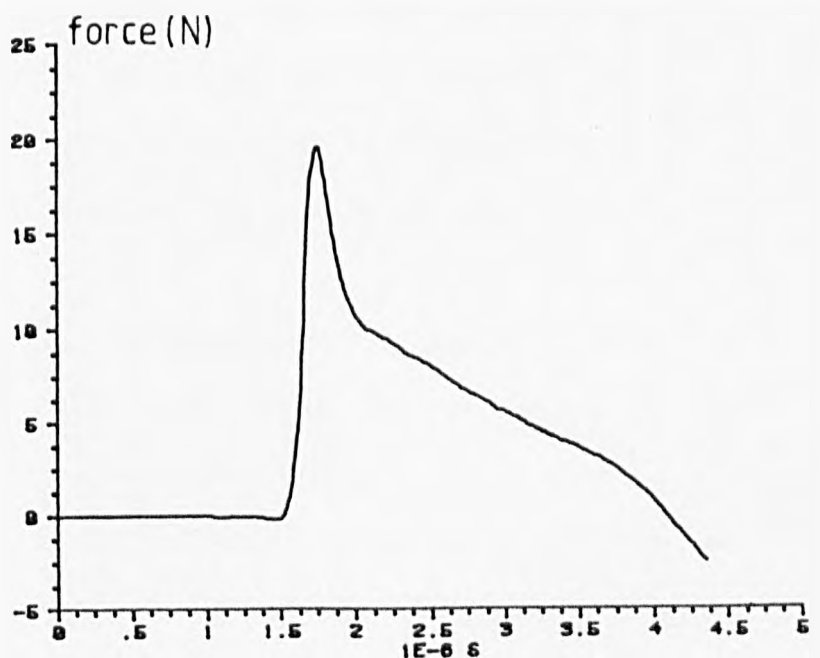
(a)  
predicted impulse  
response of a 1cm  
thick steel plate



(b)  
calculated inverse  
impulse response of  
a 1cm thick steel  
plate.



(c)  
deconvolved driving  
force function for  
the plasma source  
on a steel plate  
(shifted time base)  
32mJ, 35ns laser  
pulse



Magnitude and form of the plasma source driving force.

fig. 4.27(b) and convolution of this with the waveform shown in fig. 4.26(b) for the epicentre response from the plasma source for the conditions shown in fig. 4.26 leads to the time history of the plasma driving force shown in fig. 4.27(c). The form of this force can be seen to be in reasonable agreement with the simple model proposed for this force given in Chapter 3, although there is obviously some degree of error in this force function on longer timescales where the force appears to become negative. The form of the deconvolved force function also agrees with hypothetical force functions used previously for simulating the plasma source (Scruby et al, 1982).

## CHAPTER 5

## DIRECTIVITY OF THE LASER-ACOUSTIC SOURCE

In Chapter 4 the surface and epicentre displacements of the laser acoustic source were investigated. However, if the laser source is to be used as an acoustic "tool" in scattering experiments for NDE, then it is important to have a knowledge of the directional nature of the acoustic field. In general the acoustic modes of the different acoustic sources are not omni-directional.

A full theoretical interpretation of the directional displacement field would require the methods used in Chapter 4 applied to the general off-epicentre situation. Using these methods the wavefront displacement amplitudes have been determined for various surface harmonic driving forces, (Miller & Pursey, 1954; Cherry, 1962) and more recently for the laser generated thermoelastic source (Rose, 1984). The harmonic displacements predicted by Miller and Pursey have previously been used to explain the directional behaviour of the laser-acoustic source (Hutchins et al, 1981). However, it is possible to adapt a simplified method described by Gutin (1964) and Lord (1966) for harmonic excitation and apply this to the transient case.

The formal method of solution to these acoustic problems, which involves solving the wave equation subject to the boundary conditions, is unnecessary in the case of a harmonic driving force. The asymptotic expansion of the displacement integrals, in the far field, yield the same results as the method of ray tracing using the

appropriate reflection coefficients. The result is well known in geometrical optics (Born & Wolf, 1970) and is a requirement of the acoustic generalised ray theory (Pao et al, 1977) and was used in Chapter 4 to determine epicentre displacements. Also, for a dispersionless medium and point acoustic sources, the directivity amplitude will be independent of the driving frequency. The solution will therefore also be valid for an arbitrary driving force time dependence. In the limit of an impulsive driving force, the directivity amplitude will refer to the arrival of this impulse after propagation through the medium at the characteristic velocity.

The expected directionality of the laser acoustic source is investigated here by first considering a reciprocal problem, ie. the displacement of a free surface due to an incident wave propagating from the bulk of the material.

### 5.1 RADIAL DISPLACEMENTS

At a remote point in the bulk of the material a force  $F$  acts in the direction of the origin at the surface. In the neighbourhood of the origin the wave propagated from this source can be regarded to produce longitudinal planar displacement. The displacement in this local longitudinal wave, travelling from a direction defined by  $\theta_{pi}$  can be approximated by (Gutin, 1964)

$$d_1 = A e^{i(\omega t - K_1 x \sin\theta_{pi} - K_1 y \cos\theta_{pi})} \quad 5.1$$

Where  $x \sin\theta_{pi}$  and  $y \cos\theta_{pi}$  are the horizontal and vertical components of displacement.  $K_1$  and  $K_2$  are the longitudinal and shear wave numbers. The same notation and geometry that was used to describe reflection from a free boundary is used here, Chapter 2,

fig. 2.5. The amplitude of the longitudinal wave is given by

$$A = \frac{F}{4\pi R(\lambda + 2\mu)} e^{iK_1 R} \quad 5.2$$

At the boundary this incident wave will be reflected to give a longitudinal wave at a corresponding angle,  $\theta_{pr}$ , and it will be mode converted to give a shear wave at some angle,  $\theta_{svr}$ , fig. 2.5a. The displacements in these reflected waves will be given by

$$\begin{aligned} d_2 &= B e^{i(\omega t - K_1 x \sin \theta_{pr} - K_1 y \cos \theta_{pr})} \\ d_3 &= C e^{i(\omega t - K_2 x \sin \theta_{svr} - K_2 y \cos \theta_{svr})} \end{aligned} \quad 5.3$$

The components of displacement of these waves in the x and y directions are

$$\begin{aligned} U_1 &= d_1 \sin \theta_{pi}, \quad U_2 = d_2 \sin \theta_{pr}, \quad U_3 = d_3 \cos \theta_{svr} \\ W_1 &= -d_1 \cos \theta_{pi}, \quad W_2 = -d_2 \cos \theta_{pr}, \quad W_3 = d_3 \sin \theta_{svr} \end{aligned} \quad 5.4$$

where the subscripts, 1,2,3, will refer to the incident, longitudinal, reflected longitudinal and mode converted shear waves respectively.

Thus, the total tangential and normal components of displacement at the origin are

$$\begin{aligned} U_x &= U_1 + U_2 + U_3 = d_1 \sin \theta_1 + d_2 \sin \theta_2 + d_3 \cos \theta_3 \\ U_y &= W_1 + W_2 + W_3 = -d_1 \cos \theta_1 + d_2 \cos \theta_2 - d_3 \cos \theta_3 \end{aligned} \quad 5.5$$

and  $\theta_1 = \theta_3$ .

To maintain a normal stress free surface at the origin there must exist particular reflection coefficient relationships between the wave amplitudes A, B and C. The reflection coefficients for plane harmonic waves at a free boundary were considered in Chapter 2, eq. 2.6.

$$\frac{B}{A} = \frac{\sin 2\theta_1 \sin 2\theta_3 - K^2 \cos 2\theta_3}{\sin 2\theta_1 \sin 2\theta_3 + K^2 \cos^2 2\theta_3} \quad 5.6$$

$$\frac{C}{A} = \frac{2K \sin 2\theta_1 \cos 2\theta_3}{\sin 2\theta_1 \sin 2\theta_3 + K^2 \cos^2 2\theta_3}$$

The acoustic form of Snell's law may be written

$$\sin \theta_3 = \frac{1}{K} \sin \theta_1, \quad \text{where } K = \frac{K_2}{K_1} = \frac{V_p}{V_s}$$

The normal displacement at the origin from eq. 5.5 is thus given by

$$\begin{aligned} U_y &= -A \cos \theta_1 + B \cos \theta_1 - C \sin \theta_3 \\ &= A \left[ \left( \frac{B}{A} - 1 \right) \cos \theta_1 - \frac{C}{A} \frac{1}{K} \sin \theta_1 \right] \quad 5.7 \end{aligned}$$

This expression may now be re-written using the reflection coefficient relationships, eq. 5.6

$$U_y = \frac{-F e^{-iK_1 R}}{2\pi\mu R} \left[ \frac{\cos\theta_1 (K^2 - 2\sin^2\theta_1)}{(K^2 - 2\sin^2\theta_1)^2 + 4\sin^2\theta_1(1 - \sin^2\theta_1)^{1/2}(K^2 - \sin^2\theta_1)^{1/2}} \right] \quad 5.8$$

The denominator in this expression can be seen to have the familiar form of the Rayleigh equation, eq. 2.8.

Similarly the tangential displacement at the surface is given by

$$U_x = A \left[ \left( \frac{B}{A} + 1 \right) \sin\theta_1 - \frac{C}{A} \cos\theta_3 \right]$$

$$U_x = \frac{F e^{-iK_2 R}}{2\pi\mu R} \left[ \frac{\sin 2\theta_1 (K^2 - \sin^2\theta_1)^{1/2}}{(K^2 - 2\sin^2\theta_1)^2 + 4\sin^2\theta_1(1 - \sin^2\theta_1)^{1/2}(K^2 - \sin^2\theta_1)^{1/2}} \right] \quad 5.9$$

It is possible to obtain the bulk radiation distribution due to a surface force from the surface displacements due to a bulk source by invoking the principle of reciprocity. The principle of reciprocity for acoustic problems of this type was discussed by Burridge and Knopoff, 1964. For the case at hand this principle allows the source and observer to be interchanged. Thus the displacement in the radial direction, at an angle,  $\theta$ , due to a normal force acting at the origin, is given by the expression in eq. 5.8, and the displacement in the radial direction at an angle,  $\theta$ , due to a surface unbalanced tangential force is given in eq. 5.9.

The displacements due to the plasma source can be modelled by the expressions for the normal driving force and the displacements produced by an unbalanced tangential force can be modified in order to model the thermoelastic source.

The thermoelastic source can be considered to consist of two orthogonal surface dipolar components (Scruby et al, 1980). However, only the dipole component lying on the surface, in line with the observer contributes to displacements at the observer position. The displacements due to a surface dipole may be obtained in the following way from those for the unbalanced force given by eq. 5.9. Consider two forces separated by a small distance,  $\delta x$ , with the configuration shown in fig. 5.1. The combined displacements at some point 0 due to these two forces will be given by

$$U_R = \frac{F f(\theta) e^{-iK_1 R}}{R} - \frac{F f(\theta) e^{-iK_1 (R+\delta R)}}{R+\delta R} \quad 5.10$$

where  $f(\theta)$  is the directivity amplitude term.

But  $\delta R = \delta x \sin\theta$ , consequently

$$U_R = F f(\theta) \left[ \frac{R e^{-iK_1 (R+\delta x \sin\theta)} - e^{-iK_1 R (R+\delta x \sin\theta)}}{(R + \delta x \sin\theta)R} \right] \quad 5.11$$

as  $\delta x \sin\theta \rightarrow 0$ , then

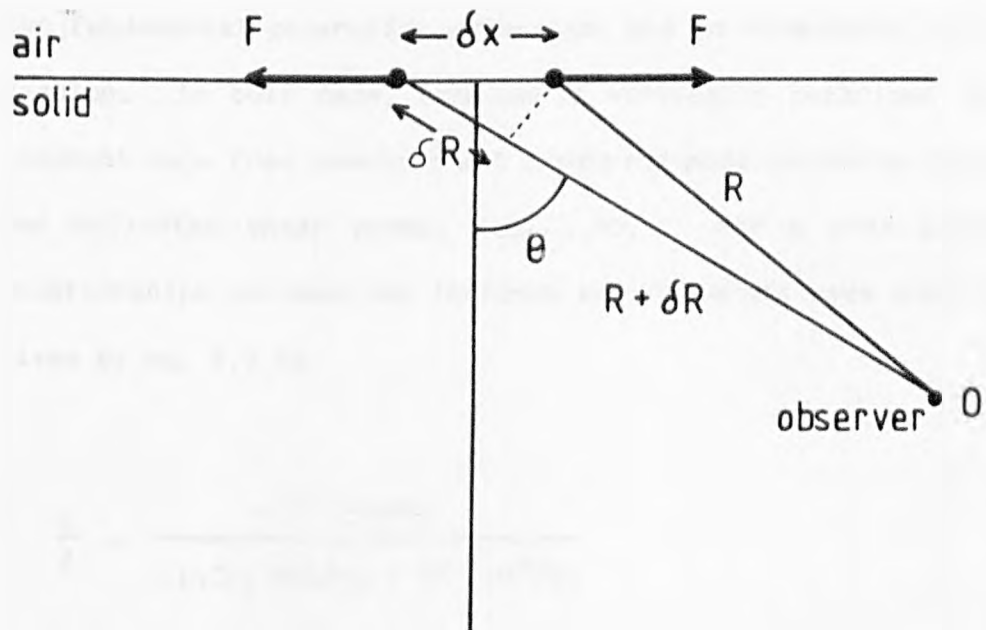
$$U_R = \frac{-F f(\theta) e^{-iK_1 R} \delta x \sin\theta (1+iK_1 R)}{R^2}$$

The longitudinal radiation field due to a surface, tangential dipolar force, from eqs. 5.9 and 5.11 is therefore

$$U_R = \frac{-M e^{-iK_1 R} (1+iK_1 R)}{2\pi \mu R^2} \left[ \frac{\sin\theta \sin 2\theta (K^2 - \sin^2\theta)^{1/2}}{(K^2 - 2\sin^2\theta)^2 + 4\sin^2\theta (1 - \sin^2\theta)^{1/2} (K^2 - \sin^2\theta)^{1/2}} \right] \quad 5.12$$

Where  $M$  is the source dipole moment. The form of the radial displacement amplitude due to a surface normal force from eq. 5.9 is

Fig. 5.1



The geometry for calculating the acoustic displacement

from a surface force dipole.

shown in fig. 5.2a and the form of the radial displacement amplitude, due to a surface dipole, from eq. 5.12, is shown in fig. 5.2b.

## 5.2 TANGENTIAL DISPLACEMENTS

The displacements corresponding to the shear arrivals for the two fundamental generation mechanisms may be considered in a similar fashion. In this case, consider a vertically polarised shear wave incident on a free boundary and producing mode converted longitudinal and reflected shear waves, fig. 2.5b. For a free boundary the relationships between the incident and reflected wave amplitudes are given by eq. 2.7 as

$$\frac{C}{A} = \frac{-K^2 \sin 4\theta_1}{\sin 2\theta_1 \sin 2\theta_3 + K^2 \cos^2 2\theta_1}$$

5.13

$$\frac{B}{A} = \frac{\sin 2\theta_1 \sin 2\theta_3 - K^2 \cos^2 2\theta_1}{\sin 2\theta_1 \sin 2\theta_3 + K^2 \cos^2 2\theta_1}$$

and Snell's law in this case becomes  $\sin \theta_3 = K \sin \theta_1$ . The components of displacement in the x and y direction are

$$U_1 = -d_1 \cos \theta_1, U_2 = d_2 \cos \theta_2, U_3 = d_3 \sin \theta_3$$

5.14

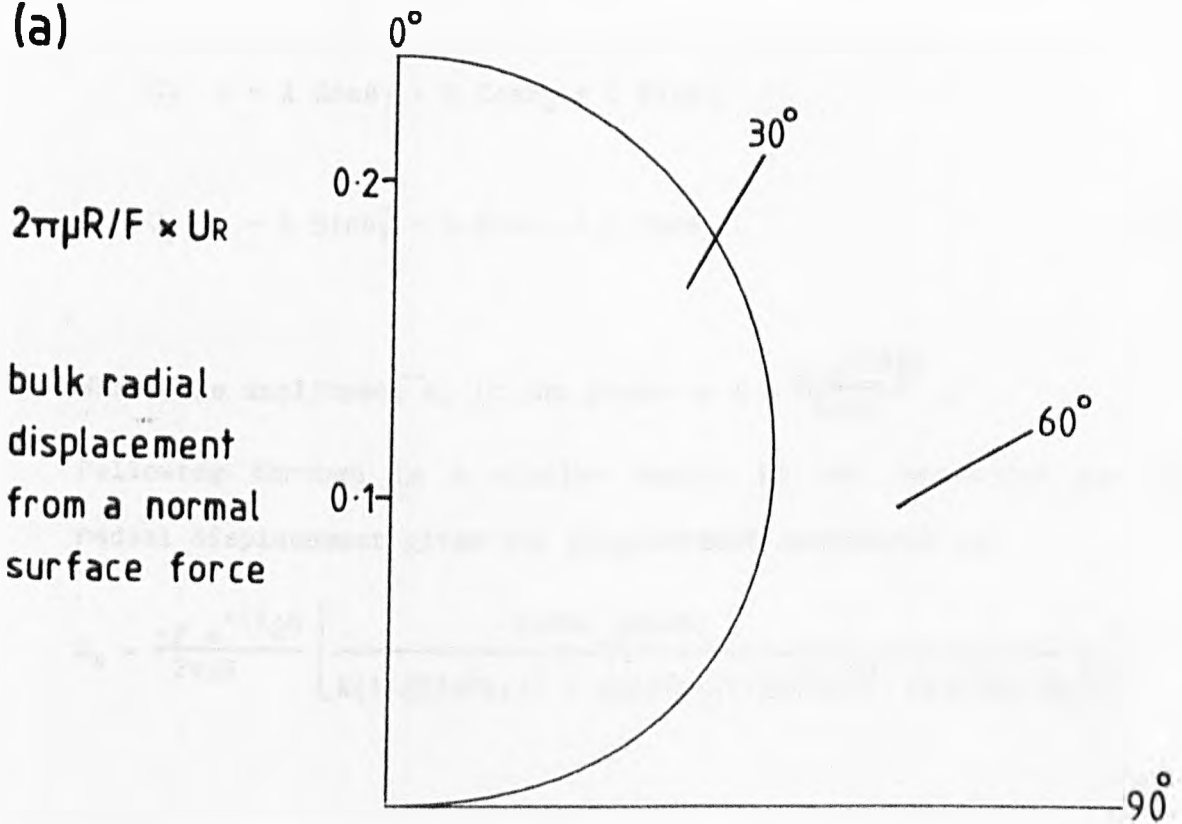
$$W_1 = -d_1 \sin \theta_1, W_2 = d_2 \sin \theta_2, W_3 = d_3 \cos \theta_3$$

and  $\theta_1 = \theta_3$ .

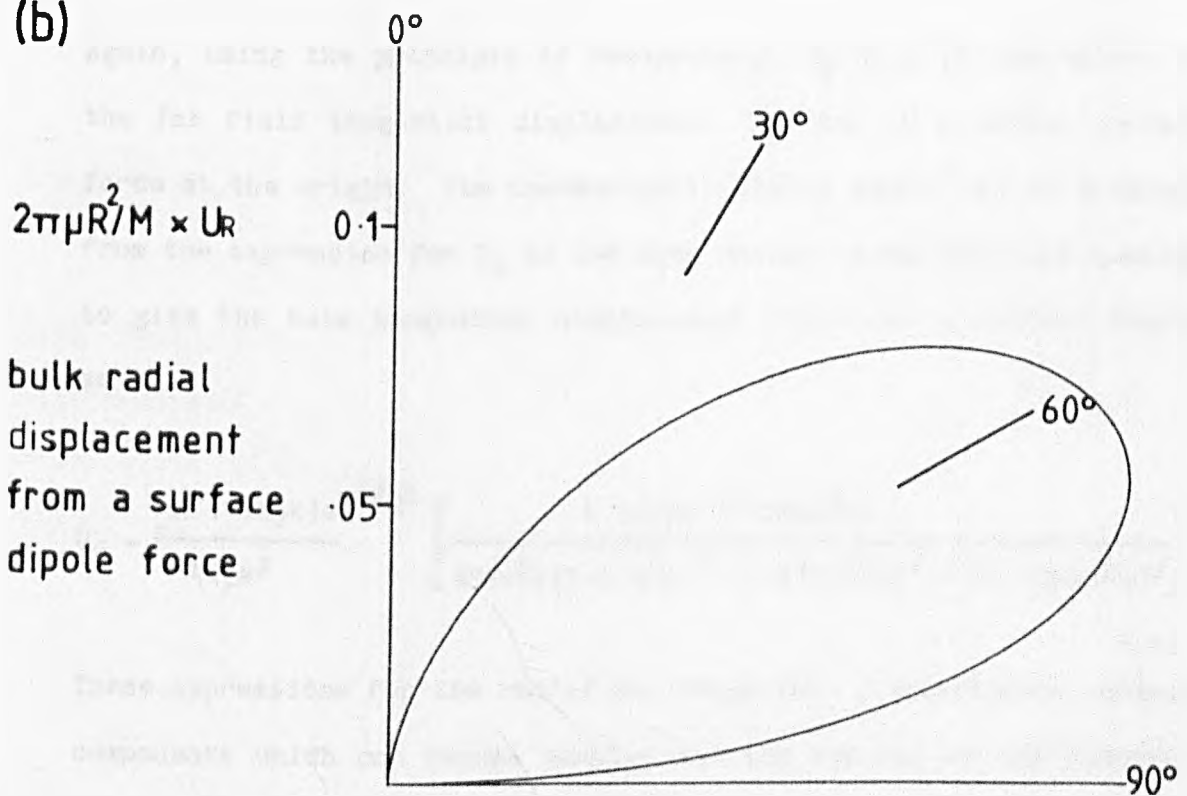
Thus the tangential and normal components of displacement at the origin are given by

Fig. 5.2

(a)



(b)



Predicted longitudinal directivity for two surface forces.

$$U_x = -A \cos\theta_1 + B \cos\theta_2 + C \sin\theta_3$$

$$U_y = -A \sin\theta_1 - B \sin\theta_2 + C \cos\theta_3 \quad 5.15$$

Where the amplitude, A, is now given by  $A = \frac{F e^{-iK_2R}}{4\pi\mu R}$ .

Following through in a similar manner to the derivation for the radial displacement gives the displacement components as

$$U_x = \frac{-F e^{-iK_2R}}{2\pi\mu R} \left[ \frac{\cos\theta_1 \cos 2\theta_1}{K(1-2\sin^2\theta_1)^2 + 4\sin^2\theta_1(1-\sin^2\theta_1)^{\frac{1}{2}} (1-K^2\sin^2\theta_1)^{\frac{1}{2}}} \right] \quad 5.16$$

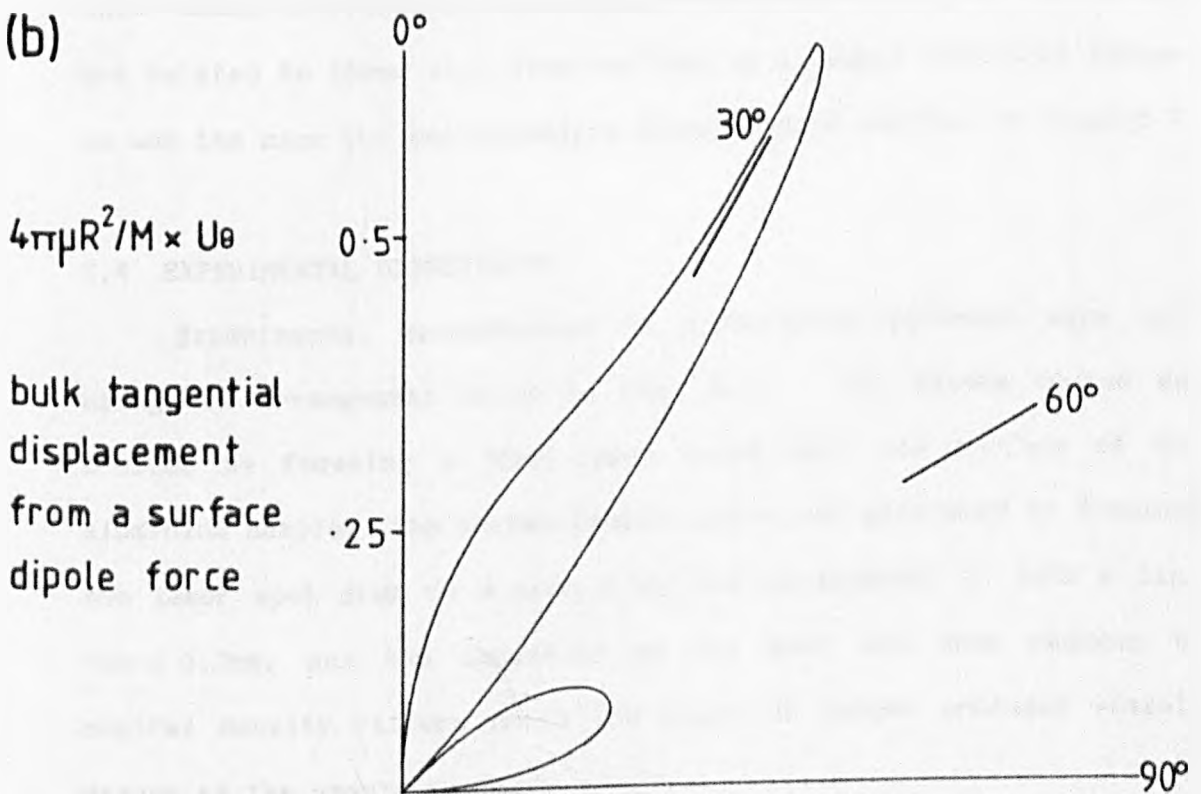
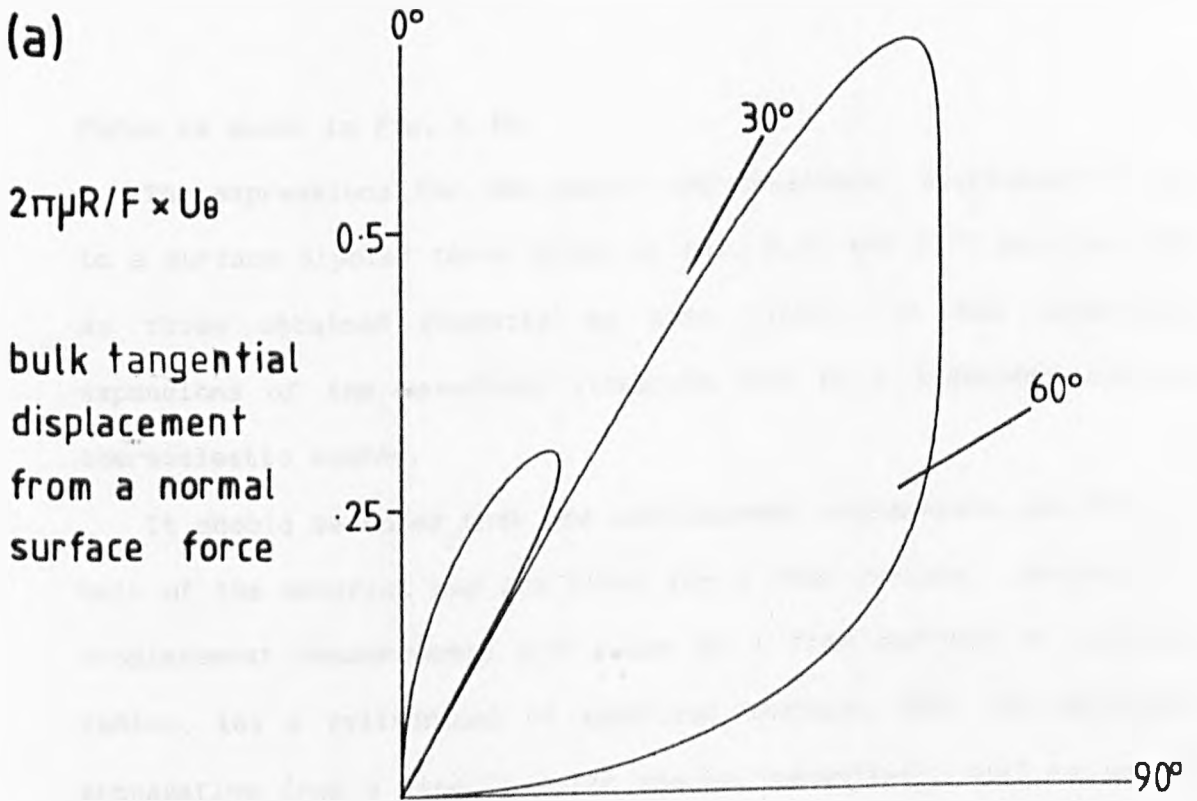
$$U_y = \frac{-F e^{-iK_2R}}{2\pi\mu R} \left[ \frac{\sin 2\theta_1 (1-K^2 \sin^2\theta_1)^{\frac{1}{2}}}{K(1-2\sin^2\theta_1)^2 + 4\sin^2\theta_1(1-\sin^2\theta_1)^{\frac{1}{2}} (1-K^2\sin^2\theta_1)^{\frac{1}{2}}} \right]$$

Again, using the principle of reciprocity,  $U_y$  will be equivalent to the far field tangential displacement,  $U_\theta$ , due to a normal surface force at the origin. The thermoelastic dipole source may be obtained from the expression for  $U_x$  in the same manner as the previous section to give the bulk tangential displacement field for a surface dipole as

$$U_\theta = \frac{-M(1+iK_2R)e^{-iK_2R}}{4\pi\mu R^2} \left[ \frac{K \sin 2\theta (1-2\sin^2\theta)}{4\sin^2\theta(1-\sin^2\theta)^{\frac{1}{2}} (1-K^2\sin^2\theta)^{\frac{1}{2}} + K(1-2\sin^2\theta)^2} \right] \quad 5.17$$

These expressions for the radial and tangential displacements contain components which can become complex and the modulus of the function is then evaluated. The form of the tangential displacement amplitude due to a normal surface force, from eq. 5.16 is shown in fig. 5.3a and the tangential displacement amplitude due to a dipolar surface

Fig. 5-3



Predicted shear directivity for two surface forces.

force is shown in fig. 5.3b.

The expressions for the radial and tangential displacements due to a surface dipolar force given by eqs. 5.12 and 5.17 are the same as those obtained recently by Rose (1984) for his asymptotic expansions of the wavefront integrals due to a transient surface thermoelastic source.

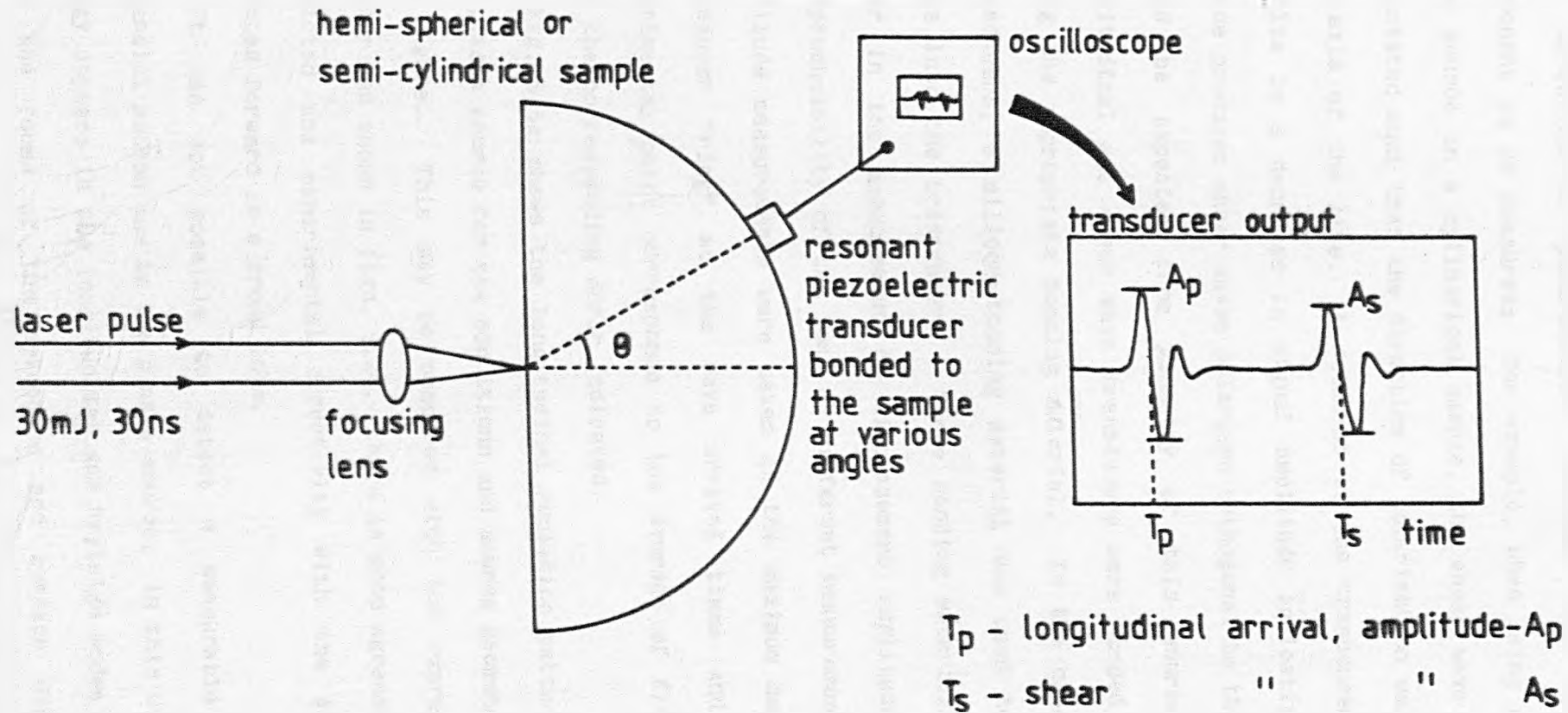
It should be noted that the displacement expressions are for the bulk of the material and not those for a free surface. However, if displacement measurements are taken on a free surface of constant radius, ie. a cylindrical or spherical surface, then the wavefront propagation from a line or point source respectively will be normal to that surface and no mode conversions of waves will take place. Under these conditions, the displacements in the bulk of the material are related to those at a free surface by a simple numerical factor, as was the case for the epicentre displacements derived in Chapter 4.

#### 5.4 EXPERIMENTAL DIRECTIVITY

Experimental measurements of directivity patterns were made using the arrangement shown in fig. 5.4. The plasma source was created by focusing a 30mJ laser pulse onto the surface of the aluminium sample. The thermoelastic source was generated by focusing the laser spot down to a spot 2 or 3mm in diameter or into a line 1cm x 0.2mm, and the intensity of the beam was then reduced by neutral density filters until the pulse no longer produced visible damage to the sample surface.

Longitudinal and shear, resonant piezoelectric transducers were used to measure the displacements at the longitudinal and shear wave arrival times. The shear wave transducers were orientated such that

Fig. 5-4



The experimental arrangement for measuring the acoustic source directivity.

the direction of polarisation coincided with the displacement component to be measured; for example, when using a thermoelastic line source on a cylindrical sample, the shear wave transducer was orientated such that the direction of polarisation was orthogonal to the axis of the line. A rotation of the transducer in this case results in a decrease in signal amplitude indicating that a line source produces shear waves polarised orthogonal to the line axis, as would be expected from geometry of this source. Both the longitudinal and shear wave transducers were bonded to the sample using the appropriate bonding material. In the case of the shear transducers, a silicone bonding material was used to couple shear waves into the transducer. These bonding materials lead to some error in the measurement of displacement amplitudes due to the irreproducibility of the bond at different measurement points. The amplitude measurements were taken as the maximum amplitude of the transducer "ring" at the wave arrival times and each plotted experimental point corresponds to the average of five measurements with the corresponding error indicated.

Fig. 5.5a shows the longitudinal radiation pattern measured for the plasma source for the conditions and source geometry indicated in the figure. This may be compared with the expressions derived earlier and shown in figs. 5.2a. There is good agreement between the predicted and experimental directivity with the acoustic energy directed forward in a broad lobe.

It was not possible to detect a measurable component of tangential motion due to the plasma source; in this case most of the energy appears in the longitudinal and Rayleigh modes as can be seen from the forms of the epicentre and surface displacements in

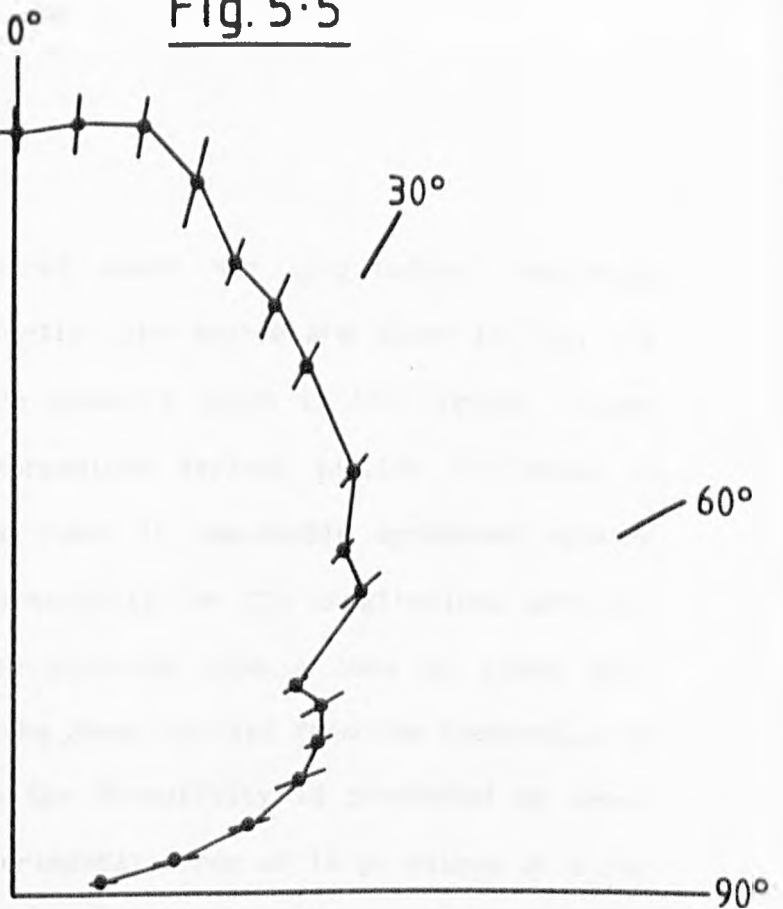
Fig. 5.5

(a)

transducer signal  
60 mV

longitudinal arrival  
directivity of the  
plasma source.

fully focused, 30mJ  
pulse, 5MHz long.  
transducer and oil  
bonding.



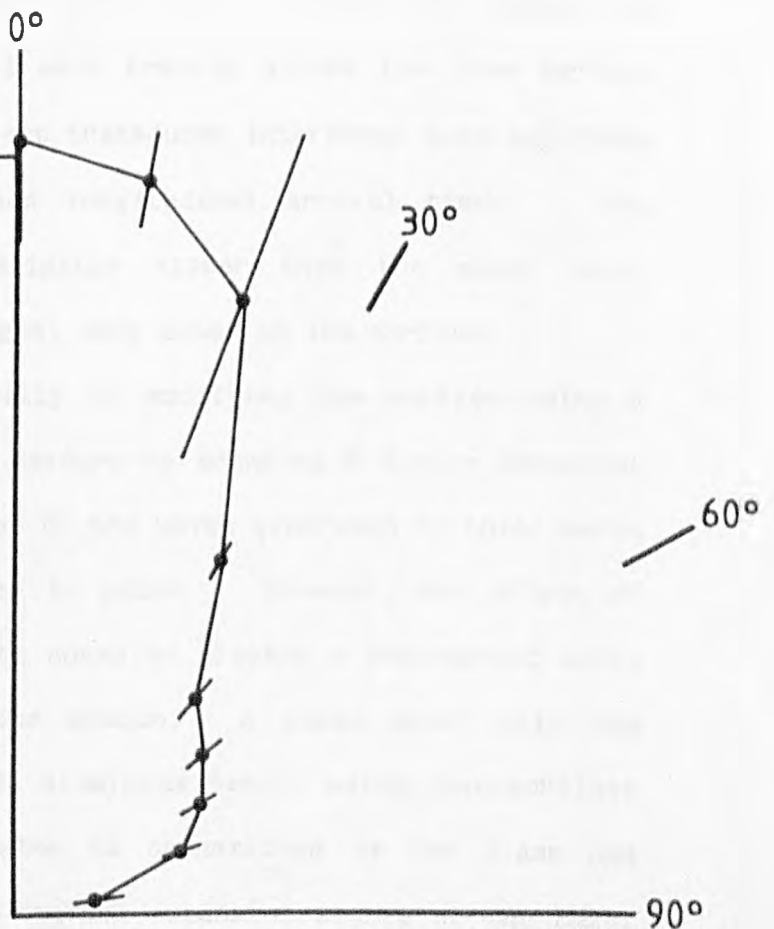
(b)

200  
mV

longitudinal arrival  
directivity of the  
constrained thermo-  
elastic source.

2mm diam. 30mJ spot,  
1MHz long. transducer  
and oil bonding.

surface constrained  
with glass cover-slip.



Experimental longitudinal resonant transducer directivity.

## Chapter 4.

The experimentally measured shear and longitudinal radiation patterns due to the thermoelastic line source are shown in fig. 5.6 for the conditions and source geometry shown in the figure. These may be compared with the expressions derived earlier and shown in figs. 5.2b and 5.3b. Again there is reasonable agreement between the predicted and measured directivity for the longitudinal arrival, with the acoustic energy now directed into a lobe at about  $60^\circ$ . Agreement is not so good for the shear arrival from the thermoelastic source although a maximum in the directivity is predicted at about  $30^\circ$ . A factor leading to experimental error at large values of  $\theta$  for the shear arrival is the confusing influence of the head waves and Rayleigh surface wave shown in fig. 4.1. The head waves are generated as the longitudinal wave travels across the free surface and their effect on the resonant transducer interferes with amplitude measurements at the shear and longitudinal arrival times. The Rayleigh wave, travelling slightly slower than the shear wave, dominates the displacement signal very close to the surface.

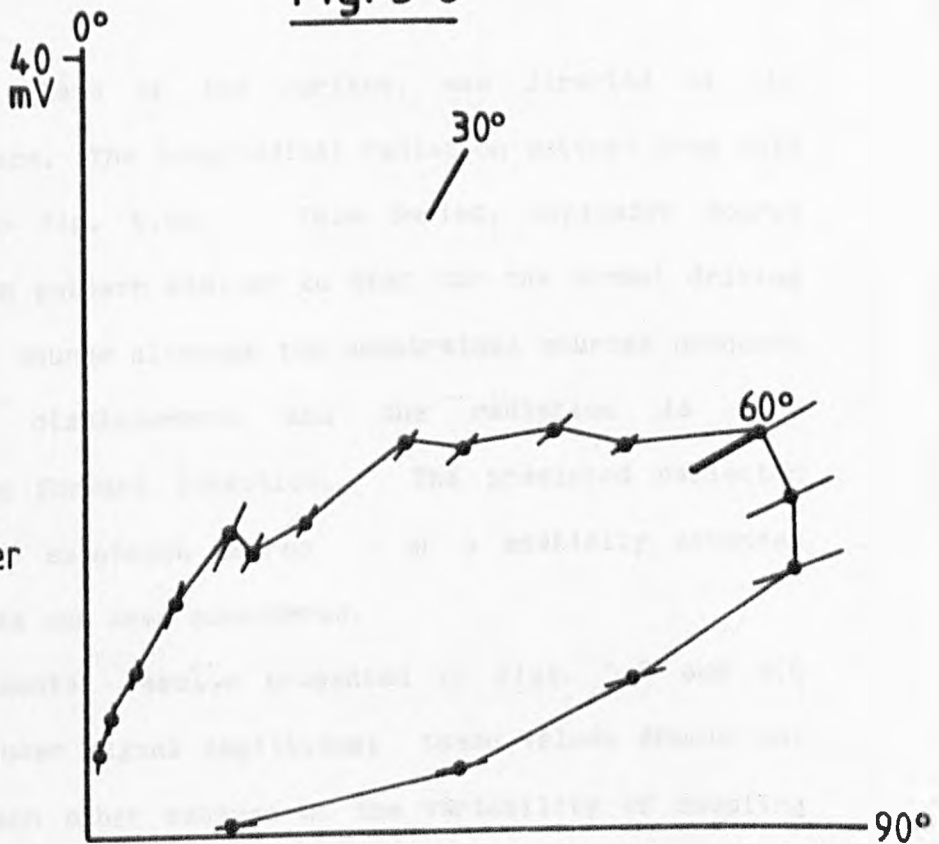
The effect on directionality of modifying the surface using a grease layer is difficult to measure by scanning a single detection transducer, since the amplitude of the waves generated by this source varies considerably from pulse to pulse. However, the effect of constraining the surface may be shown by placing a transparent solid layer over the surface of the sample. A glass cover slip was attached to the surface of the aluminium sample using cyanoacrylate "super" glue. The laser pulse is transmitted by the glass and creates a buried, constrained thermal expansion source at the metal surface. A laser pulse, of sufficiently low intensity that it caused

Fig. 5.6

(a)

longitudinal arrival  
directivity of a  
thermoelastic line  
source.

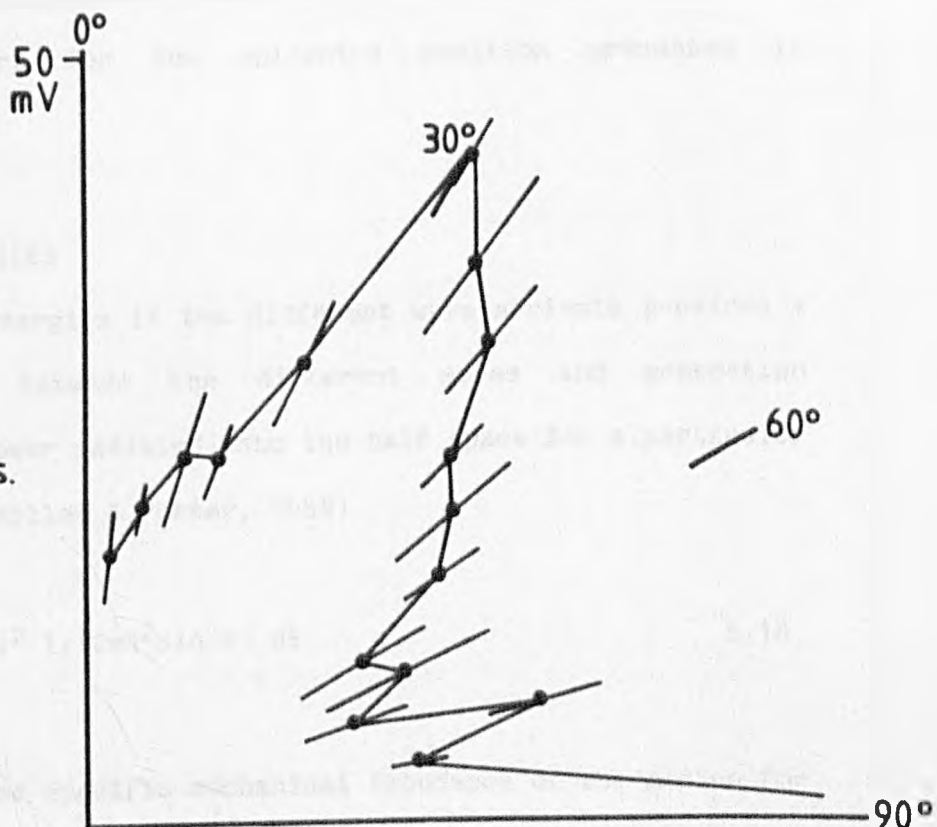
1MHz long. transducer  
and oil bonding.  
1cm x 0.3mm line,  
7.5mJ pulse.



(b)

shear arrival  
directivity of a  
thermoelastic line  
source.

3.75MHz shear trans.  
silicone bonding.  
1cm x 0.3mm line,  
7.5mJ pulse.



Experimental thermoelastic line source directivity.

no damage to the glass or the surface, was directed at the glass-sample interface. The longitudinal radiation pattern from this source is shown in fig. 5.5b. This buried, explosive source produces a radiation pattern similar to that for the normal driving force of the plasma source although the constrained sources produces greater amplitude displacements and the radiation is more concentrated in the forward direction. The predicted radiation field from a buried expansion source - or a spatially extended acoustic source - has not been considered.

All the experimental results presented in figs. 5.8 and 5.6 indicate the transducer signal amplitudes; these values should not be compared with each other because of the variability of coupling and transducer sensitivity. It is possible to assess the relative magnitudes of the shear and longitudinal wave amplitudes by referring to the absolute displacement measurements made using calibrated, wideband transducers for the epicentre position presented in Chapter 4.

#### 5.4 WAVEFRONT ENERGIES

The ratio of energies in the different wave arrivals provides a useful comparison between the different modes and generation mechanisms. The power radiated into the half space for a particular mode is given by, (Miller & Pursey, 1954)

$$U = \omega^2 \int_0^{\pi/2} 1/2 |A|^2 I_1(2\pi R^2 \sin \theta) d\theta \quad 5.18$$

Where  $I_1 = \rho V_1$  is the specific mechanical impedance of the medium for the acoustic mode, and A, the wave amplitude, may be evaluated for

the different modes and generation mechanisms from the previous expressions for the wavefront amplitude directivity. Consider the harmonic thermoelastic source, the displacements for this source are given by eq. 5.12 and 5.17 as

$$U_R = \frac{-M e^{-i\omega R/V_p} (1 + i\omega/V_p R) e(\theta)}{2\pi\mu R^2}$$

$$\text{where } e(\theta) = \frac{\sin\theta \sin 2\theta (K^2 - \sin^2\theta)^{1/2}}{(K^2 - 2\sin^2\theta)^2 + 4\sin^2\theta(1 - \sin^2\theta)^{1/2} (K^2 - \sin^2\theta)^{1/2}} \quad 5.19$$

$$U_\theta = \frac{-MK e^{-i\omega R/V_s} (1 + i\omega/V_s R)(f(\theta) + ig(\theta))}{4\pi\mu R^2}$$

$$\text{where } f(\theta) + ig(\theta) = \frac{\sin 2\theta (1 - 2\sin^2\theta)^{1/2}}{K(1 - 2\sin^2\theta)^2 + 4\sin^2\theta(1 - 2\sin^2\theta)^{1/2} (1 - K^2\sin^2\theta)^{1/2}}$$

The directionality term of  $U_\theta$  is complex for  $K\sin\theta > 1$ . Taking the real terms of  $U_R + U_\theta$  and retaining only those components which decay geometrically as  $1/R$ , since higher order terms will be relatively negligible in the far field, then the longitudinal and shear displacements may be written

$$U_R = \frac{-M \omega \sin(\omega t_p) e(\theta)}{2\pi\mu R V_p}$$

$$U_\theta = \frac{-M\omega K}{4\pi\mu R V_s} (f(\theta)\sin(\omega t_s) + g(\theta)\cos(\omega t_s)) \quad 5.20$$

Where  $t_p$  and  $t_s$  are the shear and longitudinal arrival times. The time averaged energies in the different modes then become

$$P_p = \frac{\rho \omega^4 M^2}{4\pi\mu^2 V_p} \int_0^{\pi/2} e(\theta)^2 \sin\theta \, d\theta$$

$$P_s = \frac{\rho \omega^4 M^2 K^2}{16\pi\mu^2 V_s} \int_0^{\pi/2} (g(\theta)^2 + f(\theta)^2) \sin\theta \, d\theta \quad 5.21$$

and the ratio of energies in the longitudinal and shear modes is

$$\frac{P_p}{P_s} = \frac{4}{K^3} \frac{\int_0^{\pi/2} e(\theta)^2 \sin\theta \, d\theta}{\int_0^{\pi/2} (g(\theta)^2 + f(\theta)^2) \sin\theta \, d\theta} \quad 5.22$$

The real components of the displacements for the plasma source, from eqs. 5.8 and 5.16 may be written as

$$U_R = \frac{-F \cos(\omega t_p)}{2\pi\mu R} \, l(\theta)$$

$$\text{where } l(\theta) = \frac{\cos\theta (K^2 - 2\sin^2\theta)}{4\sin^2\theta(1-\sin^2\theta)^{1/2}(K^2-\sin^2\theta)^{1/2} + (K^2-2\sin^2\theta)^2}$$

5.23

$$U_\theta = \frac{-F}{2\pi\mu R} (m(\theta) \cos(\omega t_s) + n(\theta) \sin(\omega t_s))$$

$$\text{where } m(\theta) + in(\theta) = \frac{\sin 2\theta(1 - K^2\sin^2\theta)^{1/2}}{4\sin^2\theta(1-\sin^2\theta)^{1/2} (1-K^2\sin^2\theta)^{1/2} + (K^2-2\sin^2\theta)^2}$$

and the ratio of the time averaged energies for the plasma source becomes

$$\frac{P_p}{P_s} = K \frac{\int_0^{\pi/2} l(\theta)^2 \sin\theta \, d\theta}{\int_0^{\pi/2} (m(\theta)^2 + n(\theta)^2) \sin\theta \, d\theta} \quad 5.24$$

These expressions for the energies carried by the wavefronts are independent of frequency and are therefore true for a transient as well as a harmonic driving force. The expressions in eqs. 5.22 and 5.24 have been evaluated numerically for different values of Poisson's ratio of the sample material and the energy ratios are shown in table 5.1, (see Appendix 1 for the numerical details). The values for the thermoelastic source agree, in the main, with those of Rose (1984) for his corresponding calculation and the table includes his value for the energy radiated by the thermoelastic surface wave relative to the shear wave.

From the results of the energy partition of the thermoelastic source it may be concluded that a substantial amount of energy is radiated as surface waves, which will always be dominant over the bulk waves in the far field since they decay less rapidly. Energy partition for the bulk waves for the thermoelastic source shows that more energy is radiated as shear rather than longitudinal waves as might be expected from the geometry of the source. Similarly for the plasma source, more energy appears to be radiated as shear waves. It is not intuitively apparent why this should be the case, especially in view of the fact that it was not possible to experimentally obtain a shear directivity measurement for this source. The Rayleigh wave partition energy has not been calculated for the plasma source although it may be concluded from the surface measurements presented in Chapter 4 that this source also radiates a

Table 5.1

Poisson's ratio	plasma source	thermoelastic source	
	$\frac{\text{longitudinal}}{\text{shear}}$	$\frac{\text{longitudinal}}{\text{shear}}$	$\frac{\text{Rayleigh}}{\text{shear}}$
0.2	0.293	0.536	6.93
0.25	0.267	0.311	4.65
0.33	0.185	0.093	3.58
0.4	0.968	0.019	3.14

Partition of wavefront energy for the laser-acoustic source.

considerable amount of its energy in the surface wave.

A comparison of the overall acoustic energy generated by the different mechanisms indicates that the grease-layer source is most efficient, producing mainly Rayleigh and longitudinal radiation, followed by the plasma source which behaves similarly. The thermoelastic source produces the lowest amplitudes although it should be noted that this source produces predominantly shear displacement and the broadband transducers used to obtain the results in the following chapters are devices which respond to normal surface displacements and are therefore not suited to this type of source.

## CHAPTER 6

## ACOUSTICS IN MATERIALS EVALUATION

The previous two chapters described the directional and temporal characteristics of the various laser-acoustic source regimes. A knowledge of these characteristics allows the investigation of the application of this new acoustic source to NDE. Some of these applications will be considered in the remainder of the thesis.

A brief review of the acoustic techniques currently in use for NDE will be given before going on to describe the experimental applications using the laser-acoustic source. The review is intended to cover the general methods of acoustic NDE which are common to most of the acoustic sources currently in use. There are many specific techniques for investigating particular problems, but these are usually extensions to the general methods discussed here. Emphasis is also placed on those methods which could be usefully adapted to the laser-acoustic source, especially those in which the acoustic source could provide some advantage over the conventional methods.

Acoustic wave energy at ultrasonic frequencies has been successfully employed over the past 35 years for locating internal defects in metal plates, forgings and welds. The present, common use of acoustics for evaluating materials falls into two distinct groups. Firstly, there are those techniques which employ externally generated acoustics to locate and characterise defects, ie. ultrasonic non-destructive testing. Secondly, there is the relatively new and less common method of detecting the acoustics

generated internally by materials, either from spontaneous crack propagation or from externally applied stresses, and then using this "acoustic emission" information to evaluate the material integrity. The methods of acoustic non-destructive testing also fall into two groups: those which use an acoustic field, propagated within a material, to cast shadows of cavities and defects; and those which rely upon the echo of acoustic pulses from cavities and defects. Both of these methods require a source of pulsed acoustic energy.

#### 6.1 PIEZOELECTRIC TRANSDUCERS

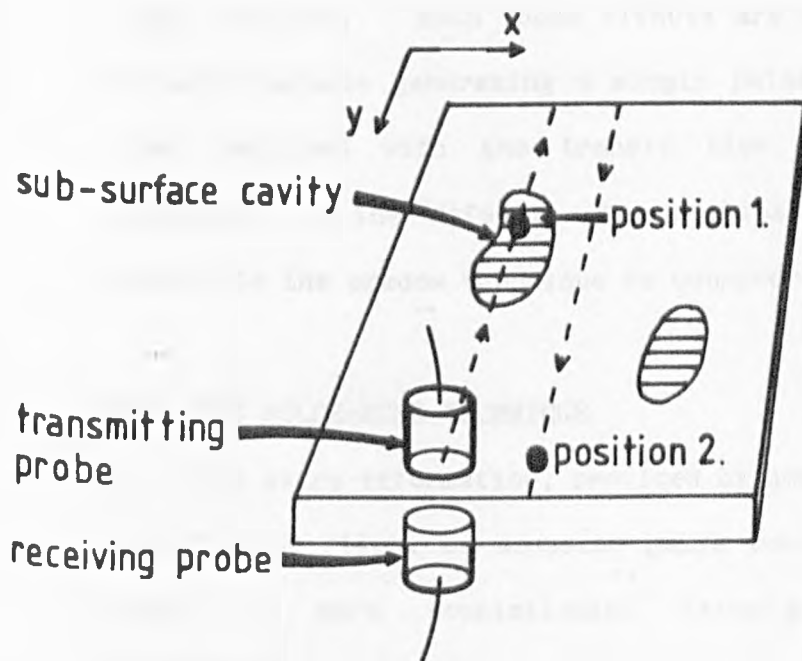
By far the most common method of producing and receiving acoustics for non-destructive testing is by means of piezoelectric transducers. These transducers provide a relatively efficient means of producing acoustic energy when compared with other methods, eg. electrodynamic, magnetostrictive and optical techniques (Krautkramer 1983 has a review of the methods and instrumentation used in NDE). However, piezoelectric transducers possess some properties which make their use undesirable in some circumstances. These transducers are inherently resonant devices and they will ring at some characteristic frequency determined by both their mechanical and electrical properties. A great deal of effort is put into manufacturing damped piezoelectric transducers which are less sensitive than undamped devices but which produce a pseudo-pulse consisting of a few cycles at the resonant frequency. However, the residual ringing creates misleading interference effects in using the shadow technique and it also introduces uncertainties when accurate "time of flight" measurements are to be made in pulse-echo methods. Piezoelectric transducers have also to be acoustically bonded to the sample under

test. This acoustic bond usually consists of some liquid smeared between the transducer and the sample. These bonds are variable in their properties and introduce uncertainty when relative acoustic amplitudes have to be determined. Another disadvantage of piezoelectric transducers is that they cannot operate in high temperature environments. Above some critical temperature ( $370^{\circ}\text{C}$  for PZT5) the piezoelectric nature of the material is destroyed and also at high temperatures there is the problem of creating a durable acoustic bond.

## 6.2 THE SHADOW TECHNIQUE

The shadow technique is usually applied to the testing of plates for laminar defects. The transmitted intensity of an acoustic field is monitored as the material passes between a transmitter and receiver, and any intervening discontinuity within the material will cause the acoustic field to be reflected leading to a decrease in the transmitted signal. The surface of the material can be scanned to build up a limited internal picture of the object. This two dimensional representation of the object is referred to as a C-scan and the process is shown diagrammatically in fig. 6.1. The technique cannot estimate the vertical position of a defect within a sample and the accuracy of the 2-D scan is limited when conventional piezoelectric transducers are used. Piezoelectric transducers usually have a large area of contact which introduces uncertainties in the estimation of the lateral position of a defect detected by the drop in the transmission signal. The diffraction of the quasi-pulse, produced by these transducers, at the edges of the defect leads to interference which modulates the detected signal and obscures the

Fig. 6.1

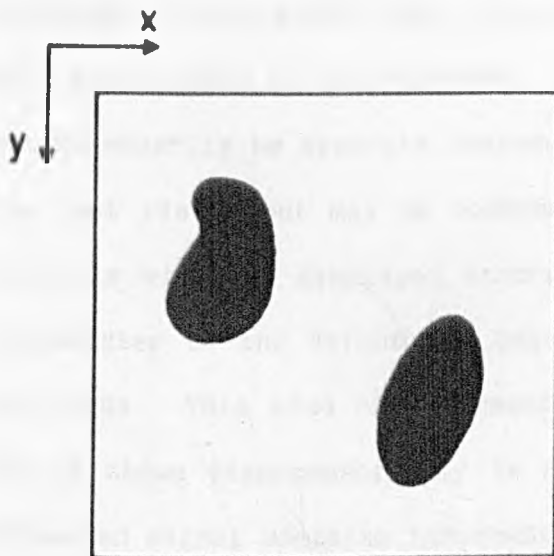
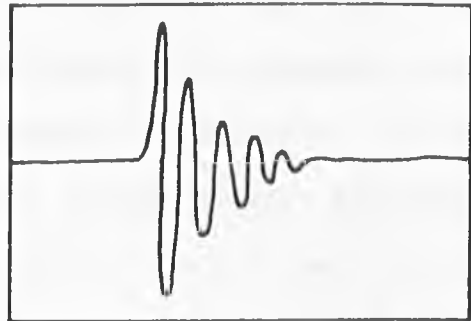
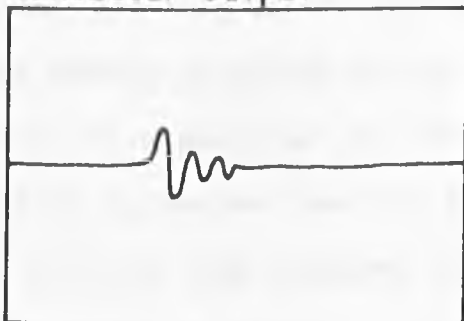


Co-incident, resonant piezoelectric transducers are scanned across the surface of the sample. The transmitted signal amplitude decreases in defect areas.

position 1

position 2

transducer output



The transmitted signal amplitude is used to build up a "C-scan" display of sub-surface defect areas.

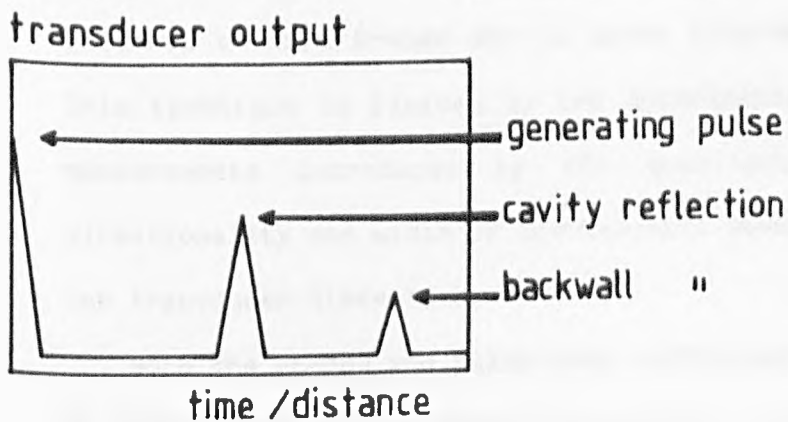
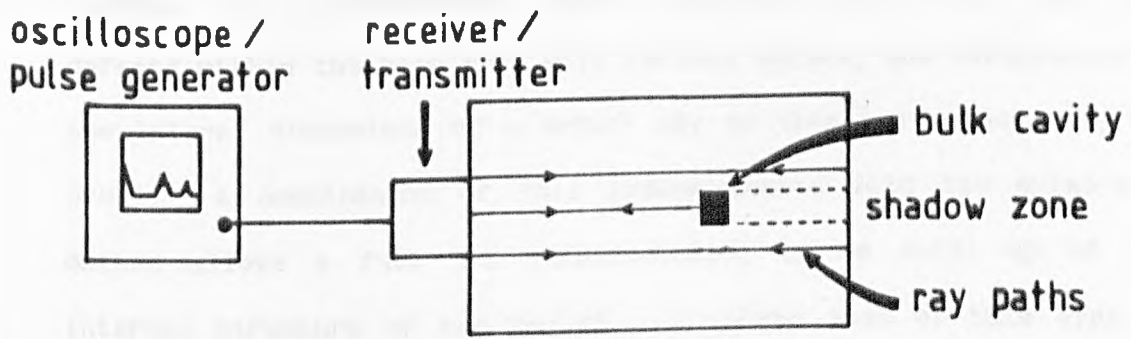
The shadow graph technique for locating laminar defects.

edge position. Both these effects are minimised by using a small acoustic source generating a single pulse of a short time duration when compared with the transit time across the characteristic dimension of the defect. The application of the laser-acoustic source to the shadow technique is considered in Chapter 8.

### 6.3 THE PULSE-ECHO TECHNIQUE

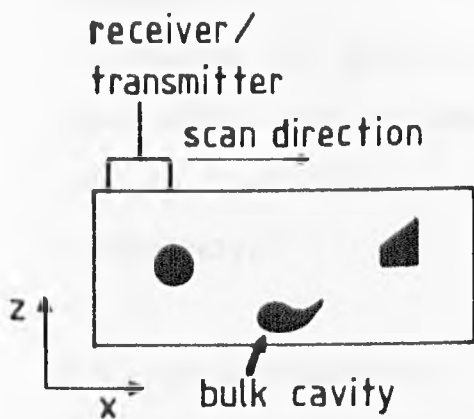
The extra information, provided by monitoring both the amplitude and time of flight of acoustic pulse echoes from defects, allows a range of more sophisticated techniques to be applied to non-destructive testing. It is possible, in principle at least, to use this extra information to locate and characterise defects both within the bulk and on the surface of the material. Fig. 6.2a shows the general principle of the pulse-echo method. The acoustic pulse from the transmitter may encounter a defect in its path; if the defect is smaller than the cross-section of the acoustic beam then part of the beam bypasses the defect, strikes the back wall of the sample and is reflected back to the receiver; the defect in turn reflects an echo pulse which, depending on the defect form and size, will be detected by the receiver. The transmitter and receiver need not necessarily be separate transducers placed at different points on the test piece, but may be combined into a single probe. The echo pulse is visually displayed according to its transit time from the transmitter to the defect and back to the receiver and also by its amplitude. This kind of representation is referred to as an A-scan and is shown diagrammatically in fig. 6.2a. The amplitude of the reflected signal contains information on the position and size of the flaw although it is difficult to extract this information from the

Fig. 6-2

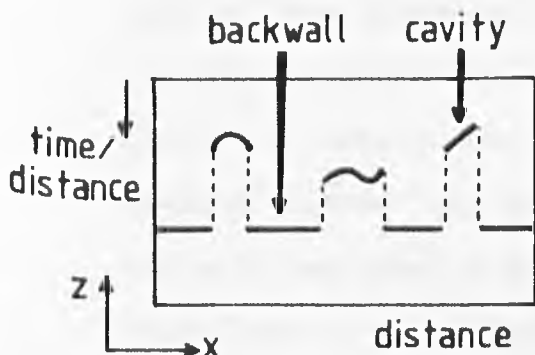


The signals received by the transducer are rectified and displayed as an "A-Scan".

(a) The simple pulse-echo method



The receiver/transmitter is scanned across the surface and the return signals are used to build up a "B-Scan" display.



The B-Scan display shows the front surface reflections from cavities and the backwall.

(b) The pulse-echo scanning technique.

signal. If a directional, narrow beam is transmitted, then only defects within the beam area will reflect pulses, and information on the lateral dimensions of a defect may be obtained by scanning the probe. A combination of this shadow method with the pulse-echo method allows a full 3-D interpretation to be built up of the internal structure of the object. A linear scan of this type is referred to as a B-scan and is shown diagrammatically in fig. 6.2b. This technique is limited by the uncertainty in the time of flight measurements introduced by the quasi-pulse, and also on the directionality and width of the acoustic beam, which again depends on the transducer dimensions.

Both the shadow and pulse-echo techniques suffer from the problem of occultation of one defect by another; measurements from several orientations are usually made in order to fully test a region of interest.

Chapter 9 presents an experimental investigation of the interaction of laser generated surface acoustic pulses with surface defects, and "time of flight" techniques have been employed extensively.

#### 6.4 ACOUSTIC EMISSION

Acoustic emission is the production of elastic waves in a material from atomic rearrangements occurring during deformation or cracking (Williams 1980). The process is usually due to steady loads beyond the elastic limit of the material or a fluctuating load. Acoustic emission from spontaneous crack growth consists of irregular bursts of the order of microseconds in duration and their number can range from a few occasional single bursts to about one hundred

thousand per second. Both the amplitude and the frequency spectrum of acoustic emission varies greatly and there has been much work in correlating the acoustic properties to the physical properties of the defect concerned. The monitoring of acoustic emission allows large structures to be continuously tested for signs of mechanical failure - an impossible task using ultrasonic NDE techniques. One role of the laser-acoustic source in modelling these events was discussed in Chapter 4.

#### 6.5 APPLICATION OF THE LASER-ACOUSTIC SOURCE TO NDE

The laser-acoustic source has some unique properties which, in certain situations, provides an advantage over conventional methods of non-destructive testing. These advantages are as a result of two properties of the laser-acoustic source; the generation mechanism is non-contacting and the acoustic transients that it produces are broadband.

The non-contacting nature of the source circumvents the bonding problems associated with piezoelectric transducers. The acoustic transients are reproducible in amplitude and, because of this property, the use of the laser-acoustic source as a standard by which other transducers may be calibrated has been previously discussed (Scruby et al 1981). The acoustic source may be used to generate on hot material where conventional transducers become inoperable. The laser beam, because of its coherent nature, is an efficient and versatile means of depositing energy at a distance. Consequently, the beam may be directed into hostile situations, eg. corrosive or radioactive environments, or under water. The laser beam may be steered easily by optical means to rapidly scan materials in a far

more efficient manner than is achieved conventionally by moving probes. The non-contacting nature of the source also means that it may be used to generate acoustics in complex shaped test pieces or those with a rough surface, eg. casts and ceramics.

The broadband nature of the source also provides some advantages. Accurate time of flight measurements can be made in pulse-echo techniques, because there are none of the uncertainties associated with the quasi-pulses produced by damped, resonant piezoelectric devices. Again, because the laser-acoustic source can be made to produce single acoustic pulses, there are no interference effects in the shadow technique. The single, narrow pulses also allow acoustic spectroscopy techniques to be used, and the increase in accessible information that is provided by single pulses means that more sophisticated defect imaging techniques may be investigated. The possible imaging techniques would require the use of computer processing to manipulate the large amount of data that is available. This latter point has some relevance in that there is a present trend in acoustic NDE to move away from "operator experience" in interpreting the data, to a more systematic data analysis by computer or microprocessor, and the display of the relevant information in an "easy to understand" format.

The laser source also has disadvantages associated with it. Overall efficiency of the laser system is far less than its piezoelectric counterpart, and in the thermoelastic regime at least, the acoustic displacements are less than those produced by conventional transducers. The laser and ancillary equipment tend to be more expensive and bulkier than piezoelectric systems, although laser devices are becoming smaller and more efficient. A battery

operated, hand held, laser device has recently been suggested for probe calibration (Dewhurst et al, 1983). The point acoustic source generates all modes at once, unlike piezoelectric transducers which are more or less selective in their ability to produce longitudinal, shear or surface motion. The directivity of the source, discussed in Chapter 5, is poor when compared with the ability of conventional transducers to produce narrow, directional lobes of acoustic energy. From the work presented in Chapters 4 and 5 it is seen that the Rayleigh surface pulse is the dominant feature produced by the laser-acoustic source. Unless a testing method uses this mode then the testing will have to be restricted to relatively small objects, (geometric and material attenuation restrict acoustic propagation to less than about a metre); on large samples geometric spread dictates that the slower decaying surface waves will dominate the bulk waves. The useful, broadband property of the source also restricts testing to small samples, since attenuation over large distances will remove the high frequencies and broaden any acoustic pulses.

Chapters 8 and 9 present some results on the application of the laser source to some of the NDE methods mentioned in this chapter. Most of the work has been carried out on artificial defects, laminar de-bond areas in plates and milled slots to simulate cracks. The results emphasize features of the fundamental acoustic pulse - defect interactions arising from the laser-acoustic source.

## CHAPTER 7

## WIDEBAND ACOUSTIC TRANSDUCERS

Wideband acoustic transients generated by the laser-acoustic source can be best exploited using wideband transducers as receivers. It has previously been mentioned that the commonly used piezoelectric devices are resonant in their nature of operation and that it is possible to damp these resonances by various mechanical and electrical techniques (eg. Silk, 1984). These damped piezoelectric devices are in general not sufficiently wideband to make best use of the laser source, and several types of other wideband transducers were used to perform the experiments described in Chapters 8 and 9, including capacitance, electromagnetic acoustic, thick piezoelectric and interferometer devices. A plate capacitance probe, described elsewhere (Scruby et al, 1978) and the ball capacitance probe, described here, were used to obtain the displacement waveforms shown in Chapter 4.

## 7.1 CAPACITANCE TRANSDUCERS

A capacitance displacement transducer is formed by placing a conducting probe in close proximity to the metallic surface of a sample and any change in the dielectric filled gap between the surface and the probe due to an acoustic disturbance will result in a change in capacitance of the system. This is the basic principle of all acoustic-capacitance detectors from audio microphones to acoustic

emission sensors and there are various ways of monitoring the change in capacitance and relating it to the absolute form of the acoustic displacement of the surface.

Some of the earlier reported work on laser generated acoustics employed a calibrated plane-parallel capacitance device to measure the epicentre displacements produced by the various laser sources (Dewhurst et al, 1982). This device consists of a flat, 6mm dia. disc that is positioned by a micrometer, within a few microns and parallel to the surface of the sample. Any change in this gap results in a change in capacitance which is monitored by a charge sensitive amplifier. Operational details of this device have been published (Scruby et al, 1978). The instrument does have some limitations. In order to calibrate the probe it is necessary to ensure that the surface of the sample is polished flat to within a fraction of a micron over the area of the probe surface and it is also necessary to ensure that the probe head and the sample surface are parallel to within the same limitations. The probe will also integrate the detected signal across its area. This will have a negligible effect in the case of a plane wavefront incident in a normal direction to the probe surface, but for non-planar wavefronts or wavefronts incident in different directions, eg. a surface wave, this introduces a geometric limitation on the bandwidth of the device. Several alternative designs of capacitance probe have been considered to overcome these disadvantages.

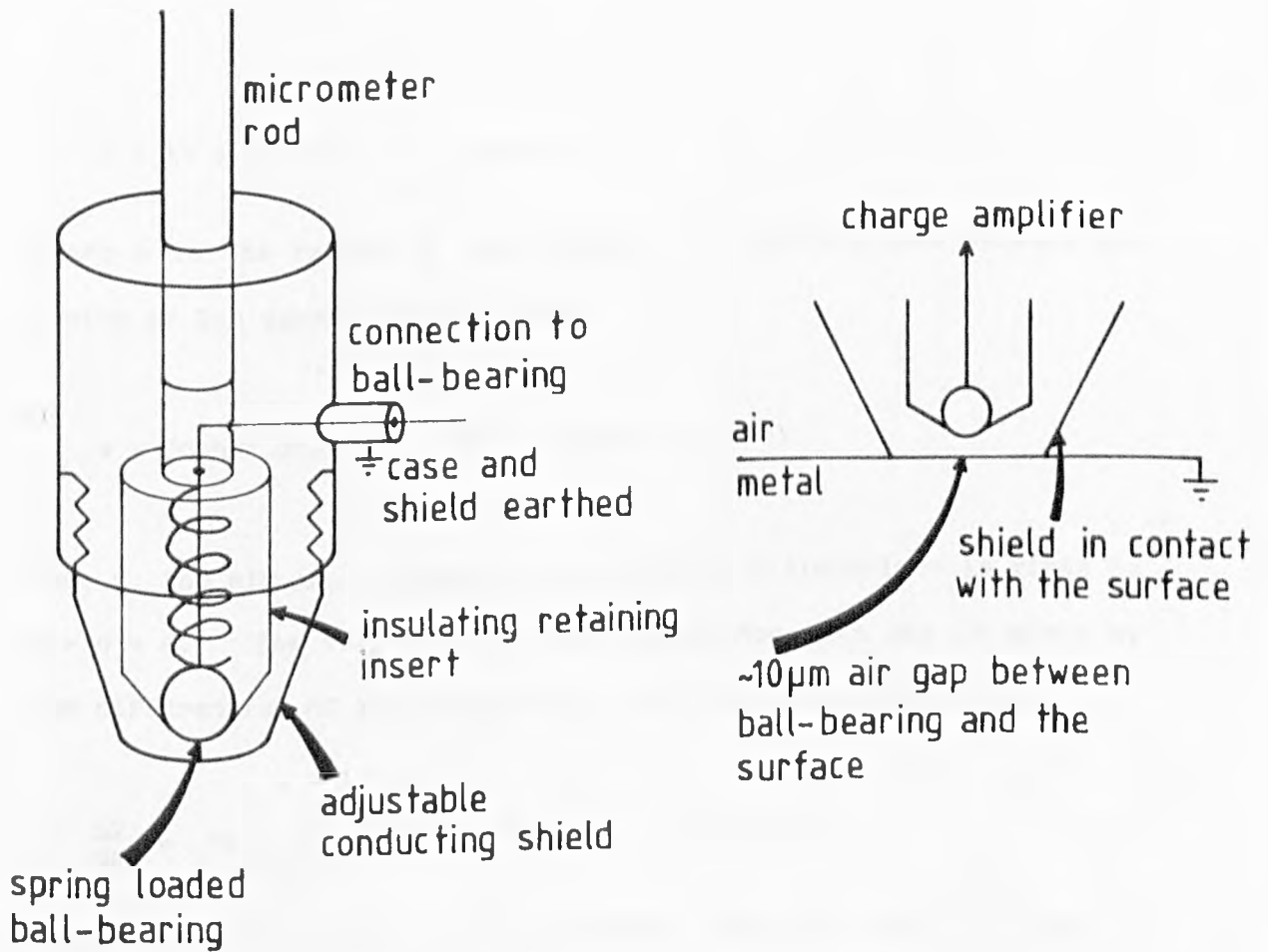
#### 7.1.1 THE SPHERICAL CAPACITANCE TRANSDUCER

Replacing the flat plate in the plane parallel capacitance devices with a spherical conductor offers several advantages. The

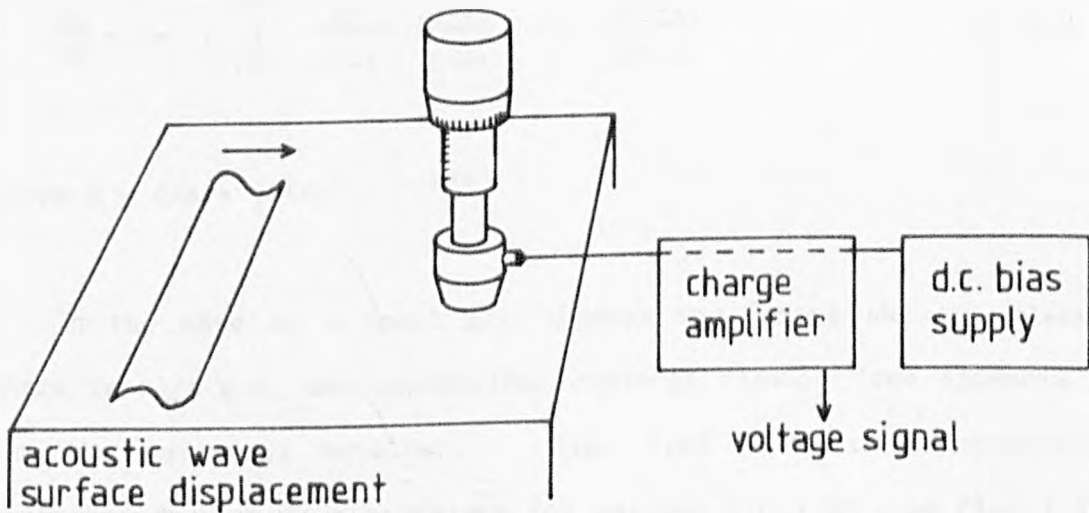
capacitance of such a device is predominantly from the relatively small surface area of the sphere which is adjacent to the surface of the sample. This active area can give a typical device a geometrically limited bandwidth approaching 10MHz. The main advantage of this geometry is that the sample does not need to meet the stringent, and sometimes impractical, requirements of being polished optically flat, and consequently the positioning of the sphere against the surface becomes an easier operation. The penalty paid for this versatility is a reduction in sensitivity of the device in comparison to a plane parallel capacitance probe. However, a typical transducer is capable of measuring the normal displacement of a surface with a sub-nanometre resolution. The device employed in the experiments presented here consists of a 4mm diameter steel ball bearing held about 10 $\mu$ m above the earthed surface of the metal sample by a micrometer head, fig. 7.1. The sphere is maintained at a constant bias potential by a highly stabilised voltage supply, and as a consequence, any change in capacitance of the arrangement due to a change in the gap between the sphere and the surface results in a net flow of charge to or from the sphere. This charge variation is monitored by a charge sensitive amplifier of the type used in semiconductor radiation detectors with some additional high voltage breakdown protection on the input stage.

The transducer sensitivity can be analysed in the following way. The charge flow,  $dq$ , from a capacitance transducer operated at a fixed voltage,  $V$ , is given by  $VdC$ , where  $dC$  is the change in capacitance of the device caused by a change in the air gap. The capacitance of a sphere next to a plane separated by a perfect dielectric is given by the series solution (Smythe, 1968)

Fig. 7-1



The ball-bearing is held a few microns above the surface of the conductor by a micrometer. Any change in the air gap due to an acoustic disturbance results in a change in capacitance of the device.



The ball-bearing capacitance transducer.

$$C = 4\pi \epsilon a \sinh \alpha \sum_{n=1}^{\infty} \text{Csch}(n\alpha) \quad 7.1$$

Where  $a$  is the radius of the sphere,  $d$  is the distance between the centre of the sphere and the plane,

$$\alpha = \text{Cosh}^{-1} d/a = \ln (d/a + (d^2/a^2 - 1)^{1/2})$$

and,  $g$ , the air gap - taken to be a perfect dielectric - is given by  $g = d - a$ . The variation of the capacitance with gap is given by the differential of the expression in eq. 7.1 with respect to  $g$ .

$$\frac{dc}{dg} = 4\pi \epsilon \sum_{n=1}^{\infty} \text{Csch}(n\alpha) [\text{Coth } \alpha - n \text{Coth } n\alpha] \quad 7.2$$

Substitution of  $\alpha$  into the exponential form of eqs. 7.1 and 7.2 yields

$$C = 4\pi \epsilon (d^2 - a^2)^{1/2} \sum_{n=1}^{\infty} \frac{2R^n}{R^{2n-1}} = 4\pi \epsilon (d^2 - a^2)^{1/2} \sum_{n=1}^{\infty} \left[ \frac{1}{R^{n+1}} + \frac{1}{R^{n-1}} \right]$$

$$\frac{dc}{dg} = 8\pi \epsilon \sum_{n=1}^{\infty} \frac{R^n}{R^{2n-1}} \left( \frac{R^{2+1}}{R^{2-1}} - n \frac{R^{2n+1}}{R^{2n-1}} \right) \quad 7.3$$

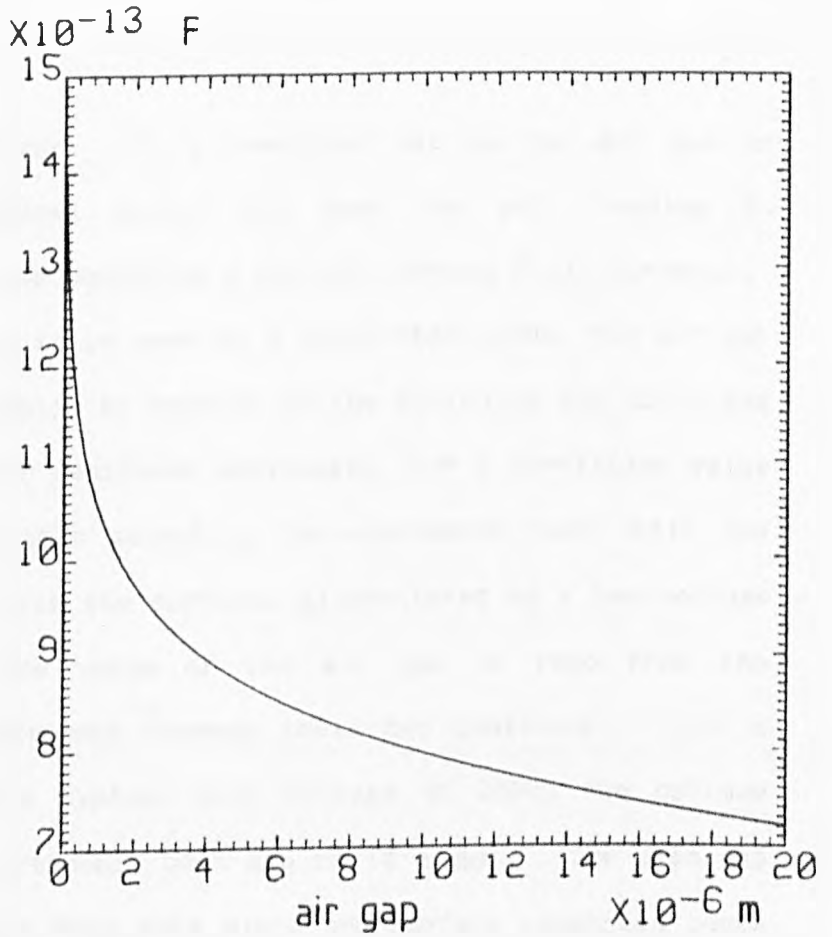
where  $R = d/a + (d^2/a^2 - 1)^{1/2}$ .

In the case of a small gap between the sphere and the plane, where  $(g+a)/a \approx 1$ , the expressions converge slowly, (see Appendix 1 for the numerical details). Fig. 7.2a shows the capacitance evaluated from these expressions for various air gaps, and fig. 7.2b shows the sensitivity, the change in capacitance with air gap, as a

Fig. 7.2

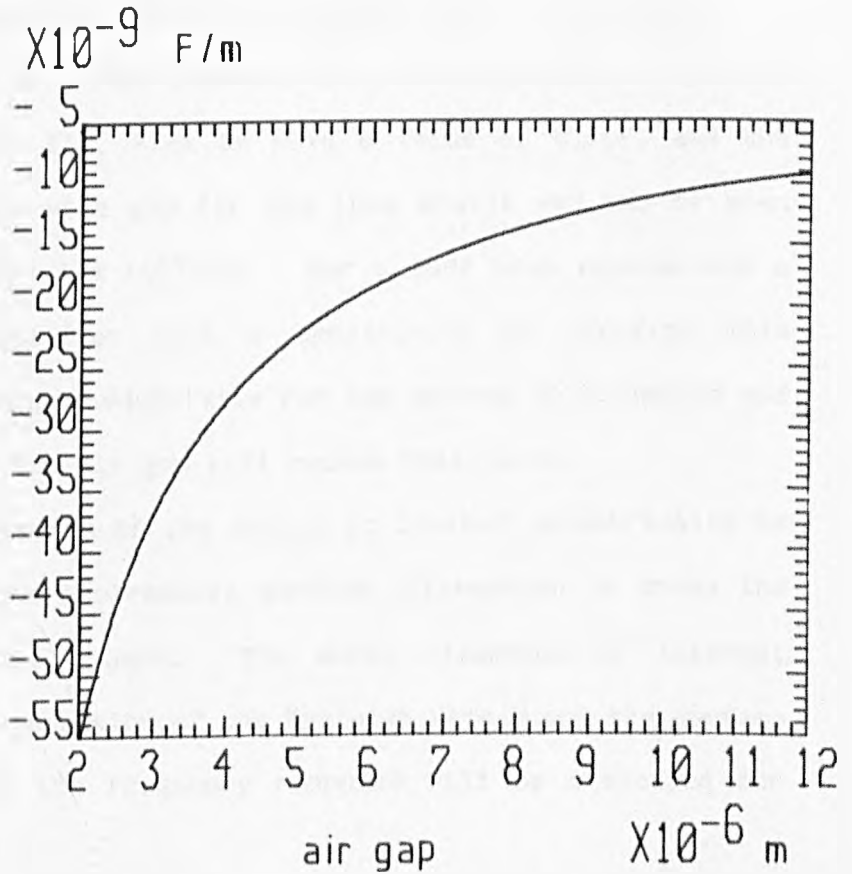
(a)

static capacitance  
of a spherical  
conductor next  
to a plane conductor  
separated by an  
air gap for a 4mm  
diameter sphere.



(b)

sensitivity of  
sphere capacitance  
to small displace-  
ments, for differ-  
ent static air  
gaps.



Capacitance and sensitivity of a sphere/plane capacitor.

function of the air gap. In a practical set up the air gap is narrowed until breakdown occurs and then the ball bearing is withdrawn a little, thus achieving a maximum working field strength.

When the device is to be used as a calibrated probe, the air gap is measured experimentally by setting up the device at the operating position, in the manner mentioned previously, for a particular value of bias voltage, and then adjusting the micrometer head until the sphere makes contact with the surface, as monitored by a low voltage resistance meter. The value of the air gap is read from the micrometer as the difference between these two positions. For a polished surface and a typical bias voltage of 200V, the optimum operating position corresponds to a gap of  $10 \pm 3\mu\text{m}$ . The mean gap is likely to be greater than this since any surface roughness peaks will result in premature contact of the sphere with the surface.

The capacitance of a 4mm diameter ball bearing with a  $10\mu\text{m}$  air gap can be seen from fig. 7.2a to have a value of 0.8pF, and the change in capacitance with gap for the  $10\mu\text{m}$  static gap can be seen from fig. 7.2b to be  $1.1 \times 10^{-8}\text{F/m}$ . For a 200V bias voltage and a charge sensitive amplifier with a sensitivity of 250mV/pc this corresponds to a voltage sensitivity for the device of 0.55mV/nm and any underestimate in the air gap will reduce this value.

The frequency response of the device is limited geometrically by the time taken for the progressive surface deformation to cross the active area under the sphere. The worst situation of interest corresponds to the propagation of the Rayleigh wave along the surface under the sphere and the frequency response will be evaluated for this case.

For small acoustic deformations of the surface relative to the static air gap - nanometres compared to microns - the active area under the sphere will be directly related to the induced charge density on the earth surface of the plane under the sphere. This charge density can be calculated from the method of images, which models the extended charge distribution as being due to an infinite number of point charges at varying distances from the centre of the sphere which maintain both the surface of the sphere and the plane as equipotentials.

The charge distribution for a plane separated from a sphere is equivalent to two spheres separated by twice the distance. The image charge distribution will maintain both the spheres and the mid-plane as equipotentials, fig. 7.3a (Page and Adams, 1969). A charge  $q$  is placed at the centre of sphere 1 and gives an equipotential surface at  $r = a$  on sphere 1 but not along the plane AB. A charge of  $-q$  at the centre of sphere 2, in conjunction with the first charge, will give the plane AB as equipotential but not the spherical surface  $r = a$  on sphere 1. Adding another charge,  $q_1$ , the image of  $q$  in sphere 1 restores the spherical surface as an equipotential but disturbs the plane. The process may be continued indefinitely to give both the sphere and the plane as equipotential. The following image charges and their positions are obtained

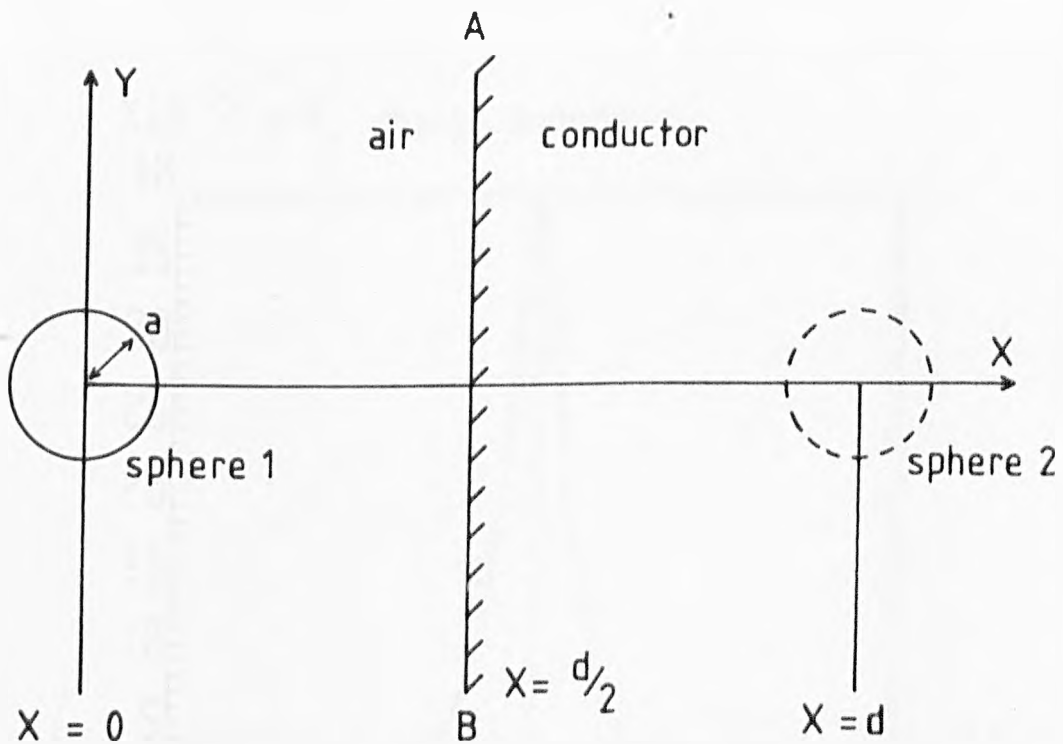
$$q \quad \text{at} \quad x = 0$$

$$q_1 = a/d \, q \quad \text{at} \quad x = a^2/d$$

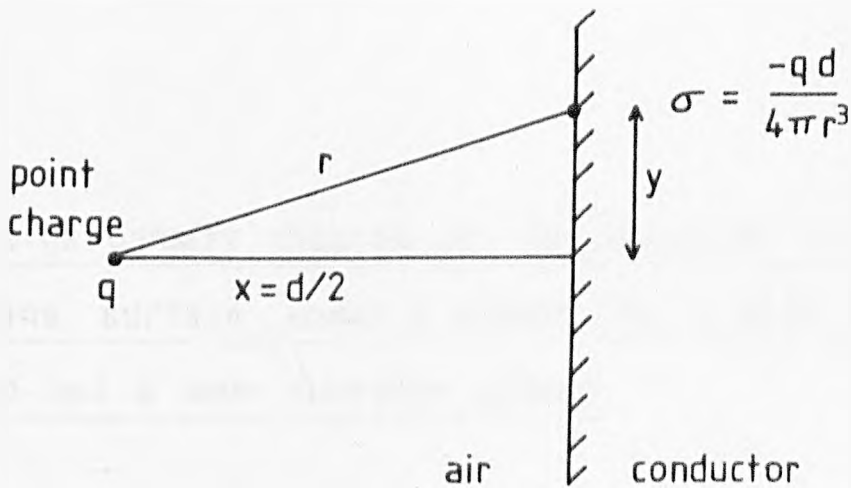
$$q_2 = m^2/1-m^2 \, q \quad \text{at} \quad x = ma/1-m^2$$

**PAGE(S) MISSING IN  
ORIGINAL**

Fig. 7.3

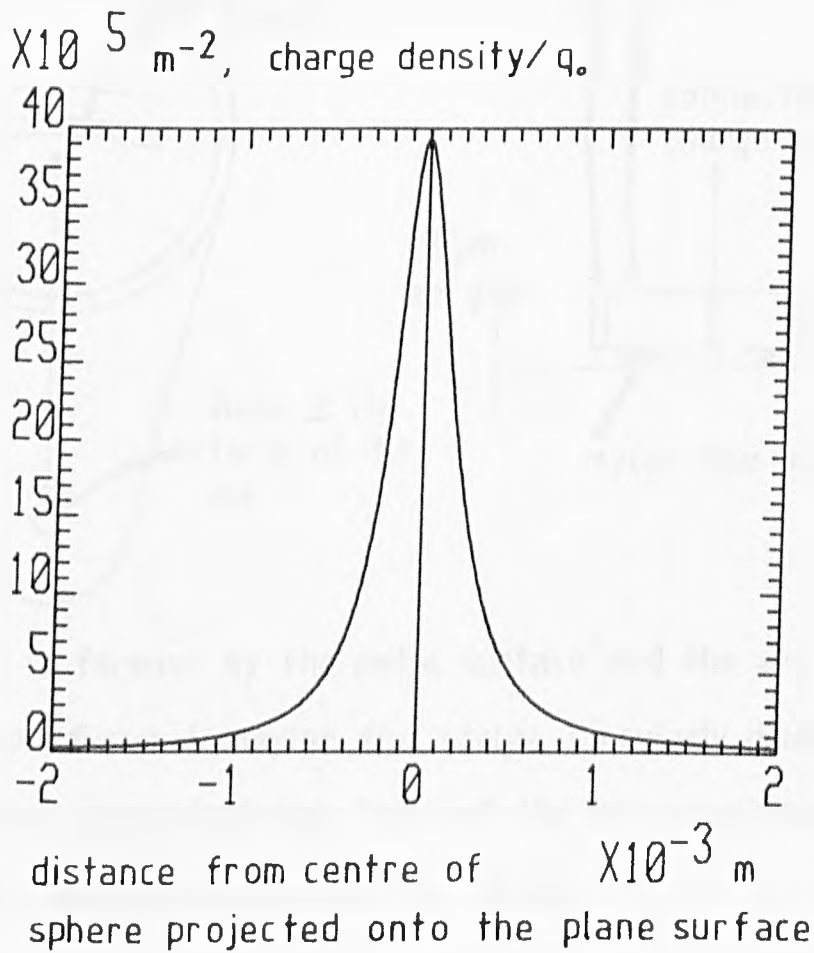


- (a) The image system for calculating the point charge distribution equivalent to a charged sphere next to a plane.



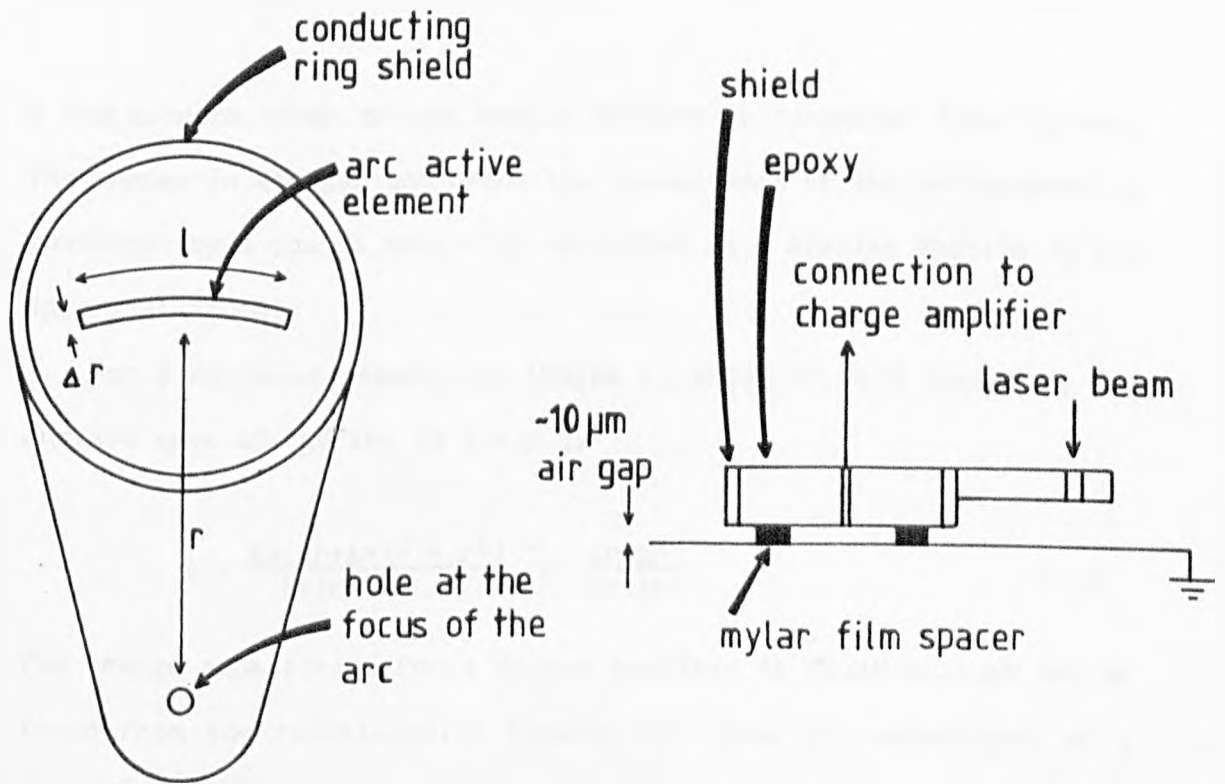
- (b) The charge density induced on the surface of a plane due to a point charge  $q$ , at a distance  $r$ .

Fig. 7.4

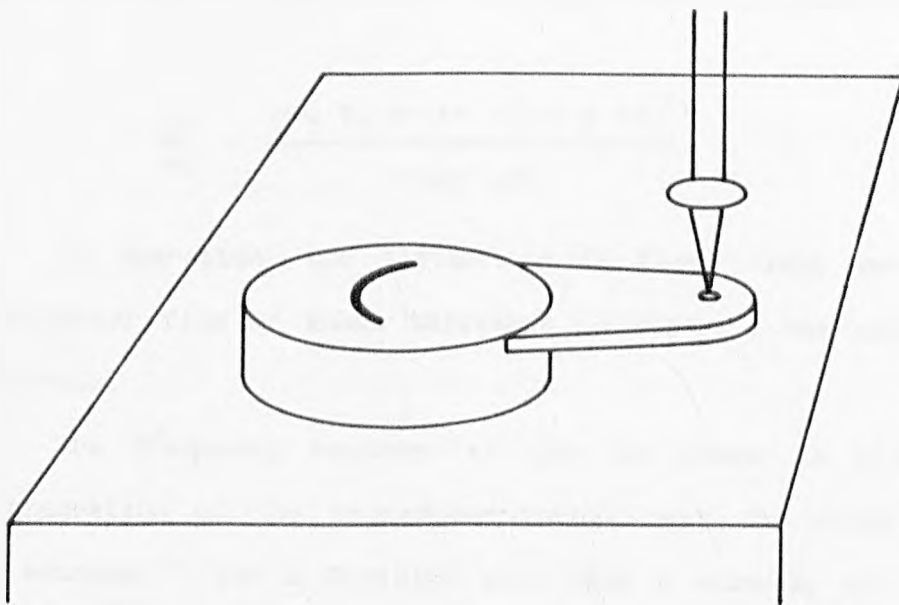


Charge density induced on the mid-line of the  
plane surface under a sphere for a  $10\mu\text{m}$  air  
gap and a  $4\text{mm}$  diameter sphere.

Fig.7-5



A capacitor is formed by the metal surface and the arc element with an air gap produced by mylar film strips. Circularly diverging acoustic surface waves created at the focus of the arc vary the air gap and consequently the capacitance of the device.



The arc capacitance transducer.

a few microns clear of the sample surface by polyester film spacers. The change in air gap and hence the capacitance of the arrangement is monitored by a charge sensitive amplifier in a similar fashion to the spherical probe.

For a circular segment of length  $l$ , width  $\Delta r$ , and radius  $r$ , the surface area of the arc is given by

$$A = \frac{l\pi((r+\Delta r)^2 - r^2)}{2\pi(r+\Delta r)} = \frac{l r \Delta r}{(r+\Delta r)} \quad 7.10$$

The charge sensitivity for a device operated at fixed voltage may be found from the relationships between the area and capacitance of a plane parallel capacitor

$$\frac{dq}{dg} = \frac{-\epsilon V_0 l r \Delta r}{(r+\Delta r) g^2} \quad 7.11$$

Where  $V_0$  is the bias voltage and  $g$  is the gap between the arc element and the surface of the sample. The voltage sensitivity, when using a charge sensitive amplifier producing 250mV/pc, is given by

$$\frac{dv}{dg} = \frac{-\epsilon V_0 l r \Delta r \times 2.5 \times 10^{-11}}{(r+\Delta r) g^2} \quad 7.12$$

In operation, the distance  $g$  is fixed using small strips of polyester film of known thickness to separate the sample from the surface.

The frequency response of the arc probe is limited by the integration of the transducer output over the width of the arc electrode. For a Rayleigh wave with a velocity of  $3.2 \times 10^3 \text{ms}^{-1}$ , travelling across the active element 0.25mm wide, the bandwidth of the device will be limited to approximately 13MHz.

## 7.2 ELECTRO-MAGNETIC ACOUSTIC TRANSDUCERS

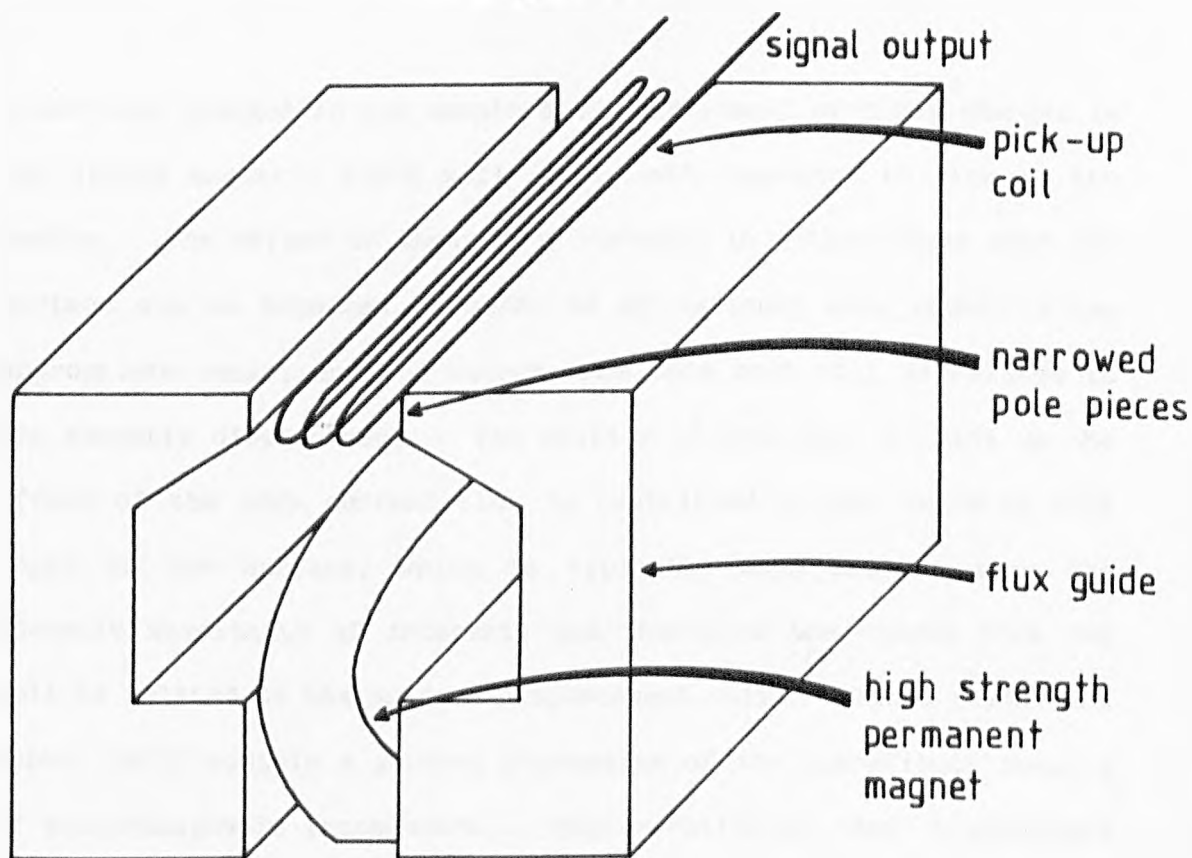
The main advantage of the electro-magnetic acoustic transducer (EMAT) lies in the fact that this device is non-contacting. Piezoelectric devices require acoustic bonding to the sample to be tested and this leads to disadvantages discussed previously. Capacitance devices are non-contacting but require very close proximity to the sample surface of the order of tens of microns. EMAT devices also require some degree of proximity to the sample surface in order to operate efficiently, but the limitations are not as stringent as those required for capacitance transducers. EMATs can operate with transducer-sample gaps of the order of millimetres. This non-contact operation is advantageous since the speed of scanning a sample need no longer be controlled purely by the mechanical considerations of maintaining acoustic contact with the sample surface.

The main disadvantage of the EMAT is its relatively low efficiency in comparison with piezoelectric devices, and the complex nature of the generating mechanism limits its usefulness as a calibrated, displacement transducer.

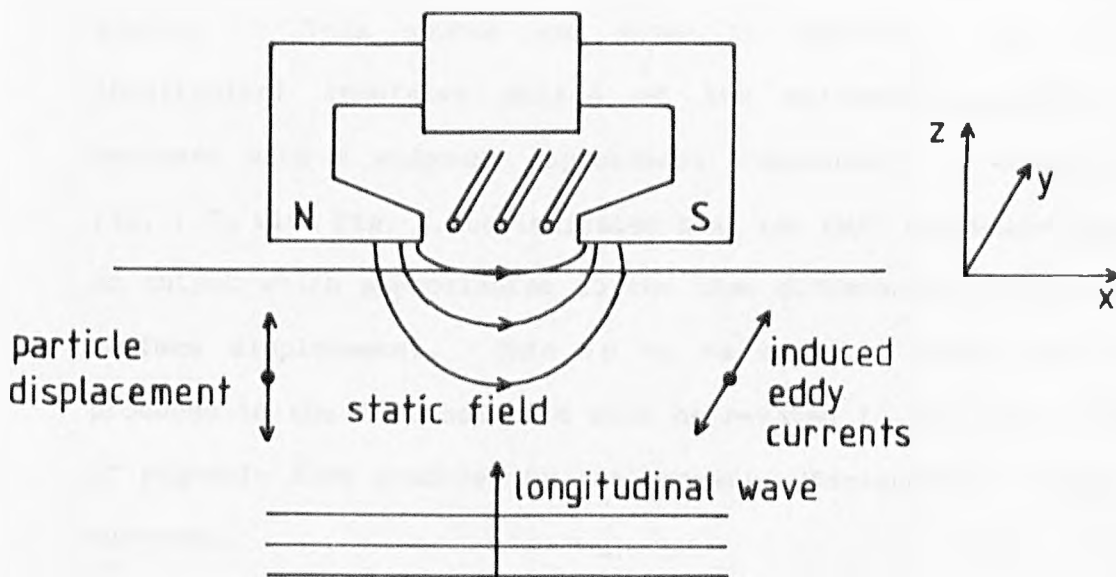
Some commercially available EMAT transducers were tested for their suitability but failed to produce the required bandwidth or sensitivity to perform the C-scan experiments described in Chapter 8. EMAT transducers were then constructed using high strength permanent magnets in the simple design shown in fig. 7.6 (Levett, 1984).

A permanent magnet produces a static magnetic field which is directed through the surface of the non-magnetic, electrically conducting sample. An acoustic wave will cause a displacement of the

Fig.7.6



Acoustic particle displacements in the static magnetic field create eddy currents which induce currents to flow in the pick-up coil.



Electro-Magnetic Acoustic Transducer sensitive to longitudinal acoustic wave motion.

electrical charges in the sample and the movement of these charges in the static magnetic field will induce eddy currents to flow in the sample. The effect of these eddy currents in a thin layer near the surface can be detected by means of an external coil wound in the appropriate sense, and the output from this coil will be related to the acoustic displacement. The ability of this coil to pick up the effect of the eddy current flow is restricted to the magnetic skin depth at the surface, which is typically much smaller than the acoustic wavelength of interest, and therefore the output from the coil is related to the surface displacement only. Szilard (1982) and Dobbs (1973) contain a general discussion of the operational details of electromagnetic transducers. The operation of these transducers on magnetic materials must include the effect of magnetostriction within the sample (Silk, 1984).

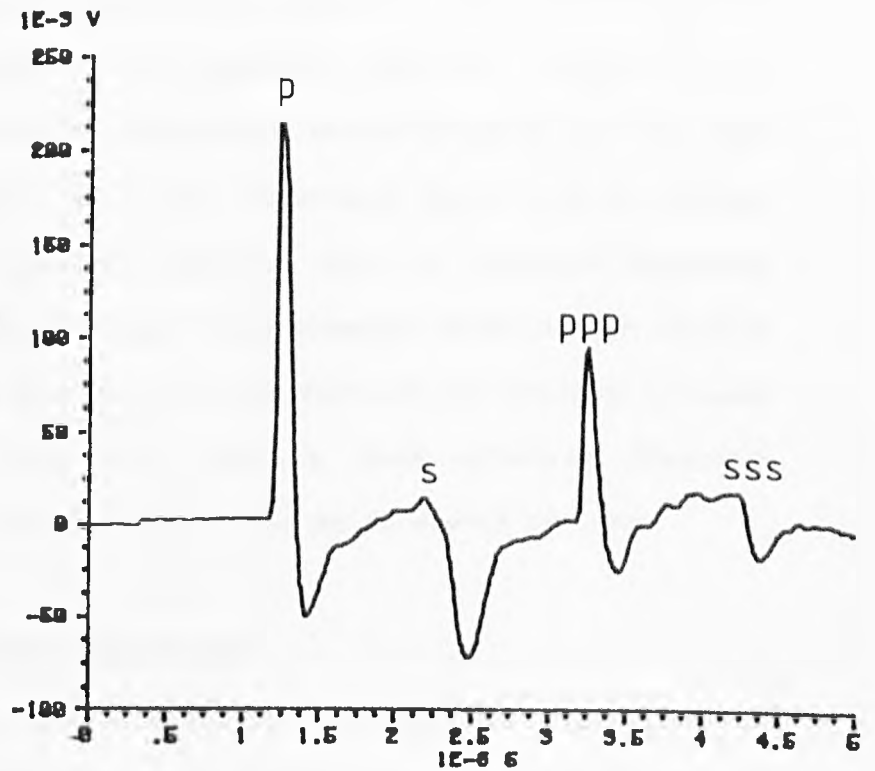
The output from an EMAT device operated on an aluminium plane, 6mm thick, is shown in fig. 7.7a for the laser generated oil ablation source. This source was shown in Chapter 4 to produce a longitudinal impulsive motion of the epicentre position, when measured with a wideband capacitance transducer. A comparison of fig. 7.7a with fig. 4.26c indicates that the EMAT transducer produces an output which approximates to the time differential of the actual surface displacement. This is to be expected since the voltage produced in the EMAT solenoid will be related to the rate of change of magnetic flux produced by the acoustic displacement induced eddy currents.

The frequency response of the device is difficult to deduce since it will be geometrically limited by the active area over which the EMAT solenoid can detect eddy current fields, and this will vary with

Fig.7.7

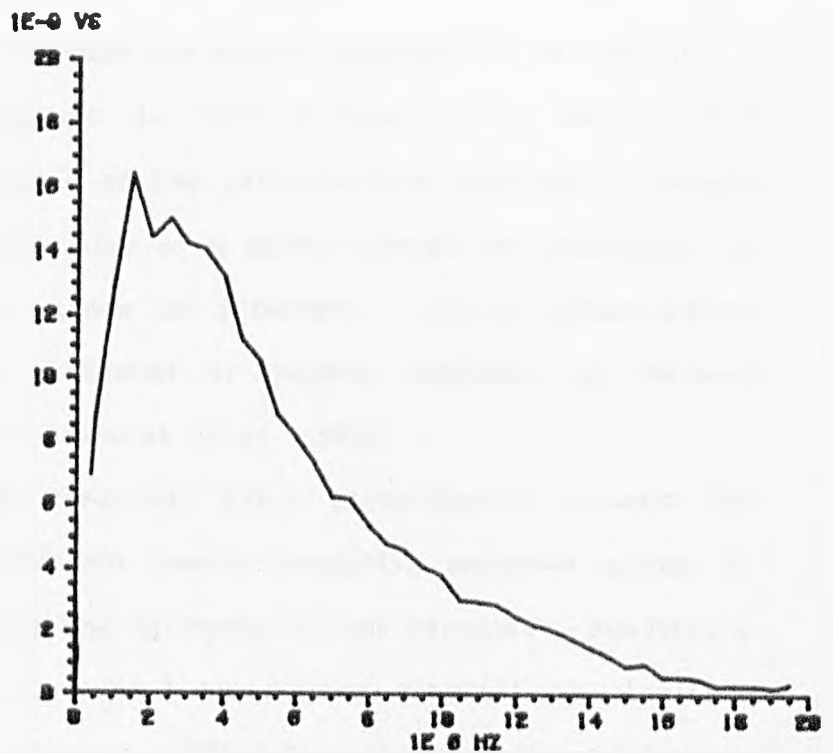
(a)

experimentally  
determined epicentre  
impulse response  
of a 6mm thick Al.  
plate using the  
oil-ablation source  
and the EMAT



(b)

FFT of the impulse  
response data  
showing the system  
frequency response



Impulse and frequency response of the EMAT system.

both the static magnetic field distribution and the gap between the surface and the solenoid. The intrinsic frequency response of the device will depend on the electrical characteristics of the EMAT solenoid in combination with the associated amplification system. Experimentally the EMAT was found to have an adequate frequency response for the "time-of-flight" measurements described in Chapter 8. Fig. 7.7b shows the Fourier transform of the impulse produced epicentre response, fig. 7.7a, and it shows detected frequency components extending from the KHz region to in excess of 6MHz.

### 7.3 THICK PIEZOELECTRIC TRANSDUCERS

The resonant nature of standard piezoelectric transducers is produced by the successive reflections from the boundaries of acoustic waves within the active element. The resonance can be reduced by the use of suitable backing materials on the active element to effectively broaden the useful bandwidth of the device.

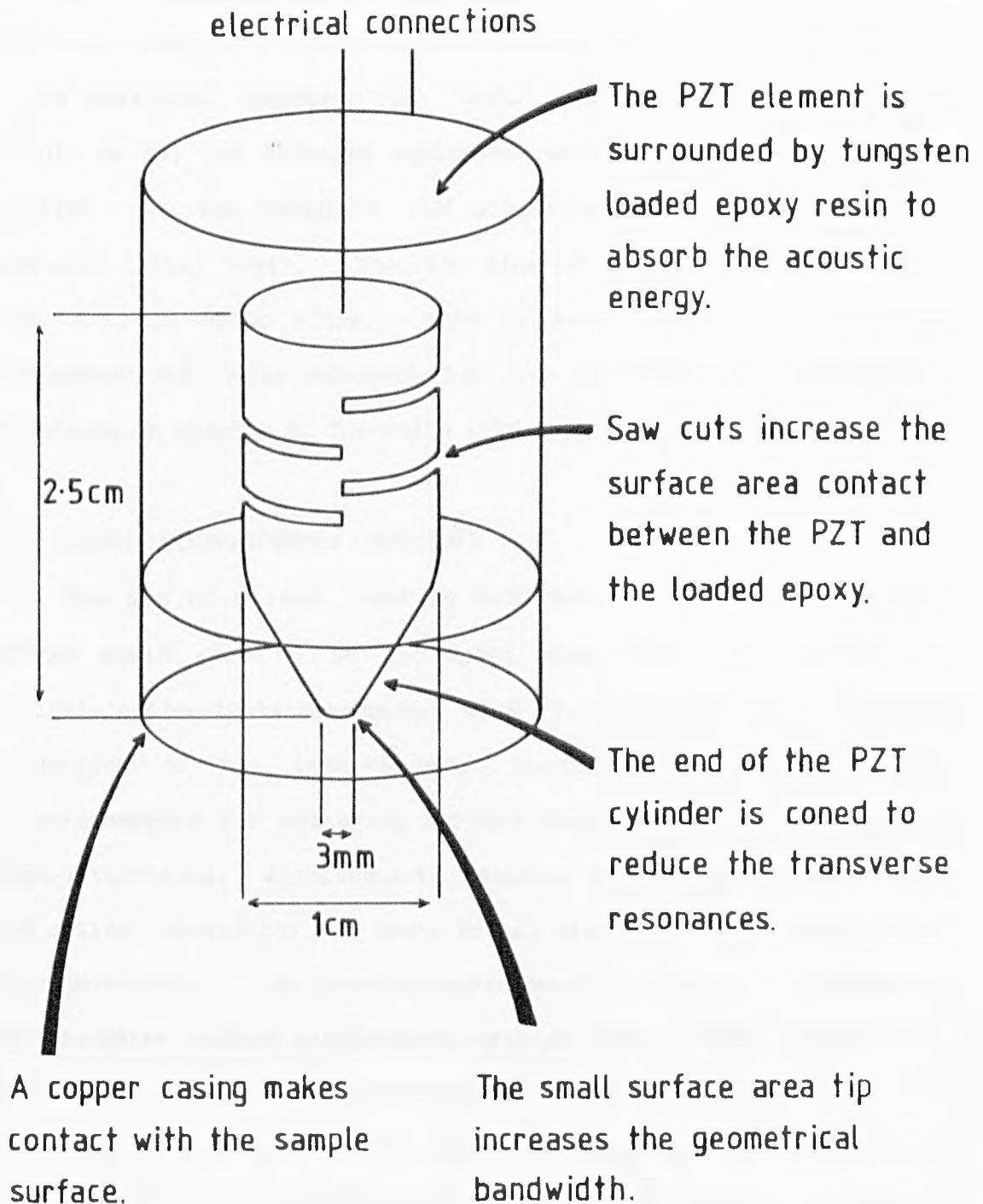
An alternative approach to this problem is to use a thick transducer. The thickness of the piezoelectric material is chosen such that the propagation time of a pulse through the transducer is greater than the time window of interest. Thick piezoelectric transducers have been evaluated by several authors, eg. Redwood (1961); Baboux (1977); Dewhurst et al (1983).

In the form of an isolated, thick piezoelectric element the transducer remains a resonant device producing repeated echoes at time intervals defined by the thickness of the element. However, a large element may be surrounded by damping material to eliminate these echoes. This arrangement differs from the technique of damping the higher resonant frequency transducers in that a substantial

amount of damping material may be placed along the length of the transducer so removing the acoustic energy efficiently within one traversal of the acoustic pulse along the element. This damping is achieved by using the construction shown in fig. 7.8. The active element consists of a 2.5cm by 1cm cylinder of poled PZT obtained from AMTE, Holton Heath. The end of this cylinder was ground into a conical shape for two purpose; firstly, the end of the cone has a small surface area - 2mm diameter - which makes acoustic contact with the sample surface, and this increases the geometrical bandwidth of the device; secondly, the acoustic pulse which propagates into the device cannot reflect back to the element tip to generate spurious echo signals from this coned sidewall. The remaining cylindrical section at the opposite end of the transducer contains several saw-cuts; these cuts and most of the element are surrounded by tungsten loaded epoxy resin. The epoxy resin contains sufficient tungsten powder to match the acoustic impedance of the PZT element to the surrounding composite material (given by approximately a 5:1 ratio by weight of tungsten powder to araldite epoxy). Acoustic energy travels along the transducer and is absorbed by the highly attenuating tungsten-epoxy composite along all the boundaries of the sidewall and saw-cuts, thus preventing the acoustic pulse from reaching the backwall where it would generate an undesirable signal at the electrode. Electrical connections are made to the electrode on the backface of the element and to the copper container which itself makes electrical contact with the surface of the metallic sample.

The signal produced by this transducer for the laser-oil ablation source on the epicentre of a 1cm aluminium plate is shown in

Fig. 7-8



The thick piezoelectric wideband transducer.

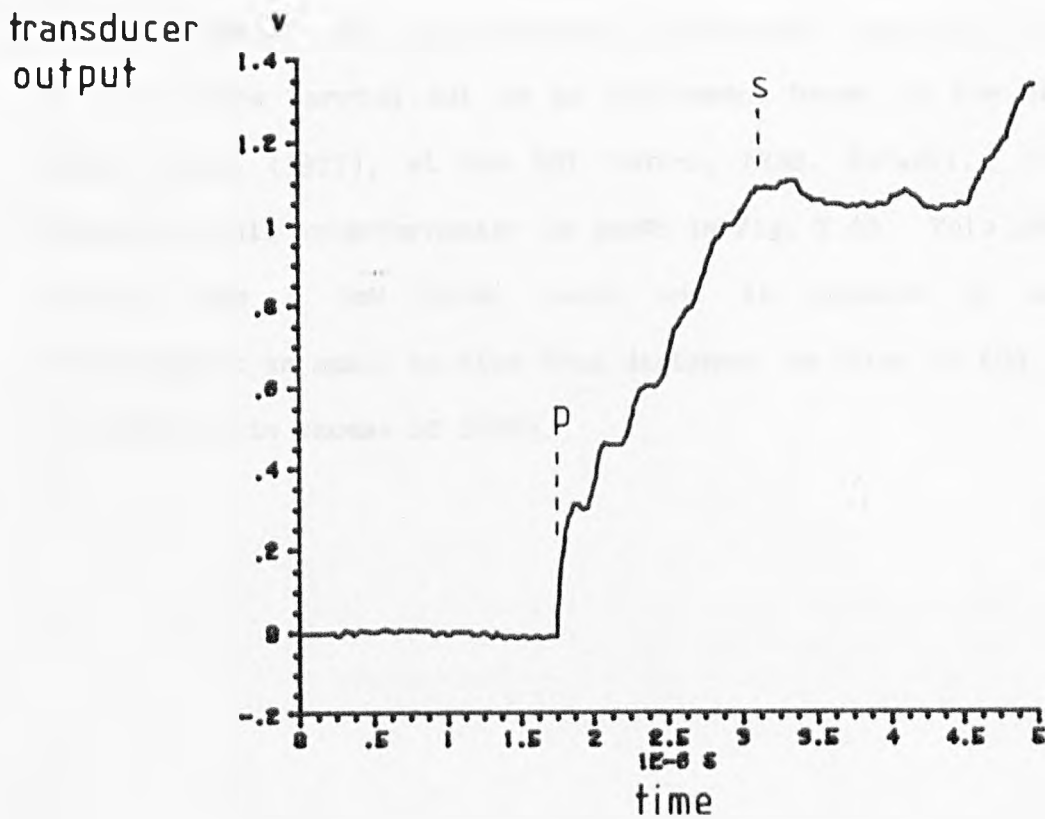
fig. 7.9. A comparison of this waveform with that measured by a capacitance transducer for the same source, fig. 4.26c, shows that the thick PZT transducer produces an output which is consistent with the time integral of the surface displacement, ie. the form of the plate Heaviside response, fig. 4.18. It is not clear why this should be so; no detailed equivalent model of the device has been studied, eg. the Mason or KLM piezoelectric equivalent response circuits (Silk, 1984). The rise time of the longitudinal arrival, fig. 7.9, is about 120ns; this is slower than the capacitance transducer but quite adequate for the laser-acoustic experiments, described in Chapter 8, for which this transducer was used.

#### 7.4 LASER INTERFEROMETER DETECTORS

The use of a laser beam to both generate and detect acoustic energy would seem to be the ideal combination in providing an entirely non-contacting technique with all the versatility and unique properties of the laser-acoustic source. The use of laser interferometers for measuring surface displacement is a relatively common technique; displacements measured are generally larger than the optical wavelength and there is not always the requirement for a wide bandwidth. An interferometer must be capable of measuring sub-nanometre surface displacement with at least a 10MHz bandwidth to be a useful device in conjunction with the laser-acoustic source.

Using a light from a He-Ne laser operating at 633nm requires the interferometer instrumentation to be capable of detecting 1/3000 of one fringe shift or a heterodyne beat frequency of about 5MHz with an interferometer bandwidth of 20MHz. Devices capable of measuring these small surface displacements with more than adequate bandwidth

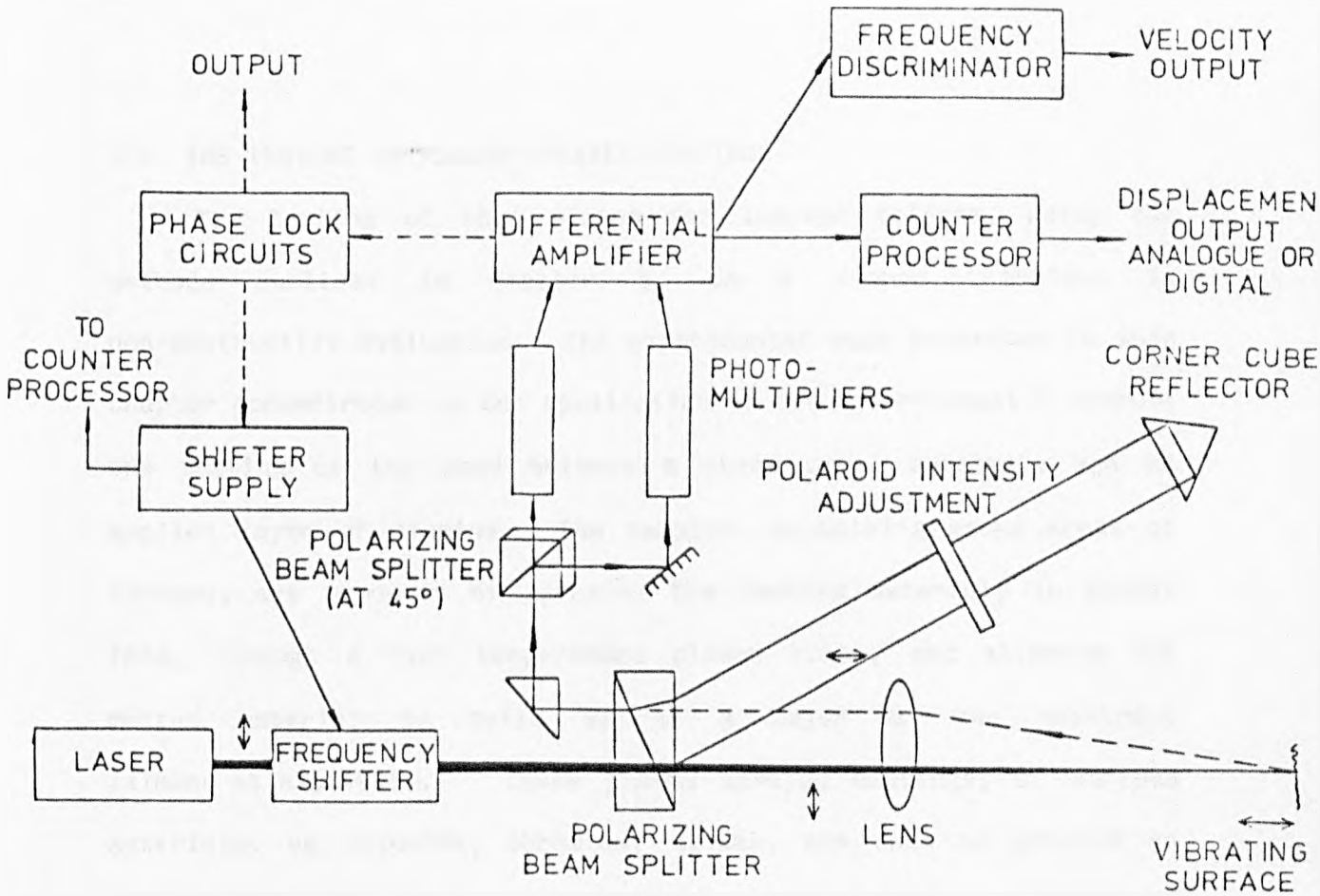
Fig. 7.9



Experimentally determined epicentre response of a 1cm thick aluminium plate using the oil ablation source and the thick piezoelectric transducer.

have been constructed (eg. Bondarenko 1976; Drain 1977; Hutchins 1983). The interferometer experiments reported in Chapters 8 and 9 were carried out on an instrument based on the design of Drain et al (1977), at the NDT Centre, AERE, Harwell. The basic design of this interferometer is shown in fig. 7.10. This particular device uses a 5mW He-Ne laser and is capable of measuring displacement as small as 10pm from distances as large as 60m and with a bandwidth in excess of 20MHz.

Fig. 7-10



An interferometer design for detecting sub-nanometre, ultrasonic surface displacements, (Drain et al., 1977).

## CHAPTER 8

## LAMINAR DEFECT TESTING

## 8.1 THE TESTING OF PLASMA-SPRAYED COATINGS

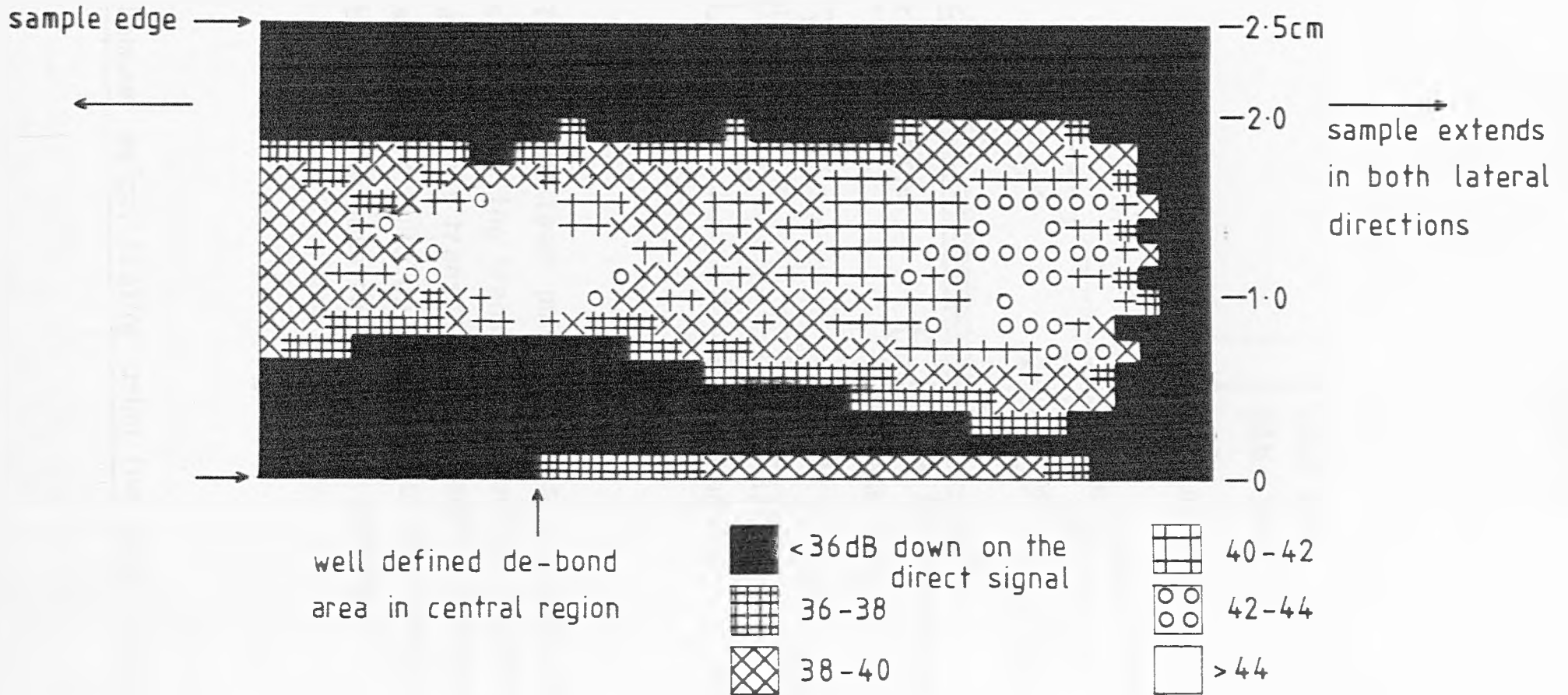
The testing of thin plates for laminar defects, using the methods outlined in Chapter 6, is a common technique in non-destructive evaluation. The experimental work presented in this chapter concentrates on one application of the laser-acoustic source; the testing of the bond between a sheet metal substrate and an applied layer of alumina. The samples, containing known areas of de-bond, are produced by spraying the coating material, in powder form, through a high temperature plasma flame, and allowing the molten material to build up as a layer on the substrate (Almond et al, 1981). These plasma sprayed coatings, of various materials, eg. alumina, chromium, nickel, are used to provide an inert coating for components which are to be used in corrosive or abrasive environments. The integrity of the bond between the coating and the substrate must be monitored, and this presents difficulties for conventional techniques, the alumina coating is granular in its composition with a rough finished surface. This makes it difficult to obtain any acoustic bond between a conventional piezoelectric transducer and the surface, and for the purpose of obtaining an accurate C-scan, it is necessary that the acoustic bond is reproducible in its acoustic properties. There is also the problem that, because of its granular nature, the coating layer is highly attenuating to ultrasound and it is therefore necessary to have an

efficient coupling of acoustic energy into the layer.

In the past, samples have been tested for de-bond areas using piezoelectric probes and water-bath immersion, C-scan equipment. The technique involves immersing the sample, transmitting and receiving transducers in a water-bath to provide efficient and reproducible acoustic coupling into the sample (Almond et al, 1981). The technique cannot be readily applied to in situ testing and has limited spatial resolution. However, it provides some comparison for the results of the new technique presented here.

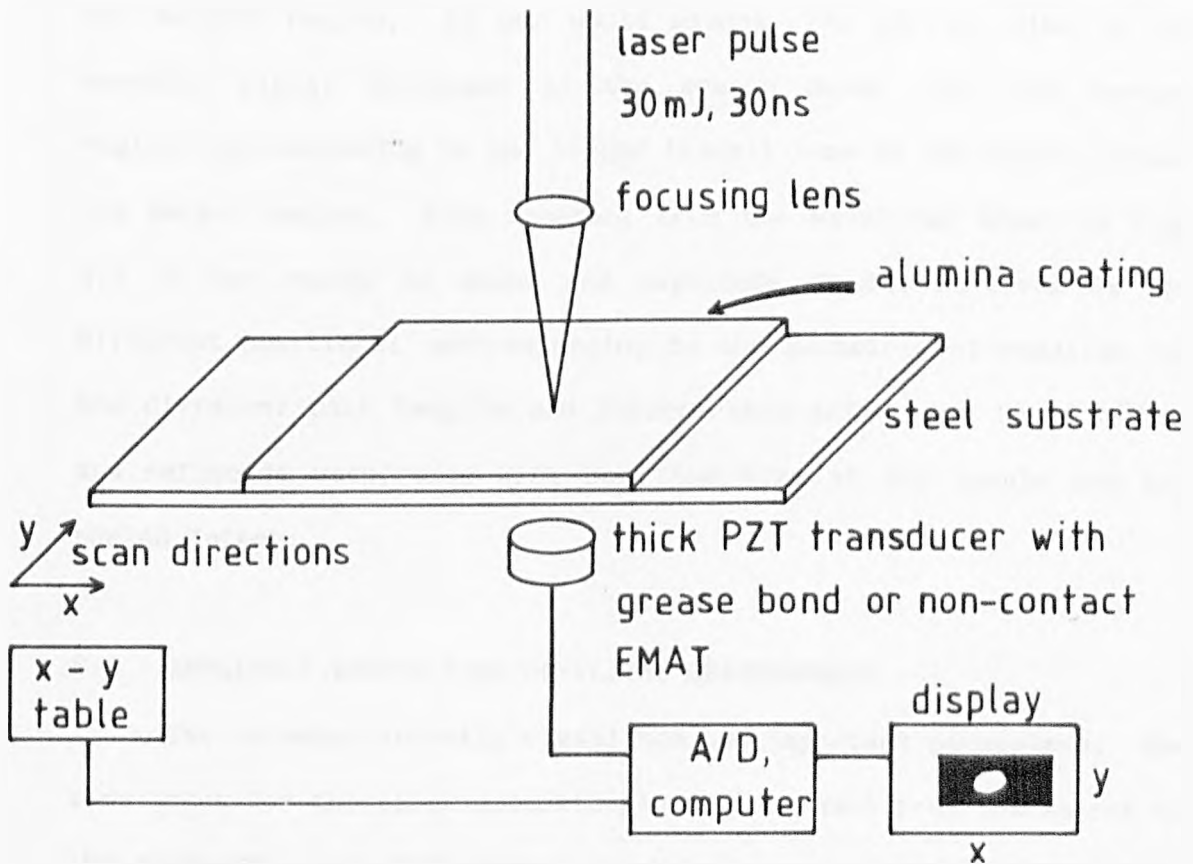
Preliminary experiments were carried out in order to evaluate the application of the laser-acoustic source to this problem. A sample was investigated which consisted of a 3mm thick steel substrate coated with a 0.6mm thick layer of alumina and which contained a known defect region created during the formation of the coating. An immersion scan, using a 10MHz transducer, is shown in fig. 8.1 and depicts an approximately circular region of clearly defined de-bond. A laser pulse was focused onto the alumina coating, creating acoustic transients by material ablation, and the acoustic signal transmitted through the coating and substrate was detected using a co-axial wideband, thick, piezoelectric transducer. This thick PZT transducer (described in Chapter 7) was acoustically bonded to the backface of the metallic substrate using a layer of grease in the basic arrangement shown in fig. 8.2. It was necessary to use the plasma acoustic source in order to generate acoustic transients of sufficient magnitude to be transmitted by the attenuating alumina layer. This focused laser-acoustic source produced negligible damage to the rough alumina surface. The signals detected by the transducer for different source-defect positions are shown in fig. 8.3.

Fig. 8.1



10 MHz immersion, ultrasonic C-scan of an alumina coated steel plate.

Fig. 8.2



The focused laser pulse produces a plasma-acoustic source and the transmitted signal is detected by a co-incident transducer. The sample is mechanically scanned to build up a display of the bond integrity between the substrate and the coating.

Fig. 8.3a shows the detected waveform at the edge of the sample in a well bonded region; fig. 8.3b shows the waveform over the edge of the de-bond area; and fig. 8.3c is the waveform over the middle of the de-bond region. As one would expect, the arrival time of the acoustic signal increases as the source moves over the de-bond region, corresponding to the longer transit time of the signal around the defect region. Also apparent from the waveforms shown in fig. 8.3 is the change in shape and magnitude of the waveform at the different positions, corresponding to the geometric attenuation for the different path lengths and interference effects of the incident and reflected wavefronts with both the edge of the sample and the buried defect.

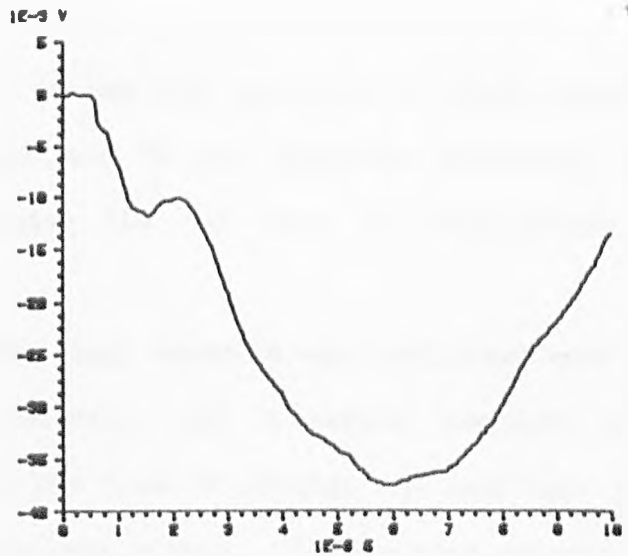
## 8.2 AMPLITUDE VERSUS TIME-OF-FLIGHT MEASUREMENTS

The detected acoustic signal has two important parameters; the time taken for the first acoustic signal to travel from the source to the detector; and the general amplitude variation of the acoustic signal arriving at the detector. An experiment was carried out to compare two sets of data based on these parameters obtained from a scan of an alumina coat de-bond area. An arrangement based on that shown in fig. 8.2 was used to enable the sample to be manually scanned in a raster fashion under the laser and transducer assembly. The waveform at each position was digitised, and information on the two parameters was extracted from the waveform and stored on magnetic disc for later analysis and display by computer. The data acquisition and storage system consisted of a Tektronix 4912 digitiser, capable of producing a 512 by 512 point sampled waveform, a Tektronix LSI-11 based minicomputer and twin 300 kbyte floppy disc

Fig. 8.3

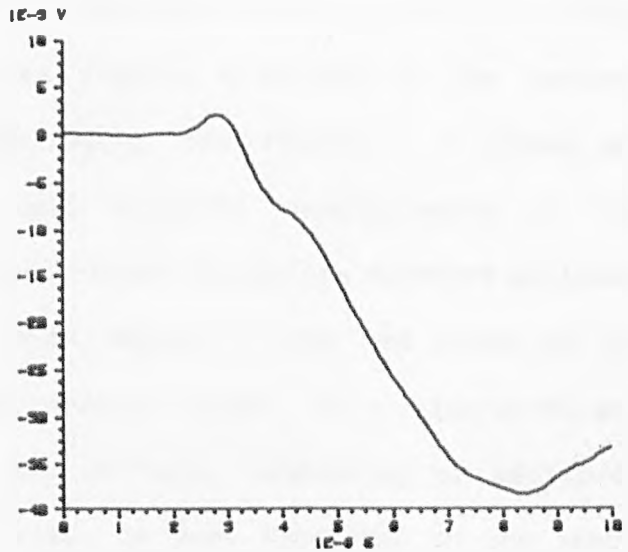
(a)

the thick piezoelectric transducer output for a well bonded region of a plasma-alumina coated steel plate



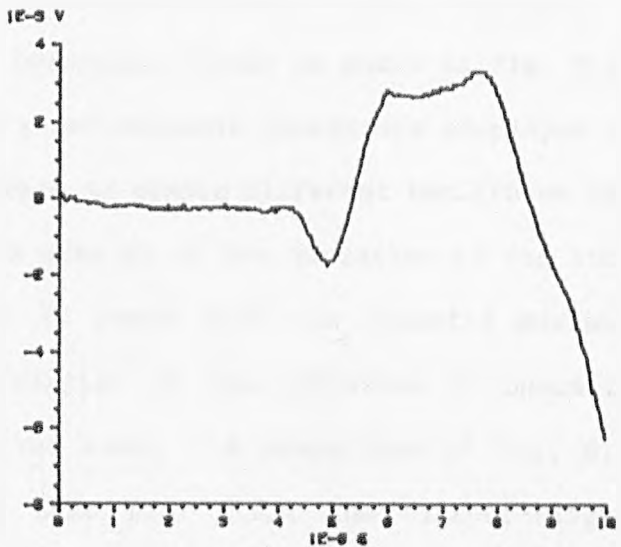
(b)

the transducer output over the edge of the de-bond region



(c)

the transducer output over the central area of the de-bond region



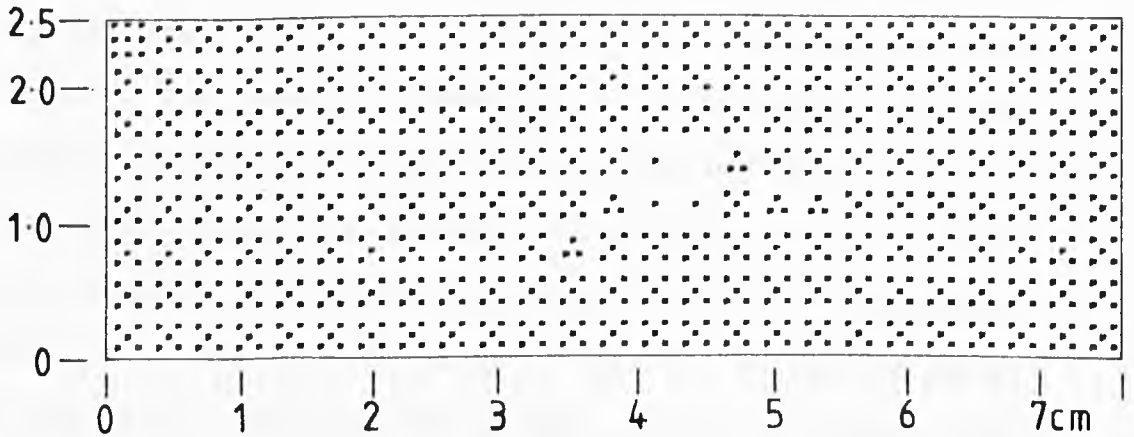
The variation of the transmitted acoustic signal with laminar defect position.

storage. Using this system it was not possible to store entire waveforms for an average scan and it was therefore necessary to reduce the information to give the two sets of characteristic parameters.

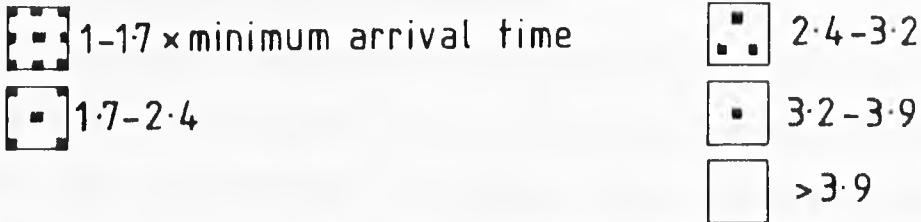
Firstly, the transducer and laser assembly was positioned over a known good region of the material and a sample waveform was recorded. From this waveform the time of arrival and amplitude of the first maximum in the signal was stored. The scanning procedure was then initiated and from the waveform at each position the times taken for the signal to reach various fractions of the maximum amplitude measured over a good region was recorded. A second set of data was recorded from each waveform corresponding to the amplitude of the signal at various times around the expected earliest arrival time recorded over a good region. Thus the first set of data, consisting of different arrival times, is a time-of-flight measurement, and the second set of data, consisting of amplitude measurements at a particular time, is more dependent on the shape variation of the waveform. An alumina coated sample was used in this experiment for which the immersion C-scan is shown in fig. 8.1. The C-scans obtained using the laser-acoustic source are displayed in fig. 8.4 using a simple grey scale to denote different amplitudes and arrival times. Fig. 8.4a is a display of the variation of the time taken for the acoustic signal to reach half its expected maximum amplitude. Fig. 8.4b is a display of the variation in acoustic amplitude at the expected arrival time. A comparison of fig. 8.4 with fig. 8.1 would indicate that fig. 8.4a, the time-of-flight variation measurements, shows the greater correlation, clearly depicting an area of de-bond corresponding to that shown in fig. 8.1

Fig. 8.4

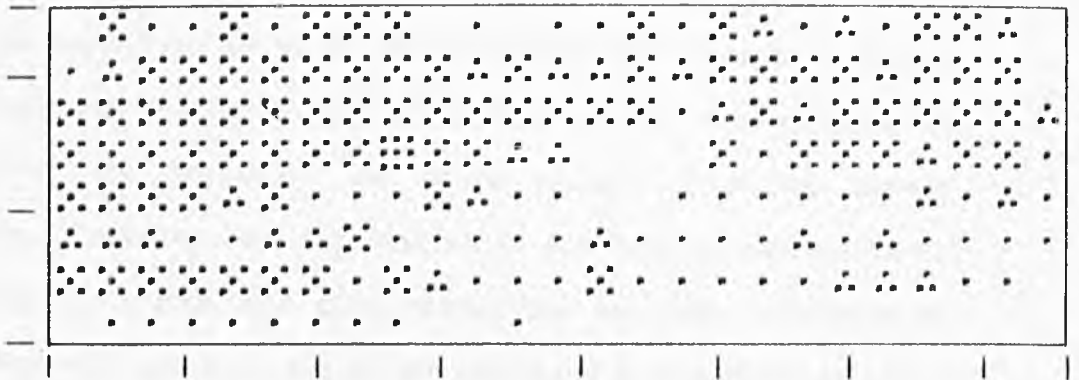
(a)



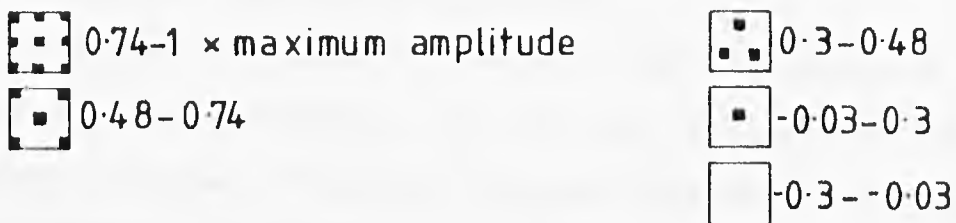
a measure of the time taken for the acoustic signal to reach  
1/2 the maximum amplitude measured in a well bonded region



(b)



a measure of the acoustic signal amplitude at the expected  
arrival time measured in a well bonded region



Amplitude and time of flight C-scans of an alumina coated  
plate using the laser-acoustic source.

for the conventional scan. The results shown in the immersion scan do not give the lateral dimensions of the sample and the correspondence between the de-bond areas has been inferred.

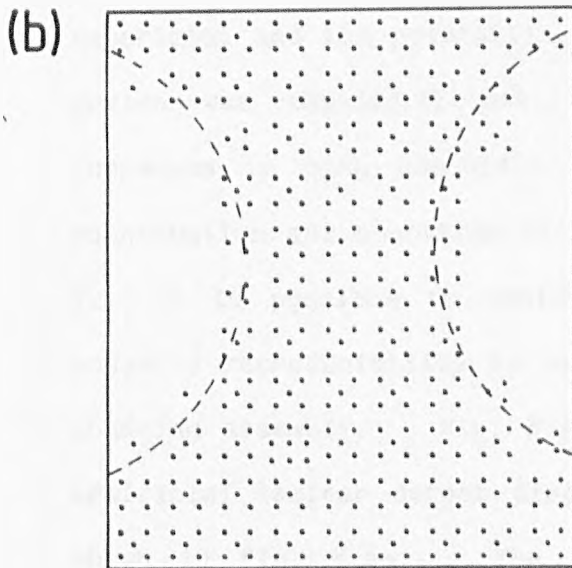
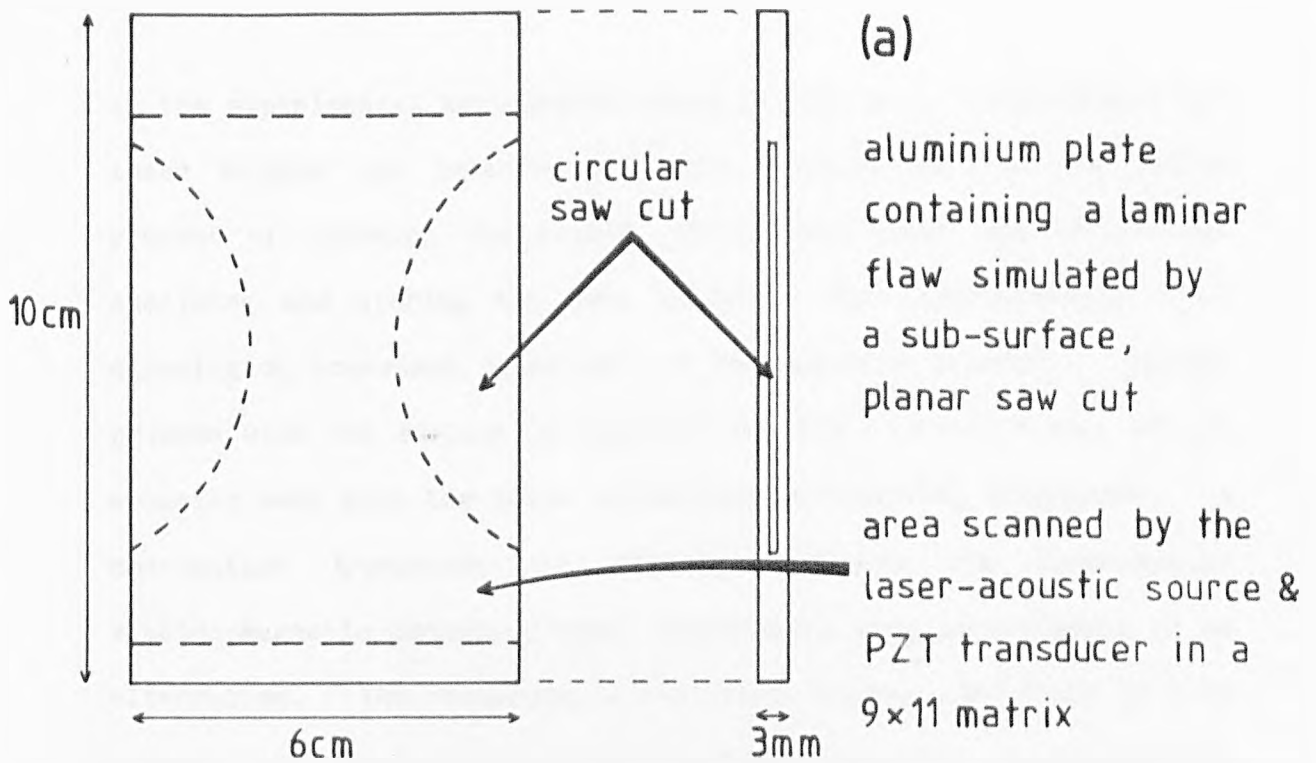
In order to clarify the situation, a laminar defect in a thin plate was simulated by a circular saw-cut, fig. 8.5a. This plate was scanned using the same arrangement used for the alumina coated sample, fig. 8.2. The data sets giving the best correlation with the known defect areas are shown in fig. 8.5b and c. Again it can be seen that the better correlation is given by fig. 8.5b, produced from the time-of-flight information.

A qualitative assessment of the information provided by these two experiments would suggest that, for the simple data gathering methods used, the time-of-flight information gives a greater indication of material integrity for the testing of laminar voids. The overall shape of the waveform, on which the amplitude measurement is based, would provide more information about the interaction because it includes both the amplitude and phase effects from the defect interactions. However, the information is not readily accessible in a simple numerical form and this method has not been investigated further. Emphasis was then placed on improving the system using the time-of-flight information.

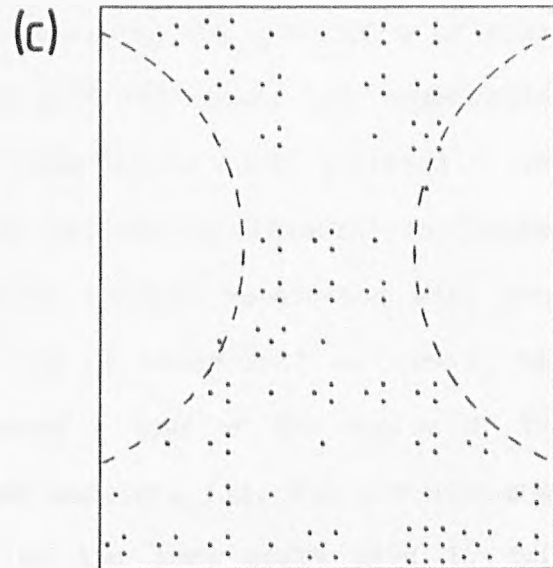
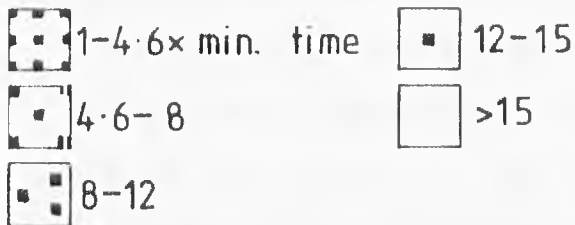
### 8.3 AUTOMATED, TIME-OF-FLIGHT, C-SCANS

Spatial resolution is limited in the laser-acoustic source scans presented previously, by the need to minimise the time consuming process of manually scanning the sample through the laser-detector arrangement. This manual arrangement was replaced by an X-Y translation table operated under computer control as indicated

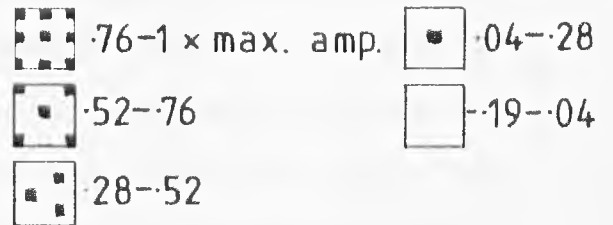
Fig. 8.5



time taken for the signal to reach 1/2 max. expected amplitude



signal amplitude at min. expected arrival time

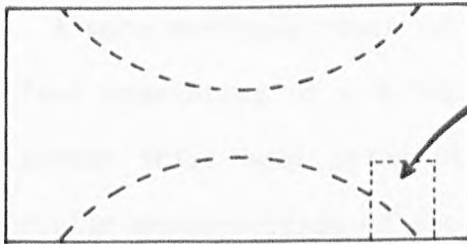


Time of flight and amplitude C-scans of a simulated laminar defect in an aluminium plate.

in the experimental arrangement shown in fig. 8.2. Furthermore the laser trigger was interfaced to the computer so that the entire process of scanning the sample, firing the laser and collecting, analysing and storing the data could be done automatically, thus allowing an increased resolution in the scanning process. Another problem with the earlier arrangement was the reproducibility of the acoustic bond with the thick piezoelectric receiving transducer. A non-contact transducer is ideally required and consequently electro-magnetic acoustic, EMAT, transducers were investigated as an alternative. The commercially available devices were found to have neither the sensitivity nor the bandwidth required to perform the experiment and the possibility of improving the efficiency of these devices was examined (Levett, 1984) with the result that substantial increases in both bandwidth and sensitivity were achieved. The construction and operation of these devices is discussed in Chapter 7. It is possible to achieve high spatial resolution with good acoustic reproducibility by using one of these EMAT devices in the scanning assembly. Fig. 8.6b shows a scan of the region of the artificial laminar defect discussed earlier, fig. 8.5 for the area shown in fig. 8.6a. The key to the grey scale used in this experiment is shown in the figure. The dark area corresponds to an acoustic arrival within one to approximately three times the arrival time in a known good area, and it contains isolated, spurious results due to electrical interference in the sampled waveform. The edge of the saw-cut is delineated by the dramatic increase in the arrival time of the signal. The width of the region over which the time-of-flight signal increases, indicating the edge of the defect, correspond to approximately 3mm or about the thickness of the plate.

Fig. 8·6

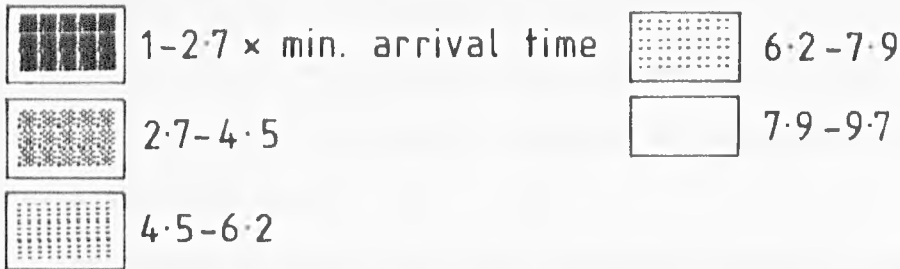
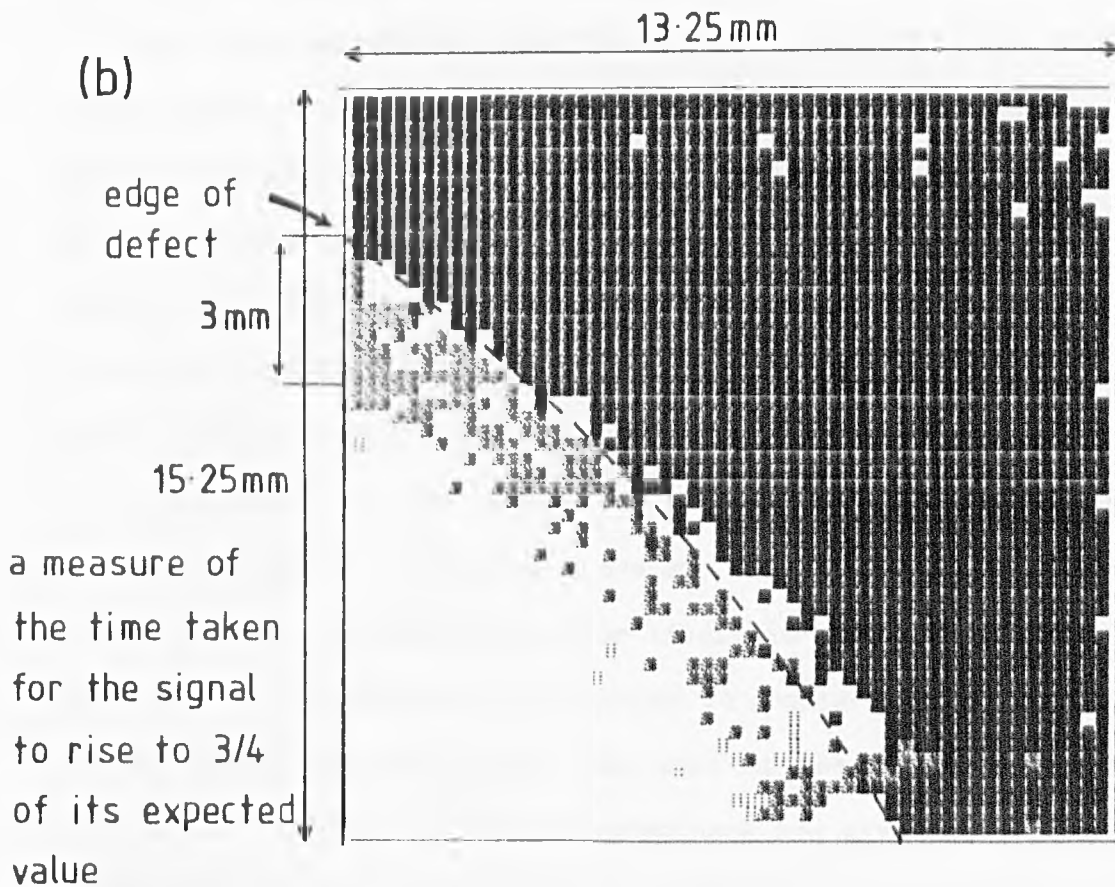
(a)



3mm thick aluminium plate  
containing laminar saw cut

a small region of the  
defect area was scanned  
using the laser-acoustic source  
and the EMAT detector.  
The area is covered by  
a 54×54 matrix of  
laser shots

(b)



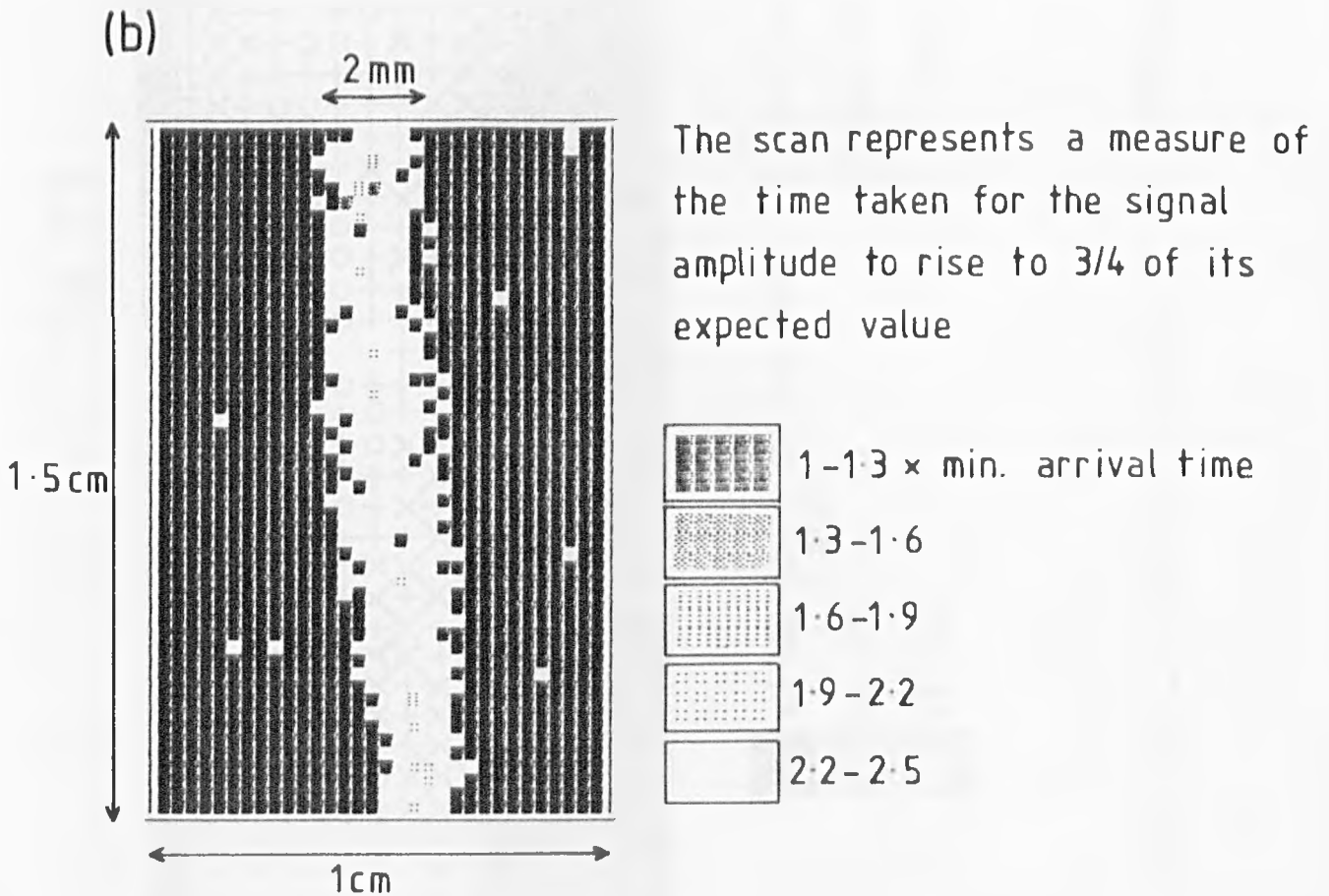
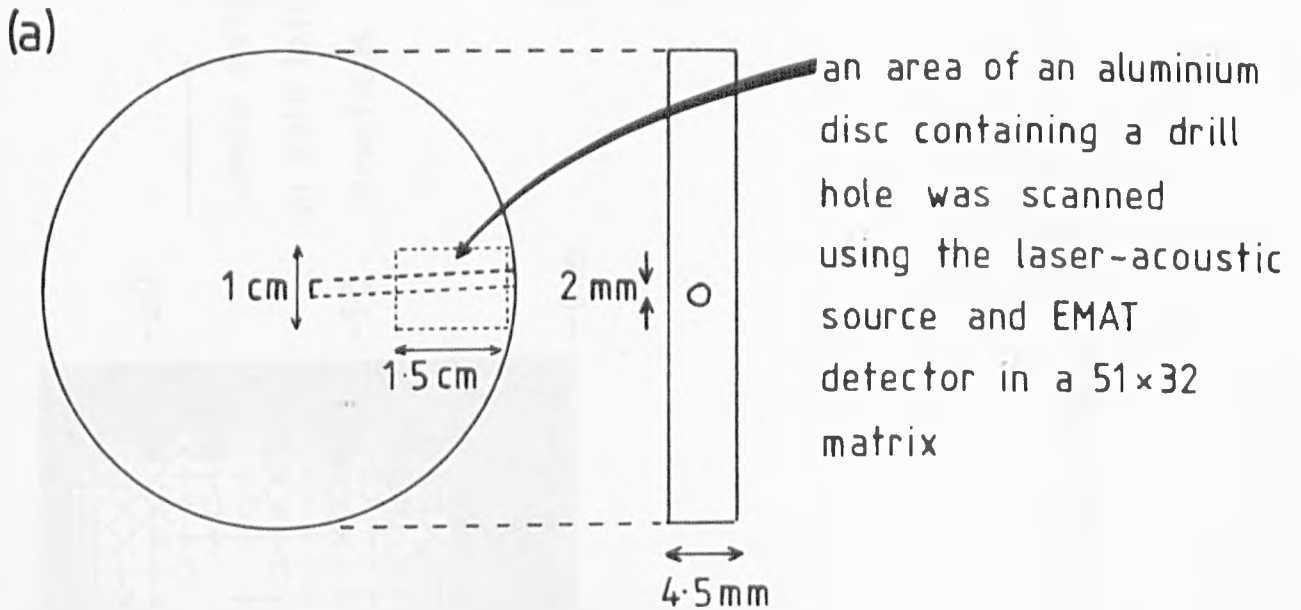
High resolution, automated C-scan of a simulated laminar defect using the laser-acoustic source and EMAT.

A more stringent test of the technique was made on an artificial defect consisting of a 4.5mm thick aluminium plate containing a 2mm diameter drill hole lying planar to the surface, fig. 8.7a. The circular cross-section of the drill hole makes it difficult to detect because the smooth boundary creates the minimum disturbance of the incident acoustic field. The laser-acoustic source C-scan, fig. 8.7b, clearly shows the defect shadow.

The automated C-scan technique employing the EMAT transducer was then applied to the alumina coated plates containing less obvious areas of de-bond. The same arrangement was used for this experiment and the conventional, immersion ultrasonic scan for the sample is shown in fig. 8.8. The sample geometry and laser-acoustic source scans obtained from this sample are shown in fig. 8.9. The de-bond areas, indicated by the conventional scan, fig. 8.8, to the right and down the middle of the sample are evident in fig. 8.9b. It is envisaged that in a practical system, a sample would be coarsely scanned by some optical system for likely de-bond areas, after which any areas of interest would be scanned in greater detail. Fig. 8.9c shows a more detailed scan of the area of the sample indicated in fig. 8.9a. All the scans presented here are given equivalent grey scale definitions corresponding to a division of the measured arrival times into five groups between the minimum and maximum times. The scans may be shown in varying degrees of contrast by altering the grey scale divisions.

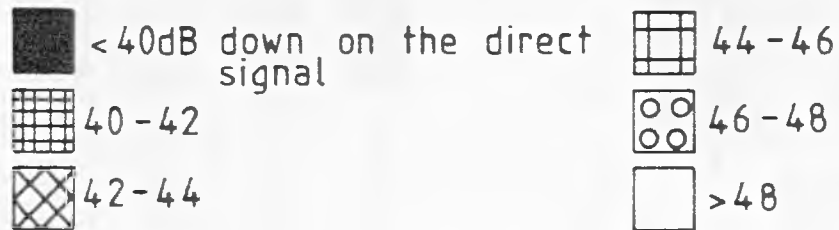
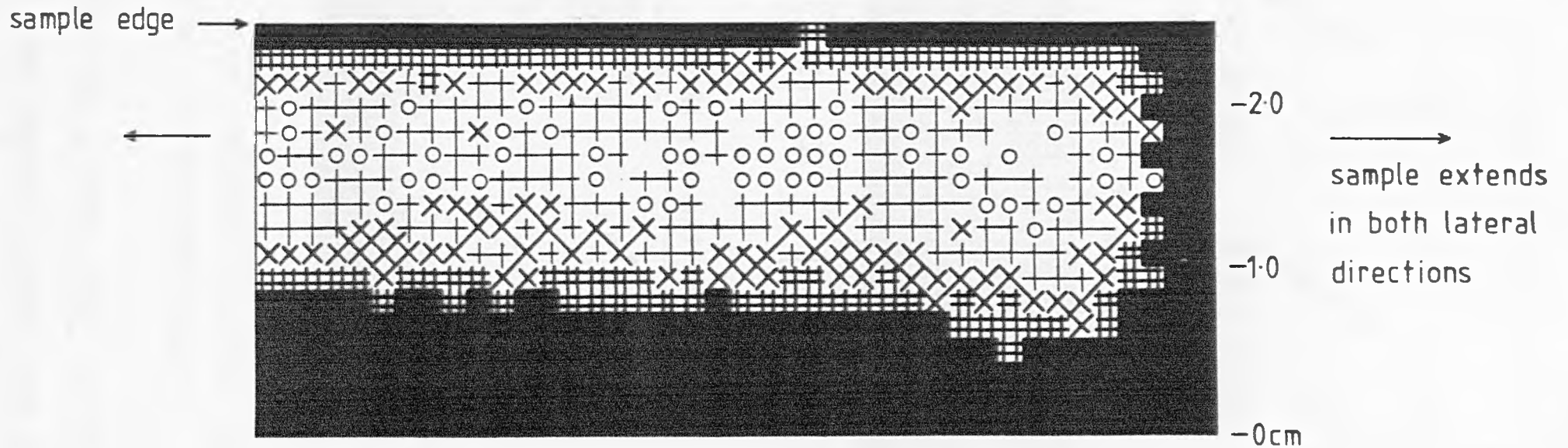
The dominant feature of both the scans shown in fig. 8.9 is the overall, gradual retardation of the signal arrival, from the bottom to the top of the scan. On examination of the sample, this retardation was found to correspond to an increase in thickness of

Fig. 8.7



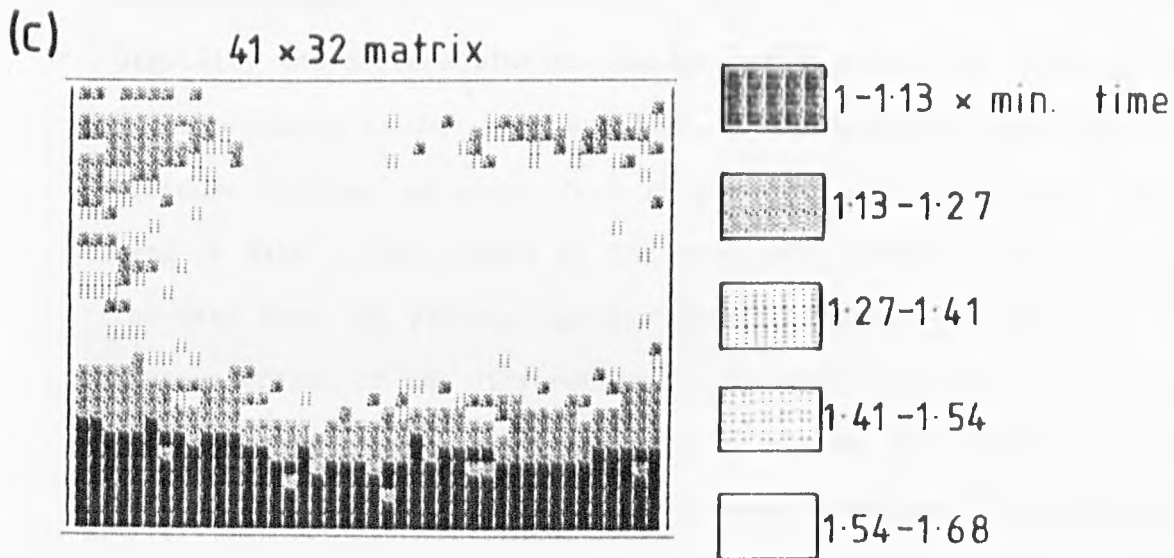
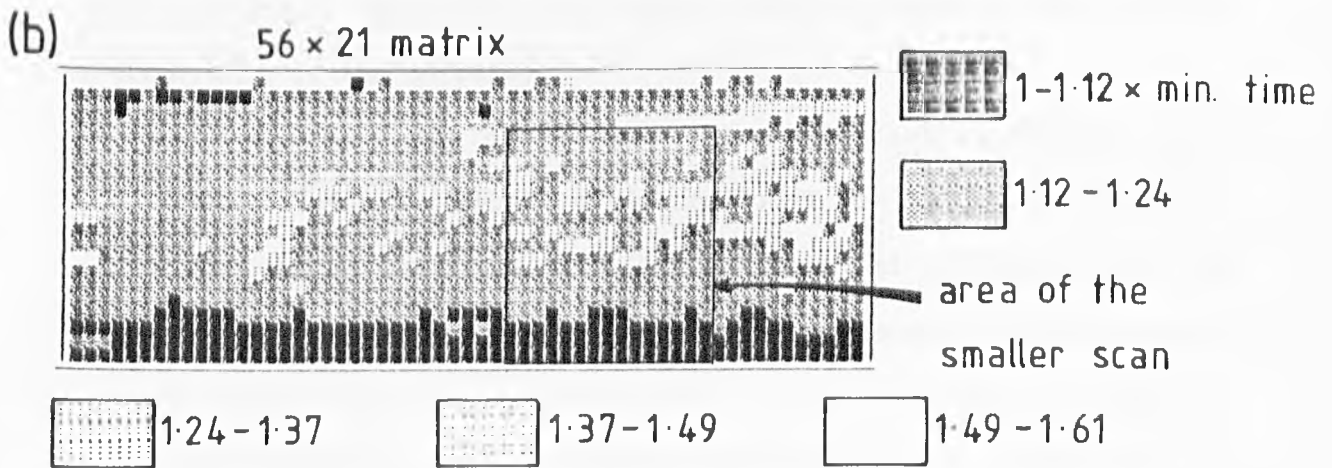
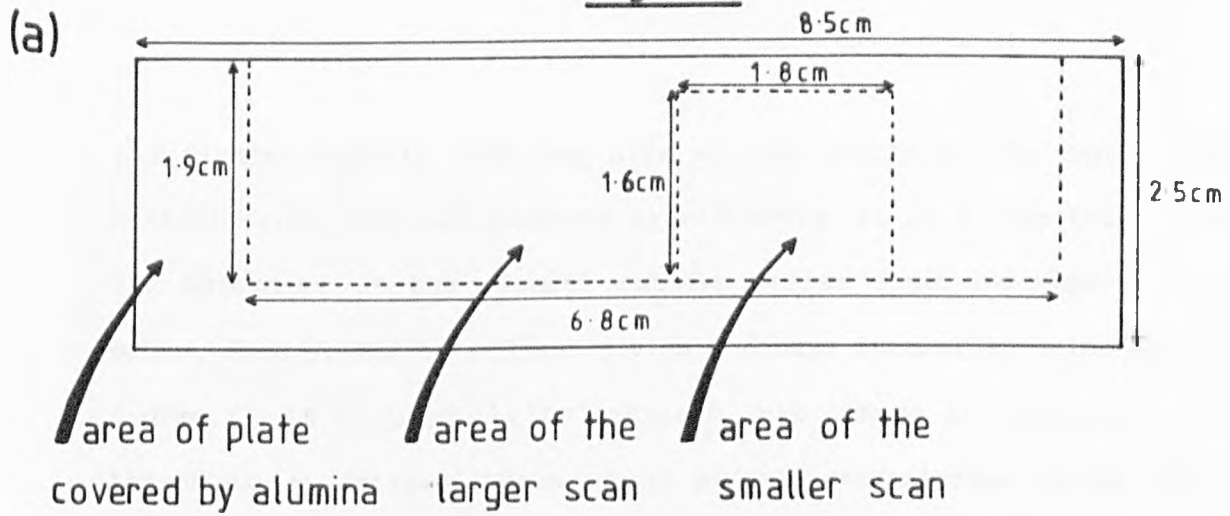
High resolution, automated C-scan of a drill hole in an aluminium plate using the laser-acoustic source and EMAT.

Fig. 8·8



10MHz immersion, ultrasonic C-scan of an alumina coated steel plate.

Fig. 8.9



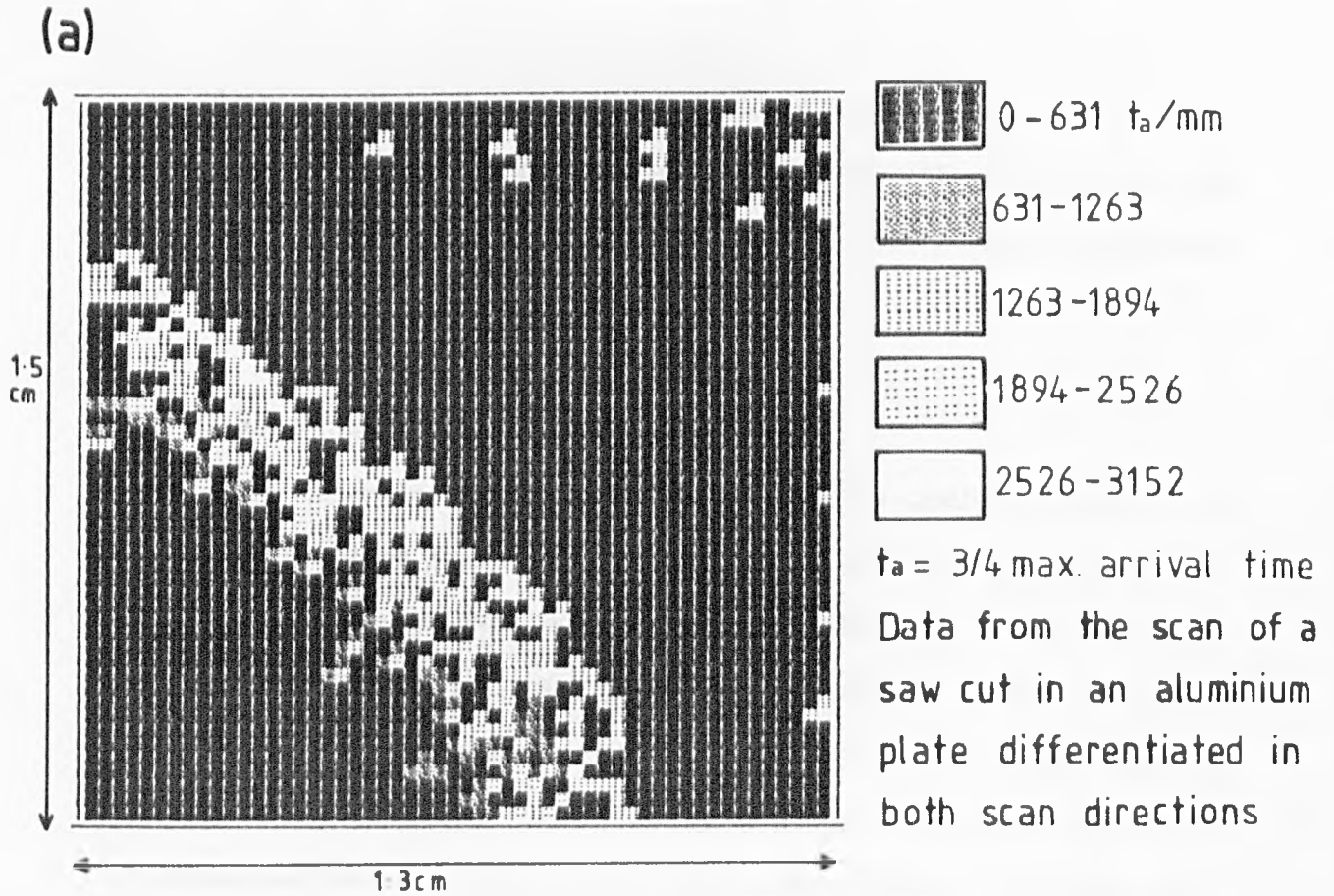
the scans represent the time taken for the signal to reach 3/4 of its expected value.

Automated C-scans of an alumina coated steel plate using the laser-acoustic source and EMAT detector.

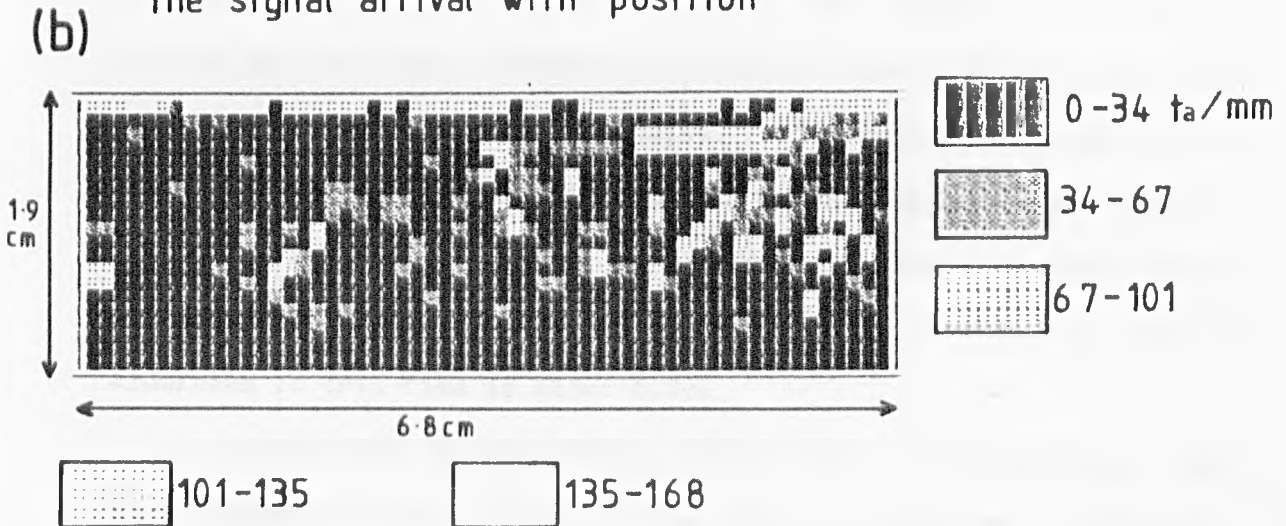
the alumina deposit from one side of the sample to the other. The metallic substrate was measured by micrometer to be 3.16mm thick, and the thickness of the alumina coating varied from one edge to the other, from 0.47mm to 0.54mm, giving a change in coating thickness of 0.07mm. It is possible to estimate this change in thickness from the change in delay of the acoustic signals demonstrated in the scan, so providing a means for monitoring coat thickness as well as the occurrence of the defects.

For the purposes of characterising the laminar defects, this retardation of the acoustic signal confuses the picture and tends to mask the defect features. A simple numerical enhancement of the C-scan data was performed to distinguish the areas of rapid signal delay from slowly varying delays such as those caused by changes in coating thickness. The numerical enhancement was carried out by differentiating the picture data in both the X and Y scan directions. Digitally the differentiation consists of subtracting adjacent pairs of data points in the rows and then in the columns, dividing by the distance between adjacent data points and then overlaying the two sets of data. The effect of the process is shown in fig. 8.10a for the data from the saw-cut laminar defect pictured in fig. 8.6. The obvious effect of the differentiation process is to pick out the edge of the defect region where the rate of change of retardation of the acoustic signal is a maximum. The process does have the disadvantage that it increases the effects of spurious noise as can be seen from the regions in the top right hand side of the scan. The C-scan data for the alumina coat depicted in fig. 8.9b was differentiated in the vertical direction only since the variation in coat thickness can be seen to occur in this direction only. The enhanced scan is shown in

Fig. 8-10



The scans represent the rate of change of retardation of the signal arrival with position



Data from the scan of the alumina coat differentiated in the vertical direction only

Defect edge enhancement using data differentiation.

fig. 8.10b. The defect areas towards the right and down the middle of the scan are now clearly depicted together with a band along the top edge which corresponds to the edge of the sample introducing interference effects in the detected signal.

#### 8.4 LASER GENERATION AND DETECTION

The laser-acoustic source C-scan results indicate that it is possible to detect laminar defects in plates with good resolution and with the advantages over conventional methods that this source can provide. The laser can be optically steered, enabling rapid scanning of large areas, and the method is non-contact giving acoustic source reproducibility and good acoustic coupling into rough finished surfaces. The acoustic source can be made to be very small - tens of microns for the diffraction limited,  $1.06\mu\text{m}$ , Gaussian profile laser beam. Because of this, the spatial resolution is limited by the defect interaction processes interfering with the rise time of the detected acoustic pulse. The absolute limit for the time-of-flight measurement is limited by the acoustic rise time of the pulse leaving the source, which cannot exceed the laser pulse rise time of 30ns. The distance propagated by a longitudinal wave in aluminium in this time is about 0.2mm.

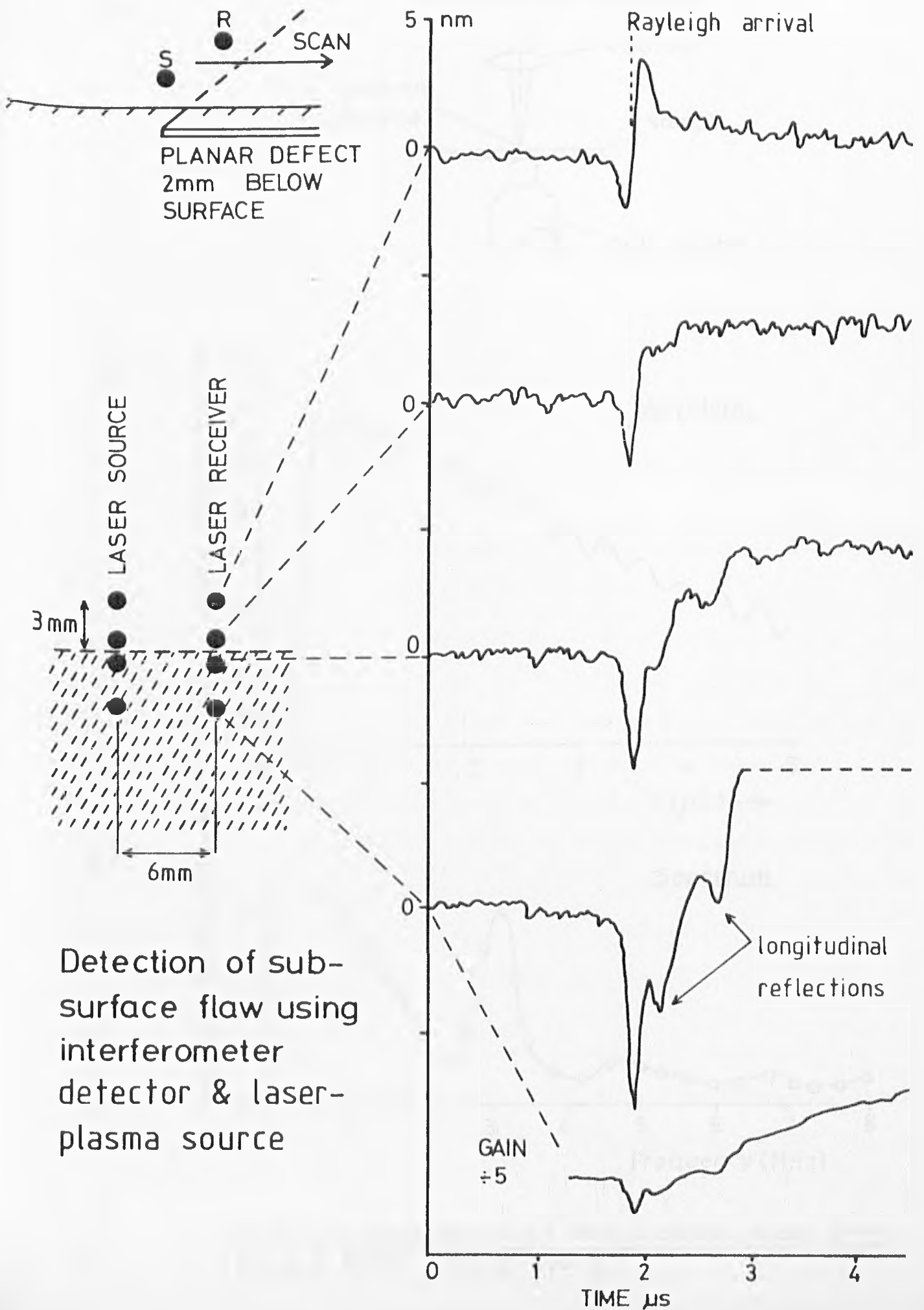
The technique, as described, suffers from the disadvantage that close access to the surface of the plate is required in order to operate the EMAT transducer. However, experiments have been performed with a displacement sensitive laser interferometer which allows optical scanning of both the source and detector and the possibility of performing the measurements on the same surface. The characteristics of the interferometer used in the following

experiment are described in Chapter 7. Fig. 8.11 shows the focused laser source, laser interferometer detector arrangement and results from an artificial laminar defect. Over the bulk of the material the surface wave arrival shows the characteristic form described in Chapter 4. The waveform over a 2mm layer of material above the defect shows a gradually increasing displacement after the Rayleigh wave arrival. The fine structure of the first arrivals over the defect area show successive reflections of the longitudinal wave within the layer, allowing time-of-flight measurements to be made in order to estimate the depth of defect below the surface.

#### 8.5 PLATE THICKNESS MEASUREMENT

The resonance of the longitudinal wave within the plate region shown in fig. 8.11 suggests the use of this feature to monitor plate thickness. The technique is used in conventional systems (Krautkramer, 1983) but again, the laser does provide some advantage over these conventional systems. The fast rise time and short duration of laser-acoustic pulses allows measurements to be made on a wide range of thicknesses of material with the advantages of having a non-contact technique. Fig. 8.12b shows the waveform produced by the laser-plasma source and detected by the ball capacitance probe on the far surface of a 0.98mm thick steel sheet, fig. 8.12a. The overall ramp time dependence of this waveform is due to the extended lifetime of the force produced by the plasma source. The modulation corresponds to multiply reflected longitudinal waves. The thickness of the steel sheet,  $h$ , should be related to the modulation period,  $t$ , as

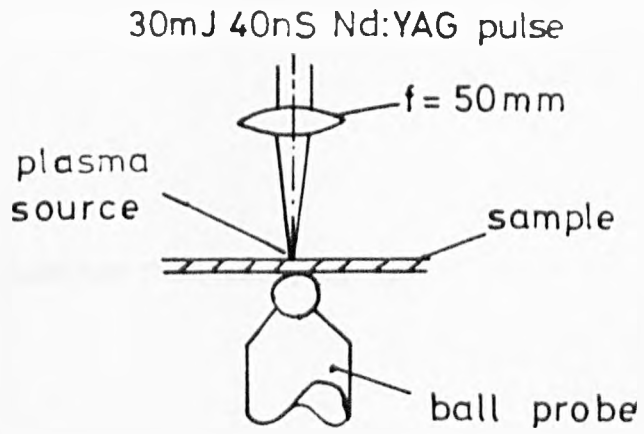
Fig.8-11



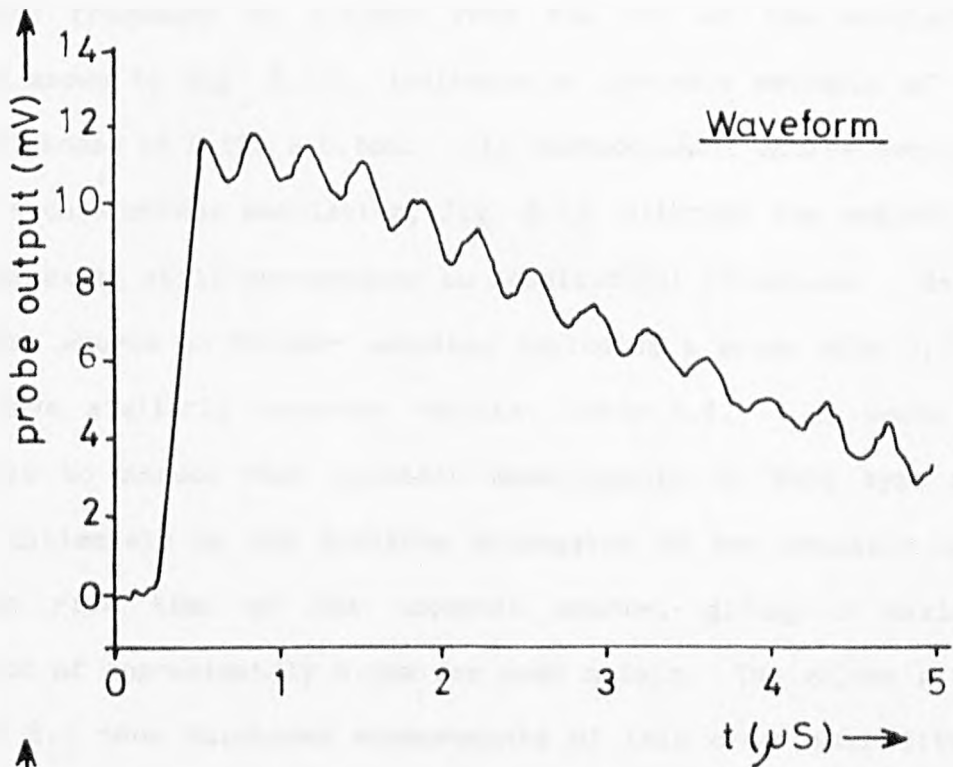
Detection of sub-surface flaw using interferometer detector & laser-plasma source

Fig. 8-12

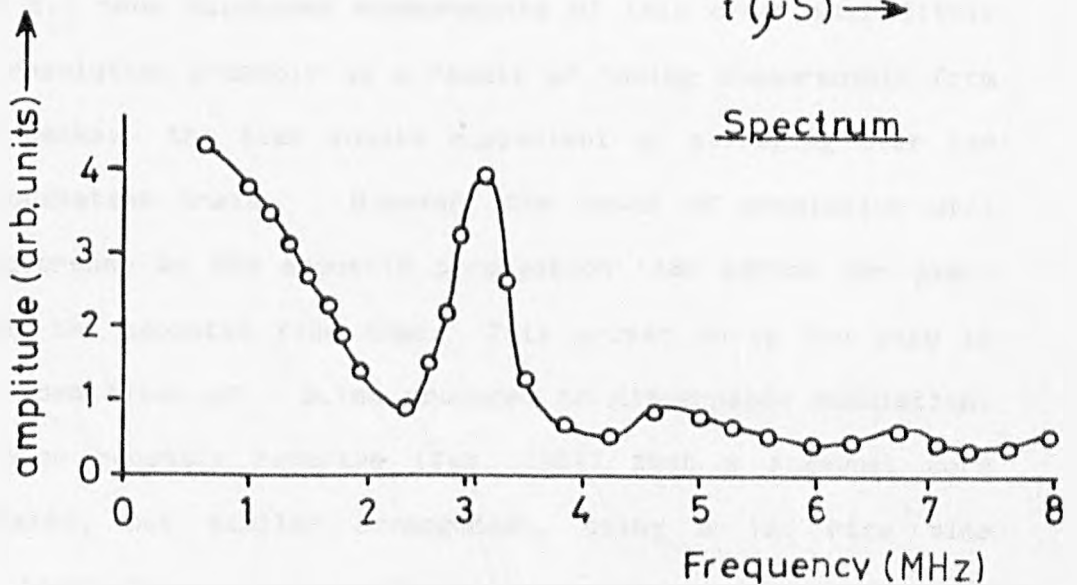
(a)



(b)



(c)



Thickness measurement of thin (0,98mm) steel sheet using a laser plasma source.

$$h = \frac{t V_p}{2}$$

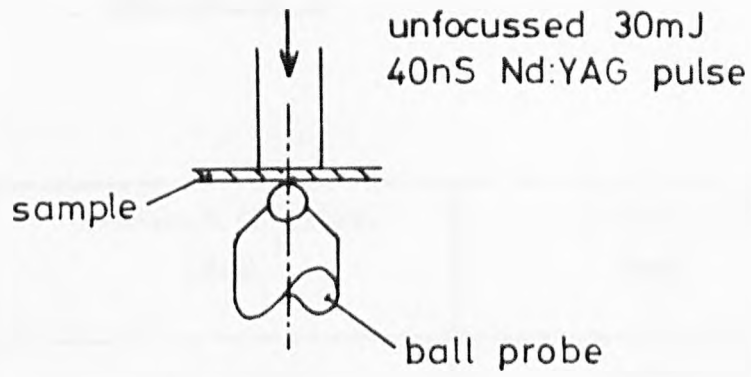
or in terms of the modulation frequency,  $\nu$ , as

$$h = \frac{V_p}{2\nu}$$

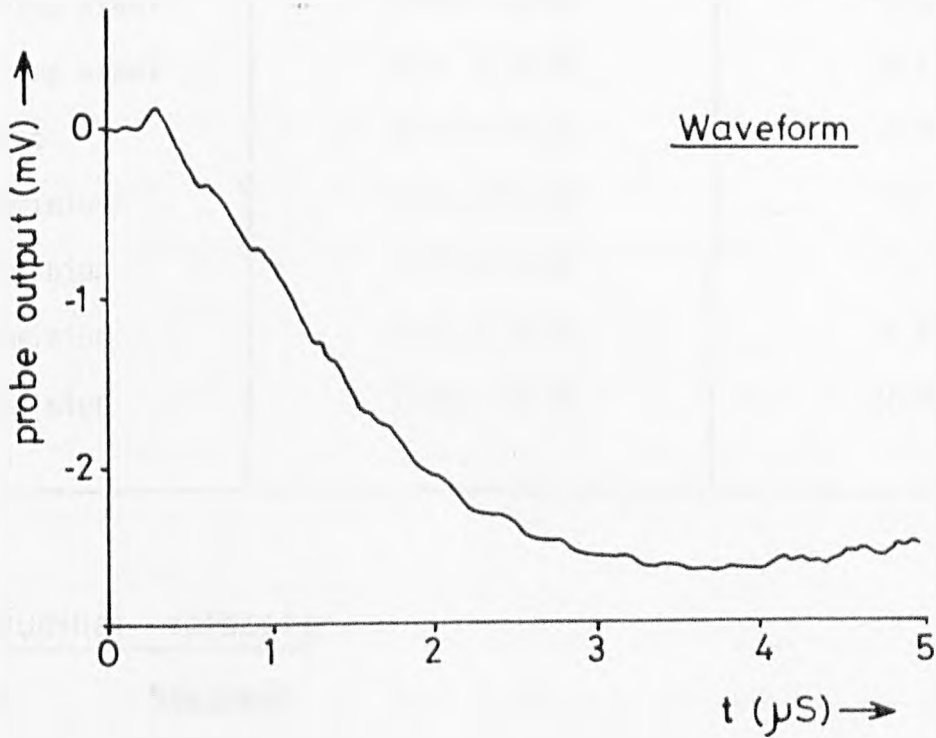
Substituting for the longitudinal velocity in steel of  $5940\text{ms}^{-1}$  and the modulation frequency of  $3.03\text{MHz}$  from the FFT of the modulation waveform shown in fig. 8.12c, indicates an accurate estimate of the plate thickness of  $0.98\text{m} \pm 0.1\text{mm}$ . The thermoelastic source does not produce such a strong modulation, fig. 8.13, although the modulation that does exist still corresponds to longitudinal resonance. Using the plasma source on thinner samples, including a brass shim  $0.21\text{mm}$  thick, gave similarly accurate results, Table 8.1. It would be reasonable to assume that acoustic measurements of this type are limited ultimately by the distance propagated by the acoustic wave over the rise time of the acoustic source, giving a maximum resolution of approximately  $0.2\text{mm}$  for most metals. The values given in Table 8.1 show thickness measurements of this order with little loss in resolution probably as a result of taking measurements from spectral peaks; the time domain equivalent of averaging over the entire modulation train. However, the depth of modulation will rapidly decrease as the acoustic propagation time across the plate approaches the acoustic rise time. This proved to be the case in practice when times of  $< 0.1\text{mm}$  produced no discernable modulation. It has been recently reported (Tam, 1984) that a somewhat more sophisticated, but similar arrangement, using a  $1\text{ns}$  rise time nitrogen laser pulse, is capable of producing acoustic pulses to measure film thicknesses as thin as  $12\mu\text{m}$  with a 1% accuracy.

Fig.8.13

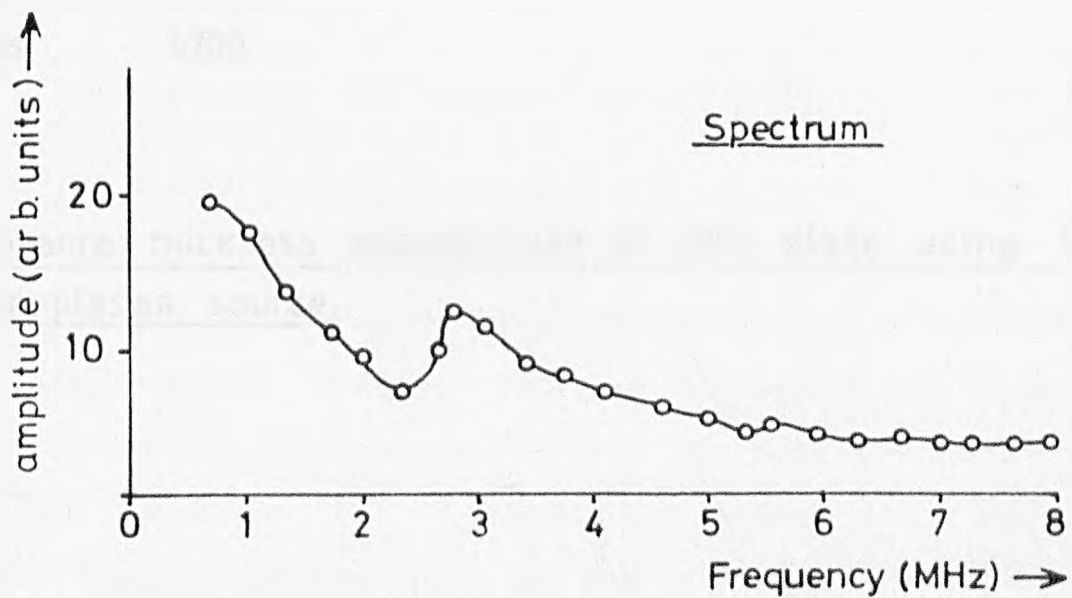
(a)



(b)



(c)



Thickness measurement of thin (0,98mm) steel sheet  
using a thermoelastic laser source.

Table 8.1

Material	Measured thickness (mm)	resonance thickness (mm)
Steel	$0.98 \pm 0.02$	$0.98 \pm 0.1$
Spring steel	$0.65 \pm 0.02$	$0.65 \pm 0.1$
Spring steel	$0.4 \pm 0.02$	$0.4 \pm 0.1$
Brass	$0.21 \pm 0.02$	$0.3 \pm 0.1$
Aluminium	$1.23 \pm 0.02$	$1.2 \pm 0.1$
Aluminium	$1.57 \pm 0.02$	$1.6 \pm 0.1$
Aluminium	$1.0 \pm 0.02$	$0.95 \pm 0.1$
Aluminium	$0.45 \pm 0.02$	$0.28 \pm 0.1$

longitudinal velocity

steel        5940 m/s  
aluminium   6320  
brass        4700

Resonance thickness measurement of thin plate using the laser-plasma source.

## CHAPTER 9

## SURFACE WAVE - DEFECT INTERACTIONS

In this chapter some experimental results are presented on the application of laser generated surface waves to NDE. It was noted in Chapter 5 that a substantial amount of the laser generated acoustic wave energy, from any of the acoustic sources, is radiated as surface waves and these waves will therefore be an important part of any proposed NDE technique employing the laser-acoustic source.

The majority of the work presented in this chapter was directed at the use of laser generated surface waves for the investigation of surface breaking cracks. Shallow surface cracks represent the origin and early growth stages of the majority of fatigue failures and it is therefore essential to have a reliable NDE technique to examine material surfaces. Surface acoustic waves provide a useful tool for investigating surfaces because the acoustic energy is confined to the surface region. This property also gives surface waves the advantage of being used over longer distances than bulk waves because the geometric decay of the wave energy is less rapid.

Surface cracks are detected conventionally by employing designs of piezoelectric transducer that specifically produce Rayleigh surface waves, and the generated waves are then used in either a pulse-echo or a pulse-transmission configuration. The presence of the crack is shown in the first case by the reflection from the crack, or in the second case by a reduction in the transmitted signal amplitude as the pulse is partially or wholly blocked by the crack

according to its depth relative to the depth of wave penetration.

Amplitude measurements of reflected and transmitted waves from cracks may be carried out using some of the laser-acoustic source generation mechanisms, usually with a greater reliability than with piezoelectric transducers because there are no bonding problems. However, it was observed from the results of the C-scan technique presented in Chapter 8 that it is usually more beneficial to use a time-of-flight based method.

#### 9.1 CONVENTIONAL METHODS OF CRACK DEPTH ESTIMATION

Several surface wave, time-of-flight techniques have been suggested in order to determine the depth of surface breaking cracks. When a surface wave reaches a discontinuity such as a crack opening or tip, part of the energy is mode converted and radiated as bulk longitudinal and shear waves and part will be reflected back as a surface wave, leaving the remainder to continue around the crack as a surface wave. Cooke (1972) measured fatigue crack depths down to 2mm by monitoring the time taken for the surface wave to pass underneath the crack. Morgan (1974) used a spectroscopic technique on reflection signals obtained using a wideband interdigital surface wave transducer to produce acoustic pulses which were incident on a slot in an aluminium surface. The acoustic pulse was not brief enough to separate out the expected echoes from the different features of the 1.4mm deep slot and the signal was frequency filtered to extract the relevant information. Lidington et al (1975) measured slot depths in the range 2mm to 30mm using the time delay between Rayleigh surface wave reflections from the opening and base of the slot. More recently Burger et al (1981) have employed a

spectroscopic technique to estimate crack depth. They based their technique on the fact that a broadband surface pulse will have frequency components which vary with depth below the surface - all frequencies at the surface and only low frequencies in deeper regions - and a shallow crack will selectively reflect a larger proportion of the high frequency than the low frequency energy. The crack will therefore act as frequency filter and a Fourier transform of either the reflected or transmitted pulse will reveal missing frequency components which may be related to the crack depth. Using this method Burger determined crack depths as small as 1.03mm using a wideband piezoelectric transducer.

The work in this chapter concentrates on the use of the reflected or transmitted Rayleigh wave to investigate surface slots. Experimental photoelastic visualisation, (Reinhardt, 1970) and theoretical numerical modelling, (Bond, 1979) of the interaction process shows that an appreciable amount of the surface wave energy is mode converted at the slot tip and is radiated as bulk wave energy. Time-of-flight techniques based on the combination of incident Rayleigh wave and crack generated bulk waves have also been used to estimate crack depth, eg. Hudgell (1974); Lloyd (1975).

In the following investigative experiments the surface breaking cracks are modelled as slots cut into the surface of aluminium samples by means of a slitting saw.

## 9.2 PULSE-ECHO SURFACE DEFECT LOCATION

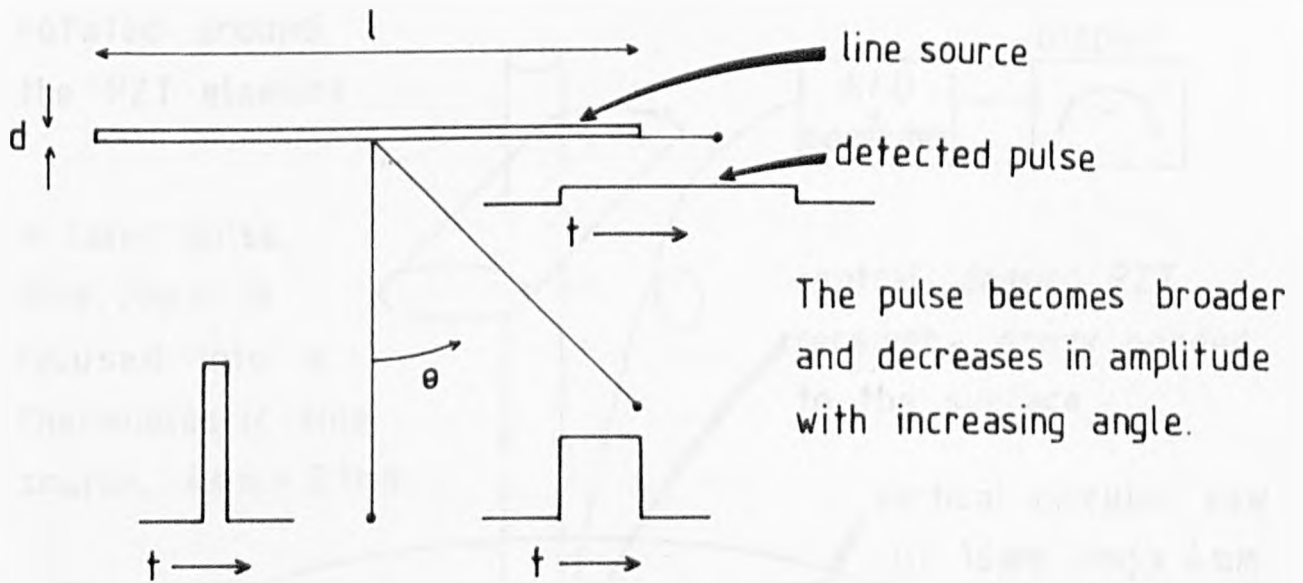
The surface of a sample may be scanned by Rayleigh waves to produce echo information that will reveal the location of surfaces breaking slots. The laser pulse will produce a circular, expanding,

surface acoustic wavefront in its usual geometry of a point or small circular spot source, from which it is not a simple process to pinpoint surface defects from echo information. One of the versatilities of the laser-acoustic source, because it is produced optically, is that the source geometry may be altered by manipulation of the optical beam. Aindow et al (1982) has shown that focusing the laser beam into a line source alters the directional nature of the surface acoustic wave amplitude. If the line source is treated as a combination of independent point sources producing acoustic displacements approximated by the delta function, then an observer at a position broadside to the array will receive signal contributions from all point emitters with minimum time delay, whereas an observer at a position in line with the source will observe maximum delay between signals from different parts of the line, fig. 9.1a. Fig. 9.1b shows the experimental arrangement and observed directionality of the acoustic amplitude measured as the maximum of the ring produced by the resonant piezoelectric transducer. The Rayleigh pulse directionality is seen to consist of two narrow lobes of increased displacement amplitude, broadside to the line source.

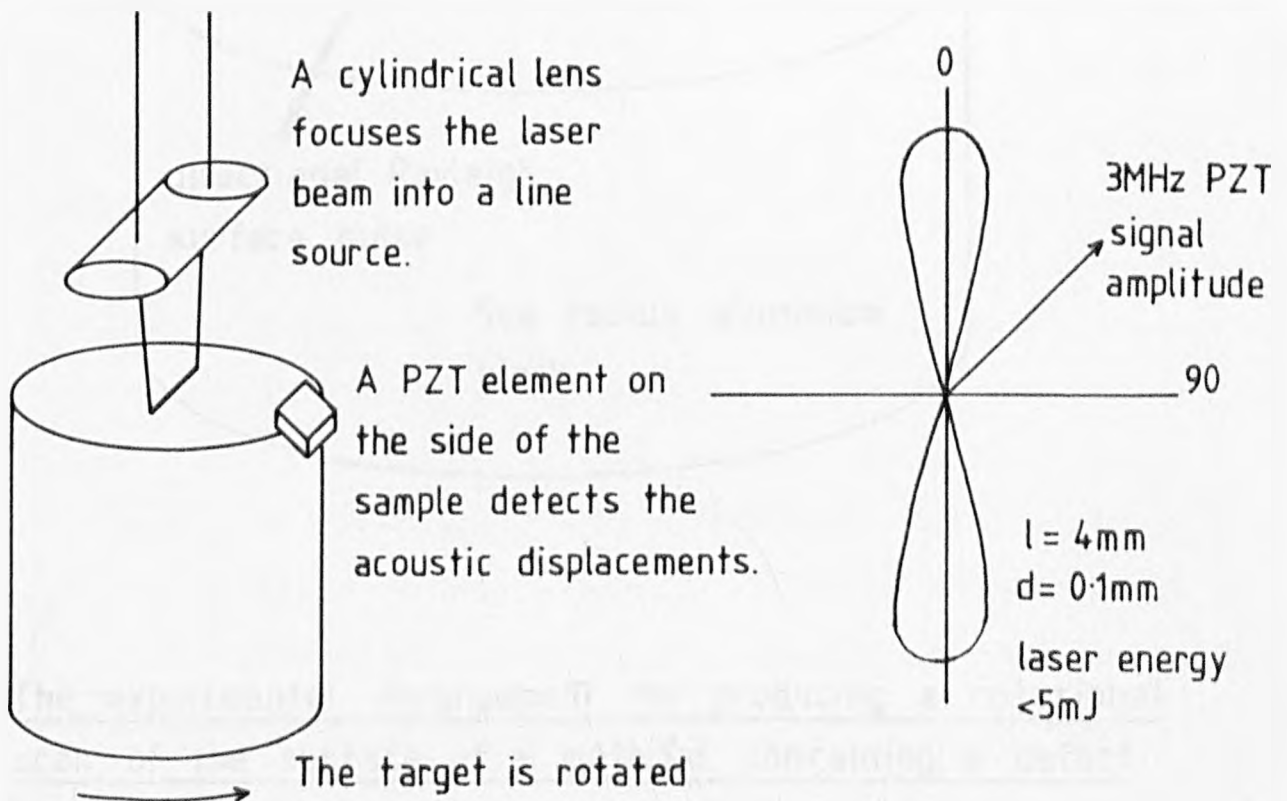
The directional beam of Rayleigh waves may be used as the acoustic source to produce a pulse-echo representation of the surface features. A practical way of scanning the directional surface pulse is to rotate the cylindrical lens and use a co-incident detector to pick up echo returns from boundaries and defects. The process is analogous to sonar and radar techniques and produces a visualisation of the surface features. Fig. 9.2 shows the arrangement for the scan. A cylindrical lens is used to focus the laser beam into a line  $4 \times 0.1\text{mm}$ . The energy density was insufficient to create a plasma

Fig.9.1

The line source is assumed to consist of an infinite number of independent point sources with equal strength and  $\delta(t)$  time dependence.



(a) The angular dependence of the pulse from a transient line source.

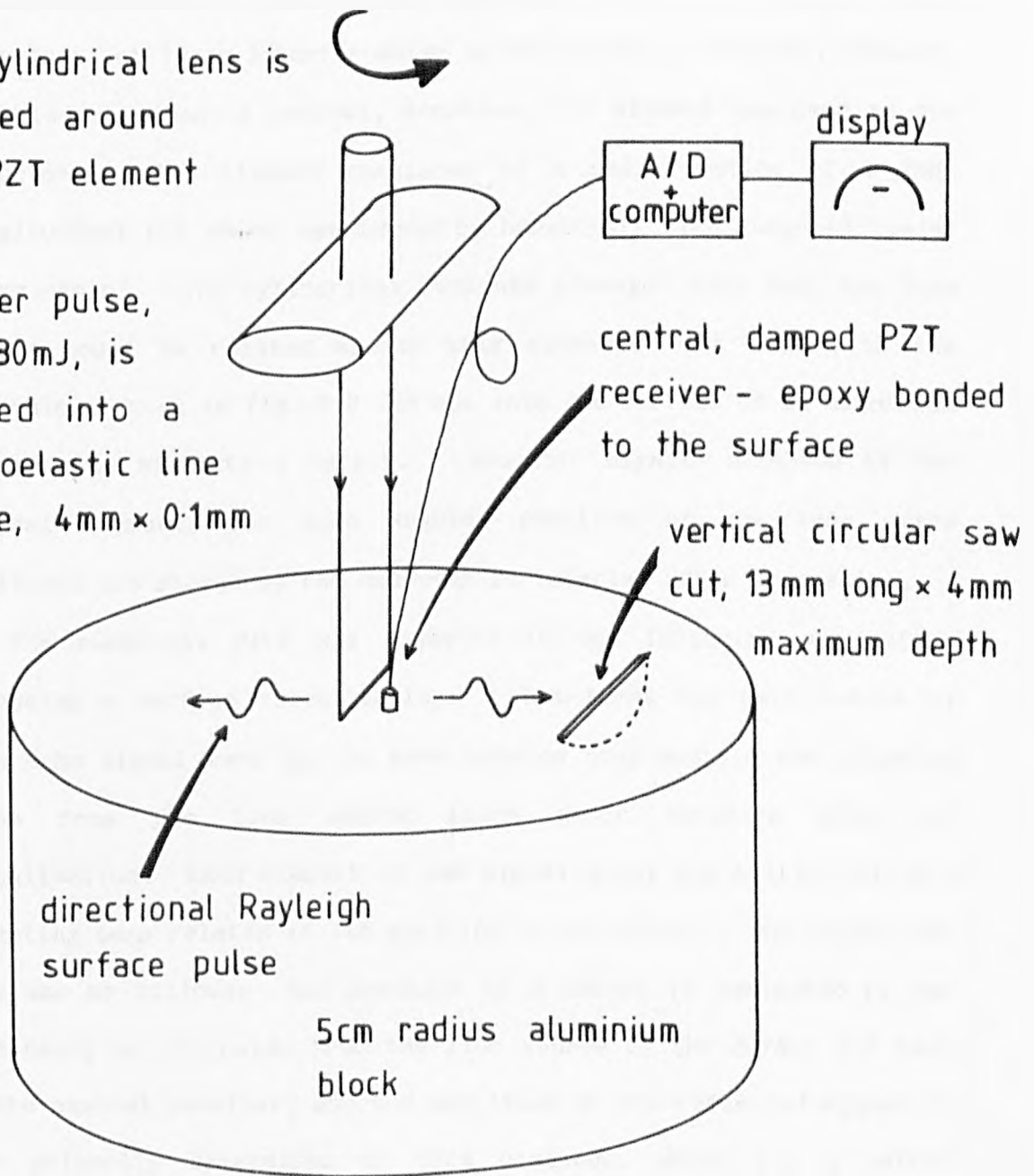


(b) The experimental arrangement and the measured directivity for a laser-acoustic line source.

Fig.9.2

The cylindrical lens is rotated around the PZT element

A laser pulse, 30ns, 30mJ, is focused into a thermoelastic line source, 4mm x 0.1mm



The experimental arrangement for producing a rotational scan of the surface of a material containing a defect using laser generated surface acoustic waves.

and directional surface waves are produced by the thermoelastic expansion process. Ideally the experiment should be performed using a co-incident laser interferometer as the acoustic detector, however, in this experiment a central, sensitive, PZT element was used as the detector. The element consisted of a small section of a 3MHz longitudinal PZT which was damped by backing it with tungsten loaded epoxy resin. The cylindrical lens was arranged such that the line source could be rotated around this element. A slot with the dimensions shown in fig. 9.2 was cut into the surface of an aluminium cylinder to simulate a defect. Acoustic signals detected by the central element, for each angular position of the lens, were digitised and stored by the computer for display after processing.

The numerical data was adjusted in the following way before producing a surface visualisation. The first few data points in each echo signal were set to zero because they contain the outgoing pulse from the line source which would interfere with the visualisation. Each element in the signal array was multiplied by a weighting term related to its position in the array. The reason for this was as follows; the position of a defect is indicated by the time delay of the pulse from the line source to the defect and back to the central receiver, and the amplitude of the reflected signal is also primarily determined by this distance, which for a defect reflection at normal incidence would introduce a  $1/r^{1/2}$  geometric attenuation dependence for the Rayleigh wave amplitude (which becomes a  $1/t^{1/2}$  dependence in the echo signal). This dependence is removed by multiplying the signal array by a  $t^{1/2}$  weighting factor, thus normalising the amplitude of the Rayleigh wave echo signals. Any differences in echo amplitude will now be due to other factors such

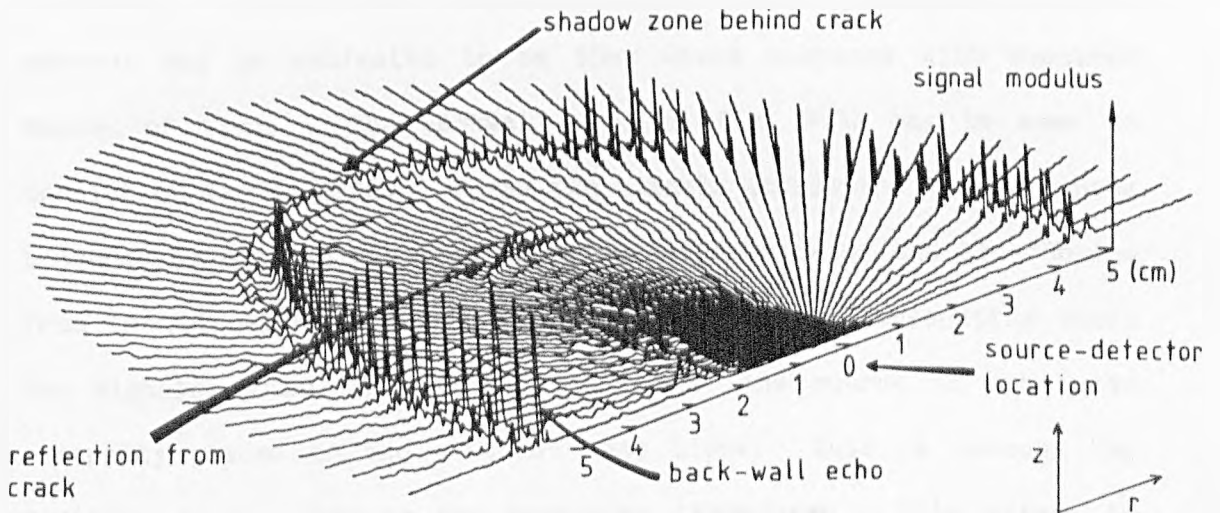
as a reflection from a discontinuity at an angle to the incident beam. This adjustment process enhances echo returns until the background noise swamps the signal on long timescales. Additionally, the form of the signal detected by the PZT transducer is oscillatory and for display purposes the signal modulus is taken.

It should be noted that using the arrangement shown in fig. 9.2, two lobes of directional Rayleigh waves are produced on either side of the line source. The consequence of this is that the signal detected by the central transducer will be an overlay of the echo returns from either side of the line source. In a practical system such ambiguity could be removed by repeating the scan at a different position on the surface.

Two ways of displaying the data are shown in fig. 9.3. Fig. 9.3a is a three-dimensional representation of the data obtained by using the arrangement shown in fig. 9.2. The radial direction in fig. 9.3a is the time dependence of the return signal and corresponds to distance along the material surface, and the Z direction gives the modulus of the echo features with the geometric attenuation factor removed. The circular edge of the block is clearly defined and, in the centre of the figure, the reflection from the saw-cut may be seen. This saw-cut produces an area of occultation or shadow zone which obscures the back wall echo. A less impressive but more practical display of the data is shown in fig. 9.3b. In this display a discrimination level has been chosen, such that signal amplitude levels above this value are displayed whereas those below this level are not. A discrimination level is chosen to produce the maximum contrast between the echo signal and the background noise. The information may now be displayed as a two dimensional plot of the

Fig. 9-3

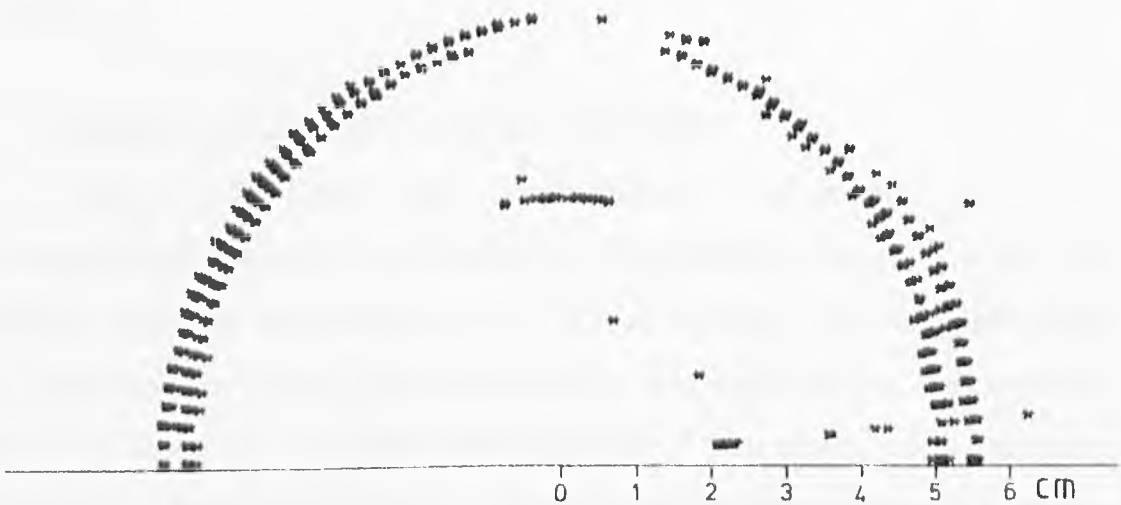
(a)



multiple, radial, A-scan display of surface reflections

(b)

DISCRIMINATION LEVEL = 0.07 \* MAX. SIGNAL



radial B-scan display of surface features

Surface defect location using directional, laser generated, surface waves.

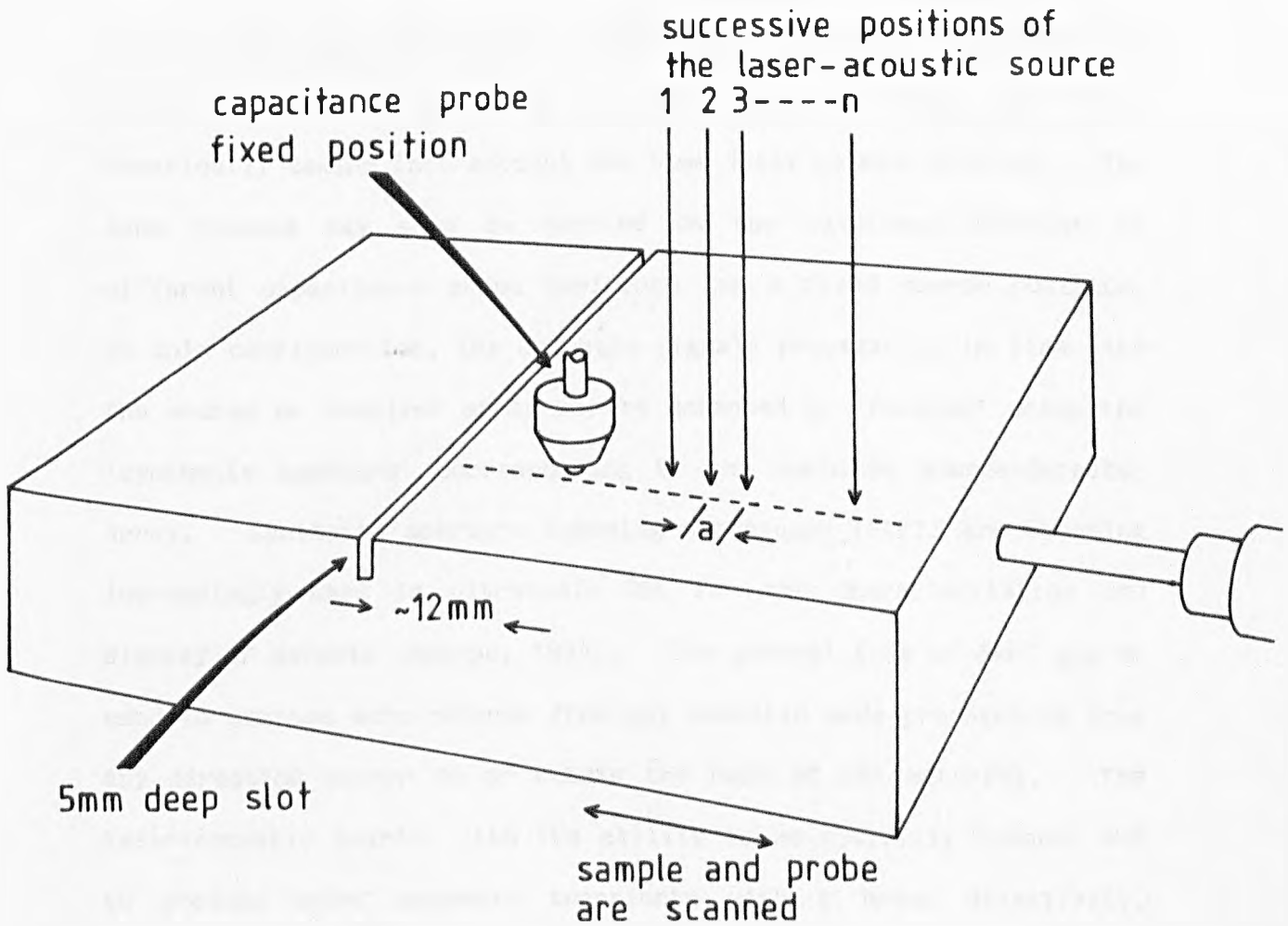
surface. Using this information the lateral dimensions of the saw-cut may be estimated to be 15mm which compares with measured value of 13mm. The backwall echo in fig. 9.3b may be seen to consist of two signals. These two signals correspond to the echoes produced by the two Rayleigh lobes on either side of the line source from the circular side-wall. The small distance separating these two signals is due to the fact that the line source is not quite centrally placed on the circular test block; this is because the position is occupied by the receiving transducer. This effect is also the reason for the slightly curved nature of the echo return from the linear saw-cut.

The acoustic line source has some similarity to the broadside array aerial arrangement used for the directional propagation of radio waves, and the idea of using aerial analogies may be extended further.

### 9.3 MULTIPLE SOURCE-DETECTOR ECHO ENHANCEMENT

Fig. 9.4 shows the experimental arrangement for the laser-acoustic source equivalent of an end-fire array; a set of discrete sources are arranged in a linear fashion. In an experiment to generate the direct equivalent of an end-fire array, the sources would be fired in a sequence from one end to the other, such that the time delay between successive firings corresponds to the time delay of the acoustic surface wave between the sources. In this way a pulse of surface wave energy would be selectively built up in the direction of the array firing sequence. The acoustic source array could be generated by the output from a repetitively pulsed laser scanned at the required velocity by an optical scanning system,

Fig.9-4



The waveforms from the different source positions are stored, shifted in time and combined to enhance the components travelling with the Rayleigh wave velocity.

Experimental arrangement for enhancing surface defect reflections

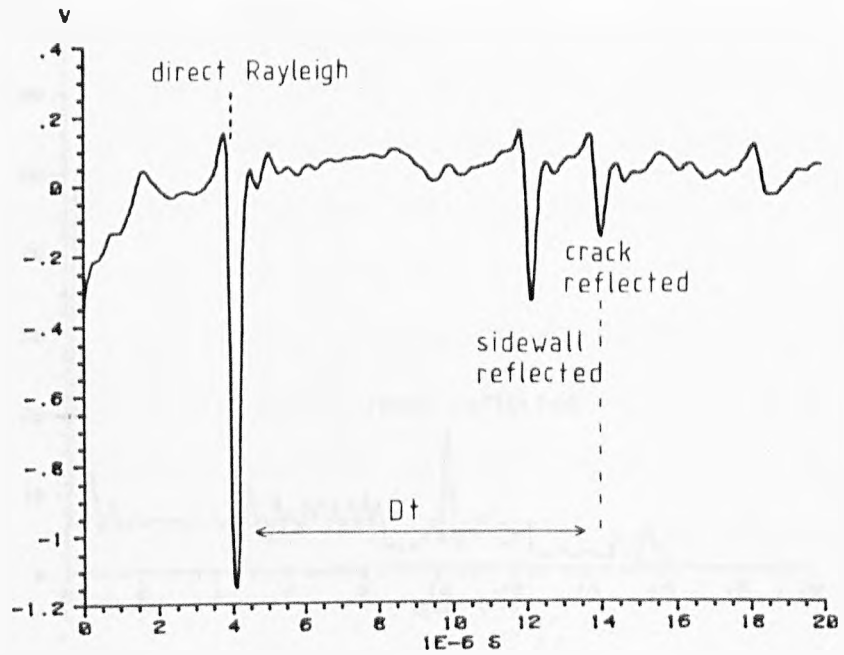
however, the same result may be achieved by digitally storing the waveforms produced by each of the discrete sources and then numerically taking into account the time delay between sources. The same process may also be carried on the waveforms detected at different capacitance probe positions for a fixed source position. In this configuration, the acoustic signals propagating in line with the source or receiver array may be enhanced or 'focused' using the 'synthetic aperture' corresponding to the combined source-detector array. Synthetic aperture focusing techniques (SAFT) are becoming increasingly used in ultrasonic NDE for the characterisation and display of defects (Sharpe, 1984). The general form of SAFT may be used to enhance echo returns from any acoustic mode propagating from any direction either on or within the bulk of the material. The laser-acoustic source, with its ability to be optically scanned and to produce brief acoustic transients with a broad directivity, provides a useful tool for these type of techniques.

Fig. 9.5a shows the displacement waveforms detected for two of the positions of the source depicted in fig. 9.4. The waveforms contain three distinct arrivals corresponding to the direct Rayleigh pulse and its reflections from the slot and side-wall of the sample. Moving the acoustic source in a linear fashion away from the slot causes a change in the position of the echo signals, fig. 9.5. However, the time delay,  $\Delta t$ , between the direct Rayleigh pulse and the echo reflection from the slot will remain constant, whilst the echo from the side-wall will not. The echo signal from the slot is therefore enhanced by adding together the array of waveforms after removing the time delay due to the movement of the source. The result of this "shift and add" method is shown in fig. 9.6a. The

Fig.9.5

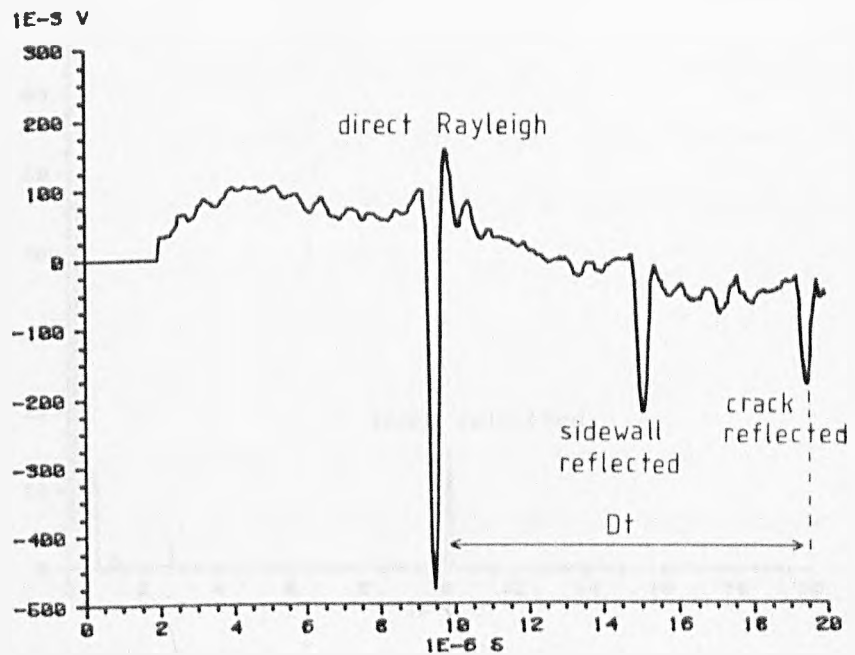
(a)

waveform  
recorded for  
the first  
position



(b)

waveform  
recorded for  
the last  
position

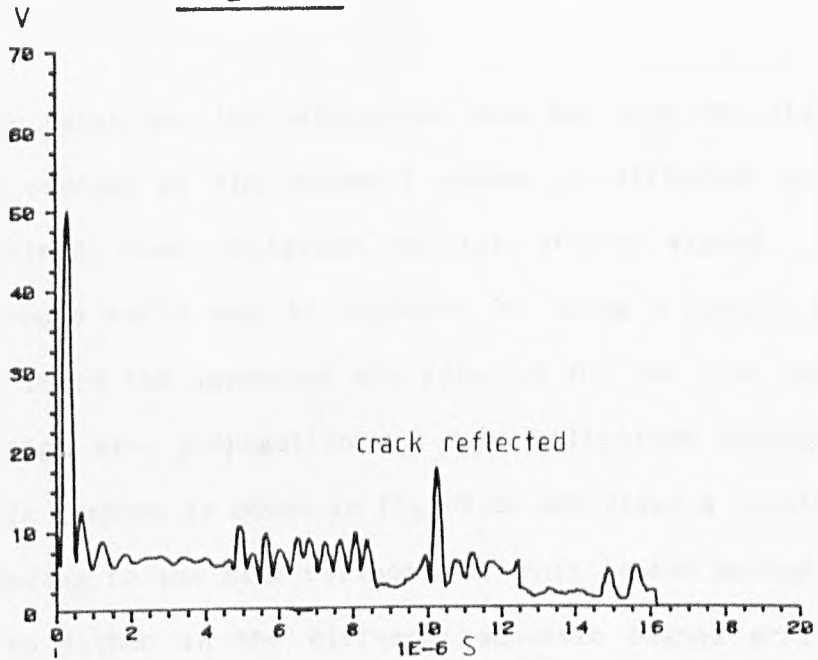


Variation of the recorded waveform with source-detector-crack separation.

Fig. 9-6

(a)

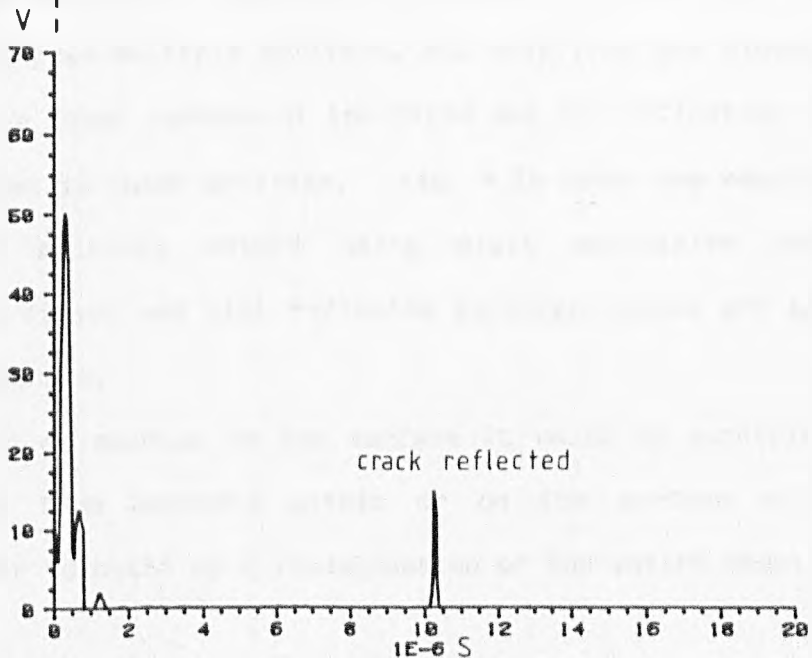
crack reflection  
enhancement  
from a "shift  
and add" method



direct Rayleigh arrival shifted  
to  $t = 0$

(b)

crack reflection  
enhancement  
from a "shift  
and multiply"  
method



Crack reflection enhancement by combining waveforms from  
from eight successive source locations.

incident Rayleigh pulse and its reflection from the slot are picked out whereas the overlay of the sidewall echoes at different times results in a combined, lower amplitude, multiple arrival signal. The signal to background ratio may be improved by using a 'shift and multiply' method where the waveforms are adjusted for the time delay due to the Rayleigh wave propagation and then multiplied together. The result of this process is shown in fig. 9.6b and gives a distinct arrival corresponding to the slot reflection. This latter method is more sensitive to jitter in the different acoustic signal arrival times.

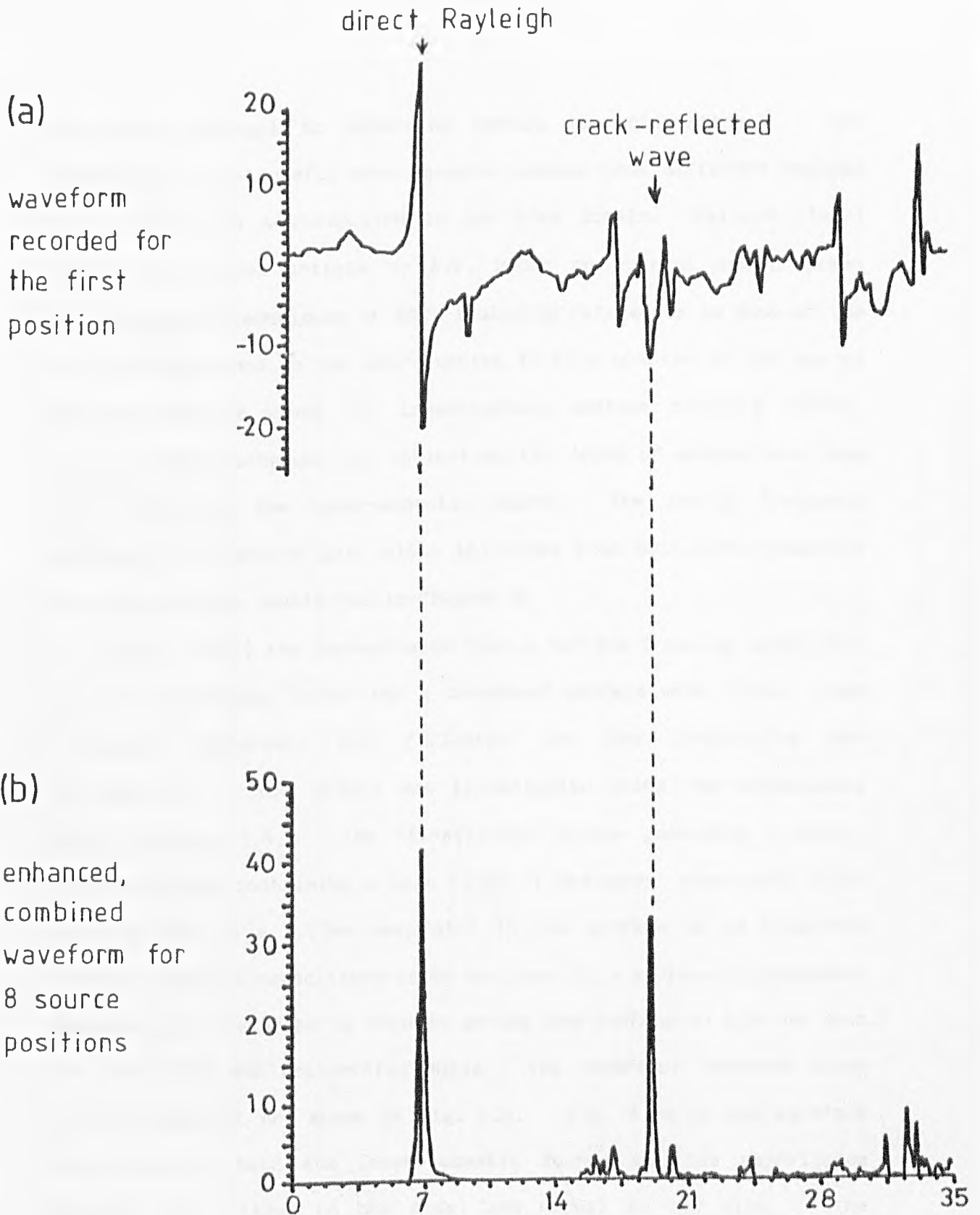
A more stringent test of the technique is shown in fig. 9.7. Fig. 9.7a is the single shot waveform for a steel plate, 2.5cm thick containing a 5mm deep slot, using the arrangement of fig. 9.4. The thin plate introduces multiple arrivals, not only from the sidewall, but also from the lower surface of the plate and any reflection from the slot is hidden in these arrivals. Fig. 9.7b shows the result of the shift and multiply method using eight successive source positions; the direct and slot reflected Rayleigh pulses are again dramatically enhanced.

Using a grid of sources on the surface it would be possible to enhance signals from anywhere within or on the surface of the material in order to build up a visualisation of the entire sample.

#### 9.4 ACOUSTIC SPECTROSCOPY

The brief surface acoustic pulses generated by the oil-ablation source allow various spectroscopic techniques to be investigated. Acoustic spectroscopy in the context of NDE refers to the use of wideband acoustic transients to produce signals which may be

Fig. 9.7

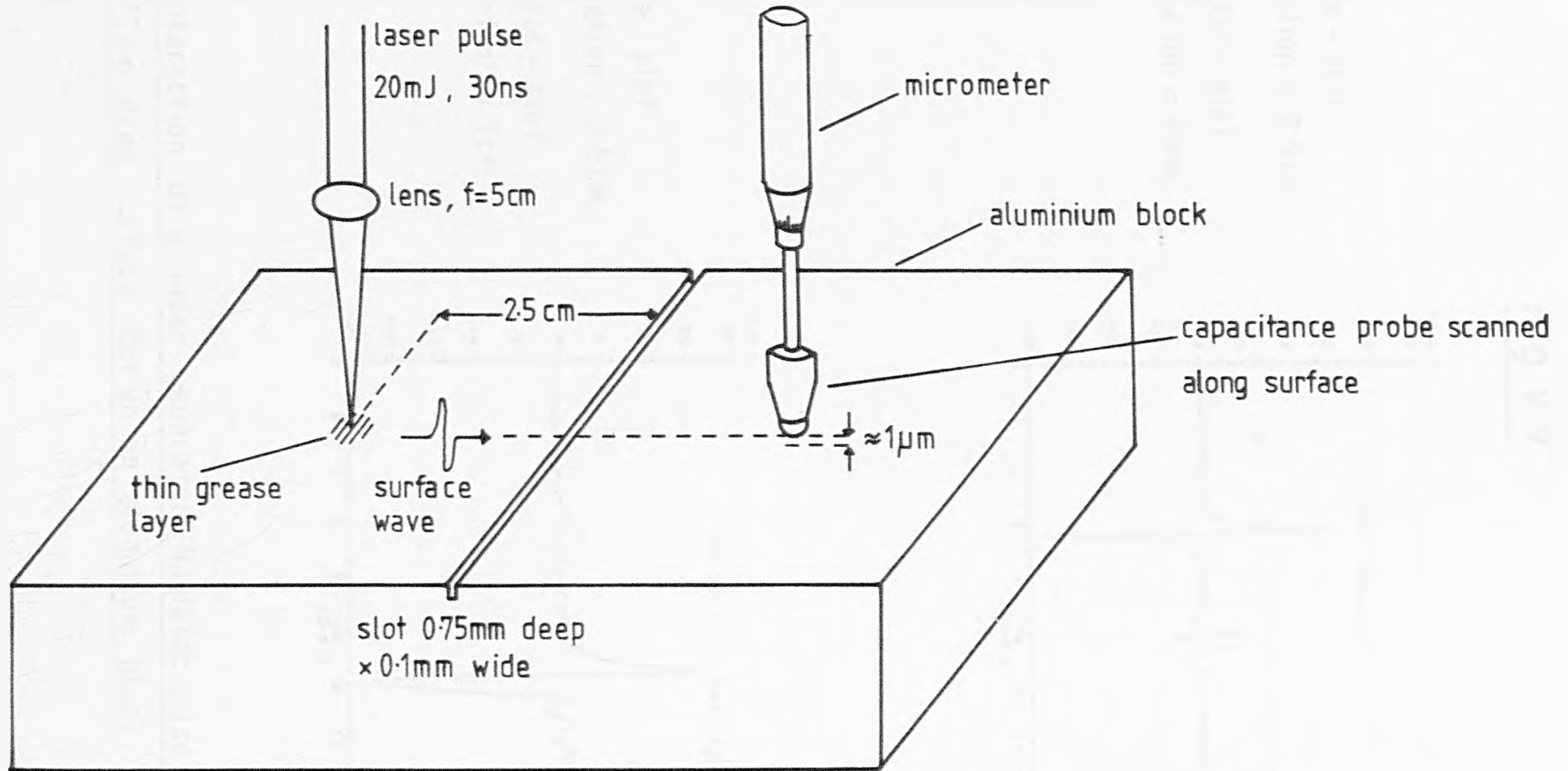


Surface wave - crack reflection enhancement on a steel plate using a "shift and multiply" method.

frequency analysed to determine defect characteristics. The technique is most useful when acoustic echoes from different regions of a defect are not resolved in the time domain. Szilard (1982) contains a review article by A.F. Brown on current and proposed spectroscopic techniques in NDE, including references to some of the articles mentioned in the introduction to this chapter on the use of surface acoustic waves for investigating surface breaking cracks. Some of these technique for estimating the depth of cracks have been evaluated using the laser-acoustic source. The use of frequency analysis to determine thin plate thickness from bulk wave resonance has already been considered in Chapter 8.

Burger (1981) has demonstrated that a surface breaking crack will act as a frequency filter for a broadband surface wave pulse; high frequency components are reflected and low frequencies are transmitted. This effect was investigated using the arrangement shown in fig. 9.8. The oil-ablation source generates a narrow Rayleigh pulse containing a wide range of frequency components which are incident on a 0.75mm deep slot in the surface of an aluminium block. The ball capacitance probe was used as a surface displacement detector and the probe is scanned across the surface to pick up both the reflected and transmitted pulse. The waveforms detected using this arrangement are shown in fig. 9.9. Fig. 9.9a is the waveform detected with both the laser-acoustic source and the capacitance detector in a line, on one side, and normal to the slot. The detector receives first the incident Rayleigh wave and then, at some time later, the reflected component from the slot. Fig. 9.9b shows the transmitted pulse detected with the laser-acoustic source on one side of the slot and the capacitance detector on the other side of

Fig.9·8

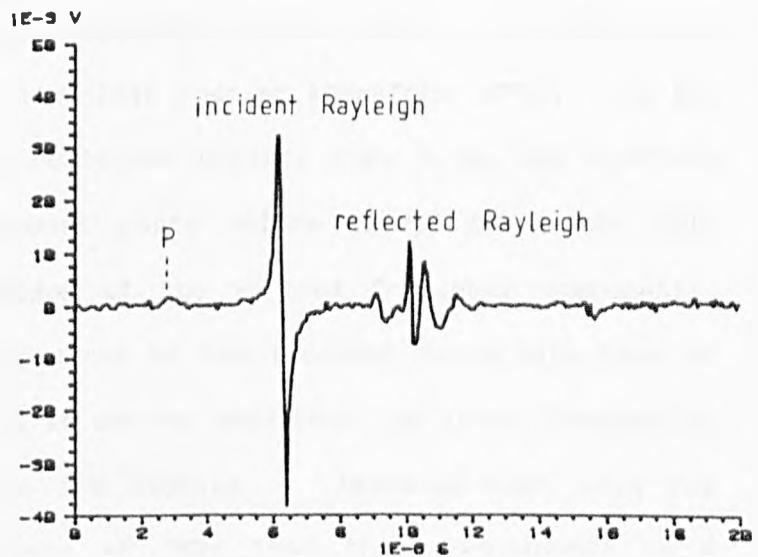


Experimental arrangement for investigating the interaction of laser generated surface acoustic pulses with surface breaking slots.

Fig. 9.9

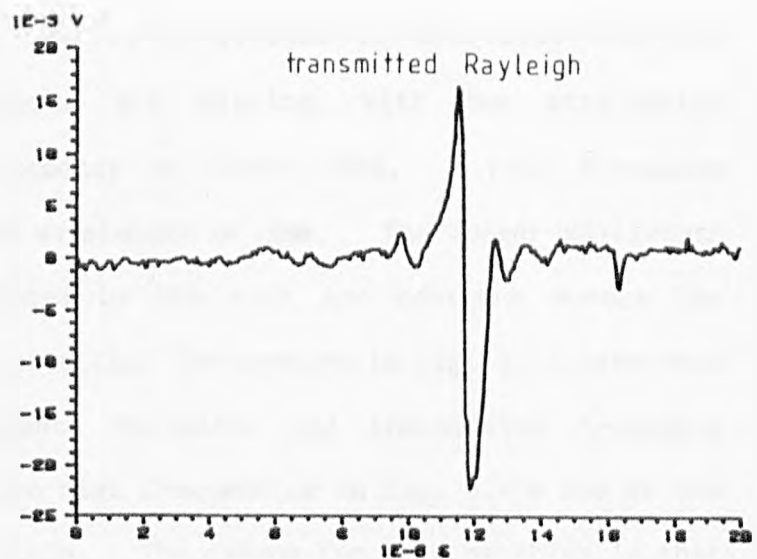
(a)

source - slot  
separation = 2.5cm,  
detector - slot  
separation = 6mm



(b)

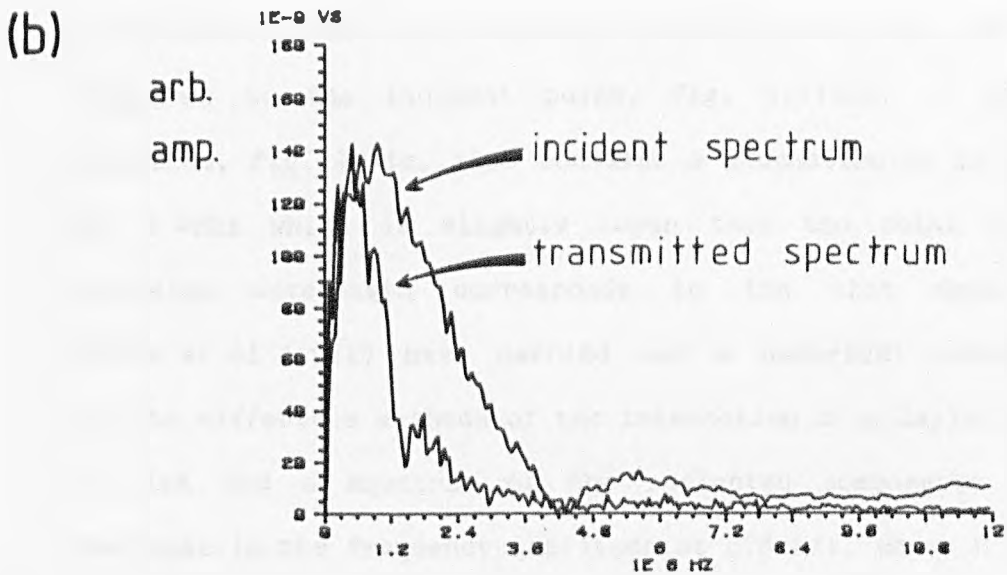
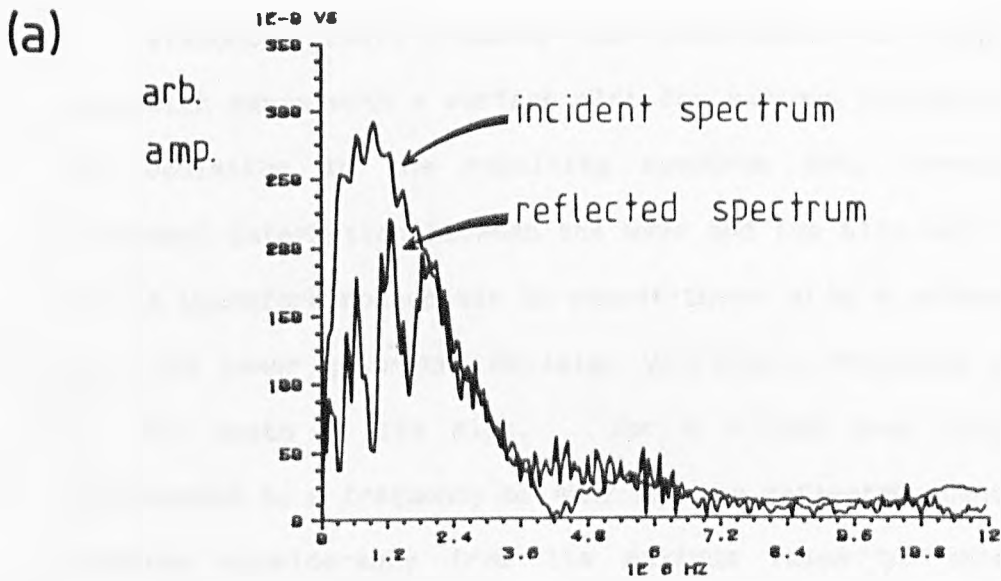
source - slot  
separation = 2.5cm,  
detector - slot  
separation = 1cm



The interaction of a laser generated Rayleigh pulse with a 0.75mm deep surface slot in an aluminium block.

the slot. The frequency components of the various waveforms were obtained by performing a numerical Fourier transform (FFT). In the case of the incident and reflected pulses, fig. 9.9a, the waveform was split into the component parts before carrying out the FFT. Fig. 9.10 shows a comparison of the various frequency components. Fig. 9.10a compares the spectrum of the incident pulse with that of the reflected waveform and it can be seen that the lower frequencies in the reflected spectrum are missing. Assuming that this low frequency attenuation starts at 2MHz then this corresponds to a Rayleigh wavelength of 1.5mm or about twice the depth of the slot. One would expect Rayleigh waves of this wavelength and less to be substantially reflected by the crack side wall. Conversely, fig. 9.10b compares the spectrum of the incident pulse with that of the transmitted waveform and it is evident in this case that the higher frequency components are missing, with the attenuation becoming rapid at a frequency of about 1MHz. This frequency corresponds to a Rayleigh wavelength of 3mm. The longer wavelength components are not affected by the slot and continue across the surface. It should be noted that the spectra in fig. 9.10 have been matched such that incident, reflected and transmitted frequency envelopes correspond at the high frequencies in fig. 9.10a and at the low frequencies in fig. 9.10b. The reason for this matching is that amplitude measurements on spectra are subject to the same uncertainties as amplitude measurements in the time domain and the oil ablation source does not generate reproducible Rayleigh pulse amplitudes. This variation limits the usefulness of this method for estimating crack depth although the frequency filtering property of the slot is quite evident.

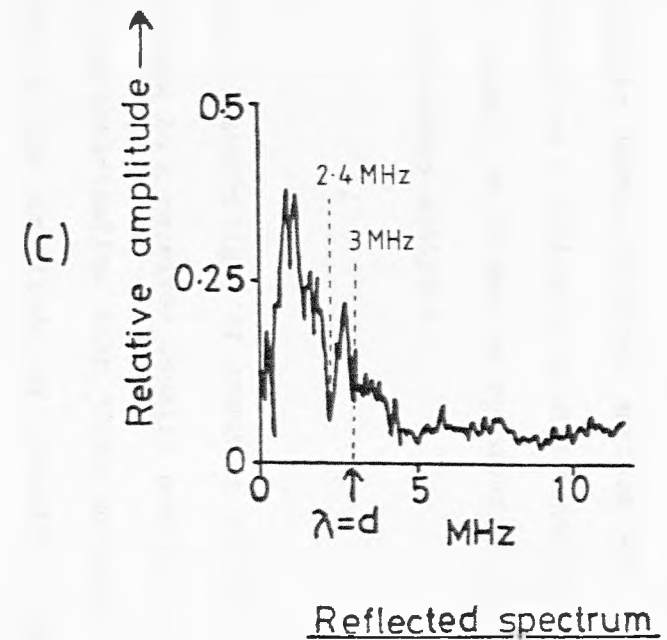
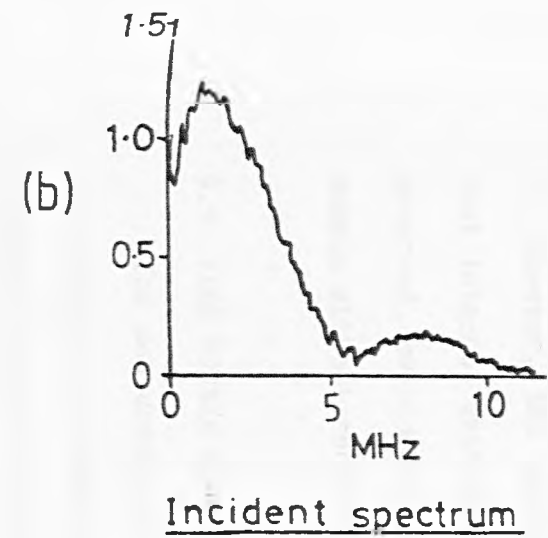
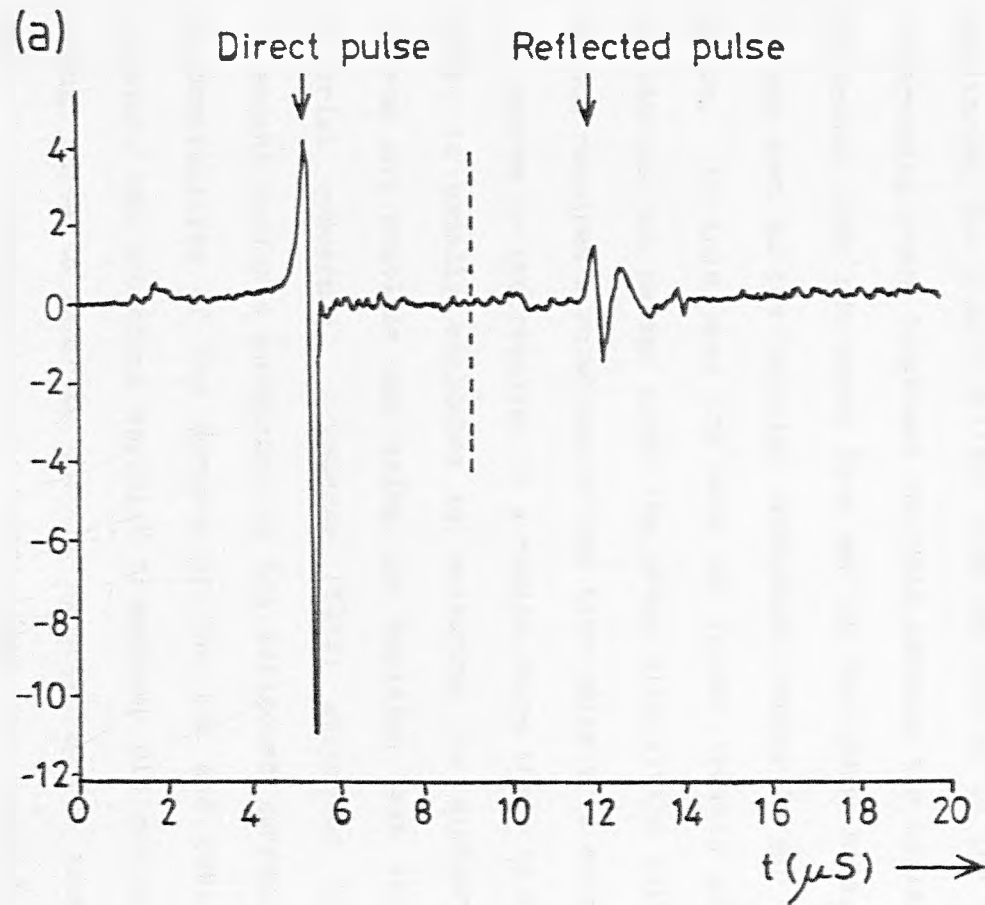
Fig. 9-10



A comparison of the frequency components in the incident, reflected and transmitted Rayleigh pulses for a 0.75 mm deep slot.

Viktorov (1967) studied the interaction of single frequency Rayleigh waves with a surface slot for various frequencies and found a modulation in the resulting spectrum that corresponded to a resonant interaction between the wave and the side wall of the slot. It is therefore reasonable to expect there to be a strong interaction for the laser generated Rayleigh wavelength component corresponding to the depth of the slot. For a 0.75mm deep slot this would correspond to a frequency of 4MHz and the reflected spectrum has been reduced considerably from its maximum value at this frequency, fig. 9.10. However, 4MHz is at the limit of the Rayleigh pulse bandwidth and the experiment was repeated for a slot depth of 1mm for which the incident and reflected pulse and their corresponding spectra are shown in fig. 9.11. Again it is possible to see a reduction in the low frequency components of the reflected pulse compared to the incident pulse, fig. 9.11b,c. The reflected spectrum, fig. 9.11c, also contains a discontinuity in the spectrum at 2.4MHz which is slightly lower than the point at which the Rayleigh wavelength corresponds to the slot depth at 3MHz. Hirao et al (1982) have carried out a numerical simulation using finite difference methods of the interaction of a Rayleigh pulse with a slot and a spectrum of the reflected components indicates a decrease in the frequency amplitude at  $0.8 h/\lambda$ , where  $h$  is the depth of the slot and  $\lambda$  is the Rayleigh wavelength. For a 1mm deep slot this would correspond to a frequency of 2.4MHz, agreeing with the discontinuity in the spectrum that occurs in fig. 9.11. This kind of analysis could provide a reliable spectroscopic approach for estimating crack depth without the uncertainties introduced by taking component amplitude measurements.

Fig.9.11



A comparison of incident and reflected Rayleigh pulses and spectra for a 1mm deep surface slot.

However, the laser-acoustic source produces surface wave pulses that interact with discontinuities - typically with dimensions of the order of 1mm - to produce signals which may be resolved in the time domain without recourse to frequency analysis.

#### 9.5 TIME DOMAIN ANALYSIS

The measurement of the time-of-flight of acoustic signals from the source to a defect and back to a receiver usually provides a more accurate means of defect characterisation than those methods which rely on the interpretation of the amplitude of acoustic signals. Cooke (1972) estimated the depth of surface breaking cracks by monitoring the time-of-flight from the source to the receiver; any intervening crack lengthens the path because the Rayleigh waves have to travel down the crack face and up the other side. This method breaks down as the Rayleigh wavelength become larger than the crack depth; in this case the wave no longer travels along the crack boundaries but passes under the crack with little interaction. The method requires a knowledge of the time delay of a surface pulse from the source to the receiver in a region where there is no crack. This delay is usually evaluated by measuring the distance between the source and receiver and using the Rayleigh wave velocity for the material concerned. Morgan (1974) attempted to relate time dependent features occurring in the reflected surface pulse to the discontinuities of the corners of the top and bottom of a slot. However, the broadband Rayleigh transducer did not provide a brief enough pulse to separate out the expected echoes from a 1.4mm deep slot. Lidington et al (1975) used the time-of-flight of the Rayleigh waves echoes from the slot top and base to estimate slot

depths from 2mm to 30mm using a short pulse surface wave probe operating at 2.5MHz. This latter approach was adopted in the experiments presented here since it should allow the estimation of crack depth using the information from a single reflected pulse without the need for information on the source-detector separation.

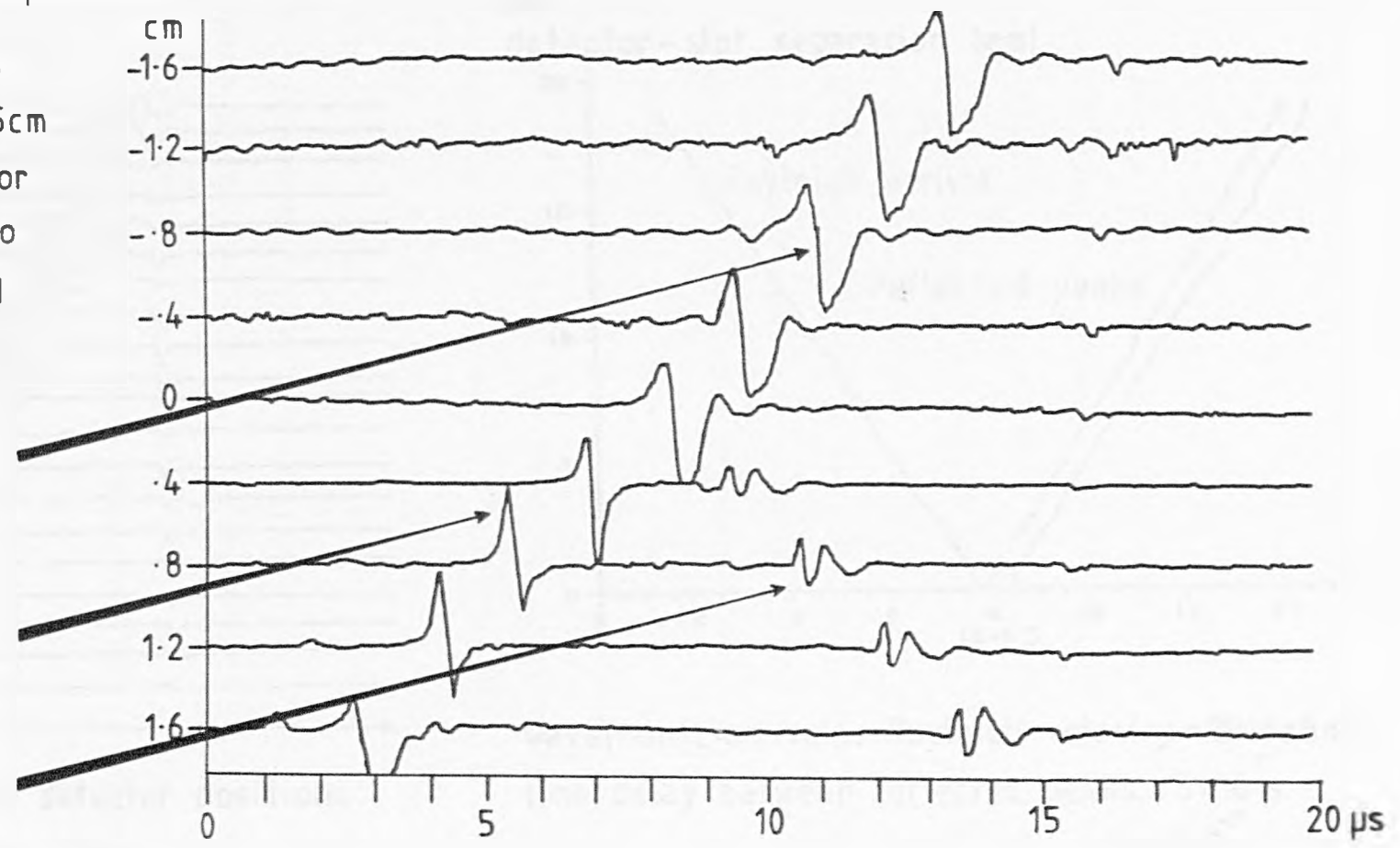
Fig. 9.12 shows a scan of surface displacements measured using the experimental arrangement shown in fig. 9.8. The crack is represented by a 0.75mm deep slot in the surface of an aluminium block, and the figure shows a scan of the displacements as the ball probe receiver is moved from one side of the slot to the other. The dimensions of the block and the source-slot separation are chosen such that there is little interference from bulk waves reflected within the block; in fact a longitudinal bulk wave reflection from the bottom of the block can be seen to occur at about  $16\mu\text{s}$  in the display. The different waveforms shown in fig. 9.12, and all the following displays of this type, have been adjusted to have the same incident Rayleigh wave peak to peak amplitude.

The transmitted surface pulse is broadened by the interaction because the high frequency components have been reflected by the crack; this was demonstrated in the previous section. The reflected pulse has the same initial bipolar form as the incident pulse but it also contains a second positive pulse feature. Fig. 9.13a shows a more detailed reflection scan of the same slot and fig. 9.13b is a plot of peak amplitude arrivals in the scan. From this peak amplitude information the mean time delay and its standard deviation have been evaluated for the time between the positive pulse components of the reflected wave, and the Rayleigh wave velocity with its error have been determined from the gradient of the incident

Fig. 9.12

detector-slot separation  
The laser-acoustic source is maintained at a position 2.5cm from the slot & the detector is scanned across the slot to show the incident, reflected and transmitted pulses.

transmitted, broadened pulse  
incident, Rayleigh pulse  
reflected double pulse



The interaction of a laser generated Rayleigh pulse with a 0.75mm deep slot.

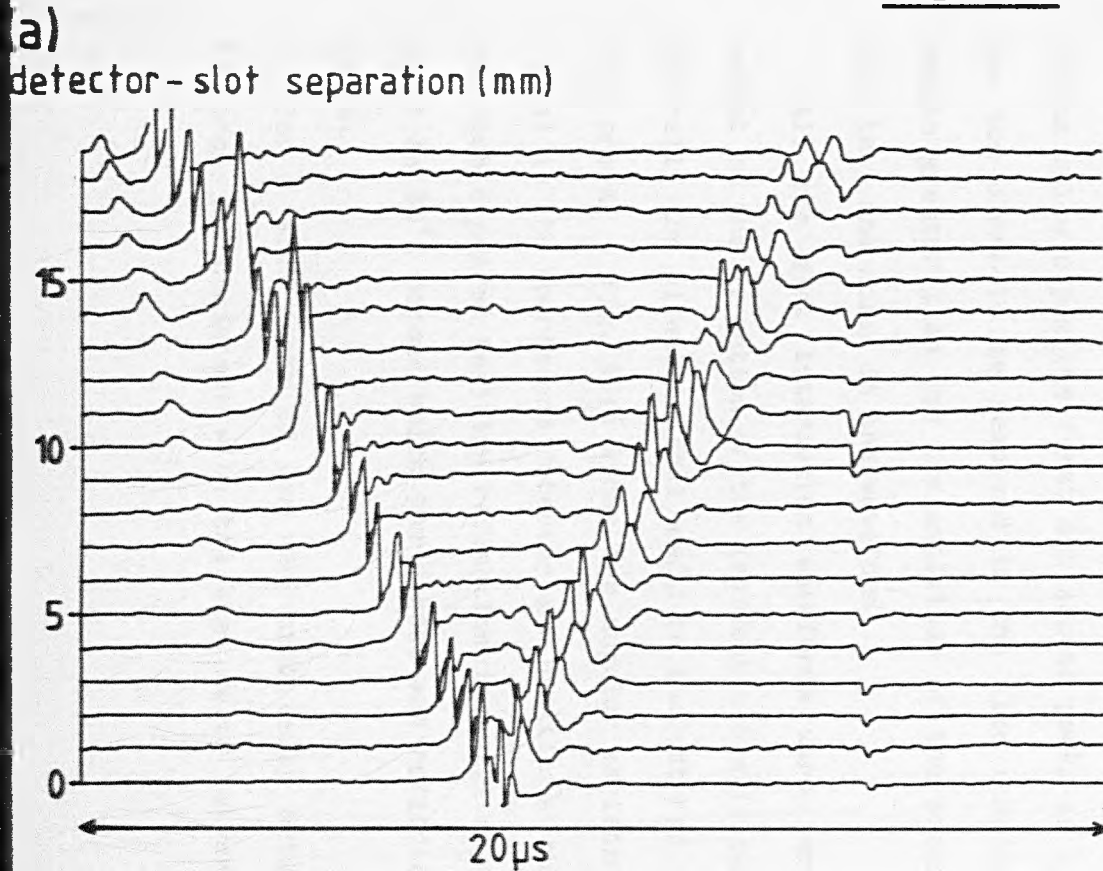


## IMAGING SERVICES NORTH

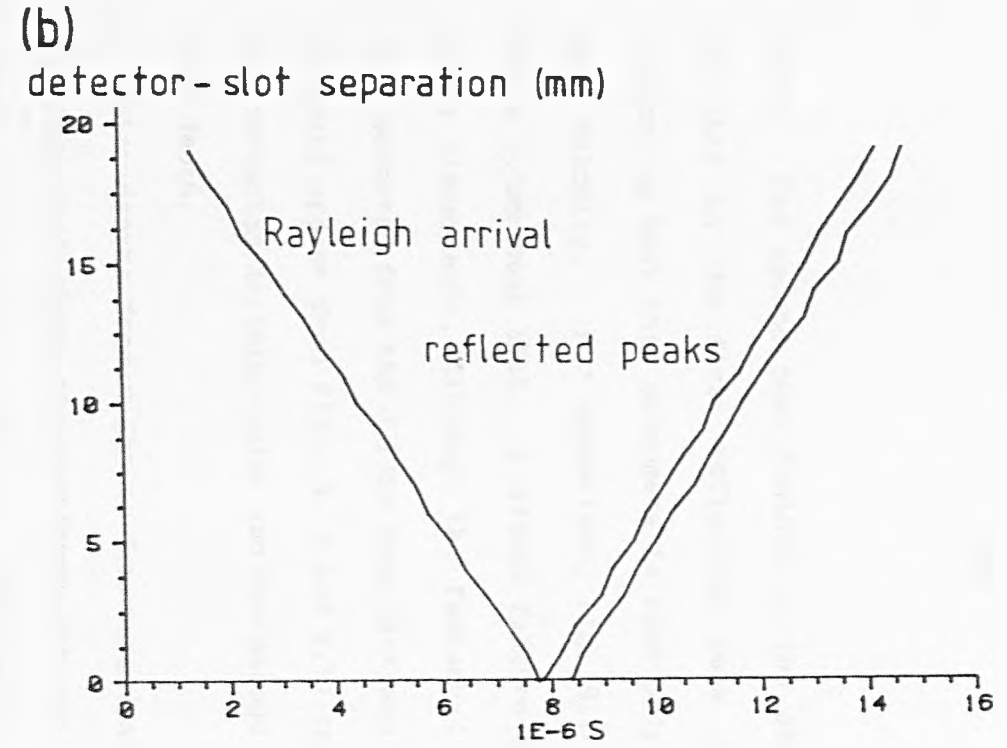
Boston Spa, Wetherby  
West Yorkshire, LS23 7BQ  
[www.bl.uk](http://www.bl.uk)

TEXT CUT OFF IN THE  
ORIGINAL

Fig. 9-13



waveforms recorded at different detector positions  
for a source-slot separation of 2.5cm



wavefront arrivals: Rayleigh velocity =  $2946 \pm 8 \text{ ms}^{-1}$   
time delay between reflected peaks =  $5 \times 10^{-7} \text{ s}$   
 $\sigma = 0.7 \text{ s}$

The reflection of a Rayleigh pulse from a 0.75mm deep slot showing the variation of the reflected components with slot-detector separation.

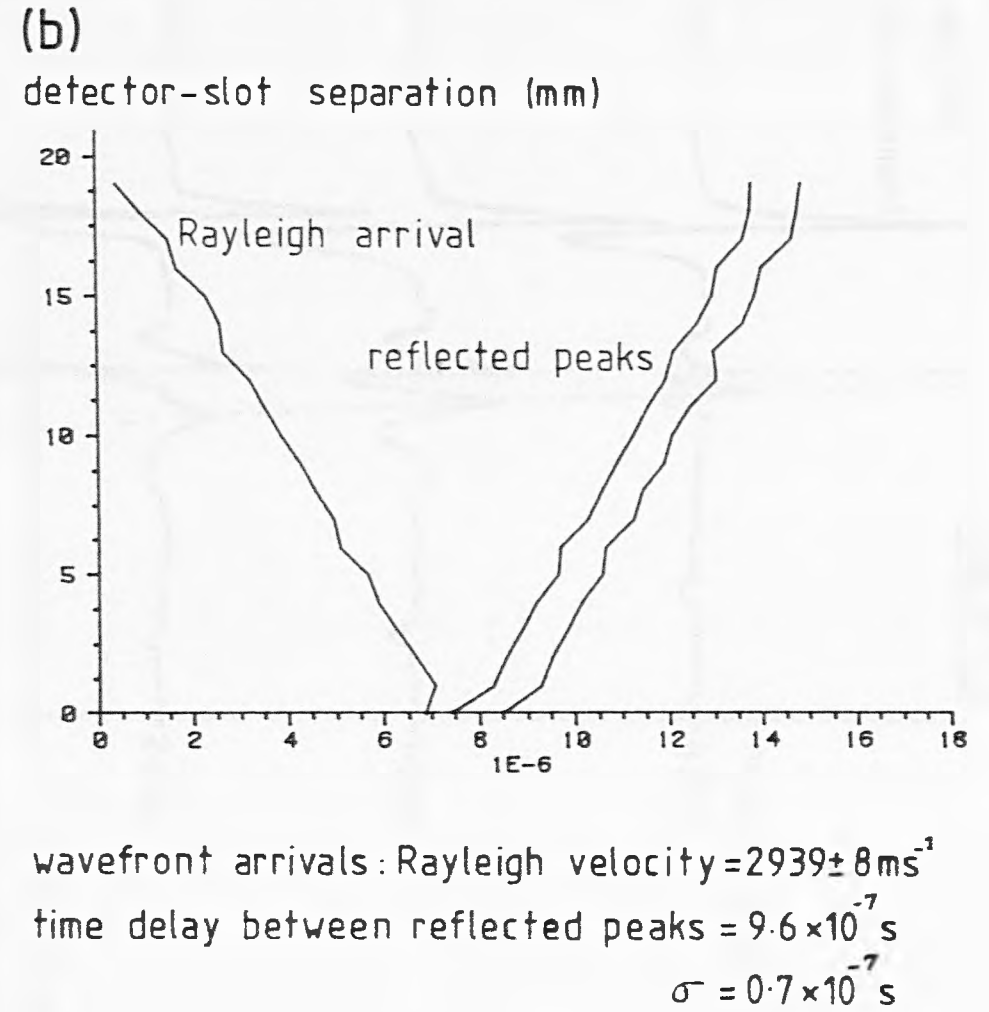
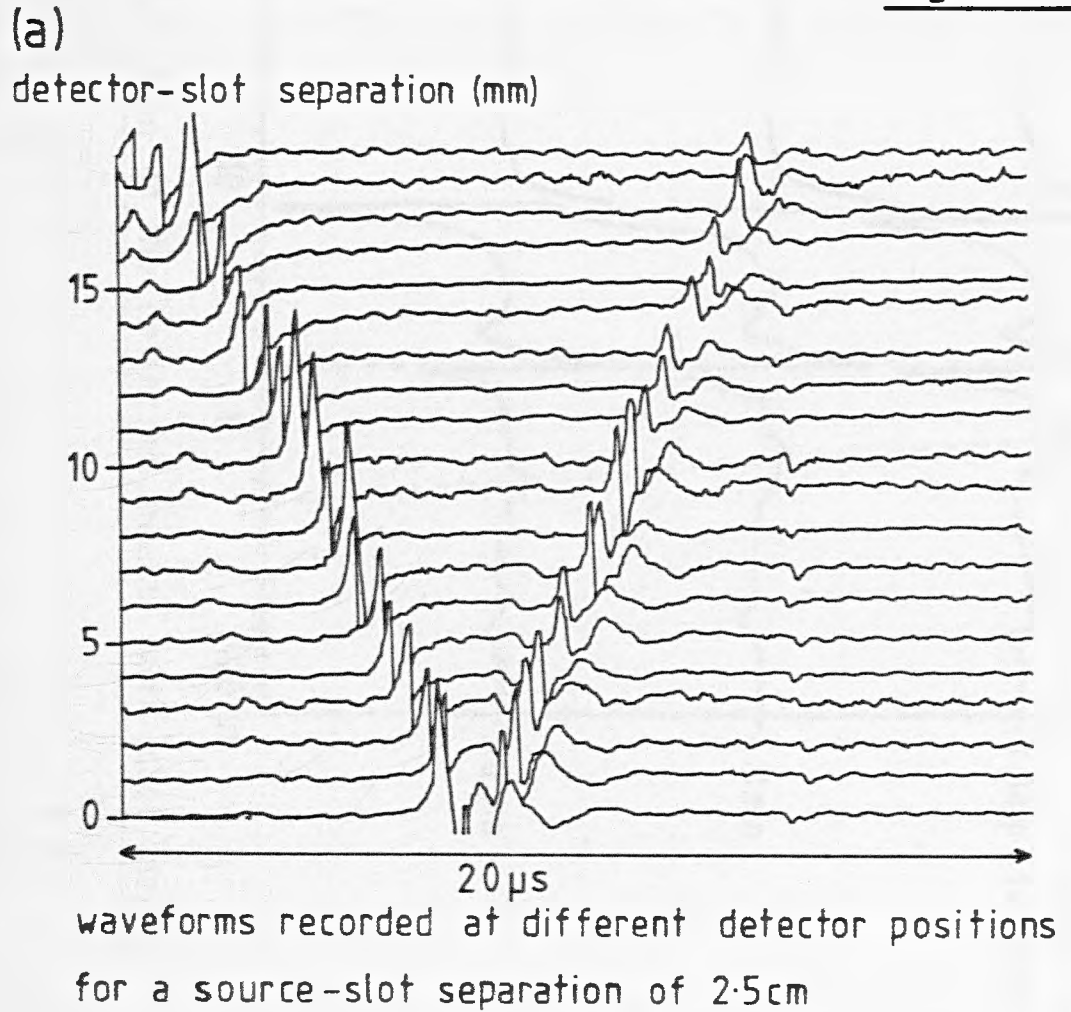
pulse. The second peak feature in the scan can be seen to remain parallel to the first reflection peak with a fixed time delay indicating that this phenomena is also propagating with the Rayleigh wave velocity. For comparison, fig. 9.14 shows the scan obtained for a 1.5mm deep slot. A second feature in the reflected pulse is again discernable, although the feature is of less amplitude than that observed from the 0.75mm deep slot and the time delay is larger. It would appear from figs. 9.13 and 9.14 that the time delay between the reflected Rayleigh pulse and the second feature is related to the slot depth.

Slot depths from 0.3mm to 5mm were investigated in the same way and fig. 9.15 shows the waveforms for six slot depths for the same source-detector-slot distance. The relationship between the second feature and the slot depth is now clearly demonstrated. For slot depths below 0.3mm the first and second peaks in the reflected pulse are too close to be resolved in the time domain, whilst for slot depths greater than 5mm the amplitude of the second feature becomes less than the noise in the waveform.

All the slot interaction waveforms were recorded for a slot normal to the direction of the incident acoustic pulse. This is not generally the situation that would be encountered when testing for a real crack. Fig. 9.16 shows the angular variation of the detected signal as the source and detector are positioned oblique to the line. The double peaked Rayleigh reflection is still apparent at angles as great as  $80^\circ$ , beyond which the direct and reflected pulses begin to merge.

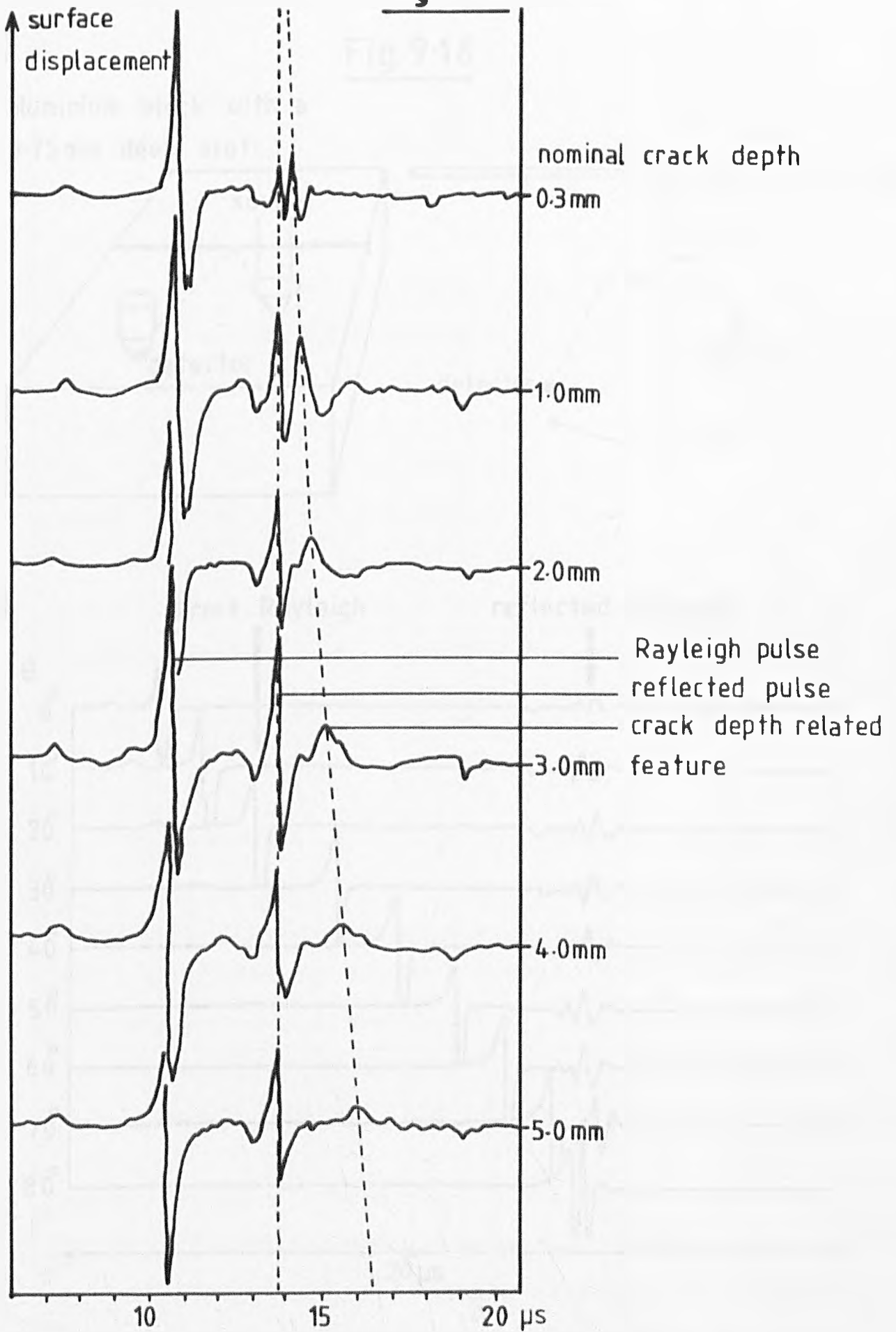
For a slot depth of 1mm the time delay between the reflected features is consistent with the time delay between a Rayleigh wave

Fig. 9.14



The reflection of a Rayleigh pulse from a 1.5mm deep slot showing the variation of the reflected components with slot-detector separation.

Fig. 9.15

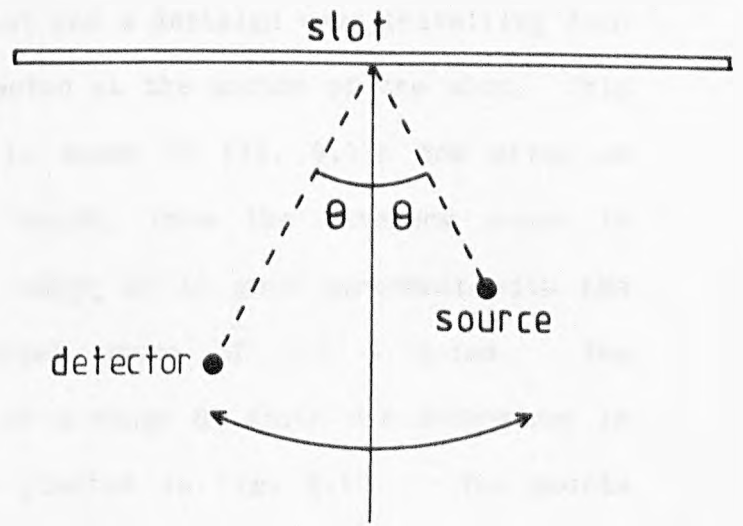
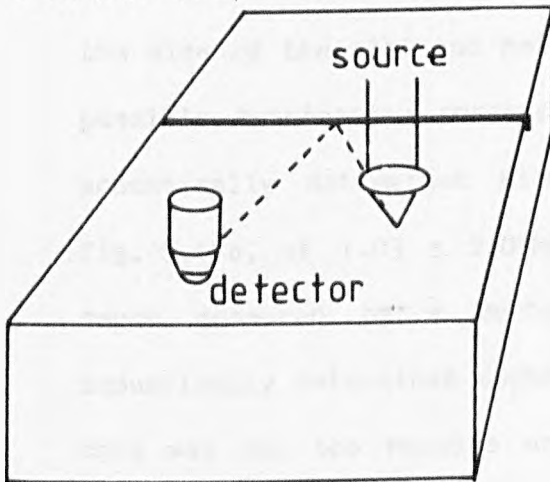


Variation of the reflected peaks with slot depth.

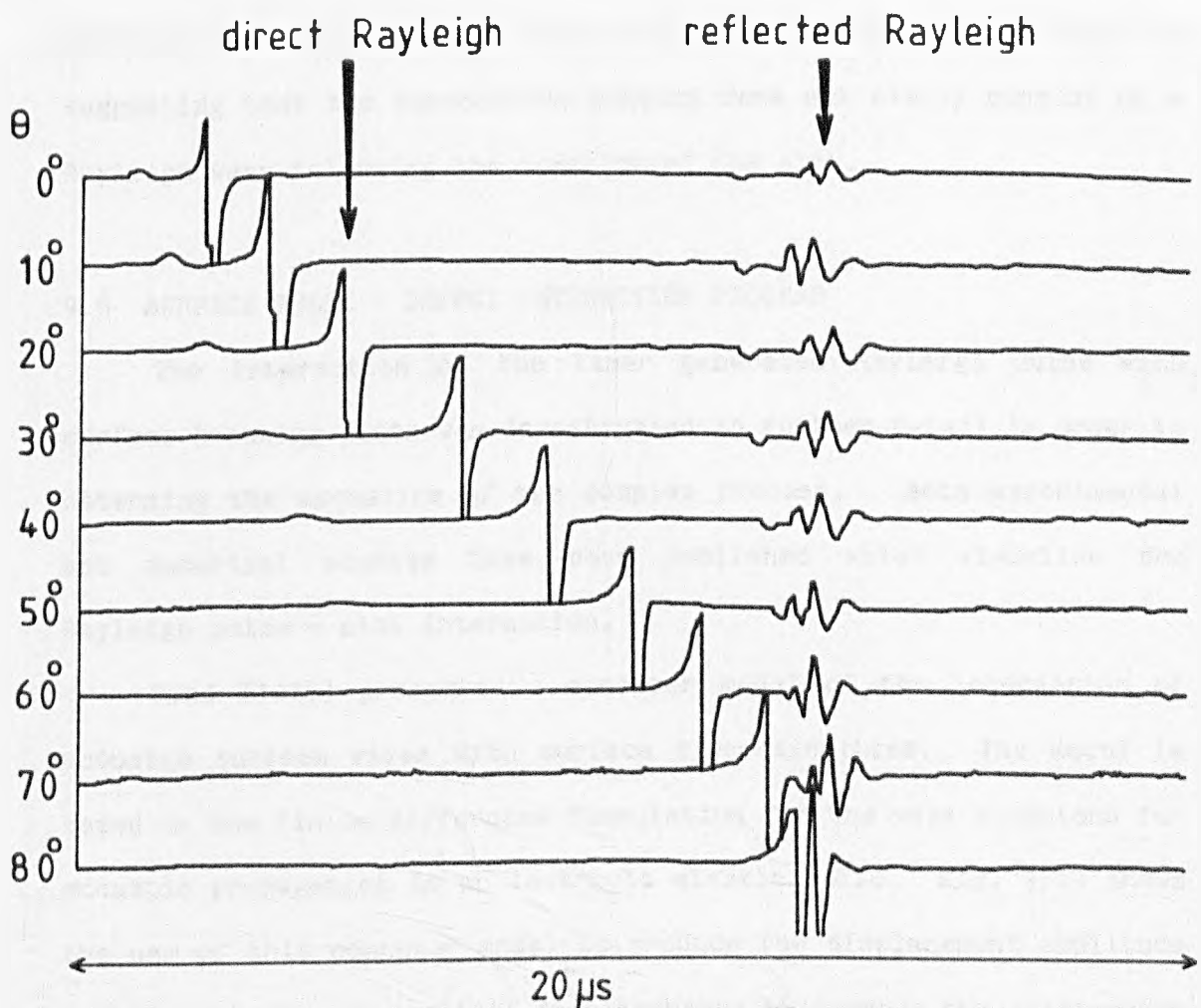
(a)

Fig. 9-16

aluminium block with a  
0.75mm deep slot



(b)



The angular variation of the reflection of a laser generated Rayleigh pulse from a 0.75mm deep slot.

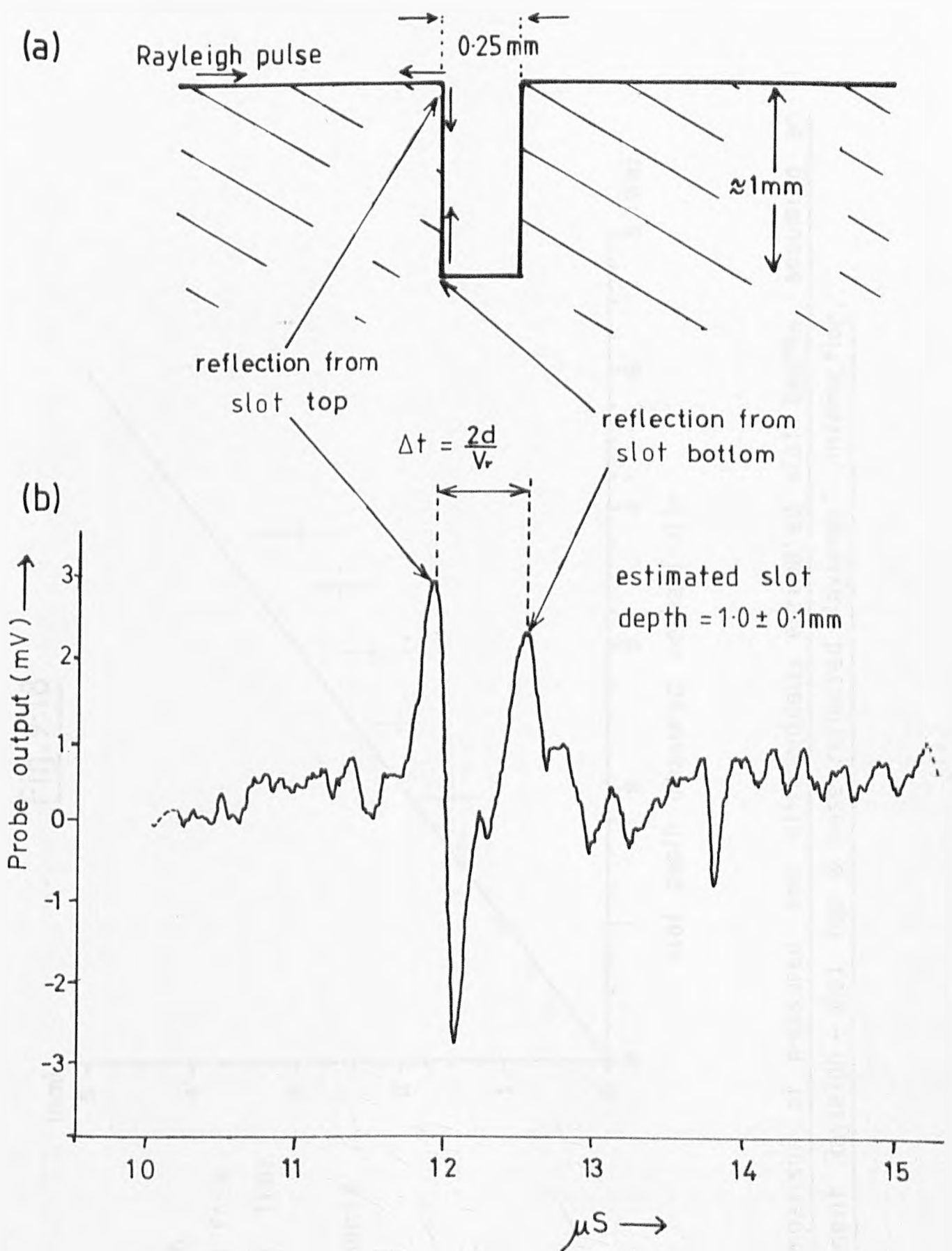
reflected at the top of the slot and a Rayleigh wave travelling down the side of the slot and reflected at the bottom of the slot. This possible interaction process is shown in fig. 9.17a and gives an acoustically determined slot depth, from the waveform shown in fig. 9.17b, of  $1.03 \pm 0.09\text{mm}$  which is in good agreement with the depth measured by a mechanical gauge of  $1.0 \pm 0.1\text{mm}$ . The acoustically determined depth of a range of slots was determined in this way and the results are plotted in fig. 9.18. The points should lie along the  $45^\circ$  line shown in the figure. The ultrasonic slot depth estimates are good for slot depths around 1mm but start to deviate from the expected values for slot depths greater than 2mm suggesting that the interaction process does not simply consist of a Rayleigh wave following the contours of the slot.

#### 9.6 SURFACE PULSE - DEFECT INTERACTION PROCESS

The interaction of the laser generated Rayleigh pulse with surface breaking slots was investigated in further detail in order to determine the mechanism of the complex process. Both experimental and numerical studies have been published which visualise the Rayleigh pulse - slot interaction.

Bond (1979) presented a computer model of the interaction of acoustic surface waves with surface discontinuities. The model is based on the finite difference formulation for the wave equations for acoustic propagation in an isotropic elastic solid. Fig. 9.19 shows the use of this computer model to produce the displacement amplitude and time history of particle displacements throughout the interaction of a Riker pulse with a 4mm deep slot. The incident Riker pulse, fig. 9.19a, contains a smooth wavenumber spectrum with a centre

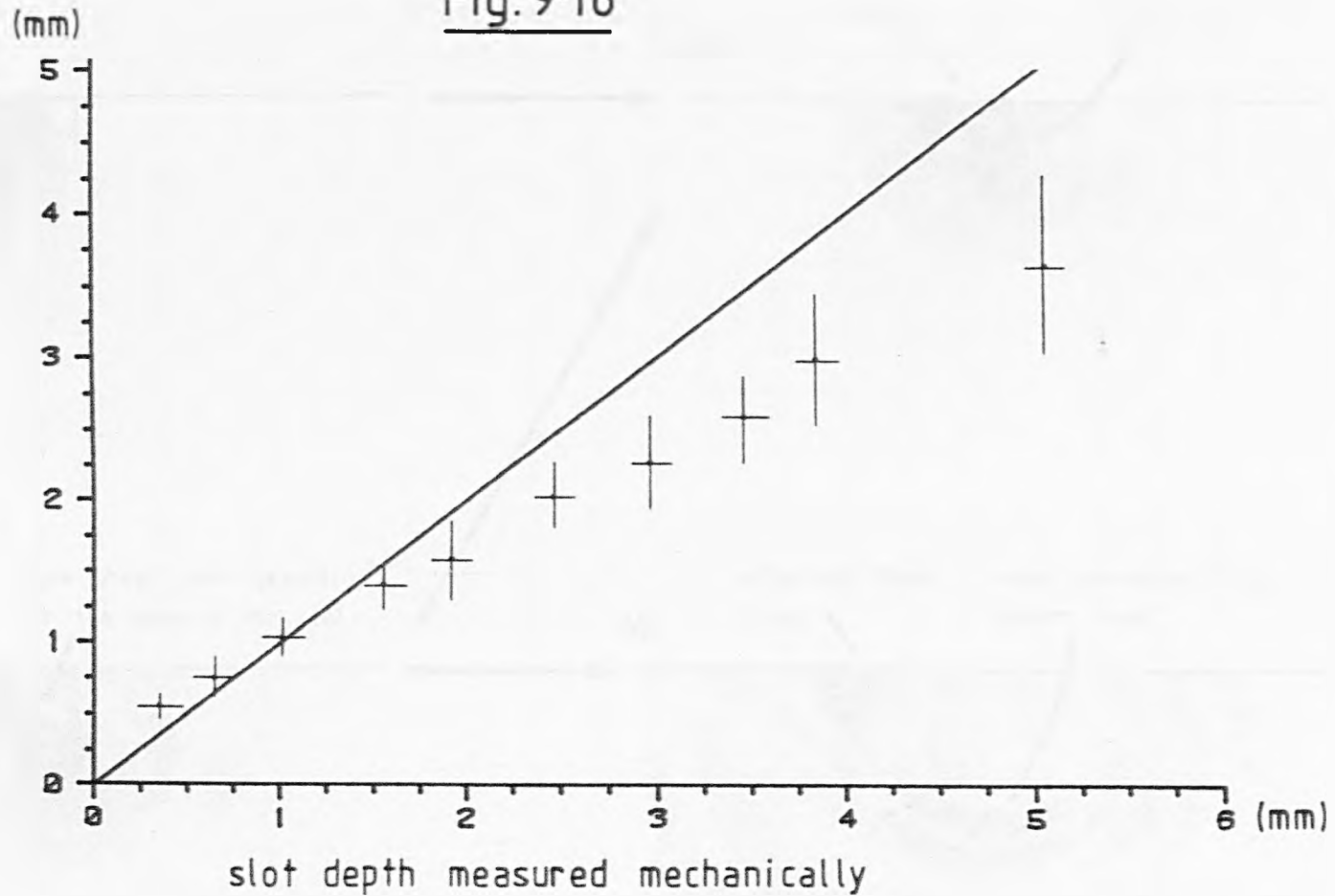
Fig.9-17



Details of the reflected pulse and the possible origin of its details.

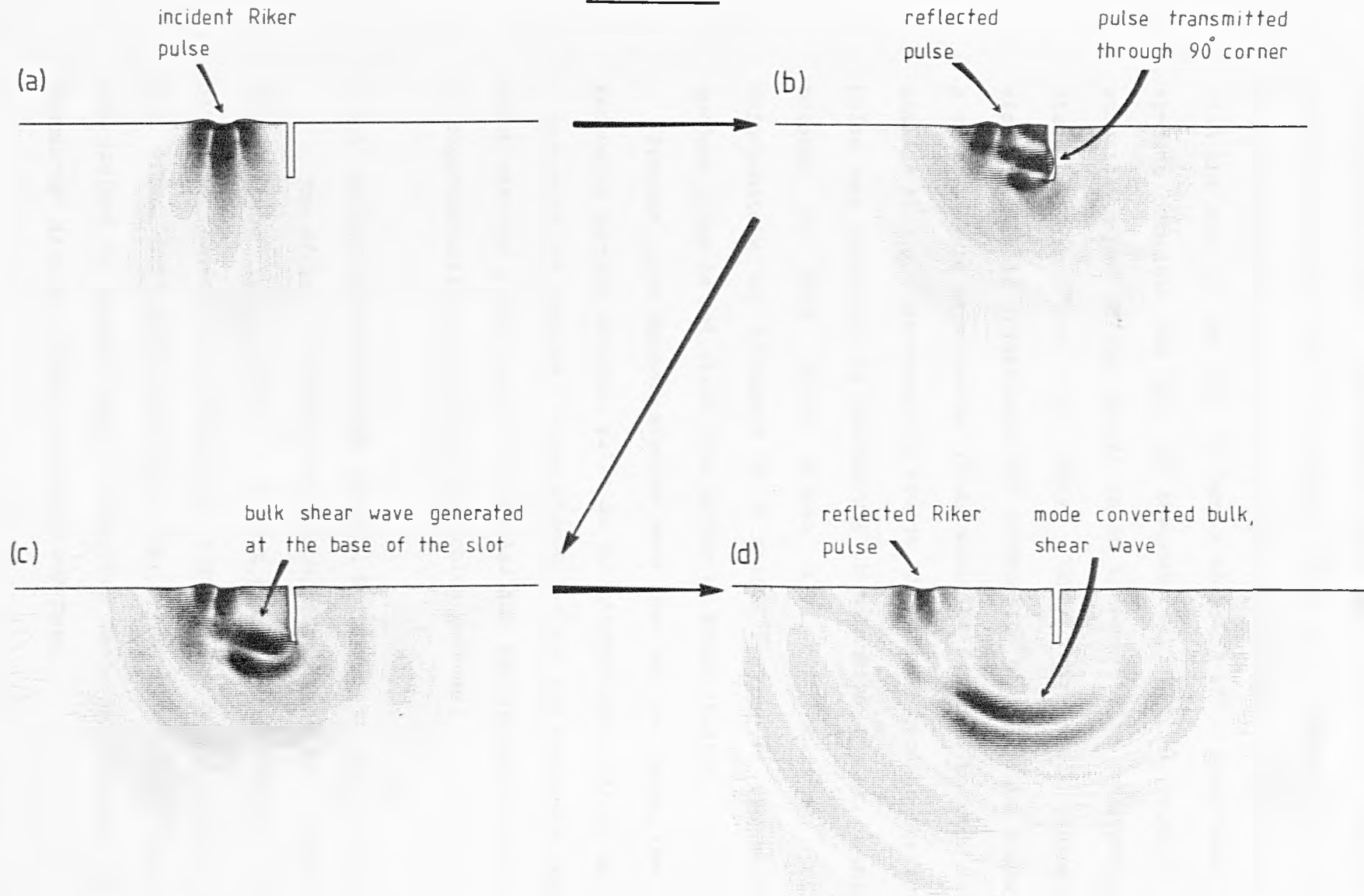
Fig. 9-18

slot depth  
estimated from  
ultrasonic, time  
of flight  
measurements



A comparison of measured and ultrasonically estimated slot depths assuming an "incident Rayleigh - slot top & base reflected Rayleigh" interaction.

Fig. 9-19



Finite difference, numerical model of the interaction of a 1MHz centre frequency Riker pulse with a 4mm deep rectangular slot in the surface of an elastic half-space.

frequency of 1MHz. The surface pulse is partially reflected at the edge of the slot, and a transmitted Riker pulse can be seen to travel down the sidewall of the slot in fig. 9.19b, after which it interacts with the base of the slot to form a mode converted shear wave which spreads out into the bulk of the material, fig. 9.19c,d. This numerical model of the events is in agreement with an experimental study by Reinhardt and Daly (1970) who used photoelastic visualisation to investigate the interaction of a surface pulse with a slot. This experimental study would be expected to show results similar to the laser-acoustic source interaction because the surface pulse was generated by detonating an explosive pellet, a similar process to that which drives the oil ablation process. Unfortunately the existence of a second feature in the reflected surface pulse is not clear from either of these studies.

Further experimental studies were carried out using the laser generated surface acoustic pulse on the interactions with an up-step, a down-step and corners. These geometries are the component features which make up a slot and the investigation was carried out in order to experimentally analyse the interaction process.

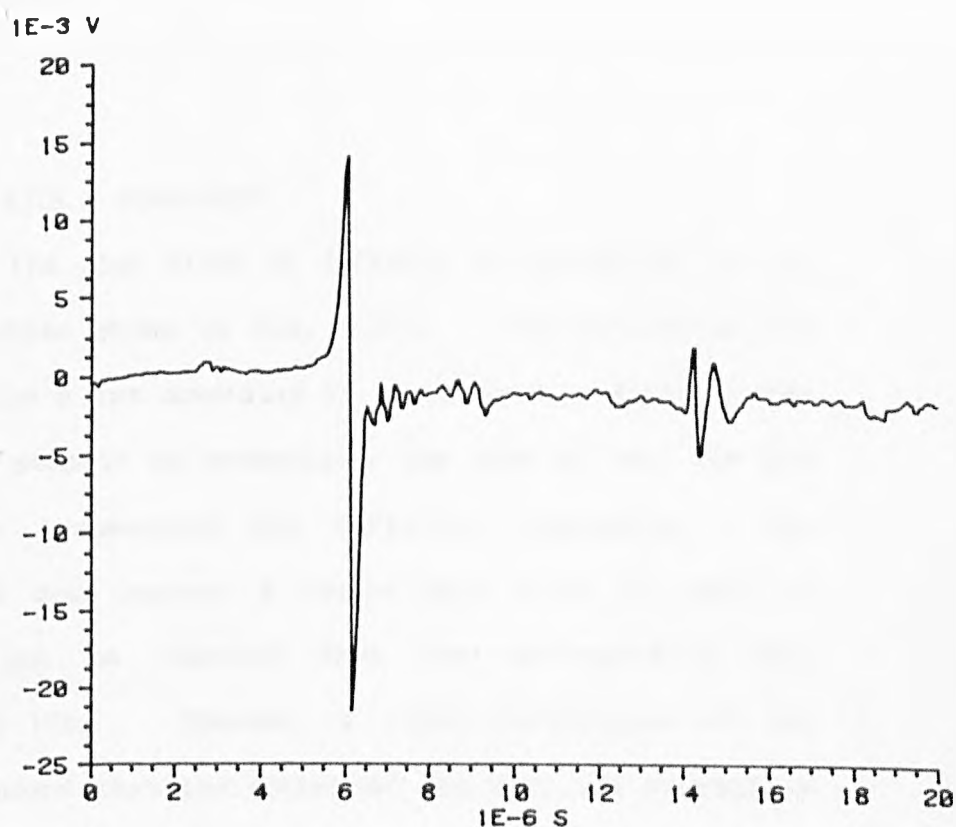
#### 9.6.1 REFLECTION FROM NARROW AND WIDE SLOTS

The effect of varying the width of the slot for a 0.5mm deep slot is shown in fig. 9.20. In fact there is very little, if any, difference between the reflection signals for a 0.3mm wide slot, fig. 9.20a, and a 0.7mm wide slot, fig. 9.20b, although Morgan (1974) has claimed to measure slot widths from features appearing in the "cepstrum" display of the reflection waveform.

Fig.9.20

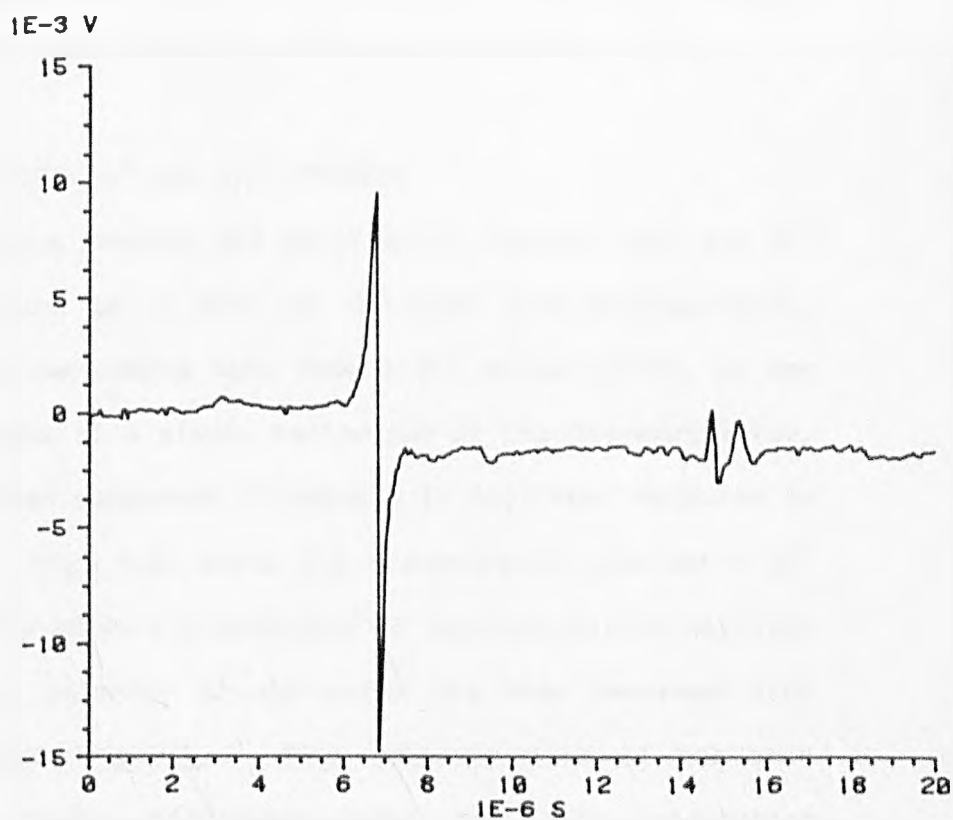
(a)

incident and  
reflected Rayleigh  
peaks from a  
0.46mm deep,  
0.3mm wide slot



(b)

incident and  
reflected Rayleigh  
peaks from a  
0.53mm deep,  
0.7mm wide slot



The variation of the reflection peaks with the slot width  
for a slot depth of approximately .5mm.

### 9.6.2 INTERACTION WITH A DOWN-STEP

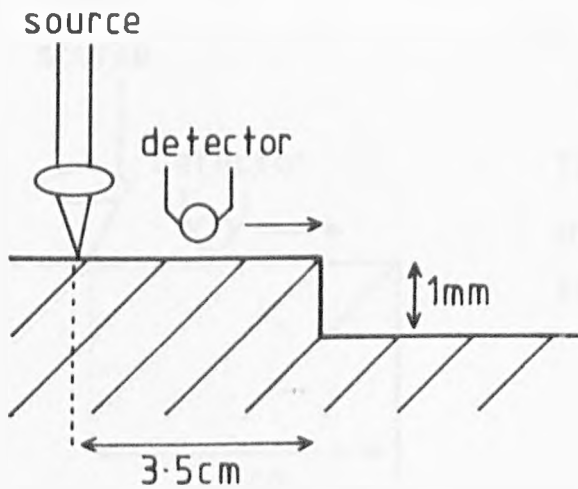
Extending the slot width to infinity is equivalent to the down-step configuration shown in fig. 9.21a. The reflection and transmission scan for a 1mm down-step is shown in fig. 9.21b. The interaction can be seen to be essentially the same as that for the slot showing both transmitted and reflected components. The reflected component does contain a second peak which is lower in amplitude than might be expected from the corresponding slot experiment, fig. 9.17b. However, a close examination of the aluminium sample showed that the corner of the step was rounded, a consequence of the practical limitations of machining the sample, and a rounded corner has been shown to interact poorly with Rayleigh wavelengths less than the radius of curvature (Viktorov, 1967).

### 9.6.3 INTERACTION WITH $90^\circ$ AND $270^\circ$ CORNERS

The interaction process was split still further into the  $90^\circ$  and  $270^\circ$  corners which go to make up the down step configuration. Fig. 9.22 shows the reflection scan from a  $90^\circ$  corner which, as one would expect, consists of a simple reflection of the Rayleigh pulse, although the reflected component is reduced in amplitude relative to the direct pulse. Fig. 9.23 shows the transmission scan for a  $90^\circ$  corner and it clearly shows the existence of the transmitted Rayleigh pulse, although the polarity of the pulse has been reversed with respect to the incident pulse. This polarity reversal has been predicted in the finite difference model for this interaction (Bond, 1979). We may therefore conclude that it is this transmitted pulse which then interacts with the bottom of the slot and eventually

Fig.9.21

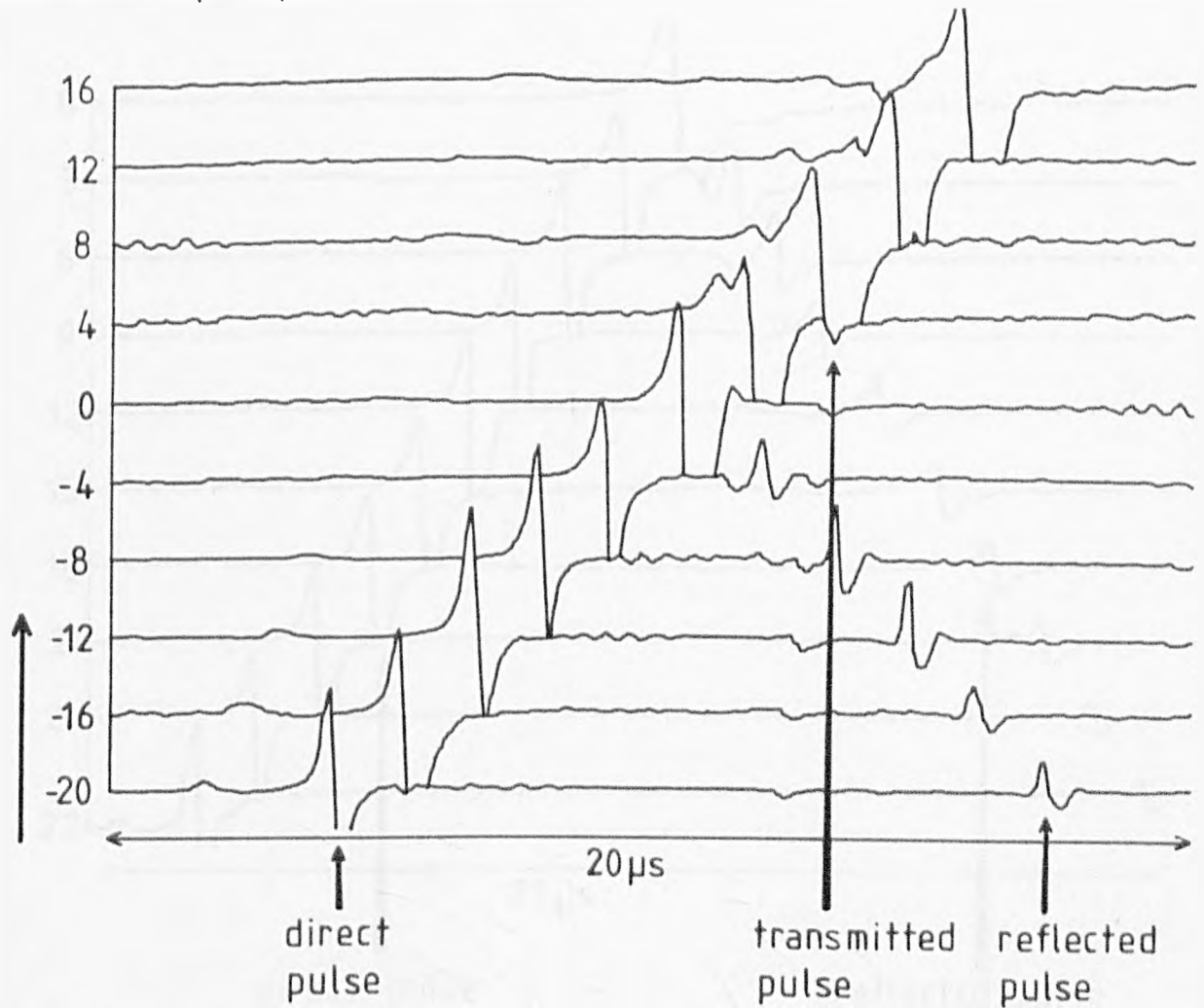
(a)



The source generates a Rayleigh pulse on the upper level of a 1mm down step and the detector is scanned from the upper to the lower level.

(b)

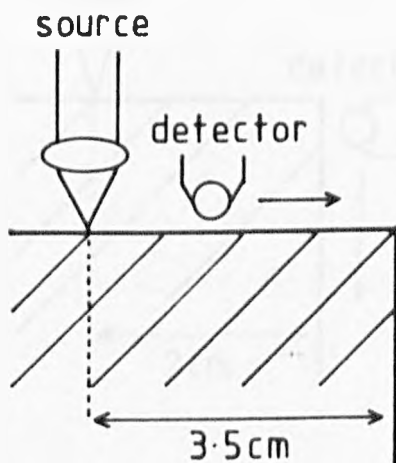
detector-step separation (mm)



The interaction of a laser generated Rayleigh pulse with a 1mm down step.

Fig.9.22

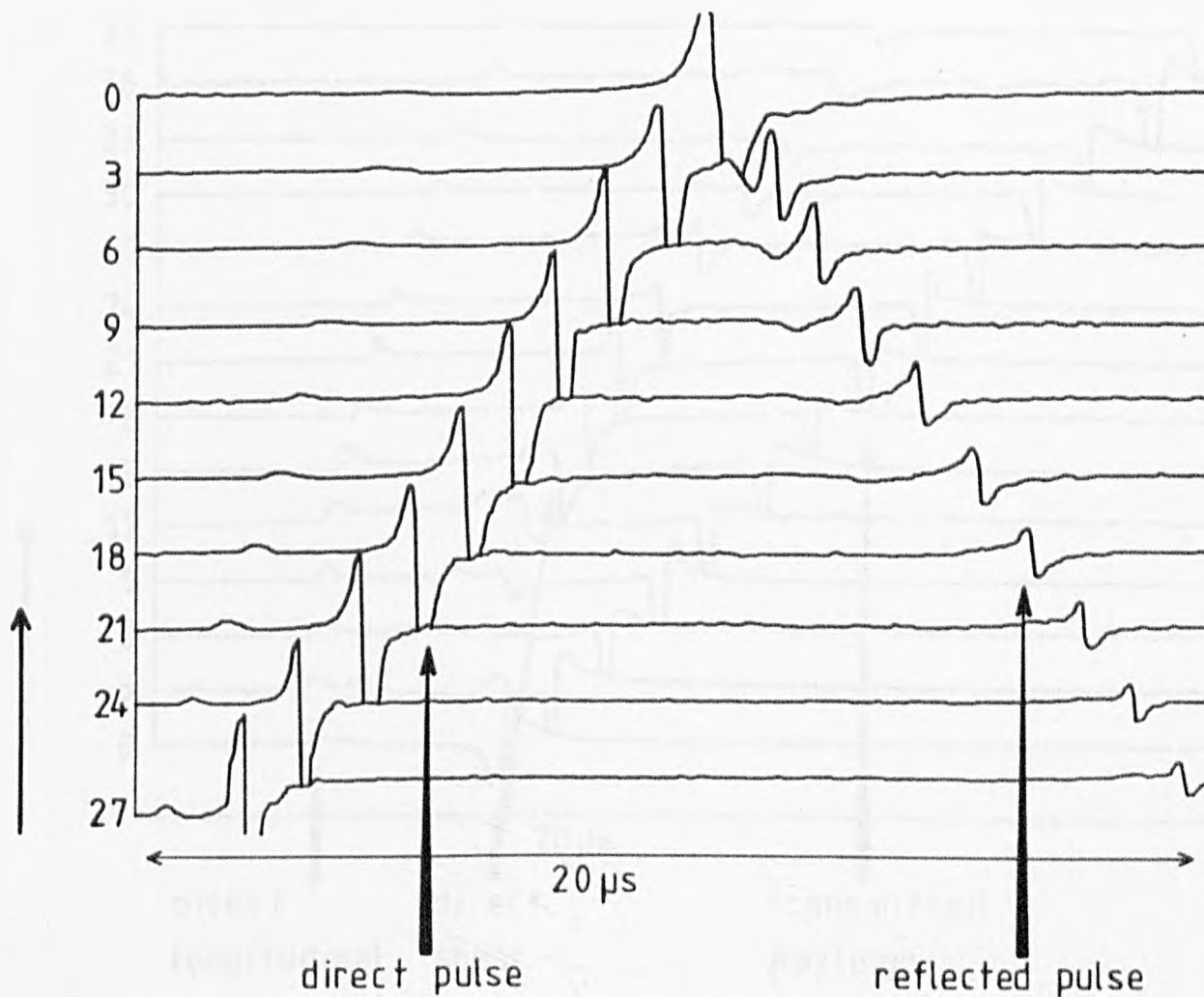
(a)



The detector is scanned in  
in 3mm increments towards  
the  $90^\circ$  corner.

(b)

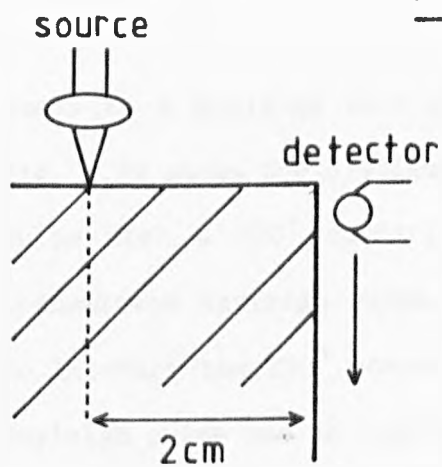
detector-corner separation (mm)



The reflection of a laser generated Rayleigh pulse from  
a  $90^\circ$  corner.

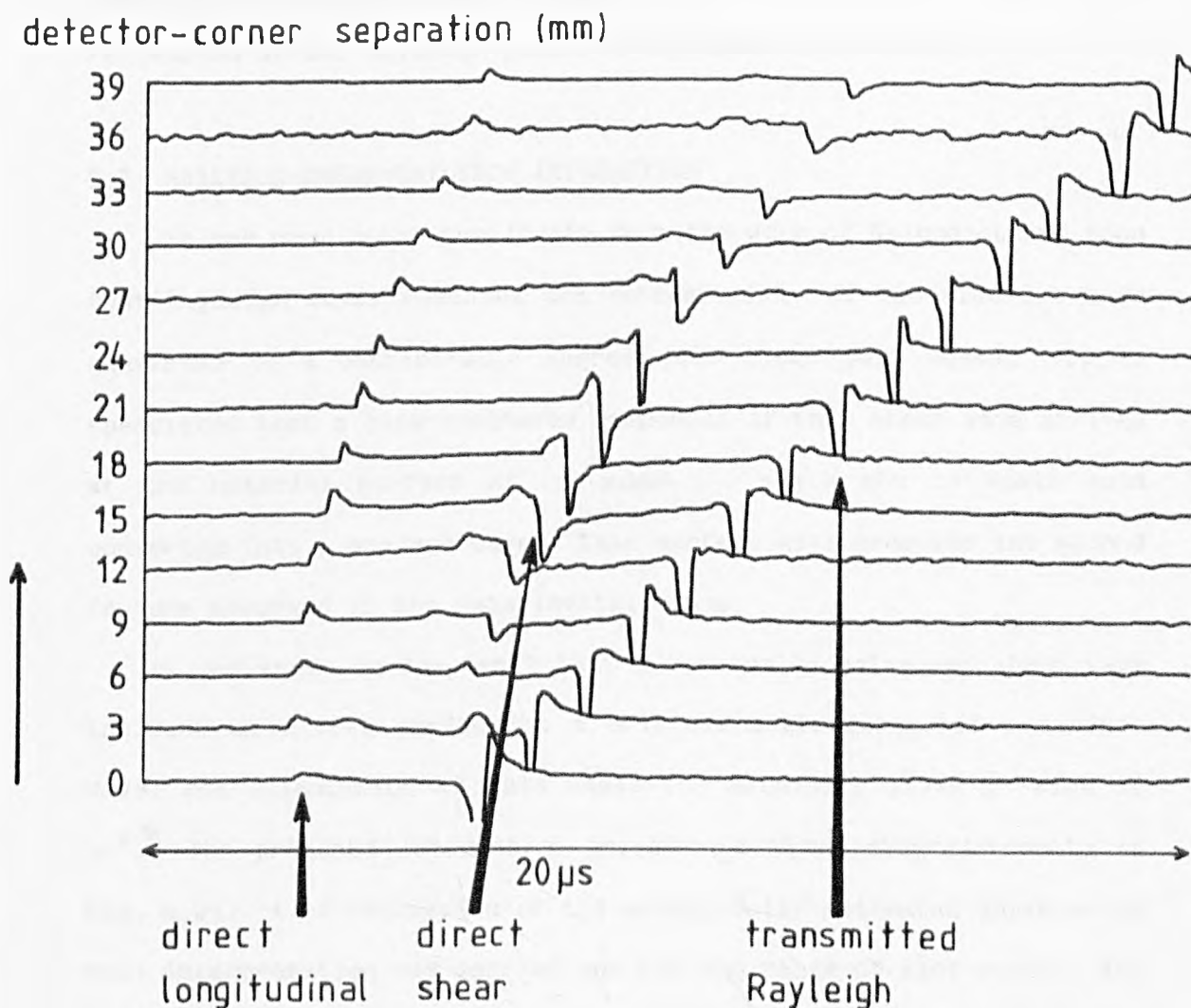
(a)

Fig.9.23



The detector is scanned in  
in 3mm increments from  
the 90° corner.

(b)



The transmission of a laser generated Rayleigh pulse around a 90° corner.

leads to a Rayleigh wave component being observed at the detector. Fig. 9.24 shows the displacement scan for the interaction of Rayleigh pulse with a  $270^\circ$  corner; this configuration corresponds to the transmitted Rayleigh pulse travelling down the sidewall of the slot to interact the  $270^\circ$  corner at the base of the slot. The incident Rayleigh pulse can be clearly seen but there is no detectable arrival corresponding to the reflection of the Rayleigh pulse at the corner. This result would indicate that it is not possible for the interaction process considered in Section 9.5 to occur; there is no reflection of the Rayleigh pulse at the base of the slot.

#### 9.7 RAYLEIGH-SHEAR-RAYLEIGH INTERACTION

It has been noted previously from the work of Reinhardt and Bond that Rayleigh waves reaching the bottom corner of the slot are mode converted to a considerable degree into shear bulk waves. It is speculated that a back-scattered component of this shear wave arrives at the material surface at some angle and is again mode converted into a surface wave. This surface wave produces the second feature observed in the experimental scans.

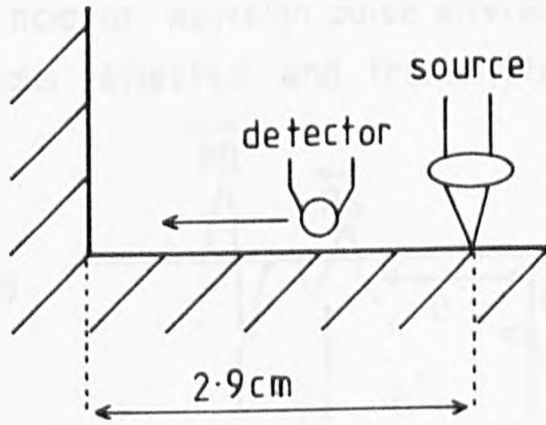
It was shown in Chapter 2 that a vertically polarised shear wave incident on a free surface at a critical angle generates a surface wave, and calculation of this angle for aluminium gives a value of  $30^\circ$ .\* The proposed interaction process is shown diagrammatically in fig. 9.25. A re-evaluation of the acoustically estimated depth using this interpretation was carried out for the range of slot depths, and a graph of the mechanically measured slot depth against the acoustic estimate is shown in fig. 9.26. Using this interpretation of the interaction process the acoustic slot depth data is in reasonable

\*

It was demonstrated by Pekeris et al (1957), that for angles greater than this a Rayleigh pulse is generated by a buried source.

Fig. 9.24

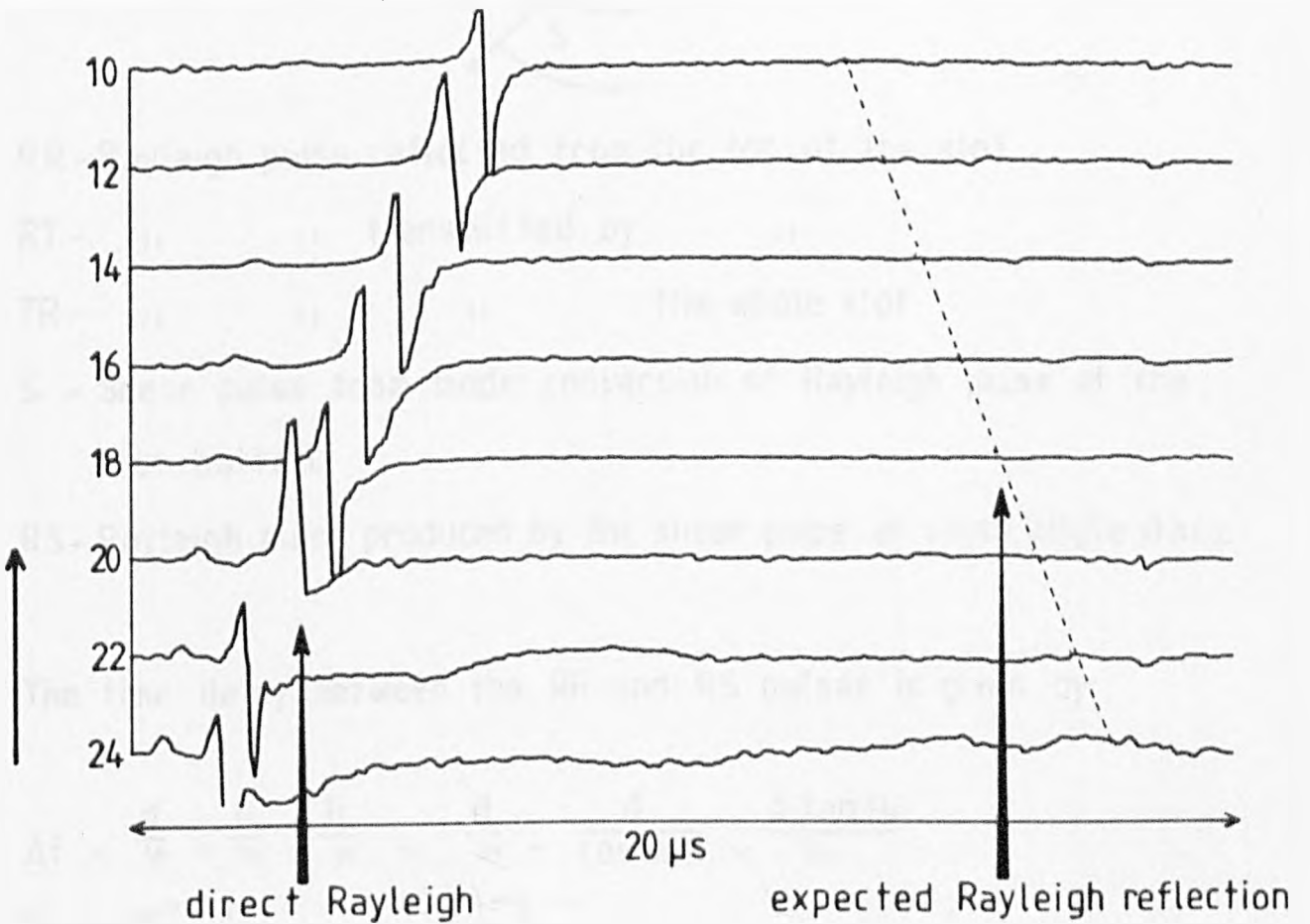
(a)



The detector is scanned in 2mm increments towards the 270° corner.

(b)

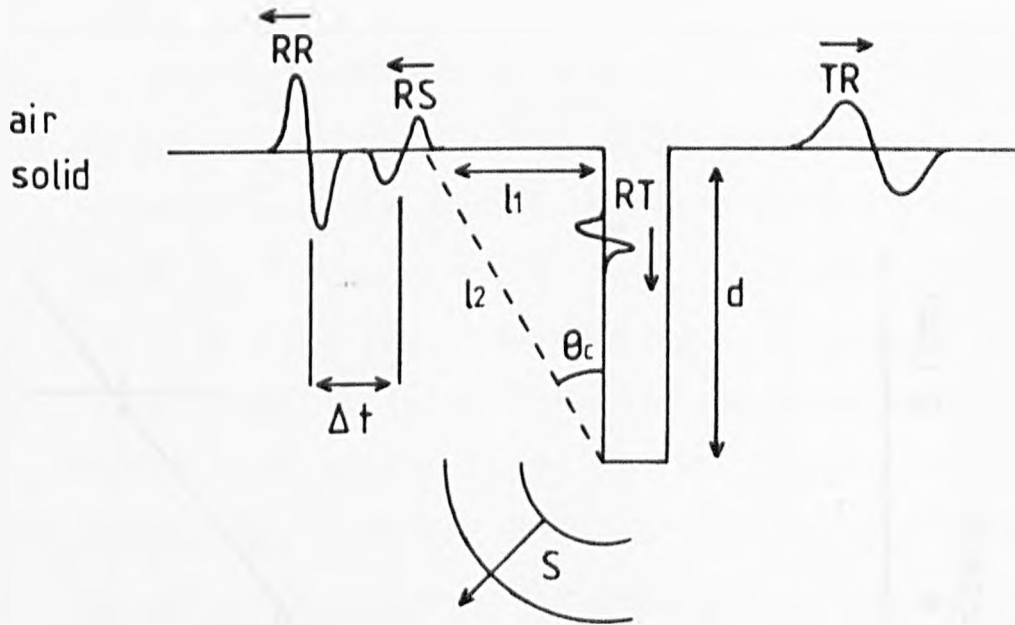
detector-corner separation (mm)



The interaction of a laser generated Rayleigh pulse with a 270° corner.

Fig.9-25

An incident Rayleigh pulse interacts with a slot to produce various reflected and transmitted pulses.



RR-Rayleigh pulse reflected from the top of the slot.

RT - " " transmitted by " "

TR - " " " the whole slot.

S - Shear pulse from mode conversion of Rayleigh pulse at the slot bottom.

RS-Rayleigh pulse produced by the shear pulse at some angle  $\theta \geq \theta_c$

The time delay between the RR and RS pulses is given by:

$$\Delta t = \frac{d}{v_r} + \frac{l_2}{v_s} - \frac{l_1}{v_r} = \frac{d}{v_r} + \frac{d}{\cos \theta_c v_s} - \frac{d \tan \theta_c}{v_r}$$

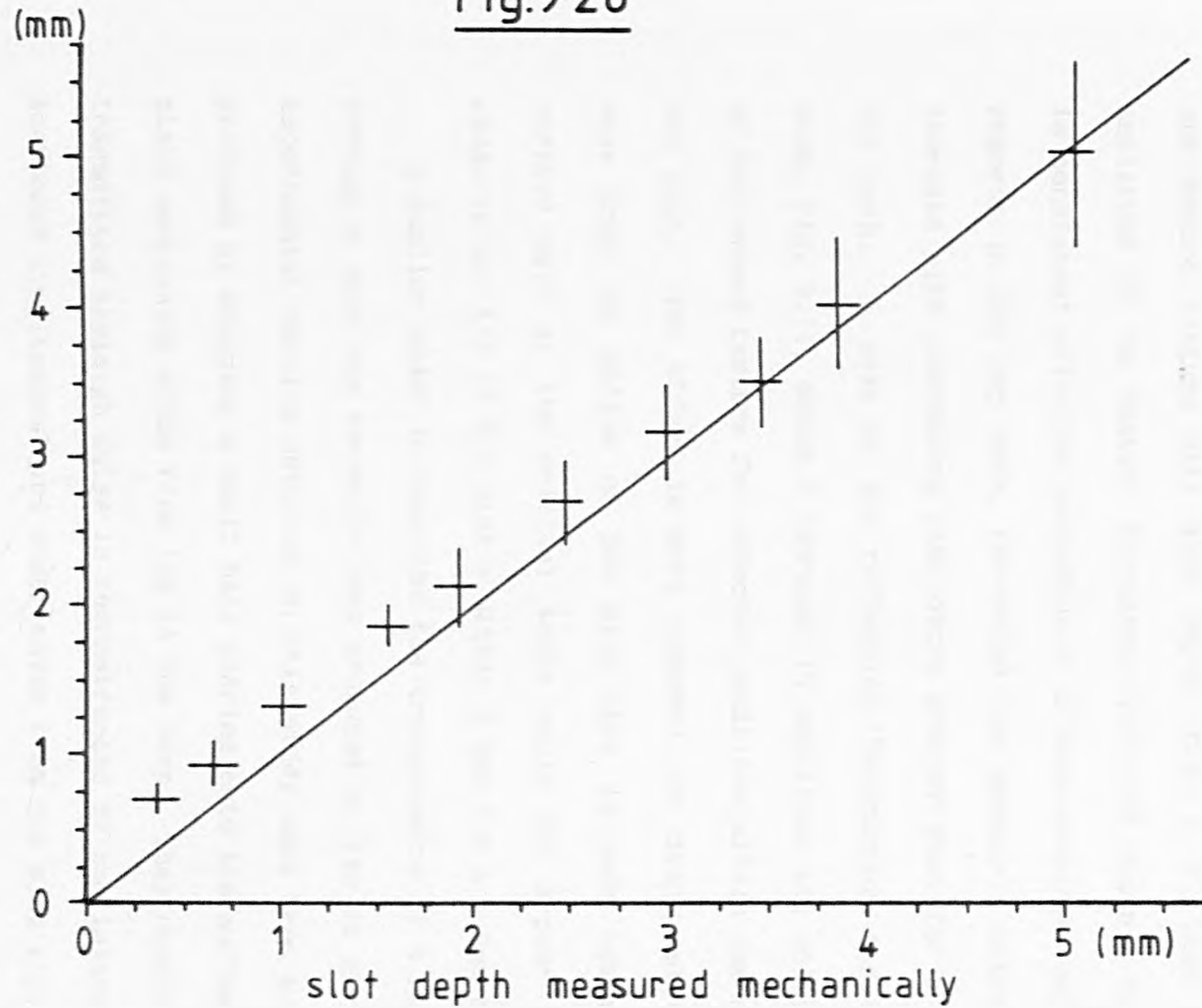
$$\theta_c = 30^\circ$$

$$\Delta t = \frac{d}{\sqrt{3}} \left[ \frac{\sqrt{3}-1}{v_r} + \frac{2}{v_s} \right]$$

A proposed reflection interaction of a Rayleigh pulse with a rectangular surface slot.

Fig.9.26

slot depth  
estimated from  
ultrasonic, time  
of flight  
measurements



A comparison of measured and ultrasonically estimated slot depths assuming a "Rayleigh - shear - Rayleigh" interaction.

agreement with the known values for slots greater than 2mm deep and overestimates the slot depth for values less than this.

Several experimentally observed features of the interaction process are consistent with the Rayleigh-shear-Rayleigh interaction interpretation. For example, it can be seen from the variation of the second feature with slot depth, fig. 9.15, that the relative amplitude of the feature decreases with slot depth; this behaviour is consistent with the inclusion of a mode converted bulk shear wave segment in the ray path, for which the geometric attenuation would increase with increasing slot depth greater than for a surface wave ray path. A scan of the reflection interaction for a 1.5mm deep slot, fig. 9.14, shows a decrease in amplitude and shift in position of the second feature for detector positions within 1mm of the top of the slot. The effect is more apparent for deeper slots. A shear wave from the bottom of the slot that is mode converted into a surface wave at the critical angle would not appear at positions close to the top of the slot - within 0.9mm for a 1.5mm deep slot.

A similar model to describe the transmission of a Rayleigh pulse through a slot has recently been proposed by Yew et al (1984). The experimental results obtained in this study were from Rayleigh waves produced by dropping a small ball bearing onto the surface of a large plate containing slots from 1cm to 8cm deep. They concluded that the transmitted Rayleigh pulse is reconstructed by the interaction of the scattered longitudinal and shear waves from the slot tip.

The interaction of laser generated Rayleigh waves with real cracks has not been investigated and it is important to note some differences between the slot mode presented here and the characteristics of fatigue or weld produced surface breaking cracks:

only the scatter from a single slot has been considered; the slots are uniform and not multi-branched; the slots are open and provide a distinct material discontinuity (fatigue cracks are generally very tight unless under stress); and any residual surface stress encountered in test components would alter the time-of-flight of the acoustic pulses. It would be necessary to investigate these processes before the method presented in this section could be used as a reliable NDE technique. However, results in this chapter confirm some of the proposed advantages of the laser over conventional methods of acoustic generation and demonstrate the versatility of the acoustic source for investigating complex defect interactions.

## CHAPTER 10

## SUMMARY AND CONCLUSION

An investigation into the use of laser generated acoustics and its application to non-destructive evaluation has been presented. Previous studies have concentrated on aspects of the generation-interaction process and have been largely qualitative in nature. Similarly, few published articles have described the possible application of this acoustic source to NDE, and again these articles have been qualitative in their conclusions.

The first part of the thesis unifies the physical mechanisms underlying all aspects of laser generated acoustics and presents a general model for the acoustic generation process. This work allows the relative merits of the acoustic source to be assessed in comparison with the conventional methods of NDE. The second part of the thesis shows some of the areas of NDE in which laser-acoustic generation might play a useful role.

The generation of acoustic transients by the laser irradiation of a metallic surface has been characterised by two extreme situations depending on the laser intensity. Low power densities,  $< 10^7 \text{ Wcm}^{-2}$  of  $1.06\mu\text{m}$  radiation, cause a rise in temperature of the surface of the material with no change in phase, and acoustic generation is due to the stresses resulting from the thermal expansion of the surface material against the surrounding colder material. At higher power densities,  $> 10^8 \text{ Wcm}^{-2}$ , the surface heating is sufficient to form a plasma and the acoustic generation is due to the recoil force as

material is evaporated into a plasma. A third mechanism of acoustic generation is discussed which arises from the constraint of the surface of the material by a transparent covering layer. The spatial dependence, magnitude and time histories of these different mechanisms have been derived in order to predict the consequent form of the generated acoustic transients.

The far-field surface displacements arising from these surface force distributions have been derived and compared with those measured experimentally using wideband calibrated acoustic transducers. Conversely the acoustic displacement data has been used to evaluate the form of the plasma driving force arising from the complex laser-plasma interactions. The derivation of the predicted acoustic displacement fields have included the first representation of the surface displacements produced by a point and extended thermoelastic expansions. The acoustic displacements on the surface of the material are seen to be dominated by the Rayleigh surface wave arrival, the form of which is determined by the spatial extent of the source in the thermoelastic regime, and the epicentre displacements are dominated by the longitudinal and shear wave arrivals.

The amplitude directivity of these bulk acoustic waves for the different generating mechanisms has been determined experimentally and shows the longitudinal motion in the plasma regime to be directed forward from the source in a wide lobe, whilst both the longitudinal and shear motion for the thermoelastic source is described by narrower, off-axis lobes. The wavefront directivities have been compared with a theoretical model of the process. This directivity model has also been used to determine the energy partition between

the acoustic modes for the different acoustic sources. These predictions and the experimentally observed acoustic displacements show that the oil-layer source produces the largest displacements followed by the plasma source and finally the thermoelastic source. For a 32mJ, 35ns, 1.06 $\mu$ m laser pulse incident on the surface of a 1cm steel plate the epicentre displacements were found to be of the order of 20nm for the longitudinal arrival from the oil-layer source, 5nm for the focused laser plasma source and 2nm for the shear arrival for the unconstrained beam thermoelastic source. The surface wave displacements were found to dominate the bulk acoustic waves in each of these cases.

The characteristics of the laser-acoustic source are now sufficiently well understood to enable it to be applied to NDE. However, these characteristics are somewhat different to those of conventional transducers and it is therefore advisable that new techniques are developed which are best suited to this new acoustic source. Some of the possibilities have been investigated experimentally using artificial defects, and new methods have been demonstrated which enable defects to be located and characterised both within the bulk and on the surface of materials.

The application of the acoustic source to NDE is demonstrated by some experiments incorporating unconventional wideband receiving transducers which have been constructed and characterised and are capable of detecting sub-nanometre displacements with a bandwidth in excess of 5MHz. The presence of laminar defects in thin plates is demonstrated by time-of-flight measurements on transmitted acoustic pulses. The use of time-of-flight, rather than amplitude information, is a new approach to this type of NDE technique and is

only possible because of the brief nature of the laser generated acoustic transients. The high spatial resolution together with the scanning ability of the laser-acoustic source is demonstrated by experiments to determine the integrity of alumina coated steel plates and artificial defects in aluminum plates. The edge of an artificial laminar flaw in a 3mm thick plate has been resolved to less than the plate thickness and, similarly, a 2mm diameter hole in a 4.5mm thick plate has been equally well resolved using the same technique. Areas of de-bond in alumina coated plates have been located which agree with those determined by conventional methods and, additionally, changes in coating thickness of  $< 0.1\text{mm}$  have been resolved. The same system was used to measure the thickness of thin plate by the resonance of the longitudinal acoustic pulses; a brass sheet 0.2mm in thickness was measured using the method.

High amplitude, brief, surface wave pulses generated by the oil-layer source are used to investigate surface breaking slots. The versatility of acoustic generation using an optical beam is demonstrated in a pulse-echo experiment to determine the position of surface defects by scanning directional surface pulses produced by a line-acoustic source. The position and length of a 13mm long surface slot is determined using this scanning technique. Directional enhancement is also achieved by numerical adjustment of the pulse-echo information from multiple source positions; the technique is demonstrated by picking out surface wave reflections from slots in echo signals containing many different arrivals. The interaction of the wideband laser generated surface acoustic pulse, generated by the oil-layer source, with a surface slot has been investigated experimentally. Spectrum analysis of the wideband acoustic transient

after reflection from, and transmission through, a surface slot reveals the dispersive nature of the process. Analysis of the time signatures of the interaction of the laser generated surface acoustic pulse with slots, steps and corners reveals the mechanism of the interaction. This information enables a new interpretation of the interaction process between the surface pulse and the slot to be used to predict slot depths in the range 0.3mm to 5mm. These experimental techniques for NDE using the laser-acoustic source demonstrate some of the possible applications and they require further evaluation using real defects before they could be incorporated into a practical system. There are many potentially useful techniques yet to be investigated.

One of the major advantages of the laser-acoustic source - its non-contacting nature - cannot be fully developed until a practical system incorporating a laser source and a remote detector, eg. a laser interferometer, has been developed. Laser interferometers capable of measuring acoustic displacements have been constructed elsewhere, but they have been less sensitive than the piezoelectric counterparts. The laser-acoustic source, in the thermoelastic regime at least, generates lower amplitude displacements than piezoelectric transducers and there is therefore a requirement to improve present interferometer systems. A combined laser source and remote detection system opens up further possibilities for new NDE applications. In particular, the ability to rapidly scan both the source and detector would enable large areas to be monitored. The scanning ability combined with large data acquisition facilities would allow imaging techniques to be used to locate and visualise defects with unprecedented resolution.

The cost of a laser-source, laser interferometer system in comparison with conventional methods of generation and detection will be a limiting factor in the application of laser generated acoustics to NDE. In view of this fact it is important to identify those areas of NDE in which the use of a laser-acoustic system would be viable, and then to direct the further investigation of the potential NDE techniques to these specific areas.

Testing methods incorporated conventional piezoelectric transducers are likely to be continued to be used for the majority of NDE applications. However, the laser-acoustic source has been shown to have unique properties which could be usefully applied to some of the problems encountered in NDE.

## APPENDIX 1

## NUMERICAL AND COMPUTATIONAL METHODS

This appendix contains a brief description of the numerical and computational details required to generate some of the information given in the previous chapters. Only those programs are included which require an additional explanation to that given in the main text.

The programs were written in Algol68-R for implementation on an ICL2960 mainframe. A description of the program is given followed by the program listing.

## A.1 CHAO'S SOLUTION FOR SURFACE DISPLACEMENT

This program evaluates the vertical displacement of a half-space at some point  $R$ , due to a horizontal surface force with Heaviside time dependence acting at the origin. The program uses the two sub-routines PIELLIP and KELLIP given in A.2 to evaluate the values of the elliptic integrals.  $R$  is the source-observer separation and  $MU$  is the Lamé elastic constant of the material.

```

C*GENERATES VERTICAL DISPLACEMENT OF A HALF-SPACE DUE
C* TO A POINT C*
C* TANGENTIAL LOADING WITH HEAVISIDE TIME DEPENDANCE C
C* CHAO'S WITH CDB1, DEVPAP, GRAF, DEVENU, PIELLIP,
C* KELLIP
C* FROM ROUTINES

BEGIN
  (REAL' R, MU, FRP, FRM, TRP, TRM, W, N, GA, R3;
  (Q : 499) REAL' T, UZ;
  MU := 2.7810;
  R := 3.308-2;
  R3 := SQRT(3);

```

```

FRP := (4 * R3 + 6);
FRM := (4 * R3 - 6);
TRP := (12 * R3 + 20);
TRM := (12 * R3 - 20);
GA := SQRT(3 + R3) / 2;
FOR I FROM 0 TO 499 DO
  BEGIN
    TCID := I + 2 / 499;
    M := (3 + TCID * TCID - 1) / 2;
    N := 1 / M;
    IF TCID < 1 / R3
    THEN UZCID := 0.0
    ELSE IF TCID < 1
    THEN UZCID := SQRT(6) * TCID / (32 * PI * PI
      + MU * R
      );
    UZCID := UZCID * (6 * KELLIP(M) - 18 *
      PIELLIP(8 * M * M,
      M
      ) - FRM * PIELLIP(-
      1 + TRM * M * M,
      M
      ) + FRP * PIELLIP(
      TRP * M * M,
      M
      )
      );
    ELSE IF TCID < GA
    THEN UZCID := SQRT(6 * M) * TCID / (32
      * PI * PI + MU * R
      );
    UZCID := UZCID * (6 * KELLIP(N)
      - 18 * PIELLIP(8.0,
      N
      ) - FRM * PIELLIP(-
      1 + TRM,
      N
      ) + FRP * PIELLIP(
      TRP,
      N
      )
      );
    ELSE UZCID := SQRT(6 * M) * TCID / (32
      * PI * PI + MU * R
      );
    UZCID := UZCID * (6 * KELLIP(N)
      - 18 * PIELLIP(8.0,
      N
      ) - FRM * PIELLIP(-
      1 + TRM,
      N
      ) + FRP * PIELLIP(
      TRP,
      N
      )
      );
  END;

```

```

                                UZ[I] 'PLUS' TC[I] / (8 * PI * MU
                                                * R * SQRT(TC[I]
                                                * TC[I] - GA * GA
                                                )
                                                )
                                'FI'
                                'FI'
                                'FI';
                                PRINT((NEWLINE, TC[I] * R / 3130, UZ[I]))
                                'END'
                                'END'
                                'FINISH'

```

## A.2 THE ELLIPTIC INTEGRALS

These two sub-routines evaluate the complete elliptic integrals of the first and third kinds respectively using a 100 point composite Simpson's numerical integration.

```

'C' GENERATES COMPLETE ELLIPTIC INTEGRAL OF THE THIRD KIND 'C'
KELLIP
'BEGIN'
  'INT' I;
  'PROC' KELLIP = ('REAL' K) 'REAL':
    'BEGIN' 'REAL' H, K1;
      'INT' J;
      J := 100;
      K1 := 0.0;
      H := PI / 2 / J;
      'FOR' I 'BY' 2 'TO' J - 1 'DO'
        (K1 'PLUS' (4.0 / SQRT(1 - K * K * SIN(I * H) * SIN(I
          * H
          )
          )
        );
      );
      'FOR' I 'FROM' 2 'BY' 2 'TO' J - 2
      'DO'
        (K1 'PLUS' (2.0 / SQRT(1 - K * K * SIN(I * H) * SIN(I
          * H
          )
          )
        );
    );

```

```

K1 'PLUS' (1 + 1 / SQRT(1 - K * K));
K1 'TIMES' (H / 3);
(K1)

```

```
'END';
```

```
I := 1
```

```
'END'
```

```
'KEEP' KELLIP
```

```
'FINISH'
```

```
'C'GENERATES COMPLETE ELLIPTIC INTEGRAL OF THE FIRST KIND'C'
PIELLIP
```

```
'BEGIN'
```

```
'INT' I;
```

```
'PROC' FUN = ('REAL' Y, X, TH)'REAL':
```

```

'BEGIN' (1.0 / (1 + Y * SIN(TH) * SIN(TH)) / SQRT(1 - X * X * SIN(
TH
) * SIN(TH)
)
)

```

```
'END';
```

```
'PROC' PIELLIP = ('REAL' Y, X)'REAL':
```

```
'BEGIN' 'REAL' H, PY;
```

```
'INT' N := 100;
```

```
PY := 0.0;
```

```
H := PI / 2 / N;
```

```
'FOR' I 'BY' 2 'TO' N - 1 'DO'
```

```
(PY 'PLUS' 4 * FUN(Y, X, I * H));
```

```
'FOR' I 'FROM' 2 'BY' 2 'TO' N - 2
```

```
'DO'
```

```
(PY 'PLUS' (2 * FUN(Y, X, I * H)));
```

```
PY 'PLUS' (FUN(Y, X, 0.0) + FUN(Y,
```

```
X,
```

```
PI / 2
```

```
)
```

```
);
```

```
PY 'TIMES' (H / 3);
```

```
(PY)
```

```
'END';
```

```
I := 1
```

```
'END'
```

```
'KEEP' PIELLIP
```

```
'FINISH'
```

## A.3 THE EXTENDED THERMOELASTIC SOURCE

The program uses the data generated by the program given in A.1 for the vertical displacement of a half-space due to a horizontal force. The effect of an extended force distribution is simulated by numerically integrating across the distribution using eqs. 4.5 and 4.6. DI is the Gaussian diameter of the source and D is the source-observer separation.

```

'C' SIMULATES EFFECT OF A GAUSSIAN DISTRIBUTION, EXTENDED 'C'
'C' THERMOELASTIC SOURCE 'C'
THERMO 'WITH' DEVEND, GRAF, DEVPAF, CCB1 'FROM' :LIB.GIND-A68

'BEGIN'

  'REAL' DI := 1&-3, D := 3.3&-2, E := 71&9, AL := 23&-6,
    EA := 3&-3, C := 913.0, RH := 2.7&3;
  'REAL' F, F0, SD, RR;
  'INT' I, K, L;
  [1 : 500] 'REAL' A, T, B;
  SD := DI / 2;
  F0 := E * AL * EA * 3 / (2 * C * RH * PI * SD * SD);
  'PROC' ARCDINT = ('REAL' RR, D, DI) 'REAL':
    'BEGIN' 'REAL' THM, TH, B, C, E, SD;
      SD := DI / 2;
      B := D - RR;
      THM := (B * B + D * D - 36 * SD * SD) / (2 * B * D);
      'IF' 'ROUND' (1000 * THM) = 1000
      'THEN' THM := 0.0
      'ELSE' THM := ARCCOS(THM)
      'FI';
      C := 0.0;
      E := 0.0;
      'FOR' J 'TO' 500 'DO'
        'BEGIN' TH := THM * (J - 1) / 499;
          TH := COS(TH);
          E := EXP(- 1 * (B * B + D * D - 2 * B * D
            * TH
            ) / SD / SD
            ) * (D * TH - B) / SQRT(B * B
            + D * D - 2 * B
            * D * TH
            );

```

```

          E := E * THM / 500;
          C 'PLUS' E
        'END';
      C := C * B * 2;
      (C)
    'END';

  'FOR' I 'TO' 500 'DO'
    (READ((TCIJ, ACIJ)));
    BCIJ := 0.0
  );
  'FOR' L 'FROM' 0 'TO' 299 'DO'
    'BEGIN' RR := 6 * SD - L * 12 * SD / 299;
      F := F0 * ARCINT(RR, D, DI) * 12 * SD / 300;
      'FOR' I 'TO' 500 'DO'
        'BEGIN' K := 'ROUND' (I * (1 - RR / D));
          'IF' K > 500
            'THEN' K := 500
          'FI';
          BCIJ 'PLUS' F * A[K]
        'END'
      'END';
  'FOR' I 'TO' 500 'DO'
    (PRINT((NEWLINE, TCIJ, BCIJ / 300)))
  'END'

'FINISH'

```

#### A.4 THE POINT THERMOELASTIC SOURCE

The program evaluates the expression for the vertical displacement of a surface due to a point, radial loading, given by eq. 4.45. The integrations are carried out using a 100 point composite Simpson's routine which is arranged to avoid the singularities in the expression.

```

'COMMENT GENERATES VERTICAL DISPLACEMENT DUE TO A POINT, RADIAL
LOADING'
'COMMENT OF A HALF-SPACE WITH HEAVISIDE TIME DEPENDANCE'
POINT

'BEGIN'

  'INT' S1, S2, S3;
  'REAL' RAT, W1, F, F1, G, GP, CD, A, B, C, D;
  [1 : 400] 'REAL' W, T;
  'PROC' INTEGRATE = ('PROC' ('REAL', 'REAL', 'REAL') 'REAL' FUNC,
    'REAL' LL, UL, TI, RAT, 'INT' NU)
    'REAL';

```

```

'BEGIN' 'REAL' H, INSTEP, INT, CHECK;
INSTEP := INT := CHECK := 0.0;
'IF' 'ENTIER' (1000 * (UL - LL)) > 0
'THEN' H := (UL - LL) / NU;
      INT 'PLUS' FUNC(LL, TI, RAT);
      'FOR' J 'BY' 2 'TO' NU - 1
      'DO'
          (INT 'PLUS' 4 * FUNC(LL + J * H,
                               TI,
                               RAT
                              )
          );
      'FOR' J 'FROM' 2 'BY' 2 'TO' NU - 2
      'DO'
          (INT 'PLUS' 2 * FUNC(LL + J * H,
                               TI,
                               RAT
                              )
          );
      INT 'TIMES' (H / 3)
'ELSE' INT := 0.0
'FI';
(INT)
'END';

'PROC' FUNC1 = ('REAL' N, T, RAT) 'REAL':
'BEGIN' 'REAL' FUN;
FUN := N * N * N * (1 - 2 * N * N) + SQRT(1 - N * N) *
      SQRT(N * N - 1 / 3);
FUN := FUN / ((0.25 - N * N) * (C * C - N * N) * (D * D
      - N * N
      ) * SQRT(T * T
      - N * N
      )
      );
(FUN)
'END';

'PROC' FUNC2 = ('REAL' N, T, RAT) 'REAL':
'BEGIN' 'REAL' FUN;
FUN := N * N * N * ((A * A - N * N) * (B * B - N * N)
      + 2 * (1 - 2 * N * N) * SQRT(N * N
      - 1
      ) * SQRT(N * N
      - 1 / 3
      )
      );
FUN := FUN / ((0.25 - N * N) * (C * C - N * N) * SQRT(T
      * T - N * N
      )
      );
(FUN)
'END';

```

```

RAT := SQRT(1 / 3);
D := 0.5 * SQRT(3 + SQRT(3));
A := 0.5 * SQRT(5 + SQRT(13));
B := 0.5 * SQRT(5 - SQRT(13));
C := 0.5 * SQRT(3 - SQRT(3));
S1 := 'ROUND' (RAT * 400 / 2);
S2 := 'ROUND' (400 / 2);
S3 := 'ENTIER' (D * 400 / 2);
'FOR' I 'TO' 400 'DO'
  'BEGIN' T[I] := I / 200;
    'IF' I <= S1
      'THEN' W[I] := 0.0
      'ELSE' 'IF' I < S2
        'THEN' W[I] := INTEGRATE(FUNC1,
          RAT,
          T[I],
          T[I],
          RAT,
          100
        )
      'ELSE' 'IF' I = S2
        'THEN' W[I] := W[I - 1]
      'ELSE' 'IF' I <= S3
        'THEN' W[I] := INTEGRATE(FUNC1,
          RAT,
          2 * S2 / 400,
          T[I],
          RAT,
          100
        )
      'ELSE' W[I] := INTEGRATE(FUNC1,
        RAT,
        S2 * 2 / 400,
        T[I],
        RAT,
        100
      ) + PI / 4 * FUNC2(D,
        T[I],
        RAT
      )
    'FI'
  'FI'
'END';

'FOR' I 'TO' 399 'DO'
  (PRINT((NEWLINE, T[I], 200 * (W[I + 1] - W[I]) / 2 / 400))
'END'

'FINISH'

```

#### A.5 NUMERICAL BANDWIDTH LIMITATION

The sub-routine simulates the effect of a finite bandwidth detection system by taking the original waveform and convolving it with an approximation to the system impulse response.

A particular system bandwidth could be imposed on a signal by Fourier transforming the time signal, multiplying the resulting spectrum by the frequency response of the system, and then Fourier transforming back into the time domain. A simpler numerical method is carried out here by imposing the bandwidth limitation on the time domain signal directly. The multiplication by the system frequency response in the frequency domain may be replaced by a convolution with the system impulse response in the time domain, and this convolution may be carried out by the relatively simple method of serial products. The impulse response may itself be obtained from frequency response by a Fourier transform. If the frequency response is assumed to have a Gaussian profile centred on zero frequency then the Fourier transform may be evaluated explicitly. The system frequency response is given as

$$R(f) = e^{-f^2/\Delta f^2} \quad \text{A1}$$

where  $R(f)$  is the system response as a function of frequency, and  $\Delta f$  is the Gaussian frequency bandwidth. The Fourier transform of this gives

$$R(t) = \int_{-\infty}^{\infty} e^{-f^2/\Delta f^2} e^{-ift} df = \sqrt{\pi} \Delta f e^{-t^2 \Delta f^2 / 4} \quad \text{A2}$$

where  $R(t)$  is now the system impulse response in the time domain. This impulse response is centred on  $t = 0$  and is therefore shifted six standard deviations towards the positive time direction. After convolution the resulting time signal is shifted back by the same amount. The convolution of the displacement waveform with this function is carried out using the method of serial products described in section 4.6.

```

'C'IMPOSES A BANDWIDTH LIMITATION ON A TIME DEPENDANT SIGNAL'C'
'C'BY CONVOLUTION WITH THE SYSTEM IMPULSE RESPONSE'C'
BANDWIDTH

'BEGIN'

  'PROC' BANDWIDTH = ([ ]'REAL' DATA, 'REAL' DF,
                    MT)[ ]'REAL':
    'BEGIN' 'REAL' DT, SD;
      'INT' CENT, L, U;
      L := 'LWB' DATA;
      U := 'UPB' DATA;
      [0 : U - L]'REAL' IMP, DAT;
      [L : U]'REAL' OUT;
      'FOR' I 'FROM' L 'TO' U 'DO'
        (DAT[I - L] := DATA[I];
         OUT[I] := 0.0
        );
      DT := MT / (U - L + 1.0);
      SD := 2 / DF / DT;
      CENT := 'ROUND' (6.0 * SD);
      'FOR' I 'FROM' 0 'TO' U - L 'DO'
        (IMPI[I] := DF * SQRT(PI) * EXP(- 1 * (I - CENT) ^ 2
                                         / SD / SD
        )
        );
      'FOR' I 'FROM' CENT 'TO' U - L 'DO'
        'BEGIN' 'FOR' J 'FROM' 0 'TO' I
          'DO'
            'BEGIN' OUTCI - CENT + LJ 'PLUS' DATEJJ
              * IMPI - JI * DT
            'END'
          'END';
        'FOR' I 'FROM' U - CENT + 1 'TO' U
          'DO'
            (OUTCI := 0.0);
          (OUT)
        'END';
      'SKIP'
    'END'
'KEEP' BANDWIDTH
'FINISH'

```

## A.6 WAVEFRONT AMPLITUDE DIRECTIVITY

These sub-routines calculate the amplitude of the wavefront arrivals for the different acoustic modes for the normal and tangential driving forces. The form of the directivities are described by eqs. 5.8, 5.12, 5.16 and 5.17, and where the result is complex, the sub-routine returns both the real and imaginary components.

```

'C'AMPLITUDE DIRECTIVITY OF RADIAL DISPLACEMENT'C'
'C'DUE TO NORMAL SURFACE LOAD'C'

```

```
PLRAD
```

```
'BEGIN'
```

```
'PROC' PLRAD = ('REAL' TH, K)'REAL':
```

```
'BEGIN' 'REAL' D1, D2, D3, S1:
```

```
S1 := SIN(TH);
```

```
D1 := COS(TH) * (K * K - 2 * S1 * S1):
```

```
D2 := 4 * S1 * S1 * SQRT(1 - S1 * S1) + SQRT(K * K
- S1 * S1
):
```

```
D3 := (K * K - 2 * S1 * S1) ↑ 2:
```

```
D1 / (D2 + D3)
```

```
'END':
```

```
'SKIP'
```

```
'END'
```

```
'KEEP' PLRAD
```

```
'FINISH'
```

```

'C' AMPLITUDE DIRECTIVITY OF RADIAL DISPLACEMENT 'C'
'C' DUE TO DIPOLAR SURFACE LOAD 'C'
THRAD

```

```

'BEGIN'

```

```

'PROC' THRAD = ('REAL' TH, K) 'REAL':
  'BEGIN' 'REAL' D1, D2, D3, S1;
    S1 := SIN(TH);
    D1 := S1 * SIN(2 * TH) * SQRT(K * K - S1 * S1);
    D2 := 4 * S1 * S1 * SQRT(1 - S1 * S1) * SQRT(K * K
      - S1 * S1
    );
    D3 := (K * K - 2 * S1 * S1) ↑ 2;
    D1 / (D2 + D3)
  'END';

```

```

'SKIP'

```

```

'END'
'KEEP' THRAD
'FINISH'

```

```

'C' AMPLITUDE DIRECTIVITY OF TANGENTIAL DISPLACEMENT 'C'
'C' DUE TO NORMAL SURFACE LOAD 'C'
PLTHET

```

```

'BEGIN'

```

```

'PROC' PLTHET = ('REAL' K, TH, 'REF' 'REAL' DIRRE,
  DIRRE) 'VOID':
  'BEGIN' 'REAL' D1, D2, D3, S1;
    S1 := SIN(TH);
    'IF' K * S1 < 1
      'THEN' D1 := SIN(2 * TH) * SQRT(1 - K * K * S1 * S1);
        D2 := 4 * S1 * S1 * SQRT(1 - K * K * S1 * S1) *
          SQRT(1 - S1 * S1);
        D3 := K * (1 - 2 * S1 * S1) ↑ 2;
        DIRRE := D1 / (D2 + D3);
        DIRIM := 0.0
      'ELSE' D1 := SIN(2 * TH) * SQRT(K * K * S1 * S1 - 1);
        D2 := 4 * S1 * S1 * SQRT(1 - S1 * S1) * SQRT(K
          * K * S1 * S1
          - 1
        );
        D3 := K * (1 - 2 * S1 * S1) ↑ 2;
        DIRRE := D1 * D2 / (D2 * D2 + D3 * D3);
        DIRIM := D1 * D3 / (D2 * D2 + D3 * D3)
    'FI'
  'END';

```

```

'SKIP'

```

```

'END'
'KEEP' PLTHET
'FINISH'

```

```

'C'AMPLITUDE DIRECTIVITY OF TANGENTIAL DISPLACEMENT'C'
'C'DUE TO A DIPOLAR SURFACE LOAD'C'
TTHET

```

```

'BEGIN'

```

```

'PROC' TTHET = ('REAL' K, TH, 'REF''REAL' DIRIM,
               DIRRE)'VOID':
  'BEGIN' 'REAL' D1, D2, D3, S1;
    S1 := SIN(TH);
    'IF' K * S1 < 1
      'THEN' D1 := SIN(2 * TH) * (1 - 2 * S1 * S1);
            D2 := 4 * S1 * S1 * SQRT(1 - S1 * S1) * SQRT(1
            - K * K * S1 * S1
            );
            D3 := K * (1 - 2 * S1 * S1) ↑ 2;
            DIRRE := D1 / (D2 + D3);
            DIRIM := 0.0
        'ELSE' D1 := SIN(2 * TH) * (1 - 2 * S1 * S1);
            D2 := 4 * S1 * S1 * SQRT(1 - S1 * S1) * SQRT(K
            * K * S1 * S1
            - 1
            );
            D3 := K * (1 - 2 * S1 * S1) ↑ 2;
            DIRRE := D1 * D3 / (D2 * D2 + D3 * D3);
            DIRIM := - 1 * D1 * D2 / (D2 * D2 + D3 * D3)
    'FI'
  'END';

```

```

'SKIP'

```

```

'END'

```

```

'KEEP' TTHET

```

```

'FINISH'

```

## A.7 ENERGY PARTITION OF THE LASER-ACOUSTIC SOURCE

The program evaluates the ratio of energies in the wavefront arrivals for the plasma and thermoelastic sources from eq. 5.18. The angular variation of the wavefront amplitudes are given by the sub-routines in A.6. The magnitude of the directivity term is taken if the value is complex. The wavefront energy is numerically integrated between  $0^\circ$  and  $\pi/2$  by simple addition. The integration step is not included since it would be removed in the ratio process.

```

'C'CALCULATES ENERGY PARTITION BETWEEN DIFFERENT'C'
'C'ACOUSTIC MODES AND DRIVING FORCES'C'
POWER 'WITH' PLRAD, THRAD, PLTHET, THTHET 'FROM' ROUTINES

```

```
'BEGIN'
```

```

'REAL' CT, K, POIS, INTP, INTT, AN, E, F, M, N,
      RE, IM;
CT := 3.2&3;
POIS := 0.2;
K := SQRT((2 - 2 * POIS) / (1 - 2 * POIS));
E := F := M := N := 0.0;
'FOR' I 'FROM' 0 'TO' 360 'DO'
  'BEGIN' AN := I * PI / 180 / 4;
          RE := PLRAD(AN, K);
          E 'PLUS' (RE * RE * SIN(AN));
          PLTHET(K, AN, IM, RE);
          F 'PLUS' ((RE * RE + IM * IM) * SIN(AN));
          RE := THRAD(AN, K);
          M 'PLUS' (RE * RE * SIN(AN));
          THTHET(K, AN, IM, RE);
          N 'PLUS' ((RE * RE + IM * IM) * SIN(AN))

```

```
  'END';
```

```

INTP := K * E / F;
INTT := 4 * M / (K * K + K * N);
PRINT((NEWLINE, "POISSON'S RATIO = ", POIS));
PRINT((NEWLINE, "PLASMA-L/S ENERGY RATIO = ",
      INTP));
PRINT((NEWLINE, "THERMOELASTIC-L/S RATIO = ",
      INTT))

```

```
'END'
```

```
'FINISH'
```

## A.8 THE SPHERICAL CAPACITANCE PROBE

The following programs calculate the static capacitance, variation of capacitance with gap, and induced charge density on a plane for a spherical conductor adjacent to a plane conductor from eqs. 7.3 and 7.9. The series solutions are evaluated by iteration until there is convergence to within 1 part in  $10^6$ .

```
'C'CAPACITANCE OF SPHERE NEXT TO A PLANE'C'
'C'IS CALCULATED FROM A SERIES SOLUTION BY ITERATION'C'
CAPAC
```

```
'BEGIN'
```

```
[1 : 499]'REAL' GAP, CAP;
'REAL' E, A, R, CO, DR, CA, D, RN;
'INT' I;
E := 8.854E-12;
A := 2.0E-3;
'FOR' J 'TO' 499 'DO'
  'BEGIN' GAPCJJ := J / 499 * 20E-6;
    D := GAPCJJ + A;
    R := D / A + SQRT(D * D / A / A - 1);
    CO := 0.0;
    CA := 0.0;
    RN := 1.0;
    I := 1;

    'WHILE' 'ABS' CO < 1E-6
      'DO'
        'BEGIN' RN 'TIMES' R;
          DR := 1 / (RN + 1) + 1 / (RN - 1);
          CA 'PLUS' DR;
          I 'PLUS' 1;
          CO := CA / DR;
        'END';
    CAPCJJ := CA * 4 * PI * E * SQRT(D * D - A * A);
    PRINT((NEWLINE, GAPCJJ, CAPCJJ))
```

```
'END'
```

```
'END'
```

```
'FINISH'
```

```
'C' CHARGE INDUCED ON A PLANE UNDER A SPHERE CALCULATED
  BY ITERATION'C'
CHARGE
```

```
'BEGIN'
```

```
'REAL' A, Q, X0, M, G, D, XN, DN, QN, RHO, RHO1,
  CO;
[- 200 : 200]'REAL' X, R;
'INT' I;
Q := 1.0;
X0 := 0.0;
A := 2.0E-3;
G := 1.0E-5;
D := 2 * (G + A);
M := A / D;
```

```

'FOR' J 'FROM' - 200 'TO' 200 'DO'
  'BEGIN' X[J] := J * A / 200;
    RHO := 0.0;
    CO := 0.0;
    I := 0;
    QN := Q;
    XN := X0;

    'WHILE' CO < 1.0E-6
      'DO'
        'BEGIN' XN := M * A / (1 - XN / D);
          QN := QN * XN / A;
          DN := (D / 2 - XN);
          RHO1 := SQRT(XEJJ * XEJJ + DN * DN) ↑ 3;
          RHO1 := - 1.0 * QN * DN / (RHO1 * 2 * PI);
          RHO 'PLUS' RHO1;
          CO := RHO / RHO1;
          I 'PLUS' 1
        'END';
      R[C] := 'ABS' RHO;
      PRINT((NEWLINE, X[J], R[C]))
    'END'
  'END'

```

```
'END'
```

```
'FINISH'
```

```
'C' VARIATION OF CAPACITANCE WITH GAP CALCULATED 'C'
```

```
'C' FROM SERIES SOLUTION BY ITERATION 'C'
```

```
CAPAC
```

```
'BEGIN'
```

```

D1 : 499 'REAL' GAP, CAP;
'REAL' E, A, R, CO, DR, CA, D, RN;
'INT' I;
E := 8.854E-12;
A := 2.00E-3;
'FOR' J 'TO' 499 'DO'
  'BEGIN' GAP[J] := J / 499 * 10E-6 + 2E-6;
    D := GAP[J] + A;
    R := D / A + SQRT(D * D / A / A - 1);
    CO := 0.0;
    CA := 0.0;
    RN := 1.0;
    I := 1;

    'WHILE' 'ABS' CO < 1E-6
      'DO'
        'BEGIN' RN 'TIMES' R;

```

```

DR := RN / (RN * RN - 1) * ((R * R + 1) / (R
      * R - 1
      ) - I * ((RN * RN
      + 1
      ) / (RN * RN
      - 1
      )
      )
      );
CA 'PLUS' DR;
I 'PLUS' 1;
CO := CA / DR
'END';
CAPIJJ := CA * 8 * PI * E;
PRINT((NEWLINE, GAPIJJ, CAPIJJ))
'END'
'END'
'FINISH'

```

## CHAPTER 1 - REFERENCES

- A.M. Aindow, R.J. Dewhurst, D.A. Hutchins, S.B. Palmer, J.A.S.A., V69, N2, p449, 1981.
- A.M. Aindow, R.J. Dewhurst, S.B. Palmer, Opt. Comm., V42, N2, p116, 1982.
- Y. Bar-Cohen, B. J. NDT, March 1979.
- G. Birnbaum, G.S. White, Res. Tech. in NDT, V5, Ch8, ed. R.S. Sharpe, (Academic Press) 1984.
- A.N. Bondarenko, Yu. B. Drobot, Sov. J. NDT, V12, p655, 1976.
- M.J. Brienza, A.J. DeMaria, App. Phys. Lett., V11, N2, p44, 1967.
- C.A. Calder, W.W. Wilcox, Lawrence Livermore Report 16353, 1973.
- C.A. Calder, W.W. Wilcox, 6th World Conf. on Stress Analysis, Munich, P181, 1978
- D.A. Giglio, Harry Diamond Lab., HDL-73-32, Dec. 1973.
- D.A. Hutchins, R.J. Dewhurst, S.B. Palmer, Acoust. Lett. V4, N6, p95, 1980.
- D.A. Hutchins, R.J. Dewhurst, S.B. Palmer, Ultrasonics, p103, May 1981(a).
- D.A. Hutchins, R.J. Dewhurst, S.B. Palmer, J.A.S.A., V70, N5, p1362, 1981(b).
- R.E. Lee, R.M. White, App. Phys. Lett. V12, N1, p12, 1968.
- J.D. O'Keefe, C.H. Skeen, App. Phys. Lett. V21, N10, p465, 1972.
- P.S. Peercy, E.D. Jones, J.C. Bushnell, G.W. Gobeli, App. Phys. Lett., V16, N3, p120, 1970.
- C.M. Percival, J. App. Phys. V38, p5313, 1967.
- J.F. Ready, J. App. Phys. V36, N2, p462, 1965.

C.B. Scruby, R.J. Dewhurst, S.B. Palmer, J. App. Phys. V51, p6210, 1980.

C.B. Scruby, H.N.G. Wadley, R.J. Dewhurst, D.A. Hutchins, S.B. Palmer, Mat. Eval. V39, N13, p1250, 1981.

C.B. Scruby, R.J. Dewhurst, D.A. Hutchins, S.B. Palmer, J. App. Phys., V53, p4064, 1982(a).

C.B. Scruby, R.J. Dewhurst, D.A. Hutchins, S.B. Palmer, Res. Tech. in NDT, V7, Ch8, ed. R.S. Sharpe (Academic Press) 1982(b).

R.J. Von Gutfeld, R.L. Melcher, App. Phys. Lett., V30, N6, p257, 1977.

R.M.White, I.R.E. Trans. Instr. I-II, p294, 1962.

R.M. White, J. App. Phys. V34, N12, 1963.

R.J. Wellman, Harry Diamond Labs. Tech. Rep., No. HDL-TR-1902, May 1980.

D.A. Hutchins, R.J. Dewhurst, S.B. Palmer, App. Phys. Lett., V38, p677, 1981c.

## CHAPTER 2 - REFERENCES

- J.D. Achenbach, Wave Propagation in Elastic Solids (North Holland) 1980.
- O.F. Afandi, R.A. Scott, Int. J. Sol. Struct. V8, p1145, 1972.
- F.R. Breckenridge, C.E. Tschiegg, M. Greenspan, J.A.S.A., V57, N3, p626, 1975.
- L.J. Bond, Ultrasoncis, p71, March 1979.
- L. Cagnaird, Reflection and Refraction of Progressive Seismic Waves, trans. by E.A. Flinn, C.H. Dix, (McGraw-Hill), 1962.
- C.C. Chao, J. App. Mech. V27, p559, 1960.
- C.H. Dix, Geophys. V19, N4, 1954.
- A. Ilan, A. Ungar, Z. Alteman, Geophys. J.R. Astr. Soc., V43, p727, 1975.
- L.R. Johnson, Geophys. J.R. Astr. Soc., V37, p99, 1974.
- L. Knopoff, J. App. Phys., V29, N4, p651, 1958.
- C.L. Pekeris, Proc. N.A.S., Geophysics, V41, p469, 1955.
- Y.H. Pao, R.R. Gajewski, A.N. Ceranoglu, J.A.S.A., V65, N1, 1979.
- Lord Rayleigh, Proc. Lond. Math. Soc., V17, N4, 1887.
- H. Lamb, Phil. Trans. VCCIII-A, p359, 1904.
- S.P. Timoshenko, J.N. Goodier, Theory of Elasticity, 3rd Ed. (Mc-Graw-Hill) 1970.

## CHAPTER 3 - REFERENCES

- J.D. Achenbach, Wave Propagation in Elastic Solids, (North Holland) 1980.
- A.N. Aindow, J.A. Cooper, R.J. Dewhurst, S.B. Palmer, Report to UKAEA, Jan. 1984.
- K. Aki, P.G. Richards, Quantitative Seismology (Freeman) 1980.
- T.P. Hughes, Plasmas and Laser Light (Adam Hilger) 1975.
- D.A. Hutchins, R.J. Dewhurst, S.B. Palmer, Ultrasonics, V19, p103, 1981.
- N.C. Maiti, Pure and App. Geophys., V116, N1, p199, 1978.
- N.C. Maiti, M. Mitra, Bull. Seism. Soc. Am., V69, N3, p713, 1979.
- M. Mitra, Proc. Camb. Phil. Soc., V60, p683, 1964.
- J.F. Ready, Effects of High Power Laser Radiation (Academic) 1971.
- L.R.F. Rose, J.A.S.A., V75, N3, p723, 1984.
- C.B. Scruby, D.A. Hutchins, R.J. Dewhurst, S.B. Palmer, in Res. Tech. NDT, V5, Ch8, p281 (Academic) 1982.
- C.B. Scruby, D.A. Hutchins, R.J. Dewhurst, S.B. Palmer, J. Appl. Phys. V53, p4064, 1982.
- D.R. Stull, G.C. Sinke, Thermodynamic Properties of the Elements, Am. Chem. Soc., Advances in Chem. Series, No.18, 1956.

## CHAPTER 4 - REFERENCES

- J.D. Achenbach, Wave Propagation in Elastic Solids (North Holland) 1973.
- A.M. Aindow, J.A. Cooper, R.J. Dewhurst, S.B. Palmer, Quantum Electronics & Electro-Optics, ed. P.L. Knight (J. Wiley & Sons) 1983.
- A.M. Aindow, J.A. Cooper, R.J. Dewhurst, S.B. Palmer, 3rd Report to AERE Harwell in a 2nd Series, 1984.
- R. Bracewell, The Fourier Transform and its Applications, (McGraw-Hill) 1965.
- C. Chao, J. App. Mech. V27, p559, 1960.
- J.W. Cooley and J.W. Tukey, Math. Comput. V19, p297, 1965.
- B.A. Eisenstein, J. Frank. Inst., V302, N2, 1976.
- B.R. Hunt, IEEE Trans. Aut. Cont. V17, p703, 1972.
- D.A. Hutchins, R.J. Dewhurst, S.B. Palmer, Ultrasonics, p103, May 1981.
- G.W.C. Kaye, T.A. Laby, Tables of Physical and Chemical Constants, 14th ed. (Longman) 1973.
- L. Knopoff, J. App. Phys. V29, N4, 1958.
- H. Lamb, Phil. Trans. VCCIII, A, p359, 1904.
- N.W. McClachlan, Bessel Function for Engineers, 2nd ed. (Oxford Clarendon) 1955.
- H.M. Mooney, Bull. Seism., Soc. Am., V64, N2, p43, 1974.
- H.M. Mooney, Geophys. V41, N2, p243, 1976.
- Y.H. Pao, R.R. Gajewski, Physical Acoustics, VXIII, Ch6, The Generalised Ray Theory and Transient Response of Layered Elastic Solids, Ed. W.P. Mason & R.N. Thurston, (Academic Press) 1977.
- Y.H. Pao, R.R. Gajewski, A.N. Ceranoglu, J.A.S.A., V65, N1, 1979.

C.L. Pekeris, Proc. N.A.S. V41, p469, 1955.

C.L. Pekeris, Rev. Geophys., V3, p25, 1965.

R.L. Rhoads, IEEE Trans. Inst. Meas., V17, N4, 1968.

L.R.F. Rose, J.A.S.A., V75, N3, p723, 1984.

C.B. Scruby, H.N.G. Wadley, J. Phys. D, VII, p1487, 1978.

C.B. Scruby, R.J. Dewhurst, D.A. Hutchins, S.B. Palmer, J. Appl. Phys. V51, N12, p6210, 1980.

C.B. Scruby, R.J. Dewhurst, D.A. Hutchins, S.B. Palmer, J. Appl. Phys., V53, p4064, 1982.

M.G.Silk, Ultrasonic Transducers for NDT (Adam Hilger) 1984.

J.E. Sinclair, J. Phys. D, V12, p1309, 1979.

I.N. Sneddon, The Use of Integral Transforms (McGraw-Hill) 1972.

## CHAPTER 5 - REFERENCES

- M. Born, E. Wolf, Principles of Optics, (Pergamon) 1970.
- R. Burridge, L. Knopoff, Bull. Seism. Soc. Am. V54, N6, 1964.
- J.T. Cherry, Bull. Seism. Soc. Am., V52, N1, p27, 1962.
- L.Ya. Gutin, Sov. Phys. Acoust. V9, N3, Jan. 1964.
- D.A. Hutchins, R.J. Dewhurst, S.B. Palmer, J.A.S.A., V70, N5, p1362, 1981.
- A.E. Lord, J.A.S.A., V39, N4, p650, 1966.
- G.J. Miller, H. Pursey, Proc. Roy. Soc. A223, p52, 1954.
- Y.H. Pao, R.R. Gajewski, Physical Acoustics VXIII, Ch6, The Generalised Ray Theory and Transient Response of Layered Elastic Solids, eds. W.P. Mason & R.N. Thurston (Academic Press) 1977.
- L.R.F. Rose, J.A.S.A., V75, N3, p723, 1984.

## CHAPTER 6 - REFERENCES

R.J. Dewhurst, NDT Comm., V1, p93, 1983.

J. Krautkramer, H.Krautkramer, Ultrasonic Testing of Materials, 3rd ed. (Springer-Verlag) 1983.

C.B. Scruby, H.N.G. Wadley, R.J. Dewhurst, D.A.Hutchins, S.B. Palmer, Mat. Eval., V39, N13, p1250, 1981.

R.V. Williams, Acoustic Emission (Adam Hilger) 1980.

## CHAPTER 7 - REFERENCES

- J.C. Baboux, F. Lakestani, P. Fleischmann, M. Perdix, NDT Int., V10, p135, 1977.
- B.I. Bleaney. B. Bleaney, Electricity and Magnetism, 3rd ed. (Oxford Univ. Press) 1976.
- A.N. Bondarenko, Yu. B. Drobot, S.V. Kruglov, Sov. J. NDT, V12, p655, 1976.
- R.J. Dewhurst, D.A. Hutchins, S.B. Palmer, C.B. Scruby, Ultrasonics, p79, 1983.
- R.J. Dewhurst, D.A. Hutchins, S.B. Palmer, S.B. Scruby, J. App. Phys. V53, p4064, 1982.
- E.R. Dobbs, Electromagnetic Generation of Ultrasonic Waves, Physical Acoustics, VX, Ch 3, ed. W.P. Mason, R.N. Thurston (Academic Press) 1973.
- L.E. Drain, J.H. Speake, B.C. Moss, Displacement and Vibration Measurement by Laser Interferometry, SPIE, V136, 1977.
- D.A. Hutchins, F. Nadeau, IEEE Ult. Symp., p1175, 1983.
- W.A. Levett, Design, Construction and Evaluation of EMATS, Final Year Project Report, Dept. Appl. Phys. Hull Univ. 1984.
- L. Page, N.I. Adams, Principles of Electricity, 4th ed, (Van Nostrand) 1969.
- M. Redwood, J.A.S.A., V33, N4, p527, 1961.
- C.B. Scruby, H.N.G. Wadley, J. Phys. D, V11, p1487, 1978.
- M.G. Silk, Ultrasonic Transducers for NDT, (Adam Hilger) 1984.
- W. Smythe, Static & Dynamic Electricity, 3rd ed. (McGraw-Hill) 1968.
- J. Szilard, Ultrasonic Testing, ed. J. Szilard, Ch. 9, (J. Wiley & Sons) 1980.

## CHAPTER 8 - REFERENCES

D.P. Almond, R.L. Cox, M. Moghisi, H. Ruter, J. Thin Sol. Films, V83, p311, 1981.

J. Krautkramer, H. Krautkramer, Ultrasonic Testing of Materials, 3rd ed. (Springer-Verlag) 1983.

W.A. Levett, Design, Construction and Evaluation of EMATS, Final Year Project Report, Dept. Appl. Phys. Hull Univ. 1984.

A.C. Tam, Appl. Phys. Lett., V45, N5, 1984.

## CHAPTER 9 - REFERENCES

- A.M. Aindow, R.J. Dewhurst, S.B. Palmer, Optics Comm., V42, N2, p116, 1982.
- L.J. Bond, Ultrasonics, p71, March 1979.
- C.P. Burger, A.J. Testa, Proc. U.I. 81, p271, (Butterworth & Co.) 1981.
- D. Cooke, Brit. Acc. Soc., Spring Meeting, Loughborough, 1972.
- M. Hirao, H. Fukuoka, J.A.S.A. V72, N2, p602, 1982.
- R.J. Hudgell, L.L. Morgan, R.F. Lumb, V9, B.J. NDT, p144, Sept. 1974.
- B.H. Liddington, M.G. Silk, B.J. NDT, V17, p165, 1975.
- E.A. Lloyd, B.J. NDT, V17, p172, 1975.
- L.L. Morgan, Acustica, V30, p222, 1974.
- H. W. Reinhardt, J.W. Daly, Mat. Eval., V28, N10, p213, 1970.
- R.S. Sharpe, Research Technique in Non-destructive Evaluation, V6, Ch1 & 2, ed. R.S. Sharpe (Academic) 1982.
- J. Szilard, Ultrasonic Testing, (J. Wiley & Sons) 1982.
- I.A. Viktorov, Rayleigh and Lamb Waves, Physical Theory and Applications, (Plenum Press, N.Y.) 1967.
- C.H. Yew, K.G. Chen, D.L. Wang, J.A.S.A., V75, N1, p189, 1984.
- C.L. Pekeris, H. Lifson, J.A.S.A., V29, N11, p1233, 1957.